MASTER

SRI International

STRUCTURAL RESPONSE OF 1/20-SCALE MODELS OF THE CLINCH RIVER BREEDER REACTOR TO A SIMULATED HYPOTHETICAL CORE DISRUPTIVE ACCIDENT

Technical Report 4

October 1978

By: C. M. Romander and D. J. Cagliostro, Project Leader
Contributors: A. L. Florence, Project Supervisor
D. W. Ploeger

Prepared for:

U..S. Department of Energy
Reactor Research and Technology
Headquarters
Germantown, MD

Attention: J. D. Griffith
Assistant Director for Reactor Safety

Contract EY-76-C-03-115
189 No. SX 032

SRI Project PYU-3929

Approved:

G. R. Abrahamson, Director
Poulter Laboratory
Physical Sciences Division

SRI International

STRUCTURAL RESPONSE OF 1/20-SCALE MODELS OF THE CLINCH RIVER BREEDER REACTOR TO A SIMULATED HYPOTHETICAL CORE DISRUPTIVE ACCIDENT

Technical Report 4

October 1978

By: C. M. Romander and D. J. Cagliostro, Project Leader
Contributors: A. L. Florence, Project Supervisor
D. W. Ploeger

Prepared for:

U.S. Department of Energy
Reactor Research and Technology
Headquarters
Germantown, MD

Attention: J. D. Griffith
Assistant Director for Reactor Safety

Contract EY-76-C-03-115
189 No. SX 032

SRI International
333 Ravenswood Avenue
Menlo Park, California 94025
(415) 326-6200
Cable: SRI INTL MNP
TWX: 910-373-1246

Blank Page

ABSTRACT

Five experiments were performed to help evaluate the structural integrity of the reactor vessel and head design and to verify code predictions. In the first experiment (SM 1), a detailed model of the head was loaded statically to determine its stiffness. In the remaining four experiments (SM 2 to SM 5), models of the vessel and head were loaded dynamically under a simulated 661 MW-sec hypothetical core disruptive accident (HCDA). Models SM 2 to SM 4, each of increasing complexity, systematically showed the effects of upper internals structures, a thermal liner, core support platform, and torospherical bottom on vessel response. Model SM 5, identical to SM 4 but more heavily instrumented, demonstrated experimental reproducibility and provided more comprehensive data. The models consisted of a Ni 200 vessel and core barrel, a head with shielding and simulated component masses, an upper internals structure (UIS), and, in the more complex models SM 4 and SM 5, a Ni 200 thermal liner and core support structure. Water simulated the liquid sodium coolant and a low-density explosive simulated the HCDA loads.

In the static loading experiment, head deflection and strain were measured as a function of applied pressure. In the dynamic loading experiments, pressures were measured in the core, along the vessel wall, and on the cover. Strains were measured on the vessel wall, on selected UIS columns, and on studs that hold the models to the support stand. Accelerations were measured on the head and the core support platform.

No plastic deformations occurred in the shear rings or head in the four dynamically loaded models. The presence of the UIS in SM 3 significantly reduced the peak slug pressure (about 34%), compared with that in SM 2 which did not have a UIS. The peak vessel strain was 4.4% and occurred in SM 2 on the upper vessel wall after slug impact. The peak core barrel strain was 1.5% and occurred in SM 3. In the more complex

model SM 5, the increased stiffness (about 79%) of the vessel wall-thermal liner combination over that of SM 3 reduced peak upper wall strains from 2.8% in SM 3 to 1.9%.

Comparisons of the pre- and posttest GE-REXCO calculations with the experiments indicate that calculated strains and some loading pressure are overestimated, but impulses, and velocities are underestimated. The comparisons are better when high-strain-rate properties of Ni 200 are used in REXCO. Remaining differences between computations and experiments stem from the difficulty in modeling the core structure and the UIS in REXCO.

PREFACE

This report presents the results of four dynamic experiments on 1/20-scale models of the Clinch River Breeder Reactor (CRBR). Technical Report 3 on the static response of a 1/20-scale model of the CRBR head was submitted to DOE in July 1977 and is summarized in Appendix A of this report.*

The work was performed at SRI International, Menlo Park, California, during Fiscal Year 1977. Models were instrumented at SRI's Menlo Park facility and were tested at SRI's remote Corral Hollow Experimental Site (CHES) near Tracy, California.

*Technical Reports 1 and 2 describe work performed under this contract prior to FY 77 and are not directly related to the work described here.

Blank Page

ACKNOWLEDGMENTS

This work was performed under Contract EY-76-C-03-115 to the Energy Research and Development Administration (ERDA) (now Department of Energy, DOE), Division of Reactor Development and Demonstration. The project was performed under the administrative and technical guidance of S. Berk and H. Alter of DOE.

Designs of the models were provided by Westinghouse, Advanced Reactor Division (W-ARD). The design and technical support effort supplied by Westinghouse was the responsibility of L. E. Strawbridge with technical direction provided by A. M. Christie. The models were fabricated by Allied Engineering of Alameda, California, under the supervision of Ted Diaz.

High strain rate material properties tests were performed by Terra Tek, Incorporated, Salt Lake City, Utah, under the direction of R. J. Reid. Quality assurance guidance and assessment were provided by T. L. Bonnough of the Quality Assurance Branch of the Clinch River Breeder Reactor (CRBR) project office and by M. McKeown and R. Jake of the CRBR project office.

From the staff of Poulter Laboratory, SRI International, J. Busma and G. Greenfield coordinated the construction of the models and were responsible for ensuring that quality assurance procedures were properly implemented. The quality assurance program was devised and monitored by W. Wilkinson. Instrumentation layouts were designed by C. Blahnik, Instrumentation was installed by J. Hannigan. G. Greenfield was the lead technician on all the experiments. D. Walter and C. Benson provided technical support for the static experiments. R. Blomenkamp designed and implemented the electronic data retrieval system. An extensive team effort was required to complete the dynamic experiments. Key team members were C. Benson (model assembly), E. Eckert and D. Lee (electronics), A. Rehbock (explosives), and H. Rudnicki and K. Stepleton (photography). Data processing was performed by B. Bain.

Pretest predictions using the REXCO code were performed by E. C. Change and B. W. Joe of General Electric Company, Sunnyvale, California. These calculations were very helpful in setting up instrumentation for the experiments.

CONVERSION FACTORS FOR U.S.
CUSTOMARY TO METRIC (SI)
UNITS OF MEASUREMENT

To Convert from	To	Multiply by
atmosphere (normal)	kilo pascal (k Pa)	1.0133 E +2
bar	kilo pascal (k Pa)	1.0000 E +2
bar-second	newton-second/m^2 (N-s/m^2)	1.0000 E +5
degree (angle)	radian (rad)	1.7453 E -2
inch	meter (m)	2.5400 E -2
Megawatt-second (MW-s)	joule (J)	1.0000 E +6
mil	meter (m)	2.5400 E -5
pound force (lb)	newton (N)	4.4482
pound force/$in.^2$ (psi)	kilo pascal (k Pa)	6.8948

Blank Page

CONTENTS

ILLUSTRATIONS

TABLES

I INTRODUCTION

A. Background

One of the important concerns in the safety analysis of the Clinch River Breeder Reactor (CRBR) (Figure 1) is the release of radioactive core materials and coolant in the unlikely event of a hypothetical core disruptive accident (HCDA). During the HCDA of interest the UO_2 fuel overheats and melts, reaching a superheated state from which it begins to flash to vapor and expand out of the core. The expanding vapor loads the core structure and drives the sodium pool above the core upward to impact the three-plug head of the reactor (Figure 2). Failure of the shear, or margin rings which restrain the plugs from upward motion or gross deformation of the head under slug impact loading could provide leak paths for radioactive materials. The structural integrity, therefore, of the head following an HCDA is of importance in the licensing of the CRBR.

Complexity of the reactor vessel and internals design makes analytical hydrodynamic and structural modeling very difficult. Thus, it is prudent to perform experiments to verify structural integrity of the vessel and its cover. The experimental results can also be used to help verify and evaluate modeling techniques used in computer codes developed to anlayze the structural response of the CRBR to HCDA loadings. While the potential for an energetic HCDA is low, margin is provided in CRBR structures to accommodate such an energy release. This margin is provided through the requirement that CRBR withstand the Structural Margin Beyond the Design Base (SMBDB) loads [1]*. These loads and the resulting structural response are

*Numbers in brackets refer to References listed at the end of this report.

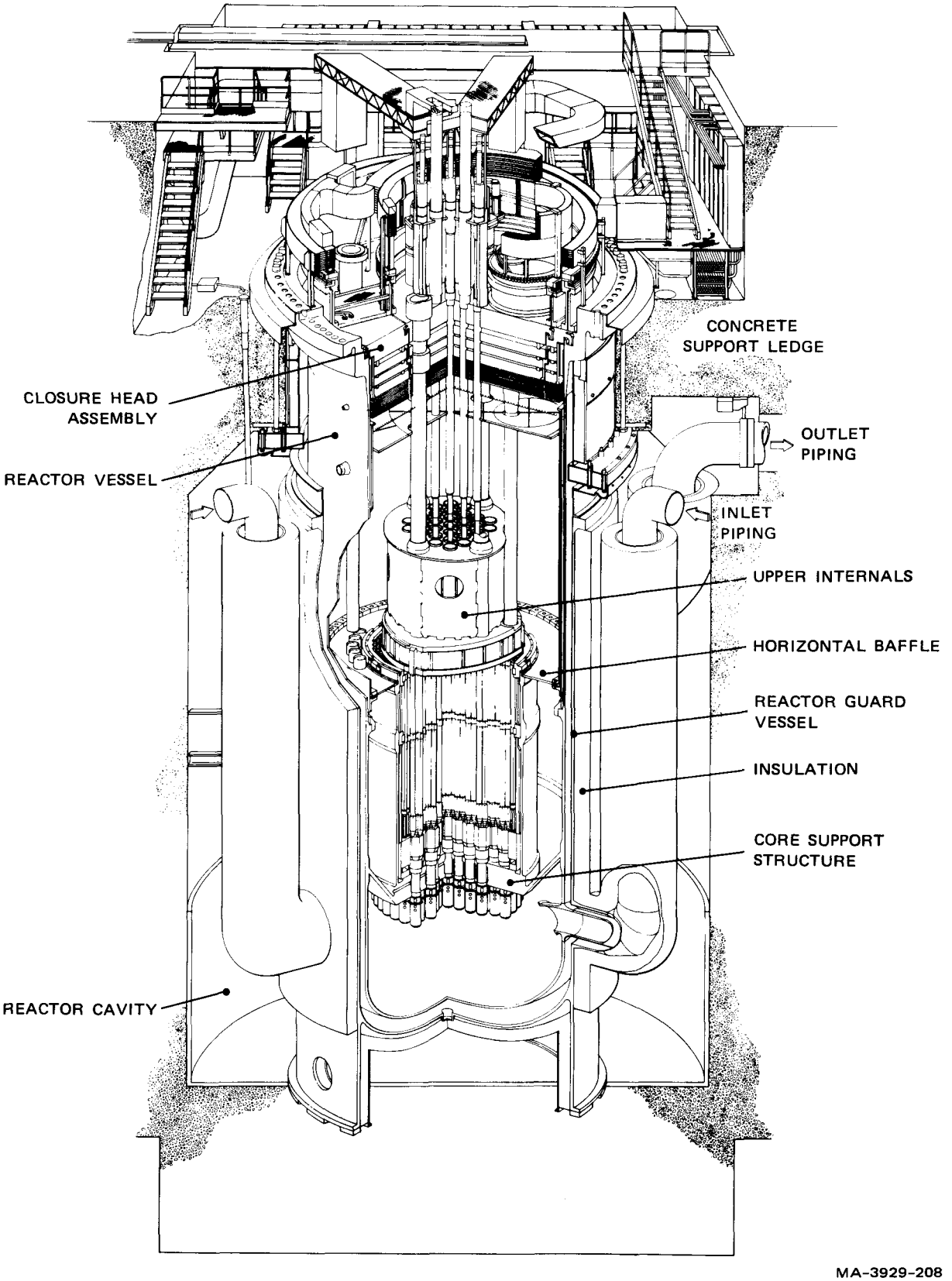

FIGURE 1 CLINCH RIVER BREEDER REACTOR

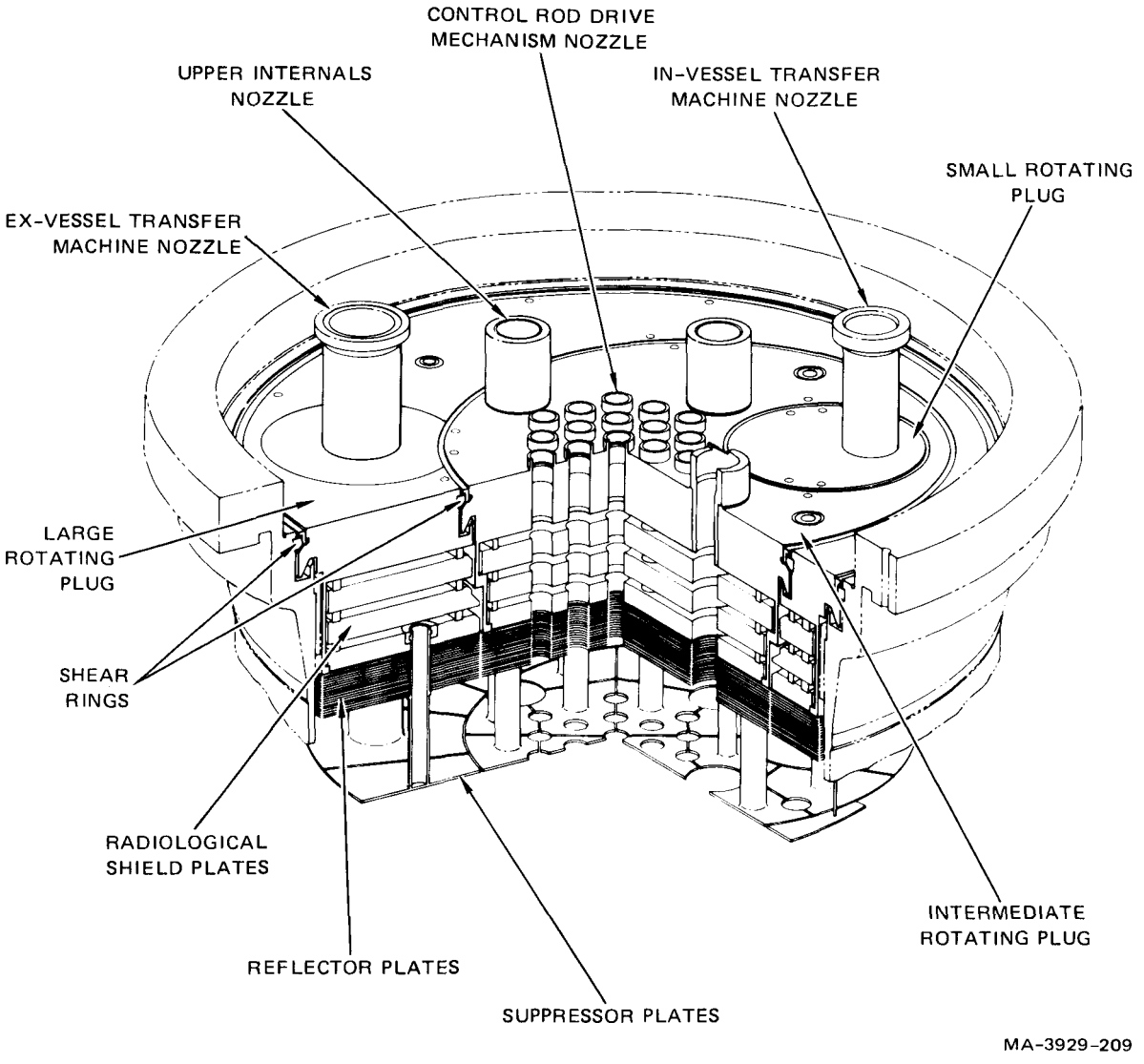

FIGURE 2 CLINCH RIVER BREEDER REACTOR ROTATING PLUG HEAD

simulated in this series of tests modeling techniques for pretest code predictions of dynamic head response. Results of this initial step are reported in Reference [2] and are summarized in Appendix A. The present report describes the results of four experiments on simple and complex models of the CRBR head and vessel under simulated SMBDB loads.

B. Objectives

The objectives are to experimentally determine the structural response of the CRBR to the simulated SMBDB loads, to evaluate the structural integrity of reactor vessel, vessel head, and other components under such loadings, and to contribute to the verification of modeling techniques used in such codes as REXCO and ANSYS [3, 4].

C. Approach

Four 1/20-scale models of the CRBR were tested. The first three, each of increasing complexity, were designed to provide a systematic approach to understanding the effects of upper planum internals structures, the thermal liner, the horizontal baffle, and the core support structure on the head load, and to facilitate the verification of modeling techniques used in computer codes. The fourth model was a more thoroughly instrumented duplicate of the most complex model. It was tested to demonstrate experimental reproducibility and to provide a comprehensive evaluation of the CRBR response.

Figure 3 shows schematics of the three types of models tested. Model SM 2, the simplest, includes a vessel wall of uniform thickness, a core barrel of uniform thickness lined with segmented steel rings to provide the proper core structure mass, a thick core support plate, and a simple one-plug head that is retained by a single shear ring around its perimeter. Slug impact pressures on the head and on the single shear ring were expected to be highest for this model because it does not have an upper internals structure to slow slug motion and redirect core energy. SM 2, therefore, represents the most conservative model for demonstrating the load capacity of the shear rings. Model SM 3 is identical to SM 2 except that it includes an upper internals structure (UIS)

that is suspended from the one-plug head by four tubular columns. SM 4 is more complex and more closely models the prototype. It includes a vessel with variable wall thickness, a thermal liner, a core support cone, a more detailed core support plate, a horizontal baffle, and a torospherical bottom head. The head includes three carefully scaled plugs and shear rings that model the prototype head.

The use of scale models in reactor safety experiments is well documented [5, 6]. To provide for a proper evaluation of the structural response of the CRBR, loading pressures, stress, strain, and slug velocity are the same in the 1/20-scale models as in the prototype. Strain rate and accelerations are not the same in these scale models. A more detailed list of the application of scale factors is given in Appendix G. Ni 200 was used in place of the 304 ss vessel materials because its stress-strain relationship at room temperature is approximately equal to that of 304 ss at reactor operating temperatures. Water was used to simulte the liquid sodium coolant because its density is close to that of liquid sodium. Use of nonprototypic materials such as Ni 200 in place of stainless steel and water in place of the liquid sodium has small effects on model response. [7]

The vessel walls and core barrels for each model were made from annealed Ni 200, The heads are made from Class 1 533-B carbon steel, which has mechanical properties similar to those of 508 carbon steel, the prototypic head material.* Tensile tests of both the nickel and 533-B steel were performed on specimens cut from parent material and heat treated along with the models as they were fabricated. Tensile tests performed at various strain rates showed that the stress-strain curves of the simulants are approximately the same as those of the prototype and provided reliable data to analyze the response of the models. Results of the material property tests are reported in Appendix B.

*533-B carbon steel was used to simulate 508 carbon steel because it is available in plate form whereas 508 carbon steel is available only as a forging.

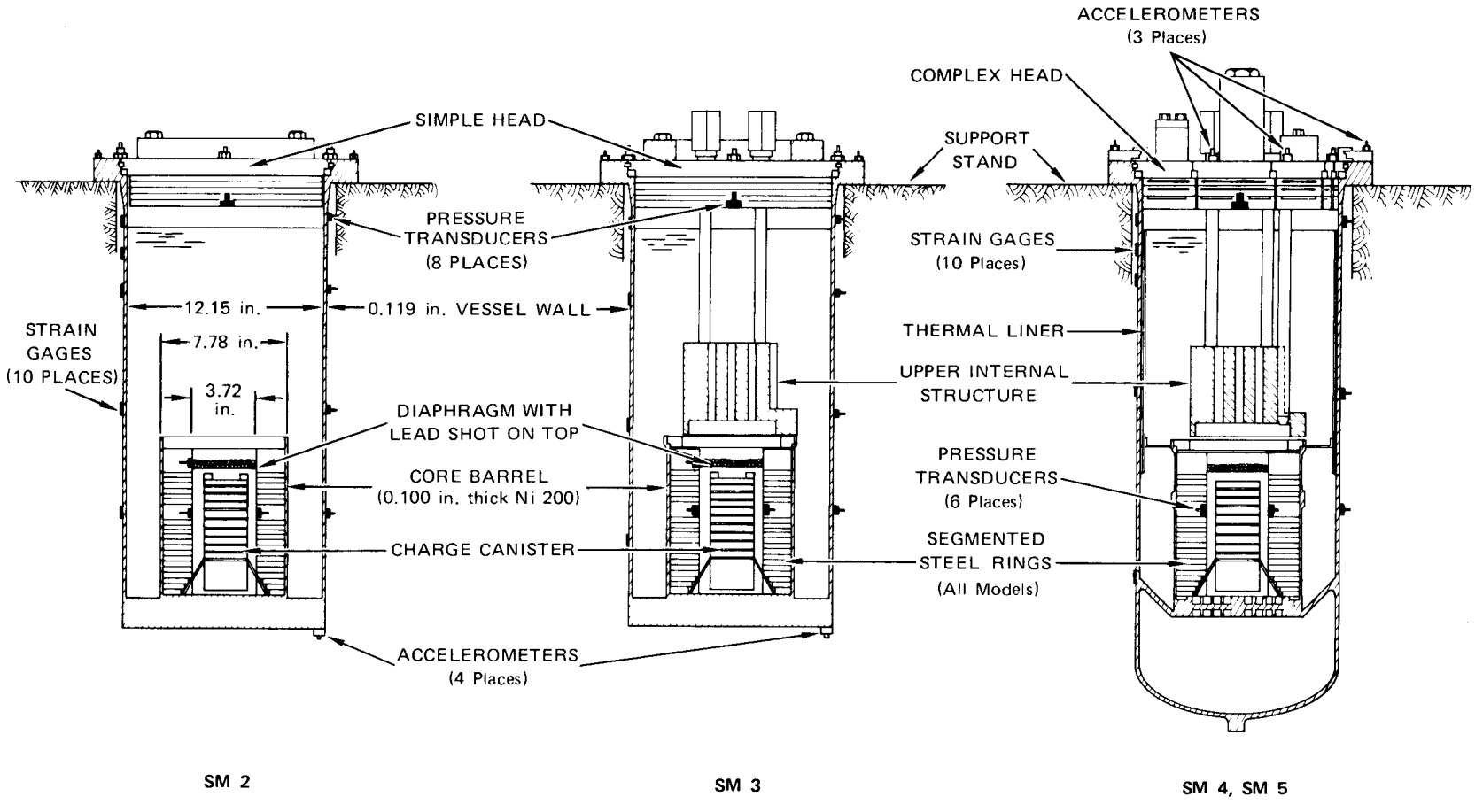

FIGURE 3 1/20-SCALE MODELS OF THE CRBR

The expansion of the detonation products from a low-density explosive is used to simulate the work potential of the HCDA. The work potential is 661 MW-sec for an expansion to one atmosphere. Use of the low-density explosive for simulating HCDA loads is well established and documented [5,8]. Calibration tests were performed in a rigid wall, rigid core, 1/20-scale model. These tests ensure that the selected explosive charge has a reproducible pressure-volume change relationship that is in good agreement with the SMBDB pressure-volume change relationship. To be conservative, we chose a charge mass that has a work potential that is about 5% greater than that of the scaled SMBDB work potential for an expansion to cover gas volume.

In the four dynamic experiments, loading pressures, vessel strains (axial and circumferential), and accelerations were measured. The final deformed shape profiles of the vessel wall, core barrel, and UIS columns were measured to evaluate the strain energy absorption by these parts and to provide a check on the strain gage measurements.

D. Summary of Results

The results can be summarized as follows:

- No plastic deformation of the shear rings or head occurred in any of the four dynamic experiments. The head remained tightly sealed by the O-rings above and below the shear rings in each experiment. The peak head pressure reached 5300 psi on SM 2, which resulted in the peak head acceleration of 4800 g.
- The upper internals structure significantly reduces the slug impact velocity, and hence, impact pressure. The peak impact pressure is reduced by 34% from 5300 psi on SM 2 to 3500 psi on SM 3. Consequently, there were reductions in the deformation of the upper vessel wall where slug impact pressures produce the largest wall strains (4.5% strain on SM 2 compared with 2.8% on SM 3). Along the vessel wall near the UIS, strain is reduced from 3.5% on SM 2 to 1.8% on SM 3.

- The overall structural response of SM 5, a complex model with extensive instrumentation, was nearly the same as for SM 4. (SM 4 is identical to SM 5 but had less instrumentation and had unannealed UIS columns.) The same load was used in both tests. The presence of unannealed columns in SM 4 did not appreciably affect slug kinetic energy, or strains in the model. The slug impact velocity in SM 4 was 62.4 ft/sec and in SM 5, 62.2 ft/sec. The peak strain in SM 5 was 1.9% and in SM 4, 1.4%.

- The good agreement in structural response between SM 4 and SM 5 demonstrates the reproducibility of the tests and the insensitivity of model response to the yield strength variation of UIS columns. Because of this reproducibility and because of the more extensive instrumentation, the results of SM 5 are used in the remaining conclusions on complex model response.

- The increased stiffness (about 79%) of the vessel wall of the more complex model SM 5, over that of SM 3 (caused by the combined effect of the thicker vessel wall and the thermal liner) greatly reduces the permanent deformation of the vessel. Peak strains in the upper vessel wall were reduced from 2.8% in SM 3 to 1.9% in SM 5. Peak strains in the vessel wall near the UIS were reduced from 1.8% in SM 3 to 0.3% in SM 5.

- The plastic strain energy absorbed by SM 2 was 6.9 kW-sec, which is 47% of the gas work expended by the explosive up to the final volume change of the vessel (cover gas volume plus volume change of the vessel). For SM 3, only 4.5 kW-sec of strain energy was absorbed, which is only 32% of the gas work expended. Thus, the presence of the UIS results in a 35% reduction in strain energy absorption. The strain energy absorbed by SM 5 was only 2.1 kW-sec, which is 15% of the gas work expended. Thus, the stiffer vessel wall on SM 5 results in a further reduction in strain energy absorption.

- General Electric (GE) compared pre- and posttest REXCO calculations with experimental results and found that pretest REXCO strain calculations were conservative: REXCO overpredicts peak strains. This inconsistency is due to the use of low-strain-rate properties of Ni 200 and inadequate modeling of the core and UIS. For example, predicted peak vessel strain of for SM 2 was 5.2% compared with a measured peak strain of 4.5%. The predicted slug impact pressure for SM 2 was 3292 psi compared with a measured impact pressure of 5300 psi. Use of high-strain-rate material properties for Ni 200 in the GE version of REXCO gave better agreement between experiment and code, but REXCO strain calculations were still overestimated and impact pressures were still underestimated.

The accuracy of the instrumentation based on manufacurers specifications and repeated calibration is estimated to be ±2% for pressure gages, ±2% for strain gages, ±5% for accelerometers, and ±4% for water surface gages. The signal conditioning and recording system for these gages reduces overall accuracy to ±5% for pressure and strain measurements, ±7% for accelerations and ±6% for water surface measurements. Pressure and accelerometer records were digitally filtered with a low pass filter that had a cutoff frequency of 1/5 the natural frequency of the gage (50 kHz for pressure gages and 16 kHz for accelerometers) which represents the linear limit of the gages. Selected pressure records and all strain records were filtered to a lower cutoff frequency (10 kHz-25 kHz) without removing important structural response information (the highest structural response frequency for the 1/20-scale CRBR model is about 5 kHz). Based on four calibration experiments, the energy source is reproducible to within ±5% at high pressures and to within ±20% when the gas has expanded to the cover gas volume. Material property tests are accurate to within ±10%.

Measured pre- and posttest radial deflections are accurate to within 1 mil. The out-of-roundness is ±30 mils for the worst case. This out-of-roundness represents 14% of the maximum deflection, in regions of large deflection.

Blank Page

II ENERGY SOURCE

A. Source Description

A low-density explosive source was used to simulate the work potential of the HCDA. The use of low-density explosives to simulate HCDA loadings in reactor models is well established [5,8]. In this program, the source consisted of a 90/10 mixture by weight of PETN* powder and Microspheres† (hollow plastic spheres) contained in a canister consisting of stacked and spaced steel rings held between steel end plates (Figure 4). The canister suppresses nonprototypic shock wave loading of the models. Gasesous detonation products vent through the gaps between the canister rings and fill an air space that surrounds the canister. The initial volume of this space is controlled by the location of a Mylar diaphragm in the core barrel (Figure 4). The exhaust area between the canister rings controls the rise time of the pressure pulse. The charge mass and surrounding air space control the peak pressure, and slug mass controls the decay of the pressure pulse.

B. Calibration Experiments

Twenty calibration experiments were performed in the apparatus shown in Figure 4. The apparatus consists of a thick-walled core barrel, a thick-walled steel cylinder, and a thick core support plate, all carefully designed to simulate a rigid (only small elastic deformations) 1/20-scale model of the CRBR vessel. The energy source was calibrated over a range of charge masses and initial core volumes to determine the appropriate

---

*PETN ($C_5H_8O_{12}N_4$) pentaerythritol tetranitrate.

†Manufactured by Dow Chemical Co., Midland, Michigan.

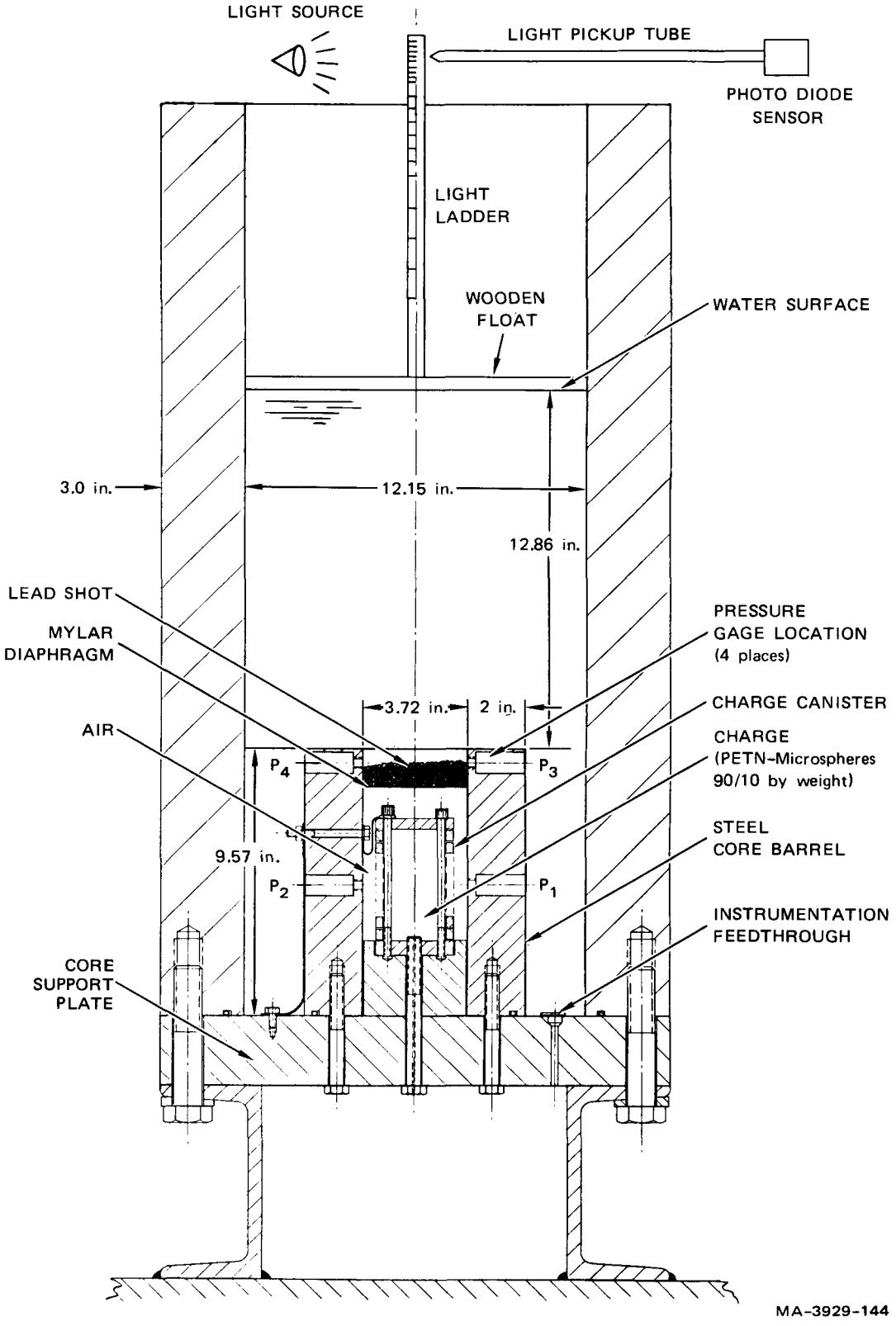

FIGURE 4 ENERGY SOURCE CALIBRATION APPARATUS

combination to simulate the SMBDB. The approach used in the calibration experiments was to measure simultaneously the pressure in the core and the volume change of the gas bubble. Pressure gages* mounted in the core barrel monitored source pressure. A light-ladder assembly floating on the water surface provided slug motion data. Appendix C describes the calibration apparatus and instrumentation in detail and lists the calibration experiments.

C. Data Analysis

The data analysis technique combines the core pressure history with the gas volume increase as measured by the upward motion of the water surface. The gas volume at any time is the sum of the volume displaced by the water surface, the increase in volume of the vessel, and the compression of the water. The volume displaced by the water surface is determined from the light ladder data, and the increase in volume of the vessel is negligible because of its relatively thick walls. The volume change due to the compression of the water before the water surface begins to move is calculated using a spherical flow model for pressure waves emanating from the core and, during bubble expansion, using the quasi-static compression of the water under a linear pressure gradient. The pressure-volume change calculation is detailed in Appendix C.

D. Results

Figure 5 shows the results of the last four calibration experiments. All use a 19.7-gram charge with an initial core volume = 962 cm^3. Reproducibility of the pressure records is $\pm$5% at high pressures and $\pm$50% at the cover gas volume. Reproducibility of the light ladder data is within $\pm$2% throughout the expansion.

The pressure-volume change relationship shown in Figure 6 is the average of the four experiments of Figure 5. The average curve is obtained by combining the averaged pressure-time history with the averaged

*PCB Model No. 113A03/61.

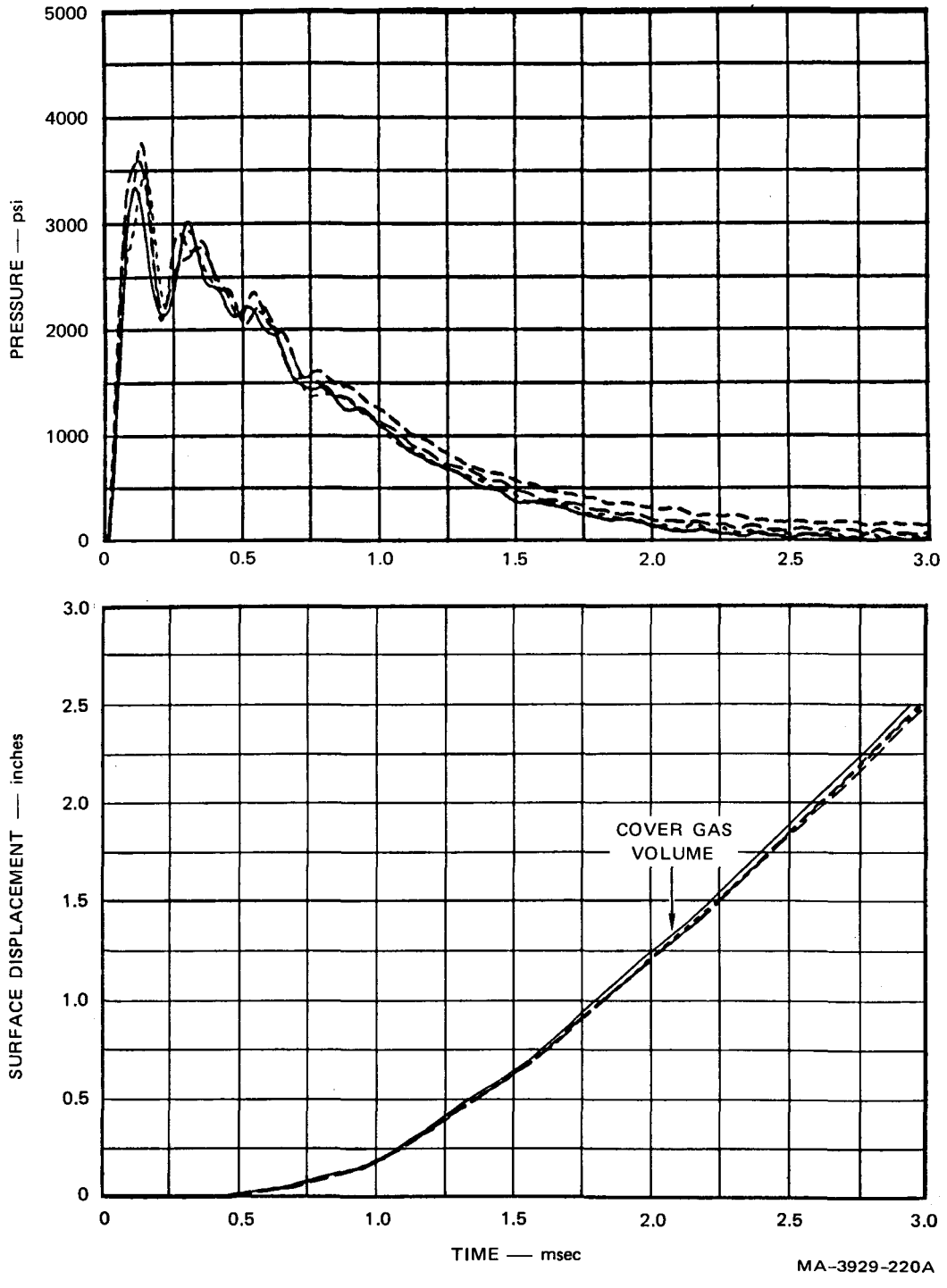

FIGURE 5 REPRODUCIBILITY OF CALIBRATION TEST DATA

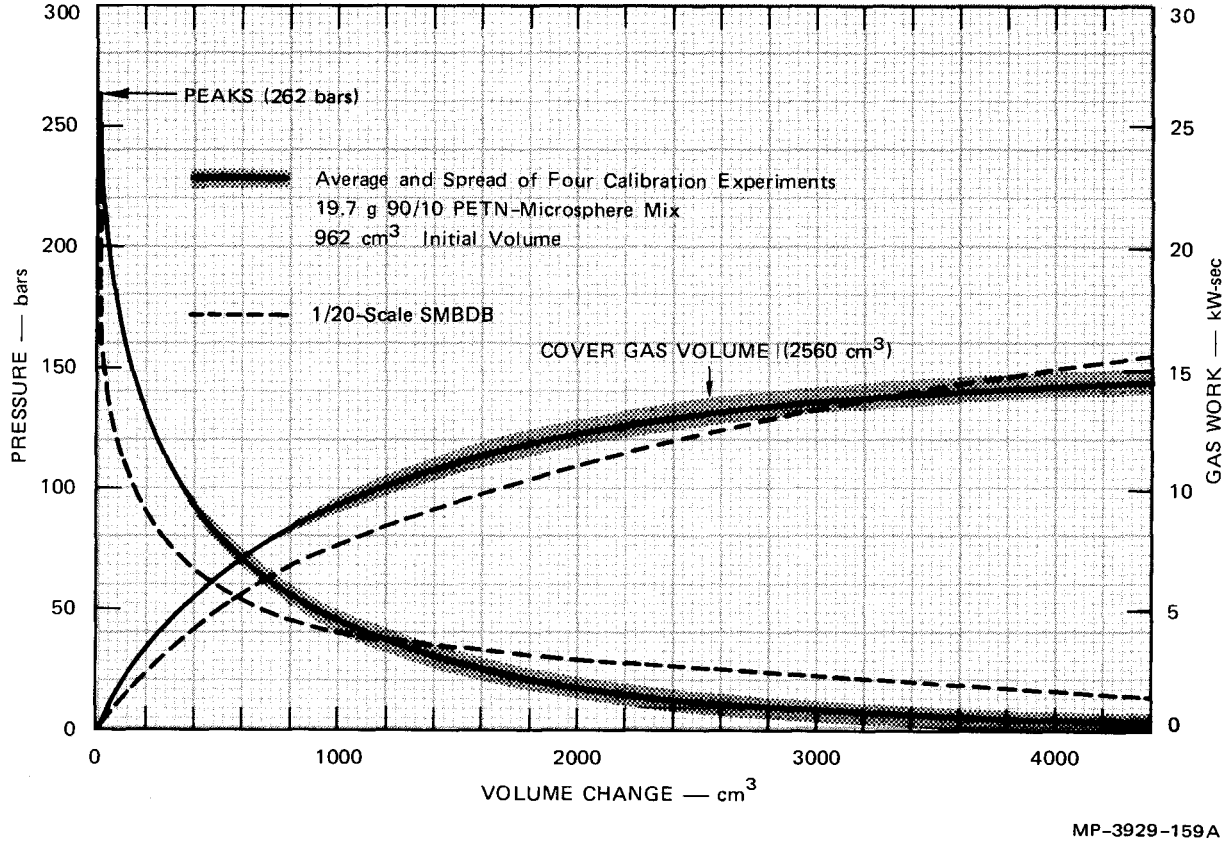

FIGURE 6 PRESSURE-VOLUME CHANGE AND GAS WORK VOLUME CHANGE RELATIONSHIPS FOR EXPLOSIVE ENERGY SOURCE AND SMBDB LOADING

light ladder data.* The gas work-volume change curve is obtained by integrating the average pressure-volume change curve. The pressure is initially 262 bars and decreases to about 10 bars as the gas expands from an initial volume of 962 cm^3 to 2560 cm^3, the cover gas volume. The gas work expended during this expansion increases from zero to 13.2 kW-sec, which corresponds to 105 MW-sec in full scale. The pressure-volume change and gas work-volume change curves are extended beyond the cover gas volume to determine the gas work done in the expanded flexible models. The shaded bands on the curves represent the spread in the data for the final four calibration tests. The spread in the pressure-volume change curve is small at small volume changes (high pressure) and increases to $\pm$30% at cover gas volume, and the spread in the gas work-volume change relationship is $\pm$5% at cover gas volume.

*See Appendix C for a more detailed description of the analysis of data.

III SIMPLE MODEL EXPERIMENTS--SM 2 and SM 3

A. Model Description

Figures 7 and 8 show schematic layouts of simple models SM 2 and SM 3, and Table 1 summarizes their materials and dimensions. Both models have the same basic design. The vessel is 0.119 in. thick and is made from Ni 200.* Both core structures include a Ni 200 core barrel (0.100 in. thick) and a combination of two thin, soft aluminum cylinders and segmented steel rings simulate the internal mass of the core. One of the aluminum cylinders is placed against the inside of the ring to prevent the detonation products from directly loading the core barrel. The other cylinder is placed between the segmented rings and the Ni 200 barrel to help distribute uniformly the loads from the rings to the core barrel. At the center of the core the charge canister is bolted to a steel tripod support stand, which in turn is bolted to the thick steel core-support platform. The tripod distributes the load from the canister more evenly over the platform. A Mylar diaphragm bonded to the inside wall of the core above the canister prevents water from entering the source region before detonation. Five hundred grams of lead shot (0.050 in. dia. solid spheres) is placed on the diaphragm to simulate the mass of the upper pin and assembly structures.

Both models have identical head structures that consist of a single 533-B steel plate with a shear ring bearing surface machined into it. Layers of steel plates are bolted to the underside of the head to simulate the mass of the head shielding. Steel and lead masses are bolted to the topside of the head to simulate the mass of head-mounted components. The segmented shear rings (4142H steel) that transmit the slug load from plug to the vessel flange fit into a shear ring groove that is machined into the

*The material properties for these models are discussed in detail in Appendix B.

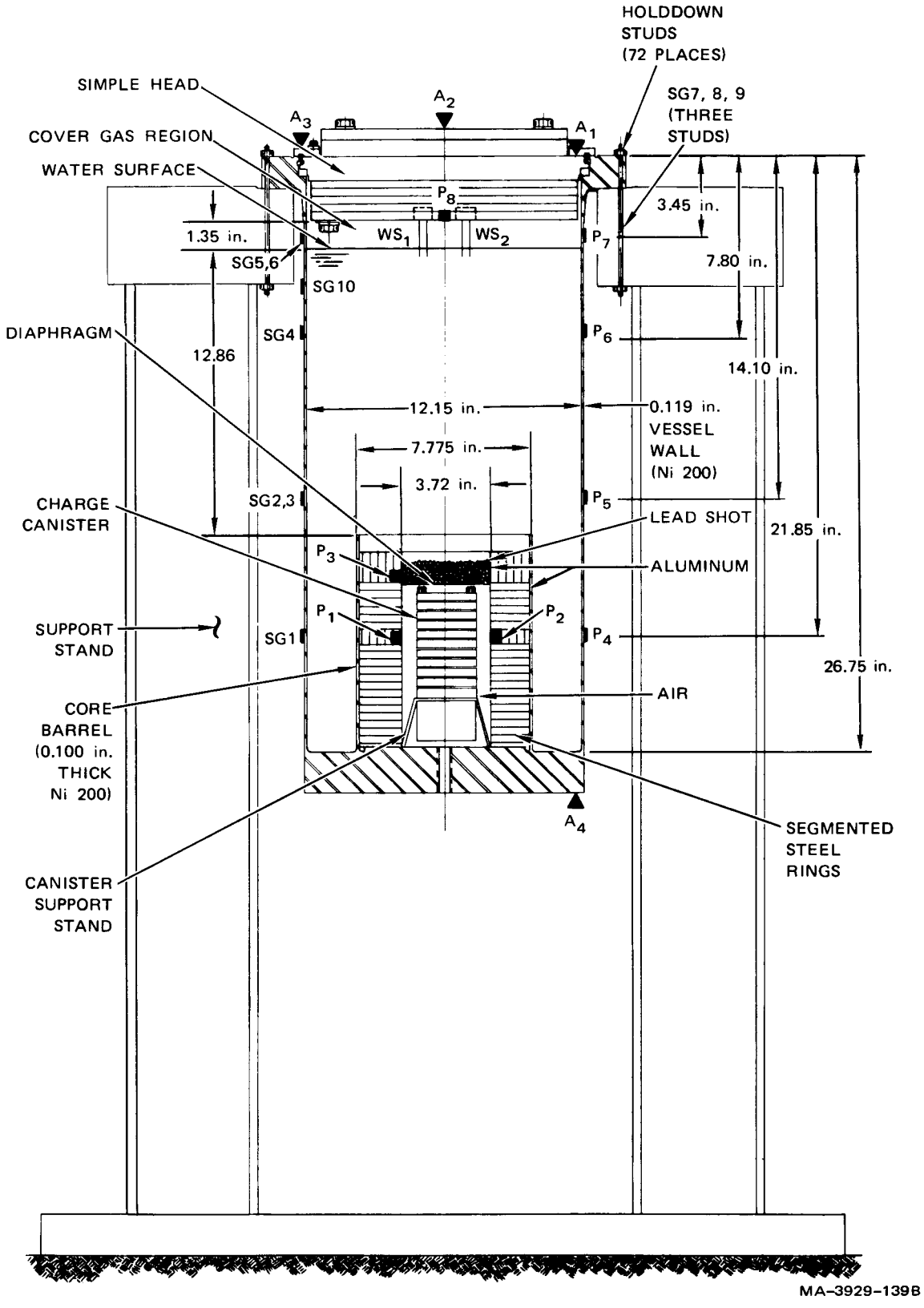

FIGURE 7 SM 2 WITH INSTRUMENTATION

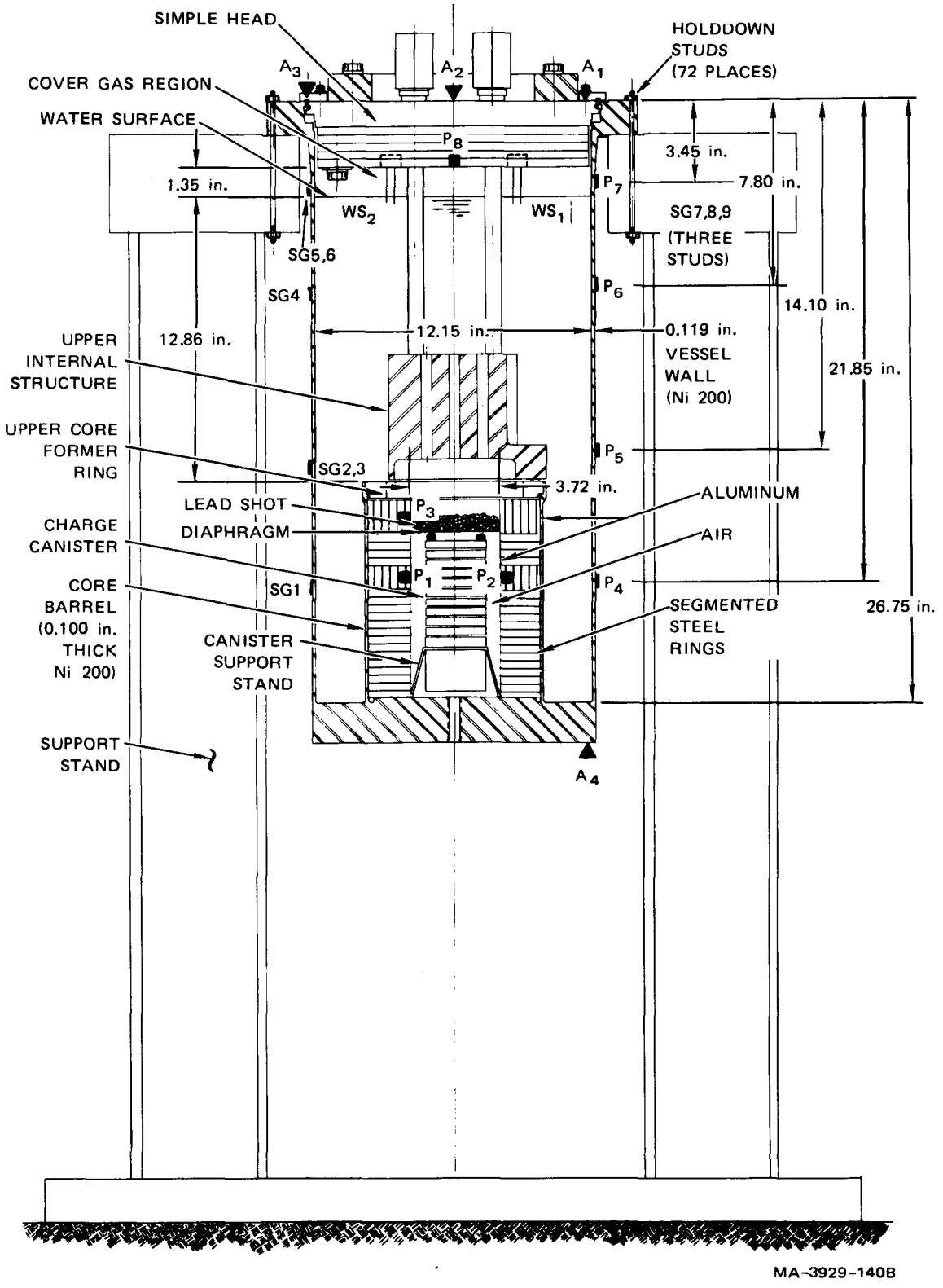

FIGURE 8 SM 3 WITH INSTRUMENTATION

Table 1

SM 2 AND SM 3 COMPONENTS--MATERIALS AND DIMENSIONS

Model	Component	Material	Diameter (inches)	Thickness (inches)	Weight (kilogram)
SM 2	Vessel	Ni 200	12.39 OD	0.119	--
SM 2	Core barrel	Ni 200	7.78 OD	0.100	--
SM 2	Core platform	Steel	12.39 OD	2.00	30.69
SM 2	Head	533B steel	12.15	1.10	62.66
SM 2	Upper internals structure (UIS)	--	--	--	--
SM 2	Core Rings	Steel	7.43	1.81	33.92
SM 3	Vessel	Ni 200	12.39 OD	0.119	--
SM 3	Core Barrel	Ni 200	7.78 OD	0.100	--
SM 3	Core Rings	Steel	7.43	1.81	33.92
SM 3	Core Platform	Steel	12.39	2.00	30.69
SM 3	Head	533B steel	12.15	1.10	63.10*
SM 3	UIS	Aluminum	5.80	--	5.01
SM 3	UIS columns	Steel/Ni 200	0.70	0.05	1.86†

*Includes UIS and UIS columns

†Wt of 4 columns

vessel flange. The vessel flange is made from 533-B steel. Dimensions of the shear ring groove, shear ring sements, and shear ring-bearing surfaces are carefully controlled to ensure that, when assembled, a 6 mil gap exists between the shear ring bearing surface.

The difference between SM 2 and SM 3 is that SM 3 includes an upper internals structure (UIS), which is suspended from the head by four columns and is situated 0.100 in. above the top of the core structure. The UIS is machined from an aluminum block and is nickel-plated to prevent corrosion. Nineteen holes (5.23 $in.^2$ total area) run axially through the UIS to simulate the penetration area for the control rods. The four UIS columns are made from 0.700-in.-O.D., 0.050-in.-thick, Ni 200 tubes (approximately 8 in. long) welded to solid steel shafts at each end. The columns are secured to the head by threaded caps.

The models are secured to a massive test stand by 72 0.130-in.-diameter, 7-in.-long steel studs located around the perimeter of the vessel flange. These studs pass through the vessel flange and the test stand and are preloaded to 825 lb each. The stressed length of each stud is 5.8 in. The test stand was designed by W-ARD to simulate at 1/20-scale the same stiffness provided by the prototype concrete and steel support ledge of the CRBR. The test stand includes a massive steel ring, six H-columns, and a steel plate base. It is secured to a large steel box-beam foundation welded to steel channels imbedded in a concrete pad. SRI designed the foundation to limit vertical test stand motion to less than 0.005 in.

B. Instrumentation

SM 2 and SM 3 were instrumented with pressure transducers, strain gages, accelerometers, and water surface gages to provide an overall measure of the response of the models. Instrumentation and instrumentation points were selected by SRI and W-ARD.

1. Pressure Transducers

Eight pressure transducers* were installed on each model. Two pressure transducers mounted in the core recorded the pressure history of the energy source. These loads were used to analyze the core barrel response and to demonstrate that core loads were in agreement with those measured during calibration experiments.

The other six pressure transducers were distributed on the head to measure slug impact pressure, and along the wall of the vessel to measure vessel loads (see Figures 7 and 8). The pressure transducers were calibrated before and after each experiment. Their accuracy is estimated to be within ±2% of peak pressure.

2. Strain Gages

Ten strain gages† were installed on SM 2 and nine on SM 3. They were installed on the vessel wall either as T-rosettes to measure circumferential and axial strain at the same point, or as single gages to measure only circumferential strain. In addition, three of the 72 studs that secure the vessel flange to the test stand were instrumented with strain gages to evaluate the dynamic ledge load. The strain gages have an estimated accuracy of ±2% of peak strain. Considering the measuring and recording instrumentation, experimental accuracy is about ±5%.

3. Accelerometers

Four accelerometers‡ were installed on each model. Three were mounted on the head--two near the edge and one at the center of the head. The fourth accelerometer was mounted on the core support platform near the vessel wall.

---

*PCB Model 113A03/61, Natural frequency about 500 kHz.

†High elongation foil strain gages manufactured by Micro Measurements, Romulus, Michigan.

‡ Endevco Model 2225, Natural frequency = 80 kHz

The accelerometers were calibrated by the manufacturer and bench-checked by SRI between experiments. The manufacturer quotes a calibration factor that is accurate to within ±1.5%. The bench check done by SRI includes all of the signal conditioning equipment used in the experiments. Peak accelerations measured in the bench check are within ±5% of known values.

4. Water Surface Gages

Two water surface gages were installed on the heads of each model. These gages, developed at SRI for use on the FFTF model tests [5], were used to measure the water surface motion in the model. The water surface gage consists of two tapered electrodes set a fixed distance apart and inserted into the electrolyte liquid (water and salt solution). As the liquid level rises or falls with respect to the starting position, the 50 kHz carrier is amplitude-modulated. The amplitude is a function of displacement of the liquid with regard to the starting conditions. These gages serve two important purposes. They measure, first, the position of the water surface with time to help check the pressure-volume change relationship of the energy source, and second, the planarity of slug impact and the slug impact velocity to provide a check on slug impact symmetry and pressure. The water surface gages are estimated to be accurate to within ±5 mils (about 4% of total slug motion).

C. Results

This section examines the effects of the UIS on the response of the simple model to simulated HCDA loads by comparing the results of tests SM 2 and SM 3. Detailed results of the experiments are presented in Appendix D.

1. Loading Pressures

Figure 9 compares the loading pressures* in SM 2 and SM 3. The average peak core pressures in SM 2 and SM 3 agree very well with the

*Pressures 1 through 6 have been digitally filtered at 10 kHz; pressures 7 and 8 have been digitally filtered at 25 kHz. The filter frequency was chosen so that important response modes were not attenuated. See Appendix E for a description of digital filtering techniques.

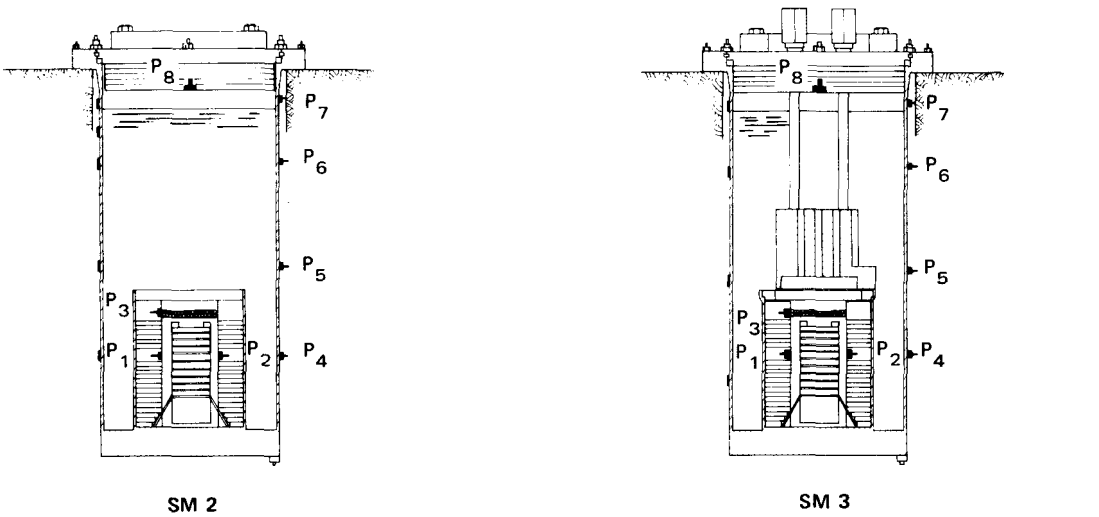

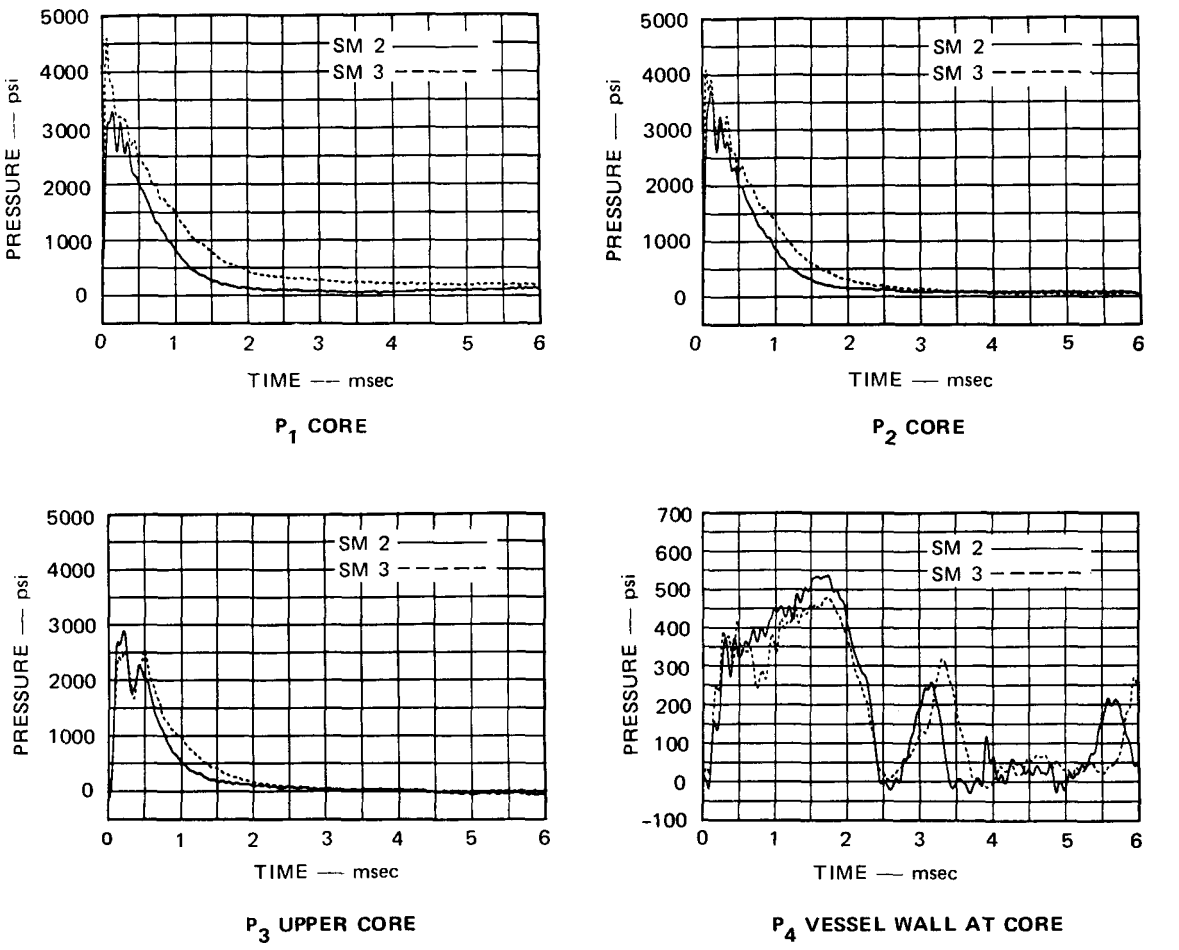

MA-3929-167

FIGURE 9 COMPARISON OF LOADING PRESSURES: SM 2 AND SM 3

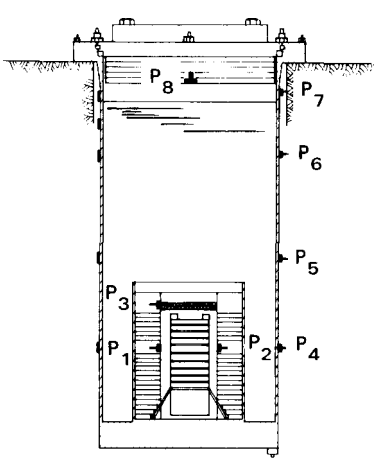

SM 2

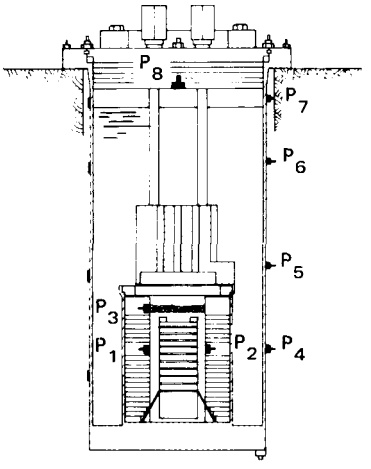

SM 3

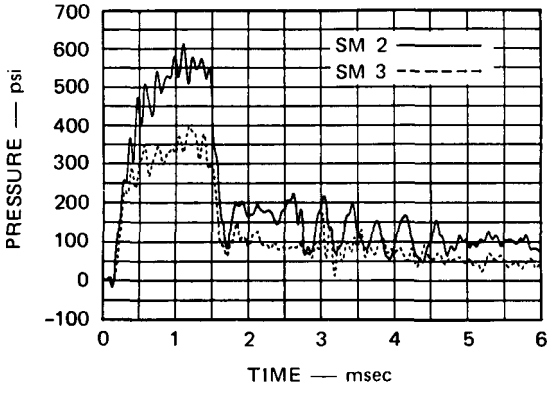

P_5 SODIUM OUTLET NOZZLE

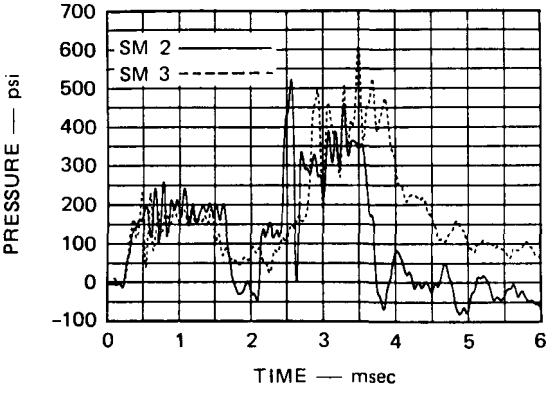

P_6 VESSEL WALL

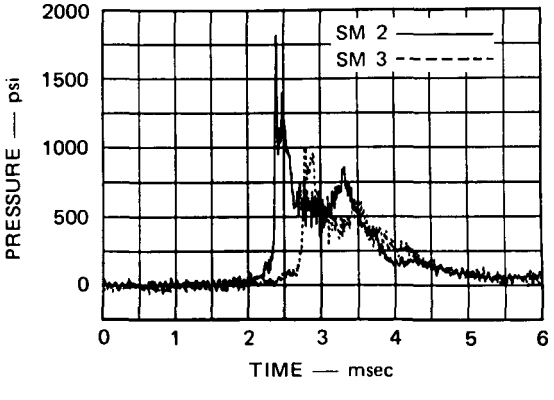

P_7 UPPER VESSEL WALL

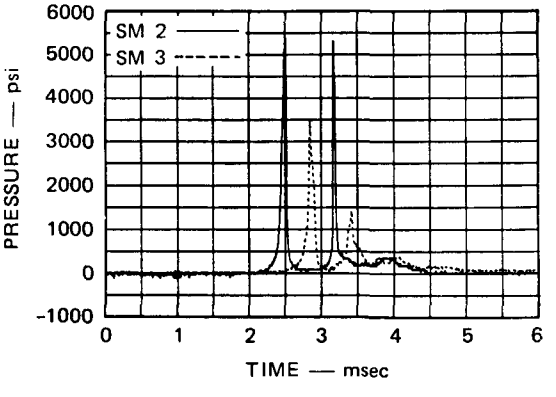

P_8 HEAD

MA-3929-168

FIGURE 9 COMPARISON OF LOADING PRESSURES: SM 2 AND SM 3 (Concluded)

average peak calibration pressures (3920 psi compared with 3840 psi for the calibration experiments). The core pressures (P_1, P_2, and P_3) for SM 3 are higher than for SM 2 throughout the pressure history, because the UIS in SM 3 restricts and redirects the flow of gas from the core region, thus keeping the pressure up for a longer time.

The peak pressure on the vessel wall opposite the core barrel (P_4) is about 10% higher in SM 2 than in SM 3. The initial pressure rise here is caused by the expansion of the core barrel followed immediately by the pressure wave from the expanding gas bubble. The pressure rises rapidly to the yield pressure of the vessel wall (about 364 psi). Once the vessel yields, the pressure rises more slowly to a peak between 480 and 530 psi at around 1.7 msec. At this time the core pressure has dropped to about 200 psi and the core reaches its maximum deflection and begins to contract, thereby reducing the pressure in the annulus between the core barrel and the vessel wall. Later (at 3.1 msec on SM 2 and at 3.4 msec on SM 3) the pressure wave from the slug impact reaches the P_4 gage location. The magnitude of the slug impact pressure has been attenuated by wave-bubble interactions and by fluid-structure interactions to below the yield pressure of the vessel so that further permanent vessel deformation does not occur.

The pressure at the sodium outlet nozzle elevation (P_5) in SM 2 is significantly higher than in SM 3. Both pressures begin at the same time and rise together to about 300 psi (vessel yield pressure = 364 psi). The pressure in SM 2 continues to rise to about 550 psi, whereas in SM 3 it rises more slowly, to about 350 psi. This difference in peak pressures can be attributed, in part, to a reduction in pressure caused by an increase in the particle velocity of the water that is being forced up around the outside of the UIS in SM 3. That this difference is a local effect of the UIS can be seen by comparing pressure records taken at the P_6 gage location. Here the pressures are again nearly the same. Initially, the pressure reaches 200 psi due to the bubble expansion from the core. The initial pressure pulse is followed at 2.6 and 2.9 msec by the slug impact pressure pulse in SM 2 and SM 3, respectively. The peak of this impact pulse is the same for both tests (about 500 psi).

On the upper vessel wall (P_7 location) and the head (P_8 location), pressures are the result mainly of the slug impact. The slug impacts the head sooner in SM 2 than in SM 3, because the UIS in SM 3 restricts the expansion of the gas bubble from the core, thus lowering the slug velocity. The slower moving slug causes a lower impact pressure, as recorded by both the P_7 and P_8 gages. Further evidence of the effect of the UIS on slug motion is shown in Figure 10, which shows the water surface gage records for SM 2 and SM 3. Both curves have the same general shape but the slug in SM 2 impacts the cover first (displacement = 1.35 in.) with a higher velocity than in SM 3 (91.5 ft/sec in SM 2 versus 62.5 ft/sec in SM 3). The 32% decrease in velocity implies a similar decrease in impact pressure, which is supported by the impact pressure measurements (5300 psi on SM 2 and 3500 psi on SM 3, a 34% reduction). The impact pressures measured by gages can be checked by calculation using the relationship $P = \rho cv$ where ρ is the density of the slug, c is the sound speed in the slug, and v is the slug impact velocity. With $\rho = 1 g/cm^3$ and $c = 1.5 \times 10^5$ cm/sec the calculated slug impact pressure in SM 2 is 6070 psi (419 bars) and in SM 3 it is 4150 psi (286 bars). These pressures are in reasonable agreement with the measurements since the actual sound speed and the density of the slug could be slightly reduced because of air entrainment. The water surface gage records also show secondary slug impact about 0.7 msec after the first impact. The pressure records show this second impact on both experiments.

Based on measured slug velocities and estimated slug masses, the kinetic energy of the slug at impact in SM 2 is 9.50 kW-sec, and in SM 3, 4.43 kW-sec, a decrease from SM 2 kinetic energy of 53%. Differences in strain energy absorption by the core and vessel wall before impact cannot explain the differences in slug kinetic energy. In fact, less strain energy is absorbed in SM 3 than in SM 2. The decrease in axial kinetic energy (47% decrease in axial kinetic energy of the slug at the slug impact between SM 2 and SM 3), therefore, is caused by the presence of the UIS that throttles and diverts the flow of water and gas from the core, thereby increasing the turbulent and radial kinetic

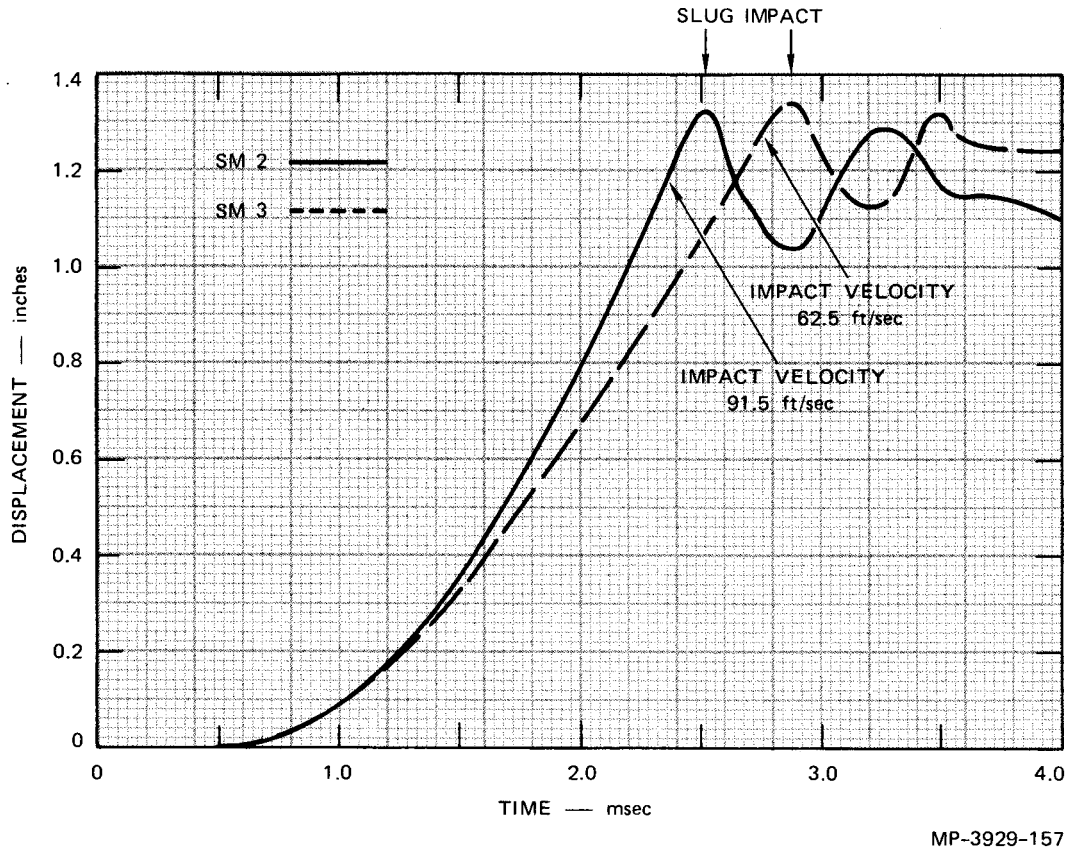

FIGURE 10 COMPARISON OF AVERAGED WATER SURFACE DISPLACEMENTS: SM 2 AND SM 3

energy of the water. It is unlikely that heat transfer plays a major role in reducing the slug kinetic energy because recent experiments with nitrogen at room temperature showed similar reductions [9].

2. Strain Response

Figure 11 compares the strain records* at corresponding locations on SM 2 and SM 3. The circumferential strains were consistently larger in SM 2 than in SM 3, as verified by posttest deformed shape profiles of each model. Further corroboration of the strain measurements is provided in Table 2, which lists peak strains measured in the experiments and peak strains calculated by using the loading pressures measured at the strain gage locations, the wall thickness and the material properties of the vessel wall at high strain rates. A simple hoop mode response is considered in these calculations. The calculations also assume a quasi-static response since the observed strain response follows the loading history. In almost every case the calculated strain exceeds the measured strain, sometimes by as much as 100% but usually by about 30%. Since the analysis assumes a hoop response only, the affects of axial strain due to bending are not considered. Bending effects will tend to reduce measured circumferential strains so it is reasonable to expect that the simple hoop mode calculations would exceed the measured strains.

The vessel wall responds to two distinct and separate loading phases--the first before slug impact and the second after slug impact. During the first phase, the lower vessel wall from the support platform to an area opposite the UIS expands under the direct loading of the bubble expansion from the core and, to some extent, the core barrel expansion. The pressure on the upper vessel wall remains well below the yield pressure of the vessel before slug impact, so no permanent deformation occurs there. During the second phase, after the slug impacts the head, a large pressure wave is reflected back down through the slug. Loading pressures on the upper wall exceed the yield pressure of the

*Each record has been digitally filtered at 10 kHz. See Appendix E for description of filtering philosophy and techniques.

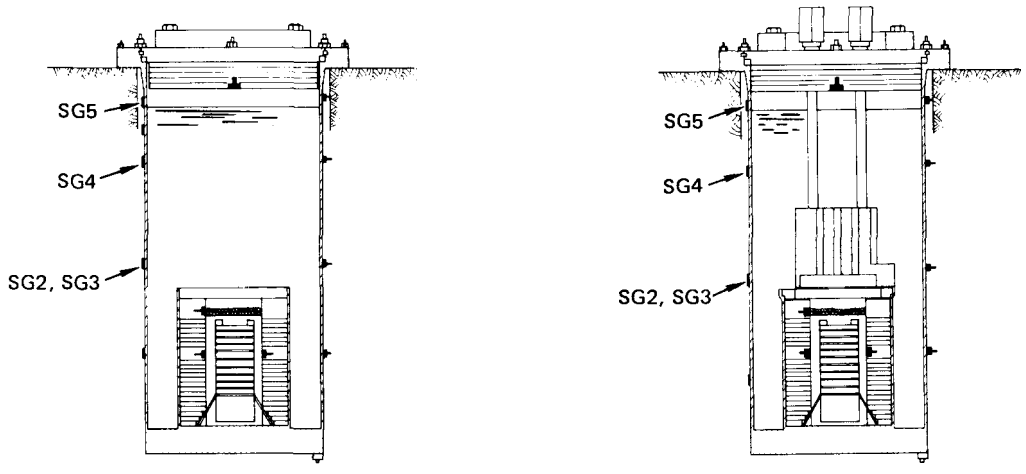

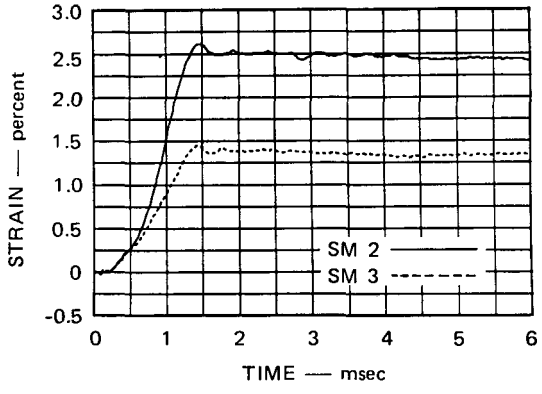

SG2 VESSEL WALL AT UIS (C)*
(SODIUM OUTLET NOZZLE)

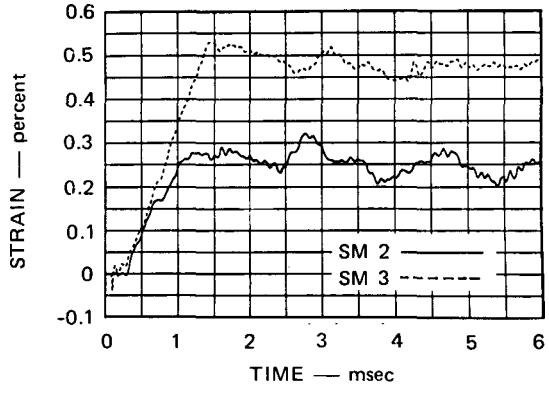

SG3 VESSEL WALL AT UIS (A)†

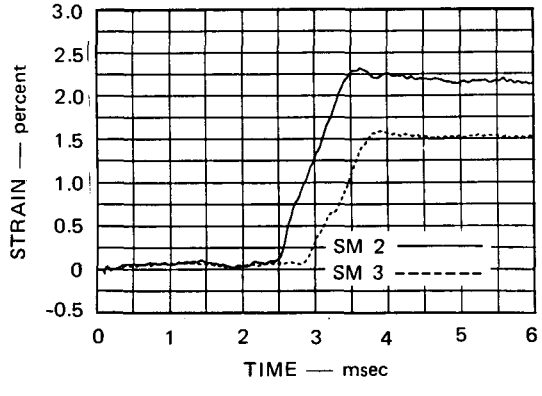

SG4 VESSEL WALL (C)

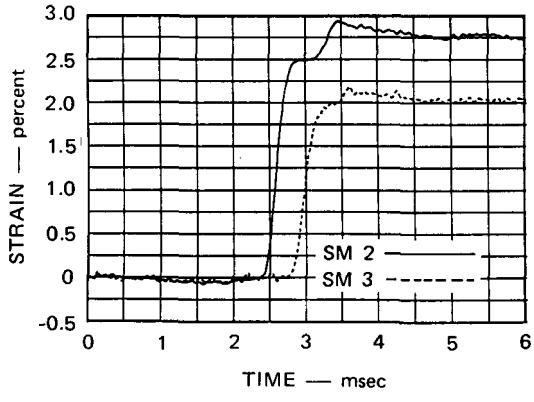

SG5 UPPER VESSEL WALL (C)

* C = circumferential
† A = axial

MA-3929-169

FIGURE 11 COMPARISON OF STRAIN RESPONSE: SM 2 AND SM 3

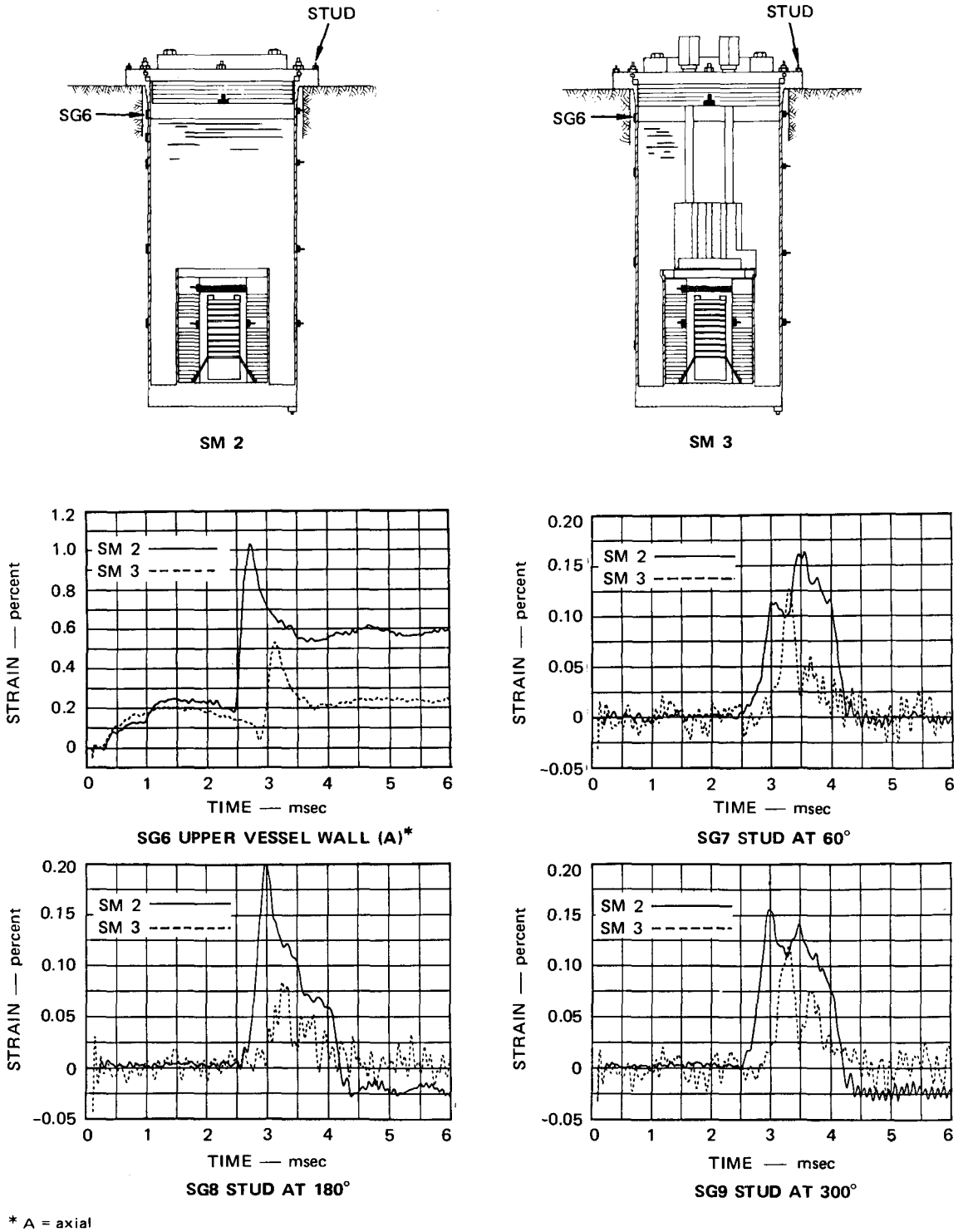

FIGURE 11 COMPARISON OF STRAIN RESPONSE: SM 2 AND SM 3 (Concluded)

Table 2

PRESSURES AND STRAINS; SM 2, SM 3

Model	Gage No.	Location	Peak Pressures (psi) Measured	Wall Thickness (inches)	Peak Strains Measured	Peak Strains Calculated[a]
SM 2	P_1, P_2	Core	3525	0.100	1.3[b]	--
SM 2	P_4, SG1	Vessel wall at core	540	0.119	1.62	2.7
SM 2	P_5, SG2	Vessel wall at UIS	570	0.119	2.65	2.9
SM 2	P_6, SG4	Vessel wall	530	0.119	2.30	2.4
SM 2	P_7, SG5	upper vessel wall	1650	0.119	2.90	--
SM 3	P_1, P_2	Core	4350	0.100	1.5[b]	--
SM 3	P_4, SG1	Vessel wall at core	480	0.119	0.87	1.7
SM 3	P_5, SG2	Vessel wall at UIS	400	0.119	1.45	0.4
SM 3	P_6, SG4	Vessel wall	520	0.119	1.60	2.3
SM 3	P_7, SG5	Upper vessel wall	1000	0.119	2.15	3.3

(a) Using high $\dot{\epsilon}$ data, quasi-static analysis and measured pressures

(b) Posttest deformed shape

of the wall, causing large plastic deformation. The reflected pressure wave is rapidly attenuated by the expansion of the upper vessel wall and by interaction with the bubble so that by the time it reaches the lower vessel, it is below the yield pressure of the wall, and no further permanent deformation occurs. These two structural response phases are distinctly separated in time, as seen by comparing strain record SG 2 with SG 4 (Figure 11).

The axial strain gages on the model (SG 3 and SG 6, Figure 11) show that the axial strain due to the downward load of the explosive source on the core support platform is between 0.20 to 0.30%. Near the core, this strain is not increased by the slug impact load. Near the top of the vessel (SG 6, Figure 11) the slug impact load suddenly increases the axial strain (tensile strain) followed by a rapid decrease in strain as the vessel wall bends. The slight bump in the axial strain gage record (SG 3, Figure 11) at about 2.75 msec is caused by the slug impact force on the head, which transmits an axial stress wave into the vessel wall. The radial effects of the slug impact pressure moving back down along the vessel wall are not seen at all at this same location (SG 2, Figure 11).

The strain records from the three instrumented holddown studs (SG 7, 8, and 9, in Figure 11) are analyzed to determine the upward ledge load. Each of the 72 steel studs (4140 steel, $E = 30 \times 10^6$ psi) that holds the models to the test stand was preloaded to 825 lb (about 0.2% strain) by torquing each stud to 30 in.-lb. This torque was determined by measuring the torque required to produce the desired strain preload in each of the three instrumented studs, and then applying this torque to the other studs. Measurement of the dynamic strain on the instrumented studs, therefore, reflects a change from the prestress load on each stud. On SM 2, the strain increase averages 0.17% (SG 7, 8, and 9, Figure 11). From the combined preload strain and dynamic strain (0.37%, which is still below the elastic limit of 0.4%) we calculate a peak load during the test of 1500 lb per stud. The total peak ledge load is 108,000 lb (72 x 1500 lb). The average peak stud strain on SM 3 is

0.11%. The peak ledge load for SM 3 is therefore 90,300 lb; 16% below that for SM 2. The reduction in ledge load is caused by the reduction in head loads (Figure 9, P_8).

3. Accelerations

Figure 12 compares the accelerometer records* from SM 2 and SM 3. To avoid the confusion of overlaying accelerometer records, comparable records are placed side by side.

The accelerometer records indicate some important differences in the response of the one-plug heads on SM 2 and SM 3. In SM 2 the initial downward acceleration of the head (A_1) at about 0.85 msec is caused by the downward force of the explosive charge on the platform, which excites the vessel in an axial vibration mode that has a period of about 0.260 msec. The period of vibration agrees fairly well with the accelerometer record. The downward acceleration is quickly damped and is followed (at 2.4 msec) by an upward acceleration of the head caused by slug impact. The upward motion of the head is halted suddenly when the head has traveled the 6-mil gap between the shear ring and shear ring bearing surface. A sudden deceleration occurs, followed by vibration of the one-plug head. The calculated natural frequency of the head is 5354 Hz with a period T = 0.186 ms. The calculation assumes a simple support around the perimeter and considers the total mass and thickness of the head including shielding and component masses.

In SM 3 the initial upward acceleration of the head occurs sooner (about 0.4 msec) than in SM 2 and is caused by the force transmitted to the head from the UIS strucure, which is directly loaded by the core pressure. As expected, the maximum acceleration for the one-plug head on SM 3 is slightly lower than that on SM 2 because of the lower slug impact load. Because of the one-plug construction of the SM 2 and SM 3 heads, the peak acceleration at the center is higher than at the edge.

*All records have been digitally filtered at 16 kHz, the upper bound for linear gage response (one-fifth of the natural frequency of the accelerometers).

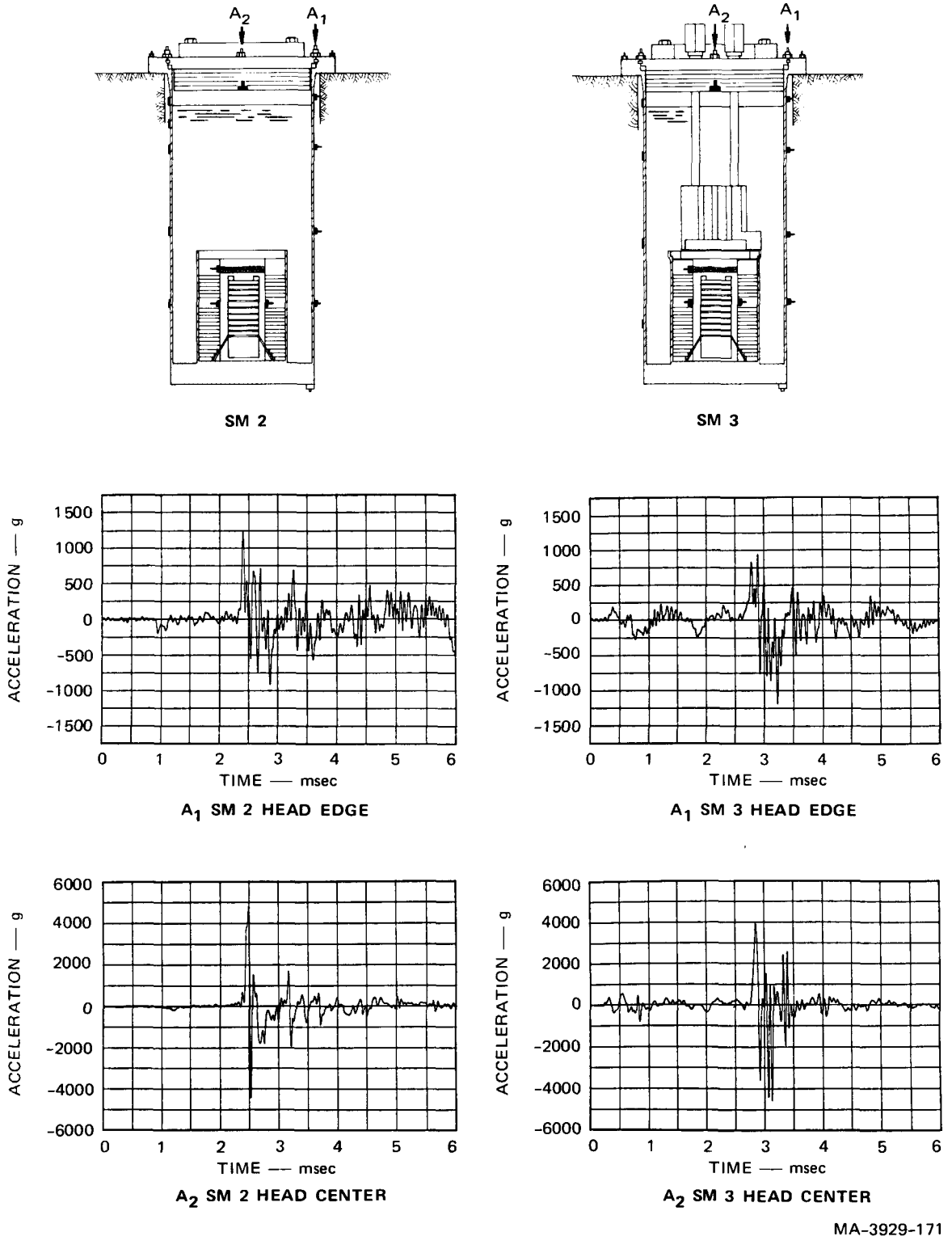

FIGURE 12 COMPARISON OF ACCELERATIONS: SM 2 AND SM 3

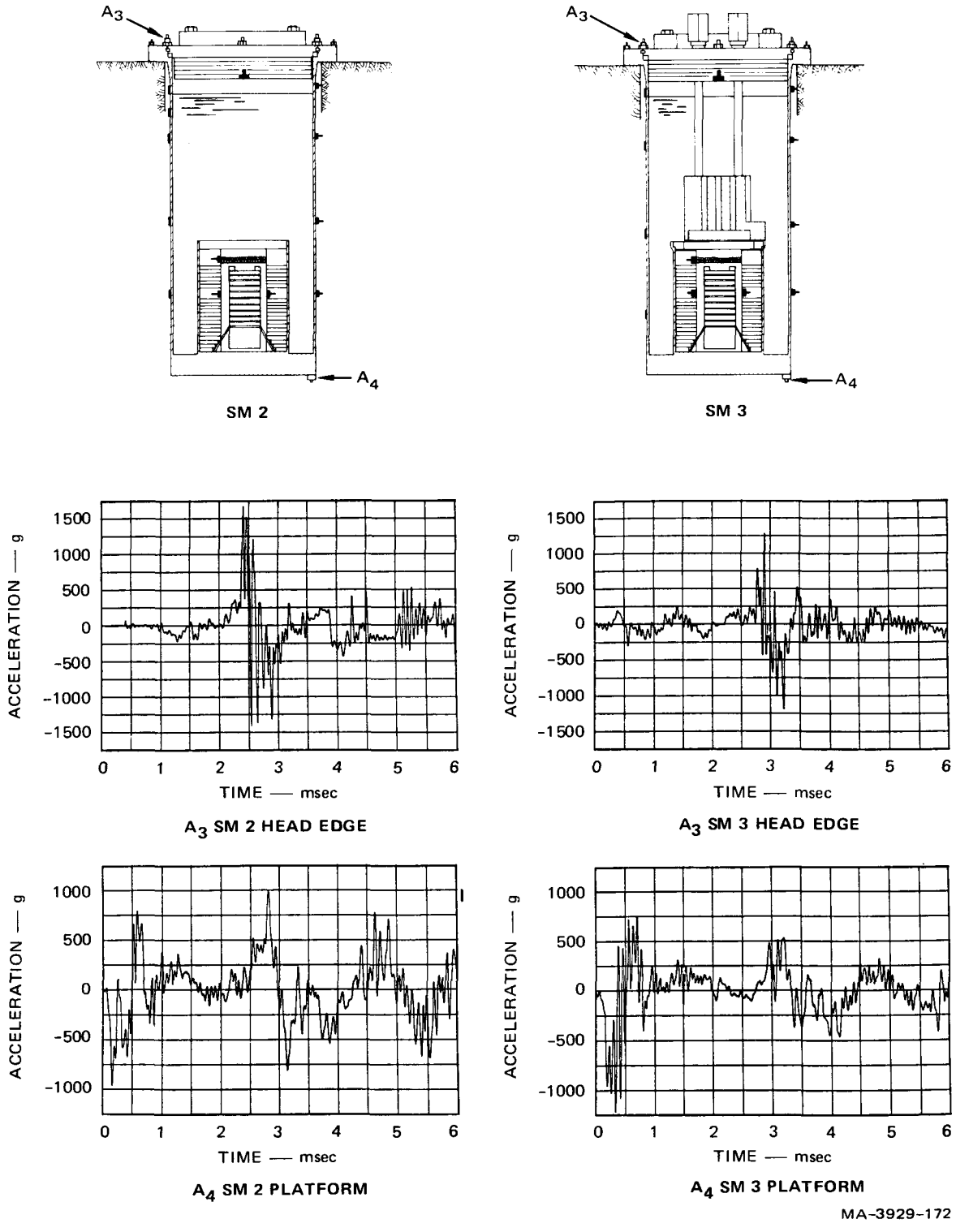

FIGURE 12 COMPARISON OF ACCELERATIONS: SM 2 AND SM 3 (Concluded)

The acceleration modes of the platform on the two models are very similar. The larger downward acceleration of the platform on SM 3 following detonation is an effect of the UIS, which restricts the flow of gas from the core, thus increasing the duration and amplitude of the core pressure and platform load.

4. UIS Column Response

The upward load from the energy source on the UIS significantly deformed the UIS columns in SM 3. Based on the strain data measured on the UIS columns of SM 5* (see Section IV, C.4), the tubular Ni 200 sections begin to compress immediately after detonation of the energy source. They compress and buckle to their maximum deformation about 1 ms before slug impact. Figure 13 shows a photograph of the UIS and the deformed UIS columns. The UIS structure is shown still attached to the head by the caps that clamp the UIS columns to the head assembly. As shown in Figure 14, the tubular Ni 200 sections of each column compressed and buckled a total of 0.55 in. each. About 0.022 in. of the axial compression can be accounted for by the lateral deformation of the columns, the balance of axial deformation is from uniform compression of the tubes, about 7% strain. Based on the measurements made on the UIS columns of SM 5 and an analysis of buckling loads (see Section 4.4) it is concluded that the columns buckled dynamically.

We examined the frabricator's annealing records and found that the columns for SM 3 had been annealed for 60 min. at 1300°F rather than the prescribed 30 min. at 1300°F. Stress-strain curves for the Ni 200 column material under these annealing conditions indicate that the yield stress is lowered from about 34 ksi to about 13 ksi during the increased annealing time. However, the longer annealing time results in a stress-strain relationship that is in better agreement with the prototypic stainless steel stress-strain curves. (See Appendix B for stress-strain curves.) From the column stress-strain curves, the peak column stress at 7% is about 47.5 ksi. The

*There were no strain gages on the UIS columns in SM 3.

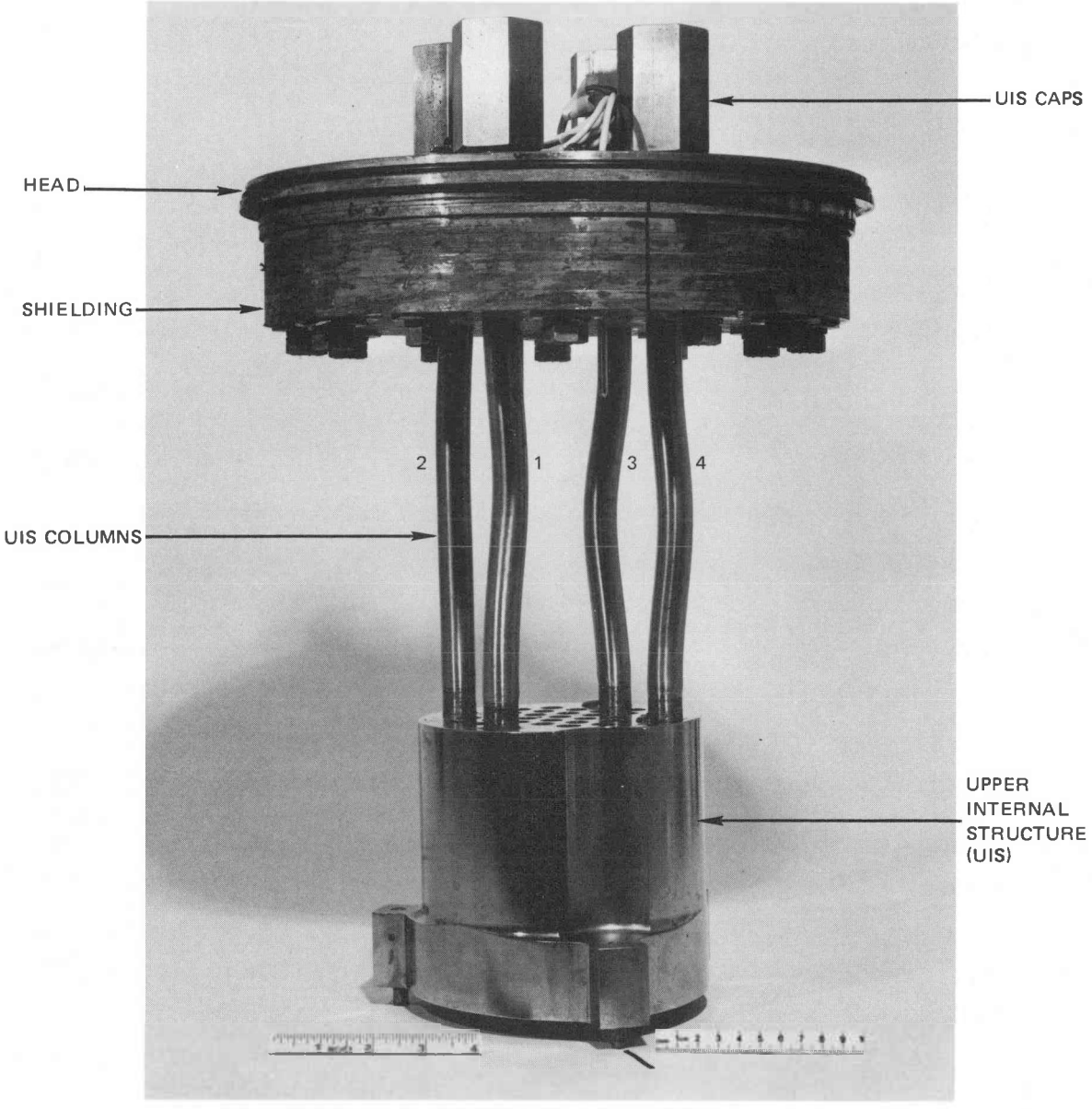

FIGURE 13 UPPER INTERNAL STRUCTURE AND HEAD ASSEMBLY FROM SM 3

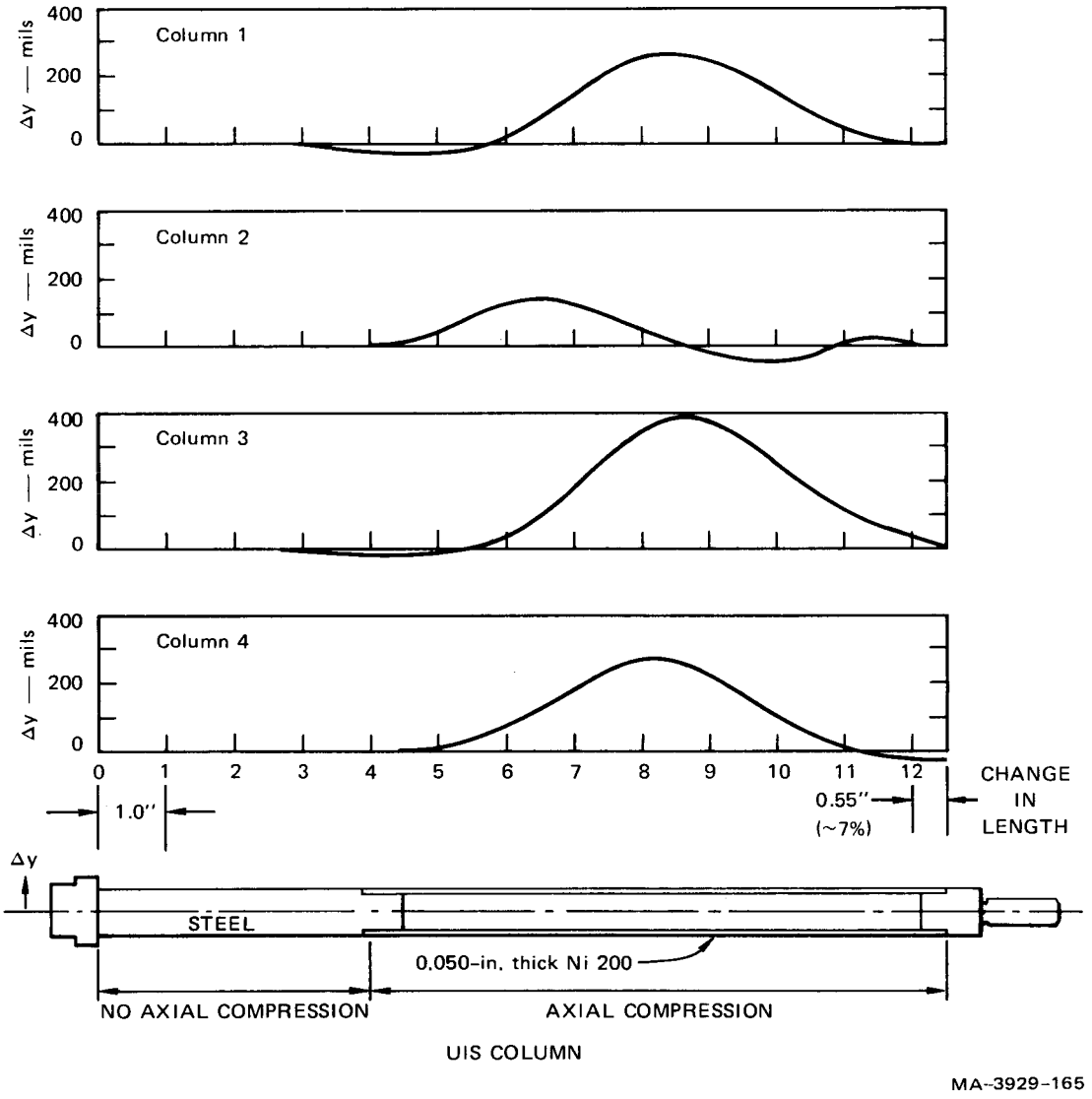

FIGURE 14 DEFORMATION PROFILES FOR UIS COLUMNS IN SM 3

buckling and deformation patterns for the UIS columns in SM 3, then, provide a realistic picture of prototypic UIS column response.

The upward motion of the UIS increases the gap between the UIS and the core barrel from 0.25 cm (0.1 in.) to 1.65 cm (0.65 in.). Hence, the exhaust area for the gases to escape from the core, including the area of the holes through the UIS (31 cm^2), increases from an initial 65 cm^2 to 115 cm^2, a 77% increase in exhaust area. The increased radial flow area around the perimeter of the core barrel and UIS permits a significant amount of gas to be directed radially out of the core. This radial flow entrains and accelerates the surrounding water, resulting in a significant portion of the work potential of the gas being converted into radial and turbulent kinetic energy of the water.

5. Deformed Shape Profiles SM 2 and SM 3

Figure 15 shows a photograph of the SM 2 deformed vessel. The upper vessel bulge (about 4.5% peak strain) and the bulge in vessel above the core barrel while not large (about 3.5 strain) are very clear. Figure 16 compares the deformed shape profile of models SM 2 and SM 3. The curves represent the average data taken along six equally spaced meridians on each vessel. The deformation scales have been exaggerated to show more clearly the deformation patterns of the models. The curves show clearly the difference in response between models SM 2 and SM 3. The lower portion of the vessel wall (below point 9) on SM 2 is deformed about twice as much as the vessel wall on SM 3. Above point 9, the vessel wall on SM 2 is deformed about 60% more than the vessel wall on SM 3. The deformation of the core barrel in both models is nearly the same.

As mentioned earlier, the vessel deforms in two distinct phases. In the first phase, the lower portion of the vessel (below point 9) and the core barrel deform to their peak level before slug impact, while the upper portion of the vessel (above point 9) remains undeformed. In the second phase, after slug impact, the upper portion of the vessel deforms to its maximum while the lower portion remains

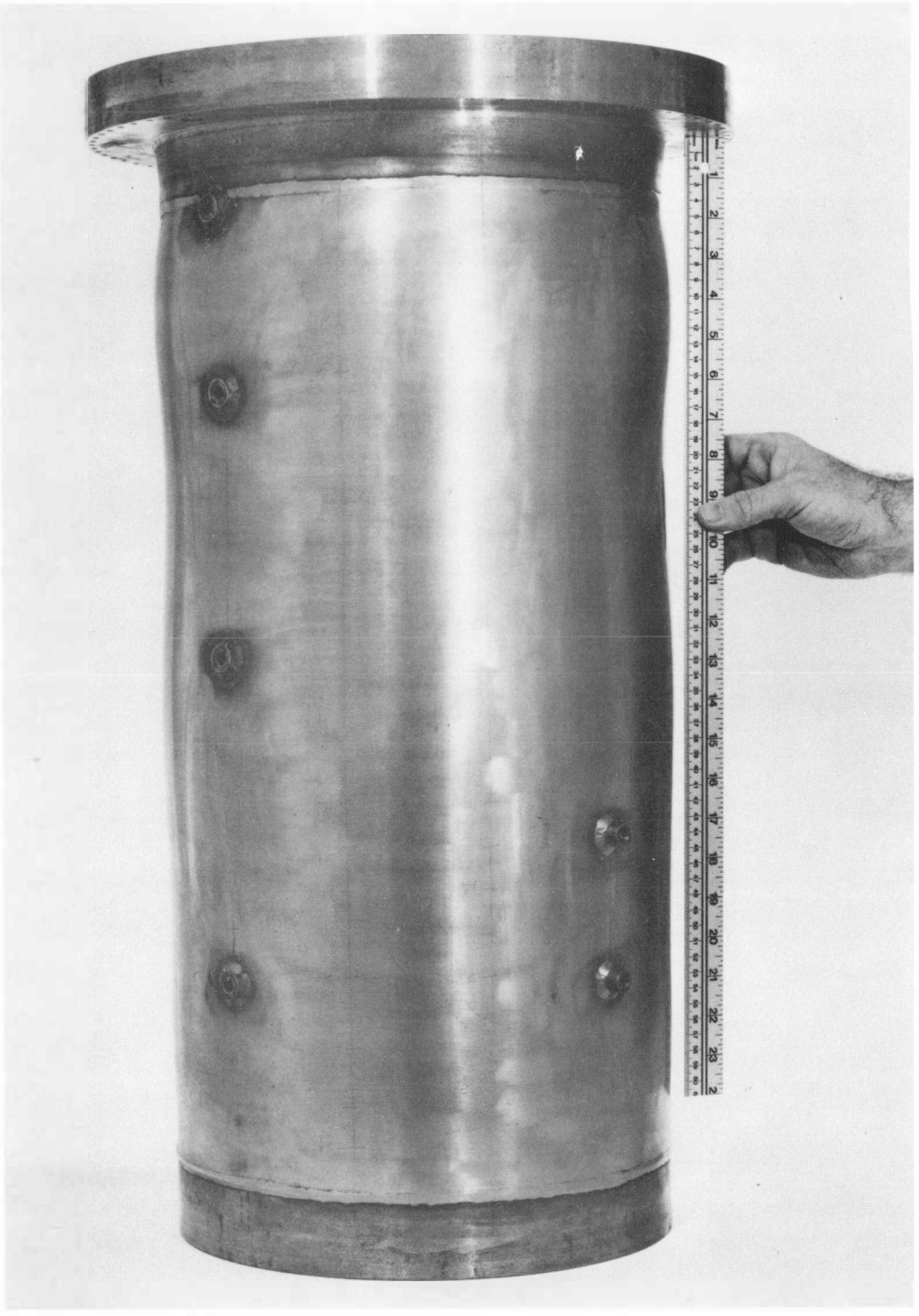

MP-3929-270

FIGURE 15 POSTTEST PHOTO OF SM 2 VESSEL

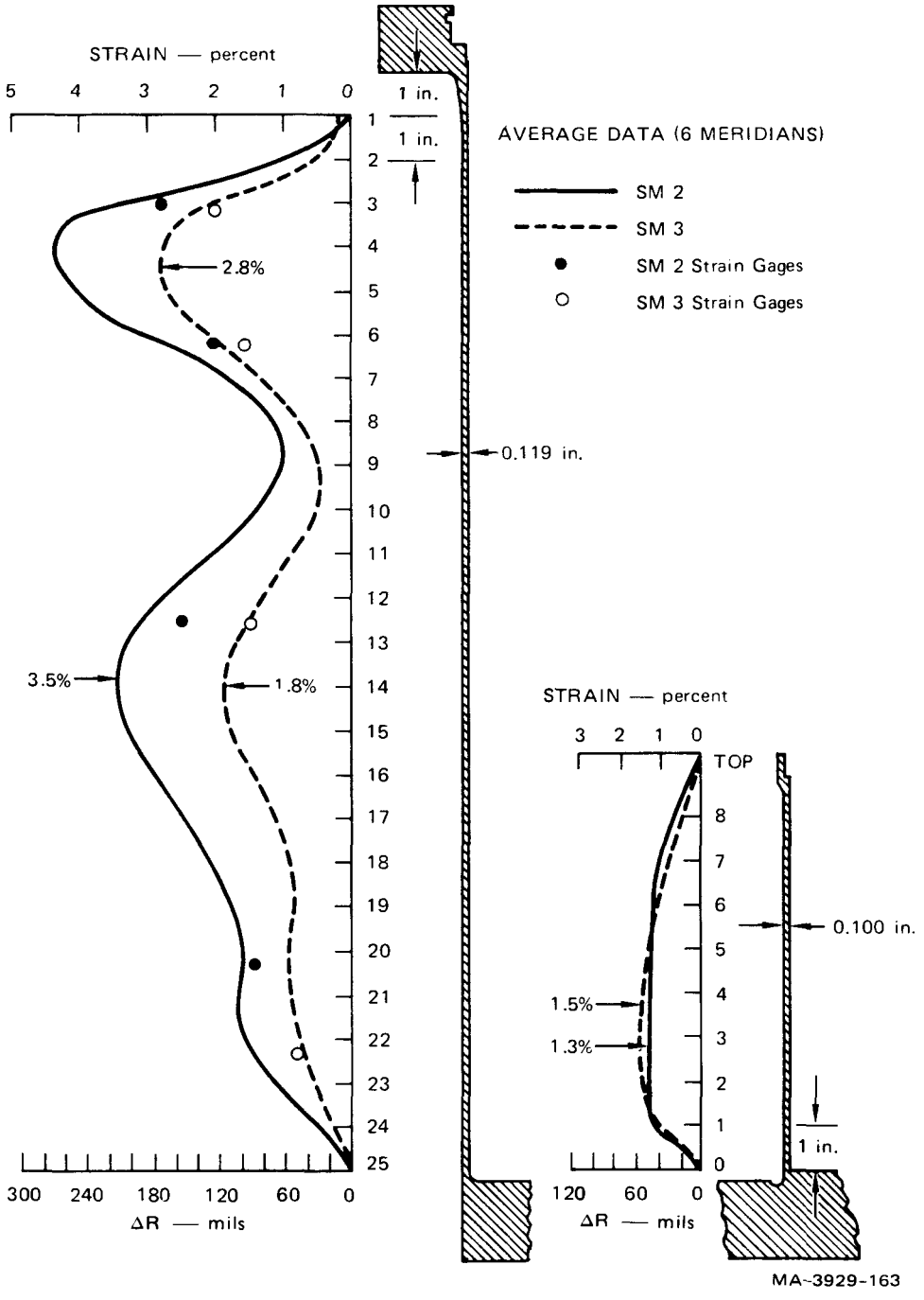

FIGURE 16 COMPARISON OF DEFORMED SHAPE PROFILES: SM 2 AND SM 3

unchanged. Evaluation of the effects of the UIS on vessel response can likewise be divided into these two phases: pre-slug impact response and post-slug impact response. As a further aid to determining the effect of the UIS on vessel response, the strain energy absorbed by the model during these two phases of response is evaluated. Table 3 lists a distribution of strain energy absorbed by each model and the gas work done by the explosive on each model. These data were calculated using high strain-rate properties of the models (see Figure B.3 in Appendix B), deformed shape profiles (Figure 16), and the pressure-volume change and energy-volume change relationships for the energy source (see Figure 6). The gas work at slug impact is obtained from the calibrated pressure-volume change and gas work-volume change curve (Figure 6). The volume change includes the volume of the cover gas (2560 cm^3) plus the change in volume of the lower vessel before slug impact. The slug kinetic energy at impact is calculated using the slug impact velocity from the water surface motion data and assuming that all the fluid above the core barrel is moving upward at this velocity. The slug also includes 500 g lead shot that sits on top of the diaphragm in the core. The strain energy calculations employ the high strain-rate properties of the Ni 200. The vessel wall and core barrel are divided into 0.5-in.-long rings. The average posttest radial deformation is used to calculate the hoop strain in each ring element. Axial strain energy is calculated by integrating the axial length change of each of the 0.5-in.-wide rings to determine the overall length change of the model. Axial strain energy is less than 5% of the radial strain energy.

The estimated energy in entrained and locally accelerated water is the difference between the gas work at slug impact and the sum of the slug kinetic energy and the strain energy at slug impact. In SM 2 before slug impact, the total strain energy absorbed by the vessel wall and core barrel is 4.40 kW-sec and the slug kinetic energy is 9.49 kW-sec. The total accountable energy up to slug impact is 12.89 kW-sec, 96% of the gas work expended up to slug impact. In SM 3 before slug impact, the total strain energy absorbed by the vessel wall, core barrel, and UIS columns is 2.86 kW-sec, and the slug kinetic energy

Table 3

ENERGY PARTITIONING IN SM 2 and SM 3

	Energy (kW-sec)		Energy distribution (%)	
	SM 2	SM 3	SM 2	SM 3
Gas work at slug impact	14.4	13.9	100	100
Slug kinetic energy at impact	9.49	4.43	65.9	31.8
Strain energy at impact				
Core barrel	0.46	0.42	--	--
Vessel wall	3.86	1.60	--	--
Thermal liner	--	--	--	--
UIS columns	--	0.83	--	--
Support platform	--	--	--	--
Axial strain energy	0.08	0.01	--	--
Total strain energy at impact	4.40	2.86	30.6	20.6
Estimated kinetic energy in entrained and locally accelerated water	0.51	6.61	3.5	47.6
Total gas work after impact	14.6	14.2	100.0	100.0
Strain energy after impact				
core barrel	0.46	0.42	--	--
Vessel wall	6.19	3.18	--	--
Thermal liner	--	--	--	--
UIS columns	--	0.83	--	--
Support platform	--	--	--	--
Axial strain energy	0.25	0.04	--	--
Total strain energy after impact	6.90	4.47	47.3	31.5

is 4.43kW-sec. The total accountable energy up to slug impact is 7.29 kW-sec, 52% of the gas work expended up to slug impact. In SM 3 the difference between accountable energy (strain energy and slug kinetic energy) and gas work to slug impact is the radial kinetic energy and turbulent energy of the water caused by the complex flow of detonation products and water through and around the UIS.

The difference in response between SM 2 and SM 3, therefore, is attributable to the presence of the UIS, which redirects the flow of gas out of the core. Part of the work potential goes into radial and turbulent kinetic energy of the water that is eventually dissipated without doing work on the vessel.

Blank Page

IV COMPLEX MODEL EXPERIMENTS SM 4 AND SM 5

A. Model Description

Figures 17 and 18 show schematic layouts of models SM 4 and SM 5 which are more complex than the simple models SM 2 and SM 3. The main differences between the complex models SM 4 and SM 5 and the simple models SM 2 and SM 3 are:

(1) Starting from the bottom of the upper vessel flange, the wall thickness is 156 mils. It tapers down in 1.68 in. to 140 mils, and decreases to 119 mils 9 in. above the top of the core. The vessel walls for SM 2 and SM 3 have a uniform wall thickness of 119 mils along the entire length of the vessel.

(2) SM 4 and SM 5 have a 78-mil-thick Ni 200 thermal liner. The liner parallels the vessel wall from the core barrel to within one in. of the head shielding (4 in. from the top of the head). There is a 0.125-in. gap between the vessel wall and the thermal liner over the length of the liner. SM 2 and SM 3 have no thermal liner.

(3) SM 4 and SM 5 include a conical core support ring that connects the core support platform to the vessel wall. In addition, the core structure includes a horizontal baffle that is welded to the upper core barrel; SM 2 and SM 3 have a rigid core support platform and no horizontal baffle.

(4) SM 4 and SM 5 include a complex model of the three-plug reactor head. Shear rings in each plug are carefully scaled. Shielding and head-mounted components are accurately represented (location and mass). SM 2 and SM 3 have a simple one-plug head with simplified shielding and masses.

B. Instrumentation

1. SM 4 Instrumentation

The instrumentation for SM 4 (Figure 17) was basically the same as for SM 2 and SM 3, but SM 4 had two less pressure transducers, one removed from the upper core and the other from the vessel wall. Ten

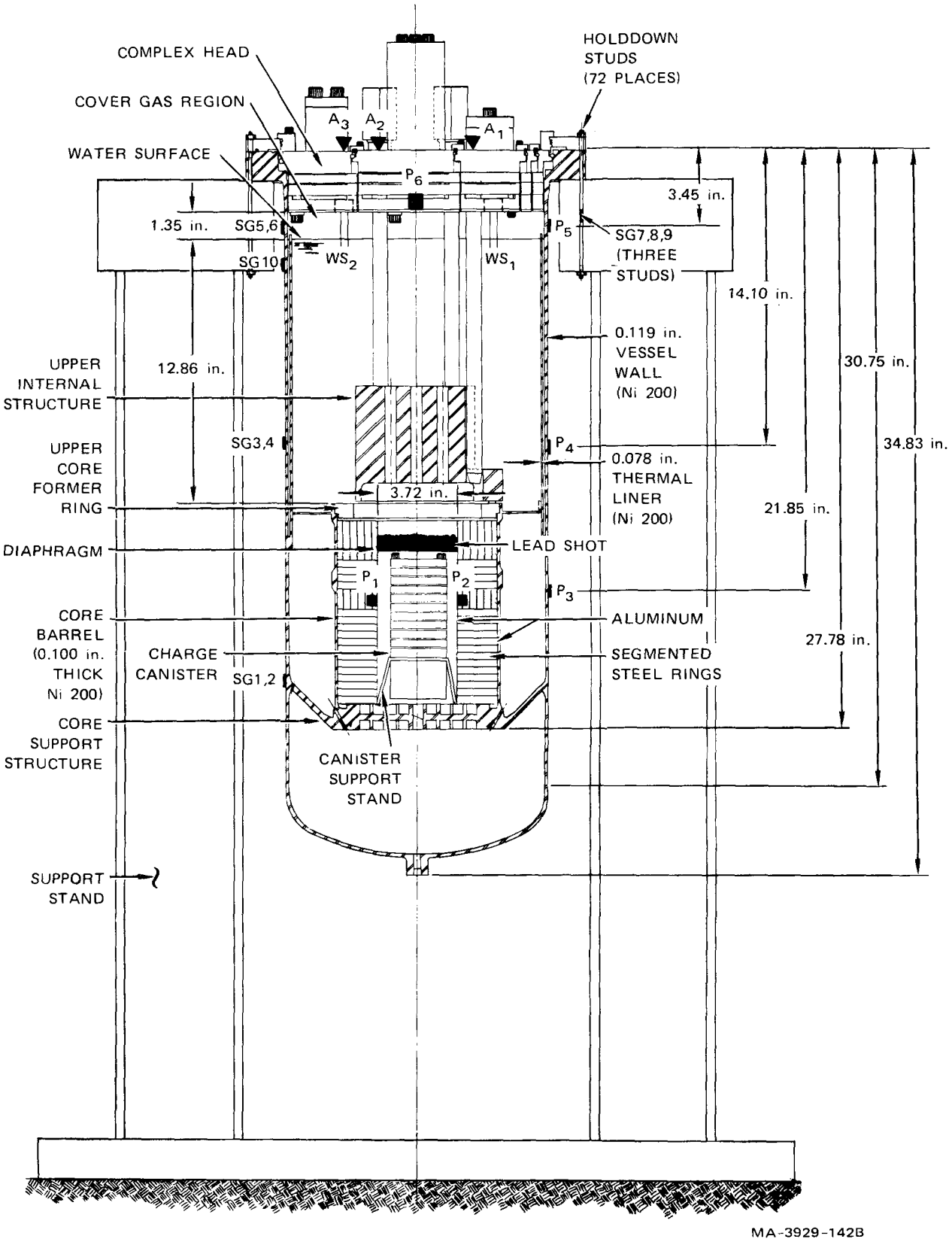

FIGURE 17 SM 4 WITH INSTRUMENTATION

strain gages were installed on SM 4. Six were bonded in pairs as T-rosettes on the vessel wall; three were installed as single gages on three of the holddown studs; and one, on the vessel wall at the expected location of the peak strain. Three accelerometers were mounted on the three-plug head, one on each plug. Two water-surface displacement gages were also installed on the head. The instrumentation provided a total of 21 channels of data.

2. SM 5 Instrumentation

A much more extensive instrumentation layout was designed for SM 5 (Figure 18) to provide a more comprehensive measure of the response of the complex model. The following list outlines the scope of the instrumentation on SM 5.

Pressure Gages--16 pressure gages were installed on SM 5, two in the core; and five, along the vessel wall. Pressure gage P_5 (Figure 18) was installed in the lower vessel; P_6, P_7, and P_9 were installed in corresponding locations opposite the core, the UIS, and the upper vessel, respectively, as in the other three models; and P_8 was installed in the vessel wall above the UIS to measure the pressure in the water between the thermal liner and the vessel wall. Pressure gages P_{10}, P_{11}, and P_{12} were installed in the head shielding to measure slug impact pressure. Pressure gage P_{13} was installed in the head above the shielding of the intermediate rotating plug (IRP) to measure the cover gas pressure in the gap between the shielding and the head. Pressure gage P_{14} was installed in the vessel flange to measure the pressure acting in the shear ring area. Pressure gages P_{15} and P_{16} were installed in the space representing the large riser gas volume to measure the pressure above the shear ring seal.

Strain-Gages--Twenty-one strain gages were installed on SM 5 (Figure 18). Strain gages SG 1 and SG 2 mounted on the core barrel were damaged in assembly and thus were inoperative. Strain gages SG 3 and SG 4 measured hoop and axial strains on the perimeter of the core support ring. Strain gages SG 5, SG 7, and SG 21 measured hoop strain on the vessel wall. Strain gages SG 6 and SG 8 measured axial strain on the vessel wall. Strain gages SG 9 and SG 10 were mounted on the large

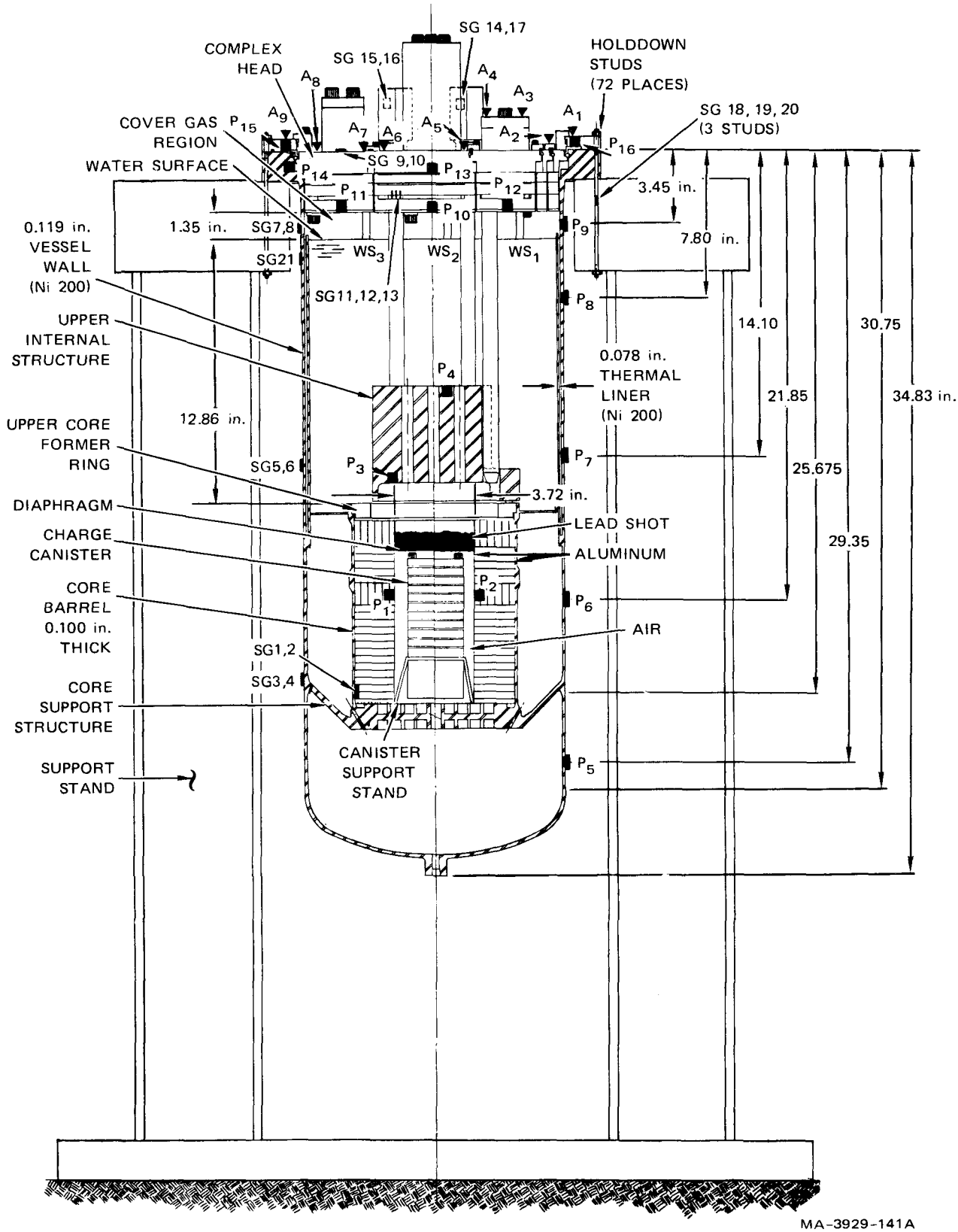

FIGURE 18 SM 5 WITH INSTRUMENTATION

rotating plug (LRP) to measure its radial and tangential strains. Strain gages SG 11, SG 12, and SG 13 were mounted on the upper end of the hollow Ni 200 portion of one of the UIS columns to measure its axial and bending strains. Strain gages SG 14 through SG 17 were mounted, one each, on the upper solid steel portion of each UIS column. Strain gages SG 18 through SG 20 were bonded to three of the studs that secure the vessel to the support stand.

Accelerometers--Nine accelerometers were mounted on the three-piece head of SM 5 to measure the accelerations of the various components of the head. The accelerometer layouts are shown in Figure 18.

Water Surface Gages--Three of the water surface gages described earlier were installed in the head to measure the slug motion. Locations for these gages are shown in Figure 18.

Displacement Gage--A linear-potentiometer displacement gage* was mounted next to accelerometer A_6 on the IRP to measure its upward displacement. Based on results of Static Test SM 1, we expected the IRP in this area to experience the largest displacement.

C. Results

This section discusses the pressure, strain, and acceleration measurements for SM 4 and SM 5. Except for the inadvertent use of unannealed UIS columns in SM 4, these two models are identical. The comparative results of these two tests demonstrate the reproducibility of the experiments.

1. Loading Pressures

Figure 19 compares the loading pressures† in SM 4 and SM 5. For all records shown, the peak pressures are nearly the same in both tests.

---

*Model 3273, manufactured by Bourns Instrument Division, Riverside, California.

†All pressure records except those for the upper vessel wall and the head were digitally filtered at 10 kHz; the upper vessel pressure records were filtered at 25 kHz and the head pressures were filtered at 25 kHz for SM 4 and 50 kHz for SM 5. See Appendix E for a discussion of filter frequency selections.

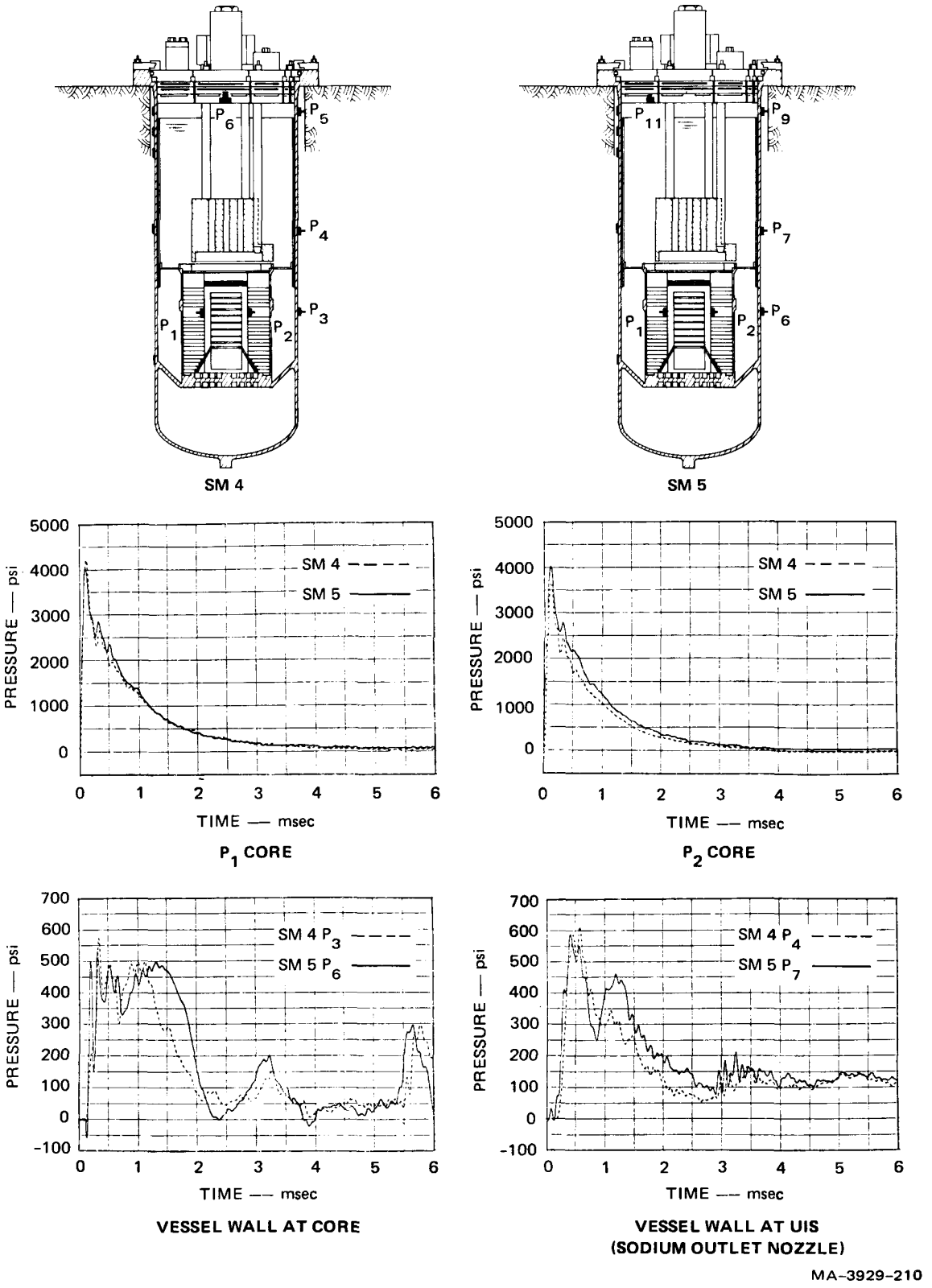

FIGURE 19 COMPARISON OF LOADING PRESSURES: SM 4 AND SM 5

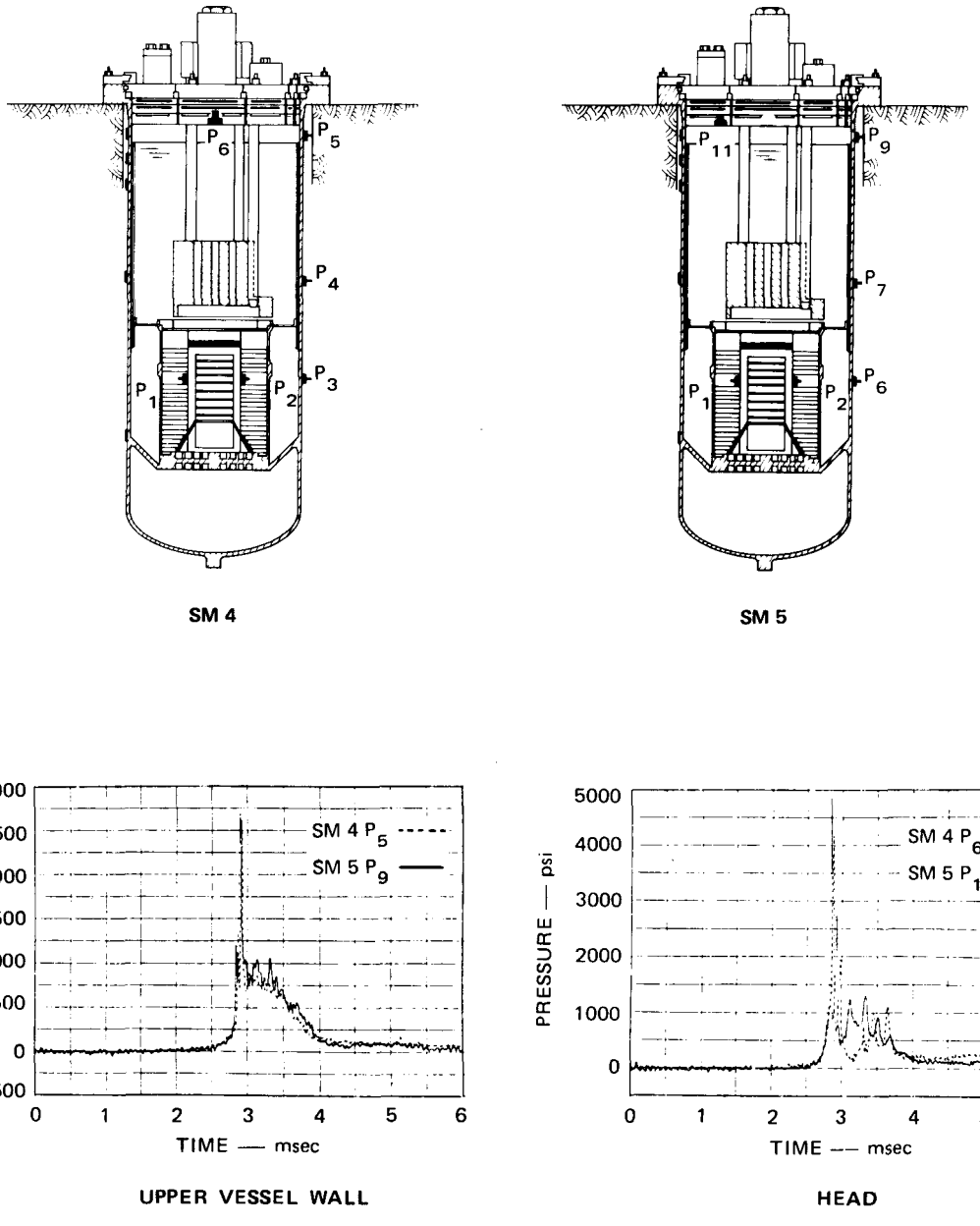

FIGURE 19 COMPARISON OF LOADING PRESSURES: SM 4 AND SM 5 (Concluded)

Some details of the pressure records, such as the decay portion of the records labeled Vessel Wall at Core and Vessel Wall at UIS, are different. These differences are probably due to the difference in yield strength of the columns in SM 4 and SM 5. The columns in SM 4 were unannealed and therefore had a higher yield strength than those in SM 5 which were annealed to specification.

The pressure in the core for both tests rises to about 4000 psi in 0.1 msec and then decays slowly to atmospheric pressure. The peak pressure is in very good agreement with calibration test results (3840 psi in the core).

The pressure on the vessel wall opposite the core rises to about 475 psi in both tests, remains fairly constant for about 1.3 msec and then drops to near atmospheric pressure in about 1 msec. The peak pressure is above the yield pressure for the vessel wall (370 psi). The drop in pressure after 1.3 msec is attributed to a change in the relative motion between the core barrel and the vessel wall. Early in the test, the core is being pushed out by the core pressure. The expansion causes the pressure to rise in the region between the core barrel and the vessel wall. The pressure in this region continues to rise until the yield pressure of the vessel wall is reached. The vessel wall then begins to expand, maintaining the yield pressure. When the core barrel stops expanding and begins to recede, the pressure between the core barrel and the vessel wall drops quickly.

The pressure on the vessel wall opposite the UIS rises to a peak pressure of about 600 psi in both tests and then drops slowly. The peak pressure is very near the yield pressure for the combined vessel wall and thermal liner (610 psi yield pressure).

The pressure records for the upper vessel wall and the head indicate that slug impact occurs at the same time in both experiments, implying very similar slug impact velocities. The sharp high-pressure spikes recorded for the upper vessel wall and the head are probably due to local compression of the cover gas around the pressure gages as the

slug moves upward. These pressure spikes are relieved very quickly as the gas mixes with the slug upon impact.

Figure 20 compares the water surface displacement for SM 4 and SM 5. The displacements are very similar. Slug impact velocities differ by less than 1%. Clearly, the difference in strength of the UIS columns did not affect slug motion. Comparison of the slug impact velocity in SM 4 and SM 5 with that in SM 3, the simple model with a UIS, reveals a difference in slug velocities that is again less than 1% (62.3 ft/sec average for SM 4 and SM 5; 62.5 ft/sec for SM 3). This result reinforces the conclusion that the difference in strength of the UIS columns did not affect slug motion.

The good agreement in slug velocity between SM 4, SM 5, and SM 3 also demonstrates that slug motion is relatively insensitive to deformation of the lower vessel wall during the early response mode. On SM 3, significant expansion of the vessel wall occurred opposite the core barrel and opposite the UIS. On SM 4 and SM 5, little vessel wall expansion occurred in these areas.

2. Strain Response

Figure 21 compares strain records* at corresponding locations on models SM 4 and SM 5. Few comprehensive comparisons of strain on the vessel wall for SM 4 and SM 5 can be made because fewer gages were used on SM 4 and because the strain gages mounted on the core support ring of SM 5 failed. On the vessel wall opposite the UIS, the peak strain in SM 5 is 300% higher than that in SM 4. The peak loading pressure on this part of the vessel wall (see Figure 19) was nearly the same. The large difference in strain might stem from the fact that the peak pressure is very close to the yield pressure of the vessel wall (P_y = 610 psi) and that very small differences in the pressure or in the material properties would greatly affect strain response. If the loading pressures on SM 4 at this location had been 10% higher, the wall would have experienced a much larger plastic strain and the difference in strain between models would not have been as great.

*Each record has been digitally filtered at 10 kHz.

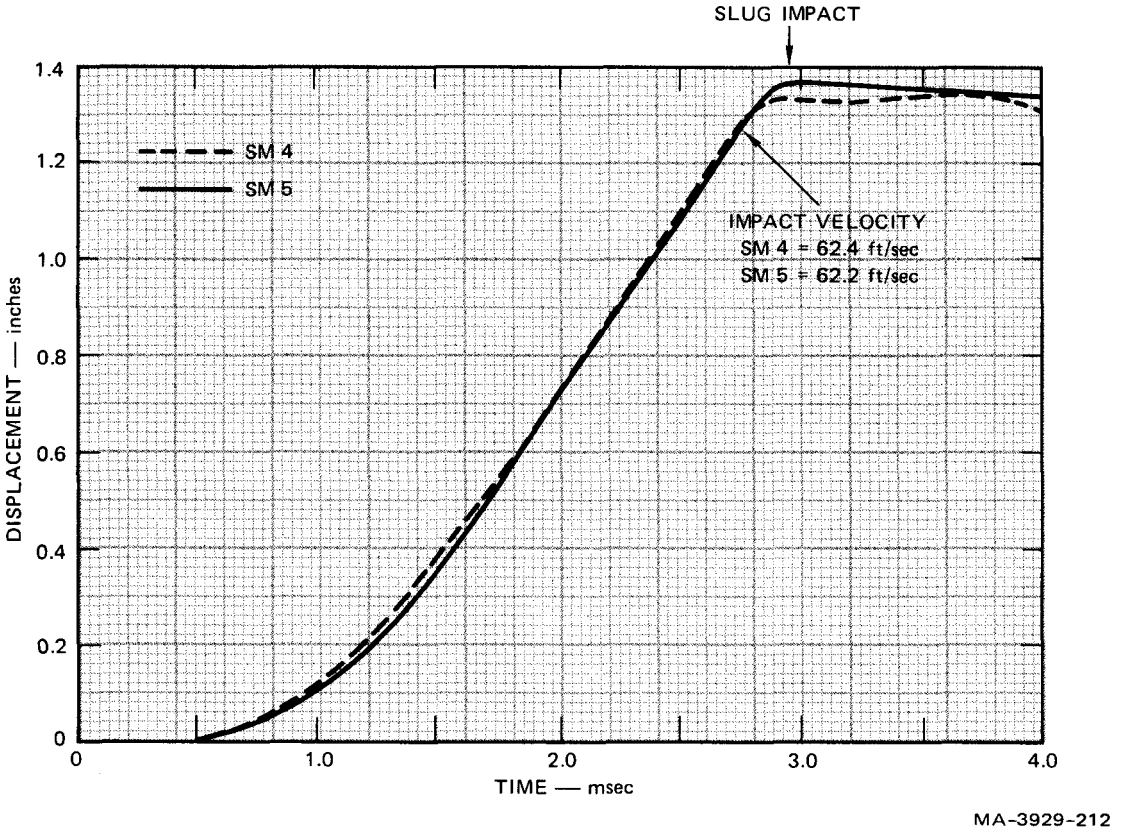

FIGURE 20 COMPARISON OF WATER SURFACE DISPLACEMENTS: SM 4 AND SM 5

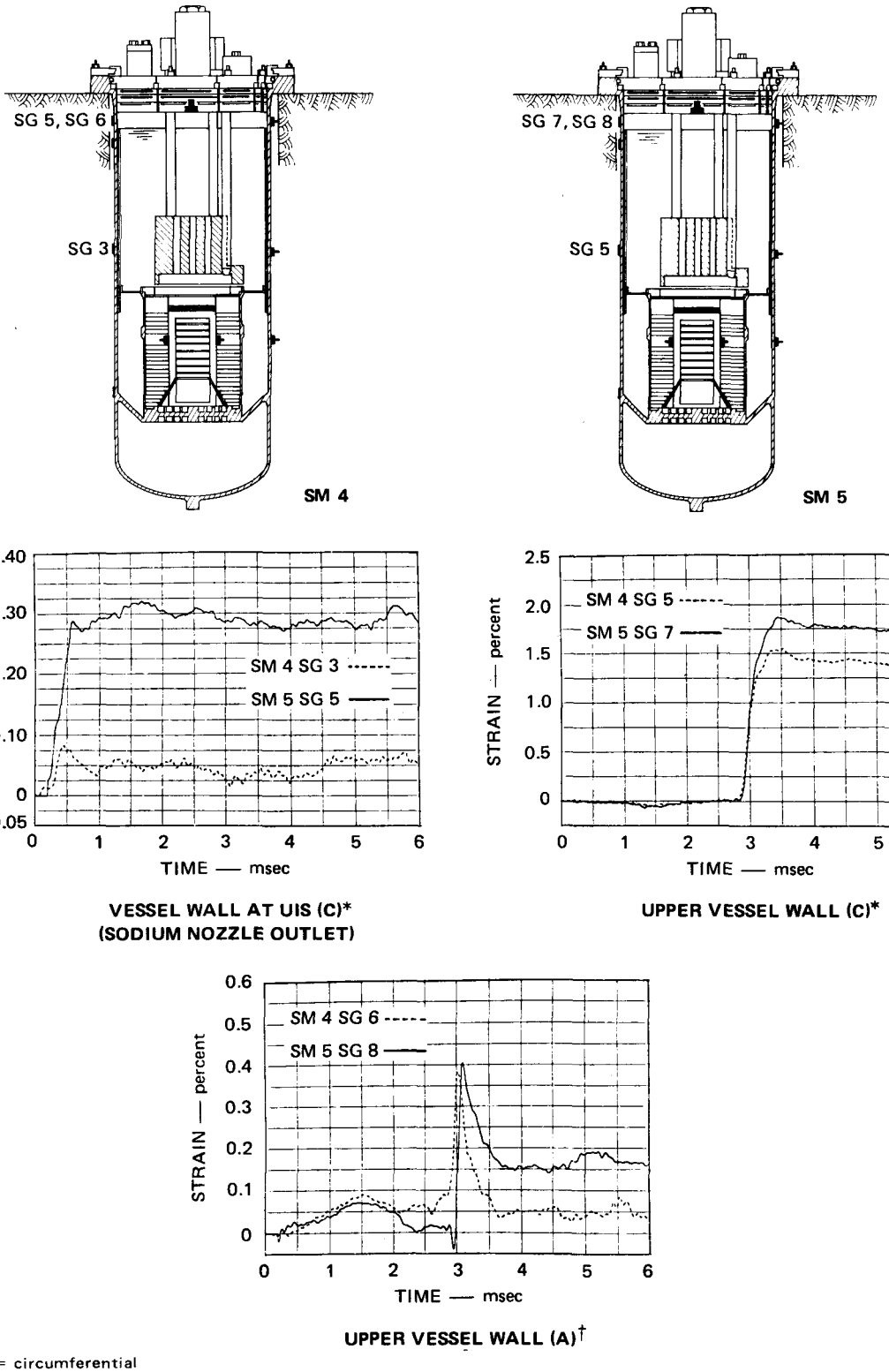

*C = circumferential

†A = axial

MA-3929-213

FIGURE 21 COMPARISON OF STRAIN RESPONSE: SM 4 AND SM 5

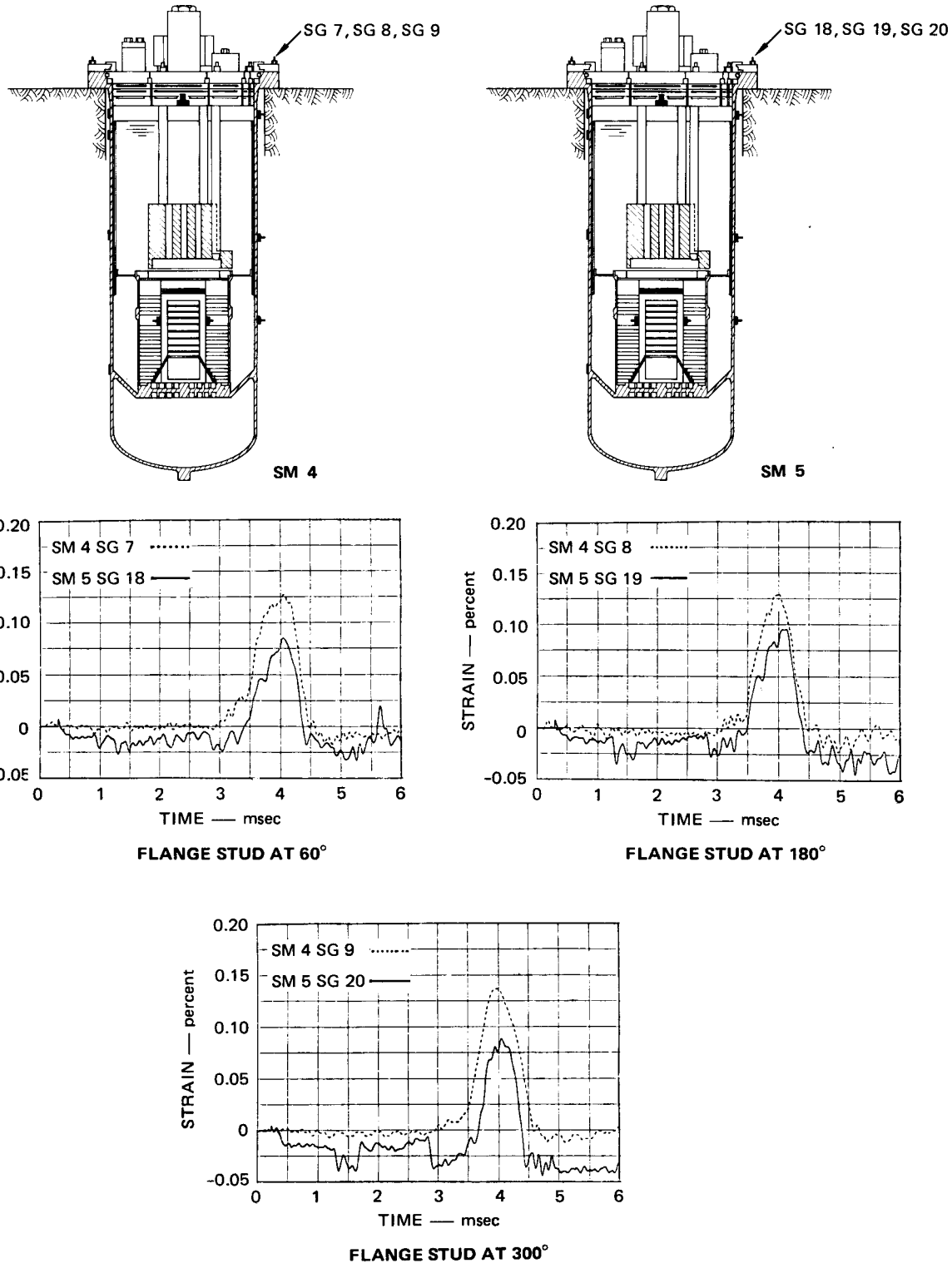

FIGURE 21 COMPARISON OF STRAIN RESPONSE: SM 4 AND SM 5 (Concluded)

The strain response on the upper vessel wall is in better agreement between SM 4 and SM 5 with the strain slightly lower on SM 4 than on SM 5. Comparison of the loading pressures in this area (Figure 19, SM 4 P_5 versus SM 5 P_9) shows that the loads on SM 4 were also slightly lower than on SM 5. In both the upper and lower vessel wall areas, SM 4 experiences lower strains than SM 5. The differences can be attributed to small differences in loading pressures and to small variations in the material properties between the two models. The upper vessel wall in the more complex models SM 4 and SM 5 experiences a tensile axial strain caused by the downward reaction of the core support plate and core support ring (also seen in SM 2 and SM 3). The amplitude of this initial axial strain is about 0.08% compared with an initial axial strain of about 0.25% in SM 2 and SM 3. The lower initial strain in SM 4 and SM 5 reflects the stiffer (thicker) construction of the vessel walls of SM 4 and SM 5. After slug impact, the axial strain at the top of the vessel suddenly increases as the vessel wall is driven outward. The axial strain reaches a peak of about 0.4% and then decreases as the vessel response mode changes from hoop expansion to bending in this area.

The strain records from the three instrumented holddown studs (SG 7, SG 8, and SG 9 on SM 4; SG 18, SG 19, and SG 20 on SM 5) are analyzed to determine the ledge load. Each of the 72 steel studs (4140 steel) that hold the models to the test stand were preloaded to 825 lb (about 0.2% strain). Measurement of the dynamic strain on the instrumented studs, then, reflects a change from the prestress load on each stud. On SM 4, the strain increase averages about 0.13%. The combined preload strain and dynamic strain is still below the elastic limit. An ealstic analysis, therefore, gives a peak load during the tests of 1355 lb per stud and a total peak ledge load (72 x 1355 lb) of 95,571 lb. The average peak strain on the studs of SM 5 is 0.087%. An elastic analysis of these data gives a peak load of 1170 lb per stud and a total peak ledge load (72 x 1170 lb) of 84,312 lb. The 10% difference in ledge loads between SM 4 and SM 5 might result from the interpretation of the strain records. On SM 5 an initial decrease in stud strain (Figure 21) occurs before slug impact. The decrease is large enough to account for the

difference in ledge load between SM 4 and SM 5. An explanation for this initial decrease in strain might be that small flecks of dirt between the flange and the ledge could compress and relieve the prestress load on the studs during the initial downward thrust of the model, or a baseline shift if the instrumentation could occur. The average of the peak ledge load for SM 4 and SM 5 is 89,941 lb, which is very near the peak ledge load for SM 3 (90,300 lb).

3. Accelerations

Figure 22 compares accelerometer records from SM 4 and SM 5. All accelerometer records have been digitally filtered at 16 kHz. To avoid confusion, comparable records are placed side by side. Examination of the records shows remarkably similar acceleration histories at comparable gage locations further demonstrating the reproducibility of the experiments.

Some of the same modes noticed in the acceleration records for the one-plug heads of SM 2 and SM 3 (Figure 12) are noted in the acceleration records for SM 4 and SM 5. The initial upward thrust of the head caused by the direct loading of the UIS near the core is seen at about 0.5 msec on all three acceleration recrods for SM 4 and SM 5. The upward thrust takes up the slack between the shear rings and the shear ring bearing surfaces for the LRP and IRP. The first downward acceleration on these records following the upward thrust of the UIS is caused by the downward thrust on the core support platform from core pressure, as was noted for SM 2 and SM 3.

The peak accelerations of the three-plug head are nearly uniform across the head, whereas the peak accelerations near the edge of the one-plug heads of SM 2 and SM 3 were about one-third of the peak acceleration at the center. The more extensive accelerometer instrumentation on SM 5 demonstrates more clearly the uniformity of acceleration across the three-plug head. The peak accelerations listed in Table 4 for SM 2, SM 3, SM 4, and SM 5 illustrate this point.

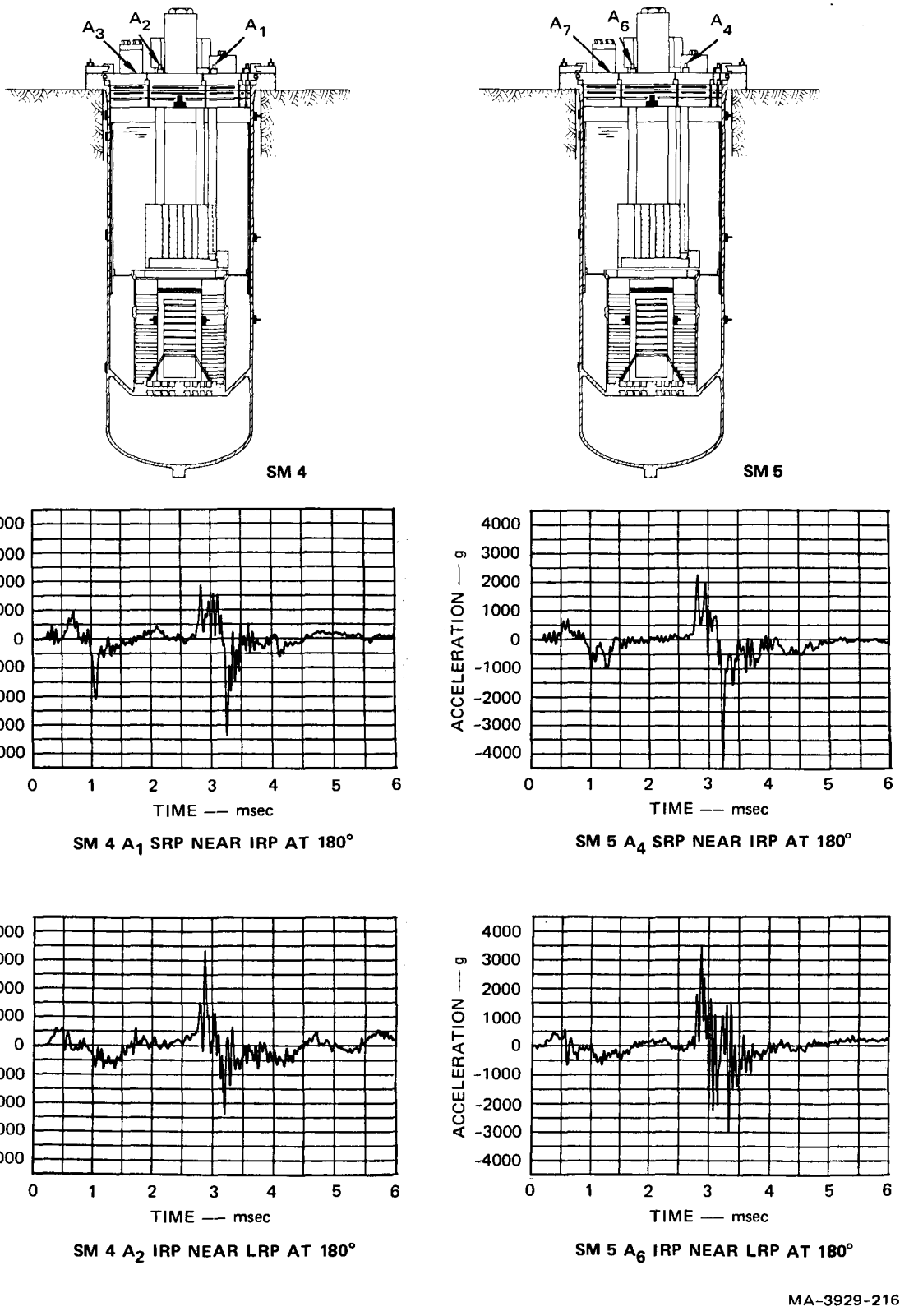

FIGURE 22 COMPARISON OF ACCELERATIONS: SM 4 AND SM 5

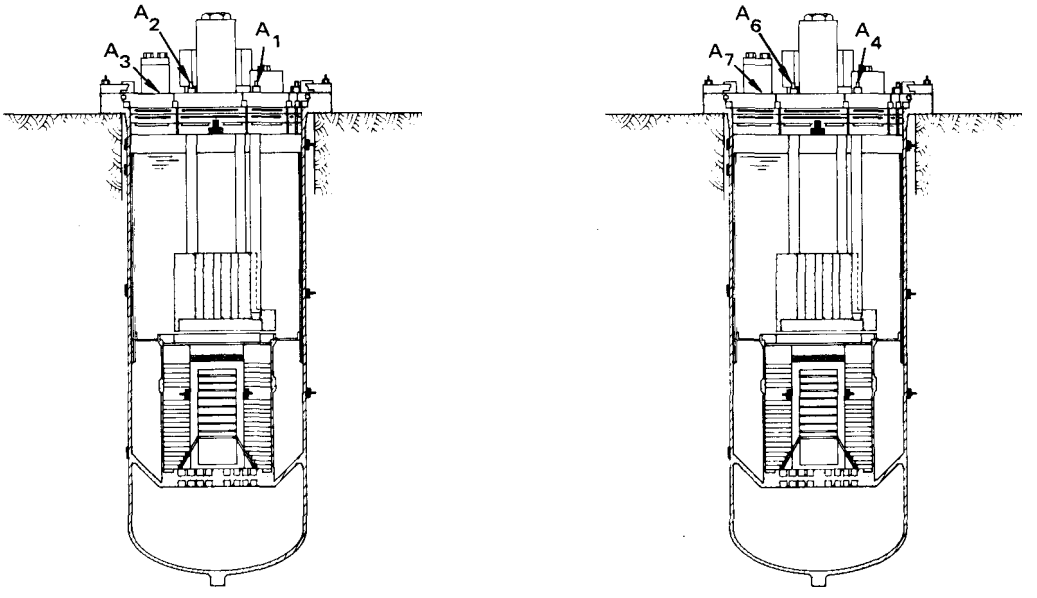

FIGURE 22 COMPARISON OF ACCELERATIONS: SM 4 AND SM 5 (Concluded)

Table 4

HEAD ACCELERATIONS ON SM 2, SM 3, SM 4, and SM 5

Gage No.					Peaks (gravity, g)			
SM 2	SM 3	SM 4	SM 5	Location	SM 2	SM 3	SM 4	SM 5
--	--	--	A_1	Flange ring at 0°	--	--	--	2100
A_1	A_1	--	A_2	IRP at 0°	1200	1200	--	3600
--	--	--	A_3	SRP at 0°	--	--	--	2600
A_2	A_2	A_1	A_4	SRP near IRP at 180°	4800	4600	3400	4500
--	--	--	A_5	IRP near center	--	--	--	3800
--	--	A_2	A_6	IRP near LRP at 180°	--	1300	3300	3500
--	--	A_3	A_7	LRP at 0° near IRP	--	--	3200	4800
A_3	A_3	--	A_8	LRP near edge at 180°	1850	1300	--	3800
--	--	--	A_9	Flange ring at 180°	--	--	--	3100

4. UIS Column Response

The UIS columns on SM 4 were inadvertently not annealed and therefore had a higher yield strength than intended. As a result, they did not deform during the experiment. The effect on the overall model response, however, was very small. Comparison of loading pressures, strains, slug impact velocities, and head accelerations on SM 5 with corresponding data from SM 4 showed only minor differences between the two experiments. The UIS columns on SM 5 compressed and buckled under the direct loading from the core. The compression as measured by strain gages on the Ni 200 portion of the UIS begins with the upward load from the gas bubble expanding out of the core and reaches a peak strain of 2.1% about 2 msec after detonation of the charge and about 1 msec before slug imact. After a small rebound (about 0.3% strain) the columns remain plastically deformed. The peak strain measured on the columns is about 2.1%. This strain corresponds to a peak stress in each column of 47,000 psi based on the measured low strain rate stress strain properties of the column material. This stress translates into a peak load carried by each column of about 4800 lbs which is significantly above the static buckling load (1970 lbs) for the columns.* It is concluded then that the columns buckled dynamically in a low order mode. Figure 23 shows the deformed shape profiles of each of the four UIS columns in SM 5. Buckling deformation is not severe and the axial compression is only about 0.17 in., which represents a 2.1% change in length of the hollow Ni 200 portion of the columns. This compression (2.1%) is in reasonable agreement with the dynamic strain measured on one of the UIS columns (about 2% peak strain reducing to about 1.75% strain at late times). The buckling of the UIS columns in SM 5 was not as severe as the buckling of the UIS columns of SM 3 (compare Figure 14 with Figure 23). Review of annealing records

*The static buckling load (assuming a fixed end condition on each end of the columns) is $P_{cr} = 4\pi^2 E_T I/L^2$ where $E_T = 5.9 \times 10^5$ psi is the slope of the work hardened portion of the Ni 200 stress-strain curve, $I = 5.4 \times 10^{-3}$ in.^{4} and $L = 8$ in. (based on the observed buckling pattern of the UIS columns).

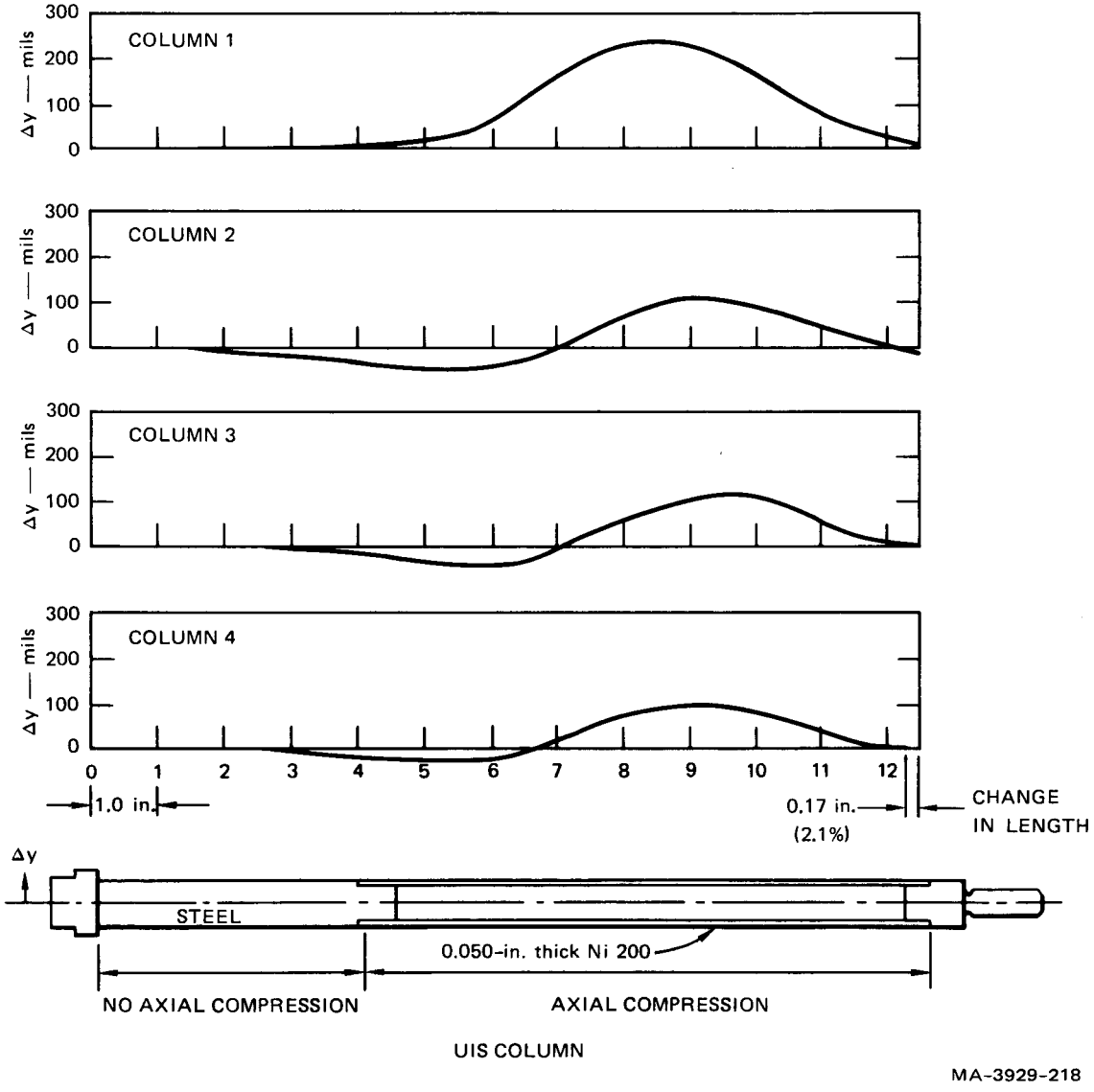

FIGURE 23 DEFORMATION PROFILES FOR UIS COLUMNS IN SM 5

indicates that the UIS columns in SM 3 were held at the annealing temperature (1300°F) for twice the specified 30-min annealing time. The static stress-strain properties of the Ni 200 used to fabricate the UIS columns for SM 3 and SM 5 are shown in Appendix B. The overly annealed columns have a much lower yield stress (13 ksi versus 34 ksi for the columns annealed to specification). From these stress-strain curves, the peak column stress for the SM 3 columns and the SM 5 columns is nearly the same (SM 3: 47.5 ksi at 7%; SM 5: 47 ksi at 2.1%).

5. Deformed Shape Profiles SM 4 and SM 5

Figure 24 compares the deformed shape profiles of models SM 4 and SM 5. The curves represent the average data taken along six equally spaced meridians on each vessel. A separate profile is shown for the vessel wall, the thermal liner, and the core barrel. In the figure, the space between the vessel wall profile and the thermal liner profile is scaled to the actual clearance tetween the wall and thermal liner on the model.

Except for the deformation of the vessel wall opposite the core barrel, the deformed shape profiles for both models are very similar. The vessel wall opposite the thermal liner deforms much less than did the vessel wall in SM 2 and SM 3, because the wall and the liner together have a greater stiffness than the single wall in SM 2 and SM 3. As mentioned earlier, peak pressures in this area barely exceed the yield pressure (610 psi) of the combined structure, so not much plastic deformation occurs. The deformations of the upper vessel wall and the upper thermal liner are very similar, further demonstrating the reproducibility of slug impact velocity and resulting pressures in this area. The inward deformation of the core support ring (points 24 and 25, Figure 24) reflects the strong downward force on the core support plate, translated to the vessel wall through the core support cone. The center of the core support plate on SM 5 was 0.133 inches lower after the test than before the test.* There was no significant axial stretch of the vessel.

*This measurement is based on the distance from the top of the vessel flange to the center of the core support plate made before and after the test. Based on measurement of the curvature of the core support plate after the test, the center of the plate deformed 0.1 in. relative to the edge of the plate.

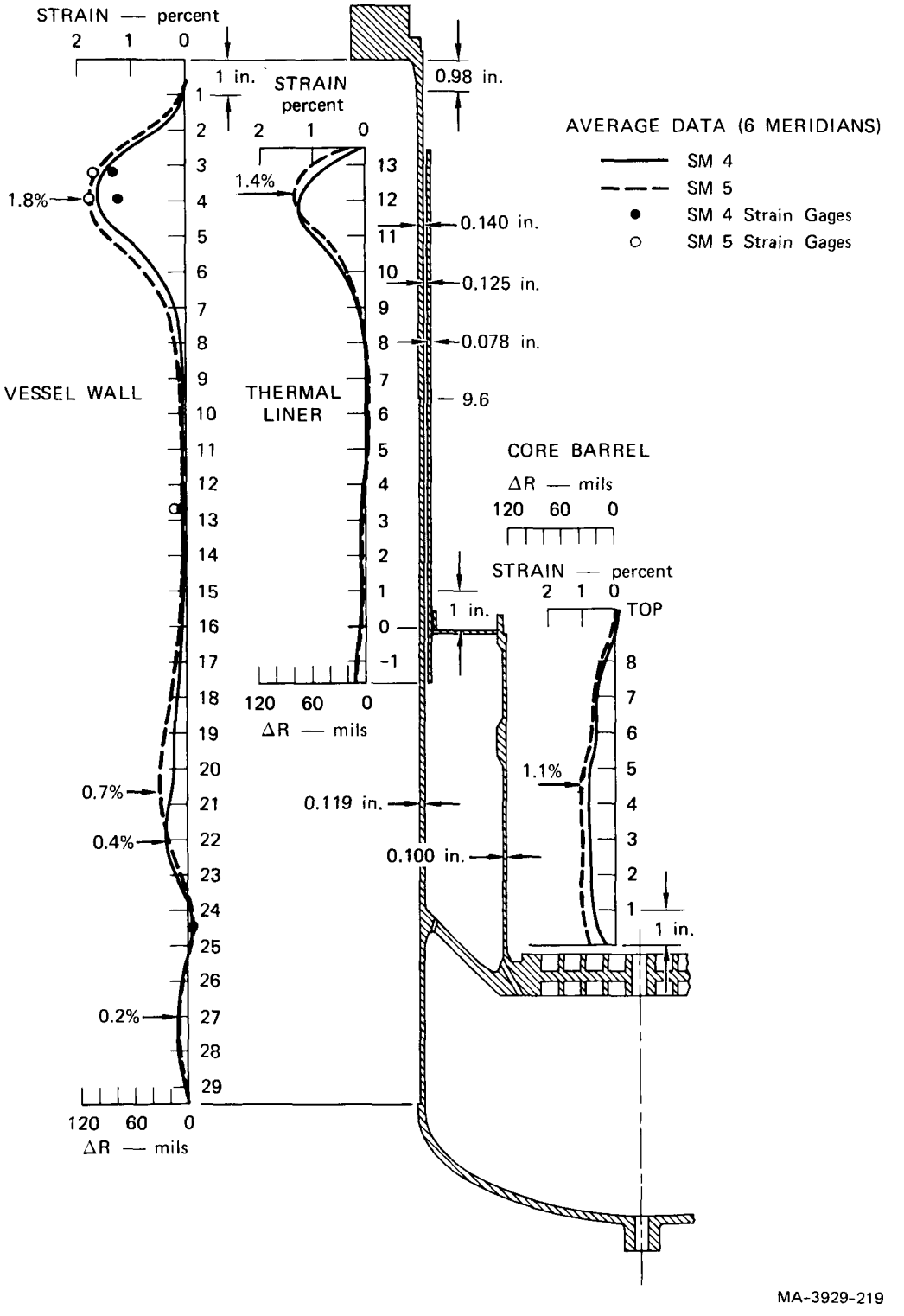

FIGURE 24 COMPARISON OF DEFORMED SHAPE PROFILES: SM 4 AND SM 5

The deformation profile of the core barrel shows the effect of the hoop stiffener on the core barrel structure. The peak deformation of the core barrel is slightly smaller than those of the core barrels in SM 2 and SM 3 (1.1% in SM 5 versus 1.3% in SM 3). The lower core barrel deformation is the result of the ring stiffener incorporated into the SM 4 and SM 5 core barrel design.

6. Strain Energy Calculations

As for Models SM 2 and SM 3, we evaluated the energy distribution in the complex models. Table 5 lists the distribution of gas work, slug kinetic energy, vessel strain energy, and an approximation of the reduction of work potential caused by the complex flow through and around the UIS for SM 4 and SM 5. The gas work at slug impact is obtained from the calibrated pressure-volume change and gas work-volume change curves. The volume change considered is the volume of the cover gas (2560 cm^3) plus the volume change of the lower vessel that occurs before slug impact. The slug kinetic energy at impact is calculated using the slug impact velocity from the water surface motion data and the mass of the fluid above the core barrel (including the 500 g of lead shot in the upper core). The volume of the slug for SM 4 and SM 5 is smaller than for SM 2 and SM 3 because the thermal liner reduces the diameter of the slug. The UIS and UIS columns further reduce the volume of the slug. The strain energy calculations are based on the high-strain-rate properties of the Ni 200. Both axial and hoop strain energy are considered. The vessel wall, thermal liner, and core barrel are divided into 0.5-in.-long rings. The average posttest radial deformations are used to calculate the hoop strain in each ring element. The strain energy absorbed by each ring element is added to obtain the hoop strain energy absorbed by the structure. The incremental axial length change of each ring element is considered when calculating axial strain energy. Before slug impact the deformed shape profile is approximated on the basis of strain gage data. The estimated energy in entrained and locally accelerated water is the difference between the gas work at slug impact and the sum of the slug kinetic energy and the strain energy at slug impact.

Table 5

ENERGY PARTITIONING IN SM 4 AND SM 5

	Energy (kW-sec)		Energy Distribution (%)	
	SM 4	SM 5	SM 4	SM 5
Gas work at slug impact	13.5	13.6	100.0	100.0
Slug kinetic energy at impact	4.15	4.12	30.7	30.3
Strain energy at impact				
Core barrel	0.24	0.37	--	--
Vessel wall	0.20	0.33	--	--
Thermal liner	0.02	0.02	--	--
UIS columns	0.00	0.27	--	--
Support platform	?	?		
Axial strain energy	0.01	0.01	--	--
Total strain energy at impact	0.47	1.00	3.5	7.4
Estimated kinetic energy in entrained and locally accelerated water	8.88	8.48	65.8	62.3
Total gas work after impact	13.8	13.9	100.0	100.0
Strain energy after impact				
Core barrel	0.24	0.37	--	--
Vessel wall	0.83	1.19	--	--
Thermal liner	0.21	0.24	--	--
UIS columns	0.00	0.27	--	--
Support platform	?	?		
Axial strain energy	0.02	0.02	--	--
Total strain energy after impact	1.30	2.09	9.4	15.0

Both models had essentially the same work potential at slug impact and nearly the same slug velocities. The average slug kinetic energy of 4.13 kW-sec for the complex models is about 31% of the work potential (gas work) at slug impact. The strain energy absorbed by the two models up to slug impact is different only because the UIS columns in SM 4 did not absorb plastic strain energy. The stiffer complex models absorbed an average of 5.5% of the work potential as strain energy compared with 20.6% for SM 3, the simple model with a UIS.

After slug impact, the upper vessel on SM 4 and SM 5 absorbs about 23% of the slug kinetic energy. This percentage of absorbed strain energy after impact compares with 36% absorbed by the upper vessel on SM 3, the simple model with a UIS structure. Again, the difference is attributed to the stiffer upper vessel of the complex models.

V INTERPRETATION OF EXPERIMENTS AND COMPARISON WITH GE REXCO CALCULATIONS

A. Background

As part of the program to demonstrate the structural integrity of the primary containment vessel and head closure of the CRBR under HCDA loading and to assist the pretest selection of instrumentation locations, General Electric Company* (GE) computed the loading pressures and strain response of the models SM 2, SM 3, and SM 4 using the HEP version of the two-dimensional, axisymmetric, Lagrangian computer code REXCO [3]. Both pre- and posttest REXCO analyses were carried out to provide information for a comprehensive evaluation of the CRBR response.

The REXCO calculations discussed in this section were from the posttest analysis on SM 2 and SM 5. Only pretest calculations were performed for SM 3. A complete evaluation of both the pre- and posttest analysis is given in Reference 7.

The input for the GE REXCO calculations is the pressure-volume change relationship for the energy source, and the dimensions and material properties of the models.

B. Objectives

The objective of the following discussion is to show the comparison between experimental records and the GE REXCO computer predictions and to discuss briefly the implications of the comparisons from an experimentalist's point of view.

---

*Sunnyvale, California

Table 6

COMPARISON OF PEAK PRESSURES AND STRAINS
GE REXCO* VS EXPERIMENTS

Gage No. SM2	Gage No. SM3	Gage No. SM5	Location	SM 2 REXCO	SM 2 Experiment	SM 3 REXCO	SM 3 Experiment	SM 5 REXCO	SM 5 Experiment
P 1	P 1	P 1	Core	4000 psi	3300 psi	4400 psi	4600 psi	4000 psi	4000 psi
P 2	P 2	P 2	Core	4000 psi	3750 psi	4400 psi	4100 psi	4000 psi	4000 psi
P 3	P 3		Upper Core	2500 psi	2900 psi	2800 psi	2600 psi		
		P 5	Lower vessel					540 psi	480 psi
P 4	P 4	P 6	Vessel wall at core	525 psi	540 psi	410 psi	480 psi	575 psi	530 psi
P 5	P 5	P 7	Vessel wall at UIS	460 psi	570 psi	350 psi	400 psi	655 psi	590 psi
P 6	P 6	P 8	Vessel wall	750 psi†	530 psi	750 psi†	520 psi	700 psi†	595 psi
P 7	P 7	P 9	Upper vessel wall	2900 psi	1650 psi	1750 psi	1000 psi	2800 psi	2850 psi
P 8	P 8	P 11	Head	5500 psi	5300 psi	7500 psi	3500 psi	4900 psi	5350 psi
SG1	SG1		Vessel wall at core	1.40%	1.62%	1.90%	0.87%		
SG2	SG2	SG5	Vessel wall at UIS	0.80%	2.65%	1.25%	1.45%	0.15%	0.32%
SG4	SG4		Vessel wall	4.15%	2.30%	6.70%	1.60%		
SG5	SG5	SG7	Upper vessel wall	1.70%	2.90%	4.10%	2.15%	1.65%	1.87%

*
General Electric calculations using high strain rate properties for SM 2 and SM 5, low strain rate properties for SM 3.

†Average

C. Summary

Comparison and analysis of experimental results and computer predictions lead to the following conclusions:

(1) The GE REXCO predictions of the maximum vessel wall and core barrel strain and the maximum head loads were greater than those measured in the experiments. Thus, the GE REXCO predictions are conservative.

(2) Both experimental results and the GE REXCO results are self-consistent. That is, measured and predicted strains agree with measured and predicted loads, respectively, even though measurements and predictions do not agree. This conclusion is based on simple calculations of the peak vessel and core barrel deformations, assuming a quasi-static response and using measured and computed loading pressures and appropriate stress-strain curves (either low strain rates or high strain rates depending on the analysis) for the models.

(3) Better agreement between experiment and the GE REXCO calculations is afforded by using high strain rate properties for the Ni 200 vessel and core barrel. The high strain rate properties ($\dot{\varepsilon}$ = 100 sec^{-1}) are more in line with the peak strain rates measured in the structure (about 50 sec^{-1}).

(4) Most of the differences between the experiment and the GE REXCO calculations stem from differences in the measured and predicted response of the core structure. The GE REXCO modeling of the core structure results in a more rapid expansion of the core barrel under the initial core loading than occurs in the experiment. This rapid expansion reduces the calculated core pressure more rapidly than in the experiment. Consequently, the calculations predict lower loading pressures on the vessel wall and reduced slug kinetic energy.

(5) In REXCO the Upper Internals Structure (UIS) is modeled as a very dense fluid that moves with the slug and gives the slug more mass. This modeling technique leads to additional differences between experimental results and REXCO calculations. For example, the experiments show that the presence of the UIS significantly reduces slug impact velocity, whereas REXCO shows no significant reduction. Table 6 summarizes the comparison between the GE REXCO calculations and the experiments.

D. Results

1. Comparisons of SM 2 Response

Figure 25 shows the zone layout for the GE REXCO model of SM 2 [10]. Two posttest calculations were carried out for this model. Response was calculated, first, using low stratin rate properties, ($\dot{\varepsilon} = 8 \times 10^{-3}$ Sec^{-1}) and second, using high strain rate properties ($\dot{\varepsilon} = 100$ sec^{-1}). Figures 26 and 27 compare experimental and GE REXCO results for SM 2, and Figure 28 compares the final deformed shape with the calculated deformed shape. It can be seen that use of high strain rate properties bring experimental and GE REXCO results closer together. However, the rapid expansion of the core barrel of the GE REXCO model causes the core pressure to drop more rapidly than in the experiment. The excessive core expansion extracts energy from the source in the form of strain energy in the Ni 200 core barrel and reduces source pressure. The lower source pressure reduces the loads on the lower vessel wall above the core barrel and reduces the slug velocity. Consequently, no bulge in the vessel wall above the core barrel is predicted by the code, in contrast to the experiment. Also, the upper vessel is not deformed as greatly by the slug impact loads calculated by GE compared to the experiment, mainly because the REXCO slug impact velocities are lower (about 61 ft/sec compared with 91.5 ft/sec in the SM 2 experiment).

2. Comparison of SM 3 Response

Figure 29 shows the GE REXCO zone layout for SM 3, which is very similar to that for SM 2 except that a UIS is included in SM 3. Low strain rate properties for the Ni 200 vessel and core barrel were used. Figures 30 and 31 compare the experimental results with the calculations. The differences between calculated and measured pressure and strain records for SM 3 are similar to those differences for SM 2. However, the calculated slug impact pressure for SM 3 is significantly higher than that for SM 2, whereas the calculated slug velocity for SM 3 is 12% lower. The UIS, modeled in the REXCO calculations by dense fluid elements moves with the slug. The higher density of the slug results in a higher slug impact pressure than would be expected if the slug had the density of

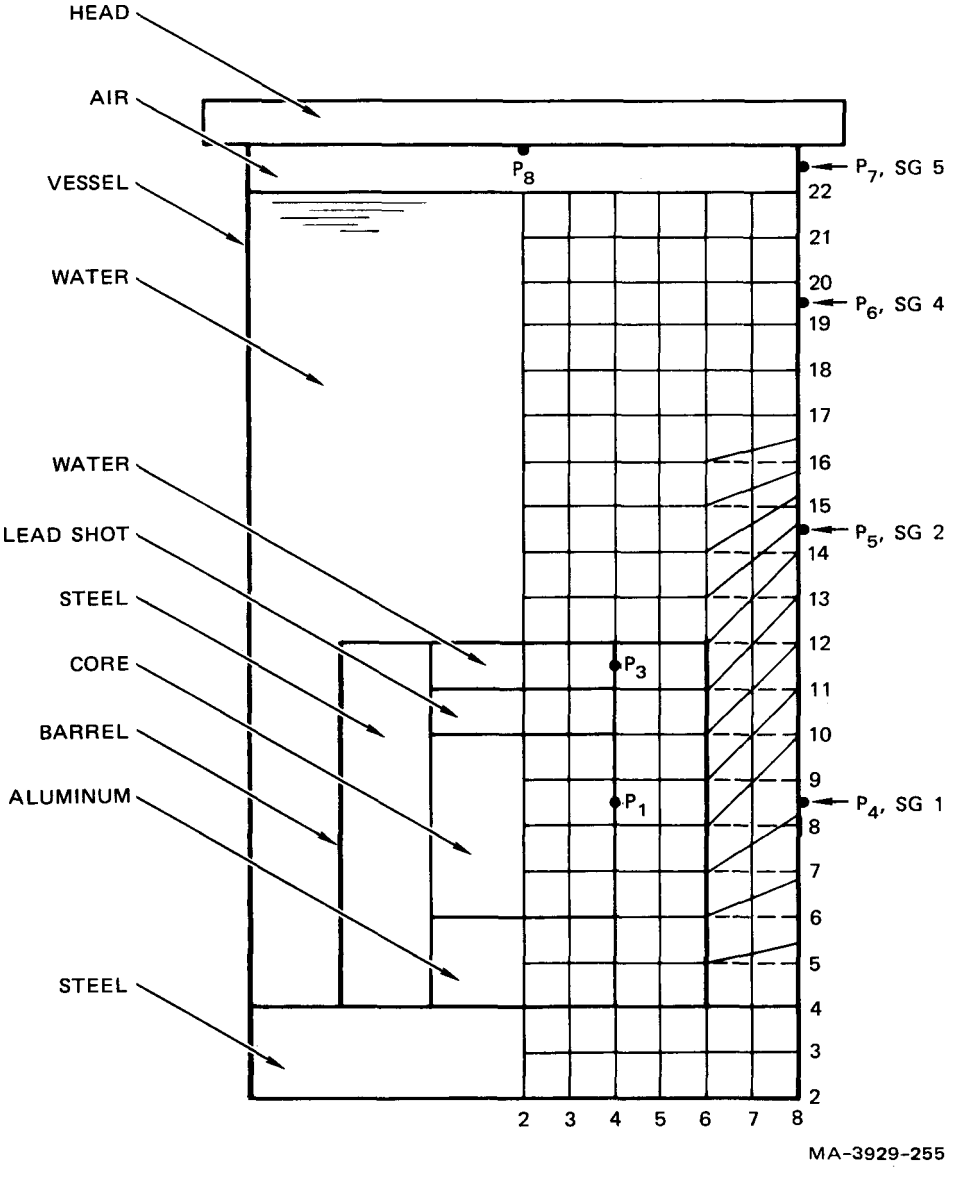

FIGURE 25 ZONE LAYOUT FOR SM 2 GE REXCO MODEL

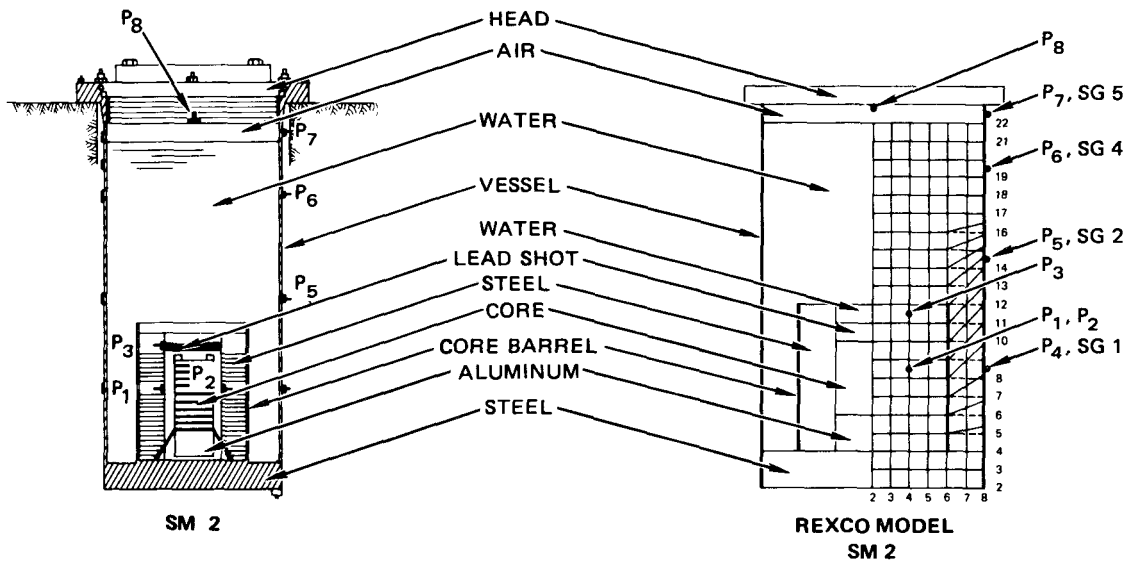

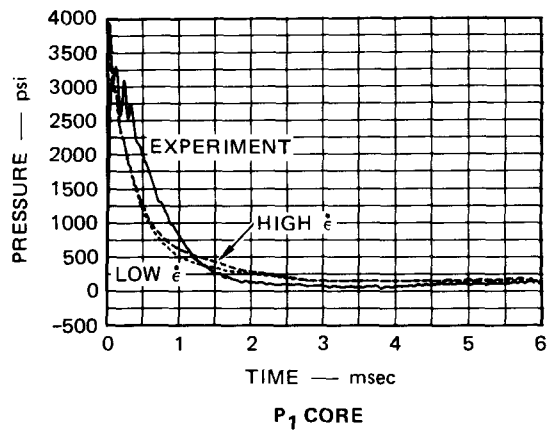

P_1 CORE

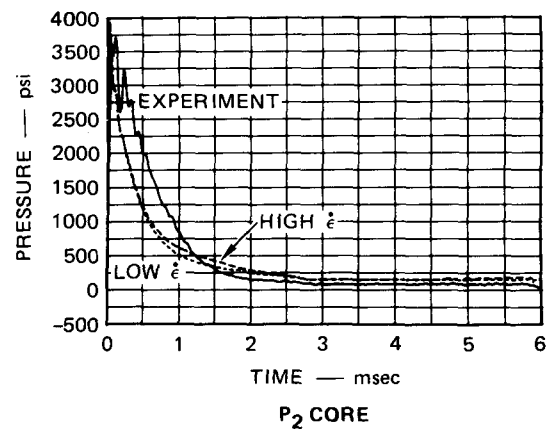

P_2 CORE

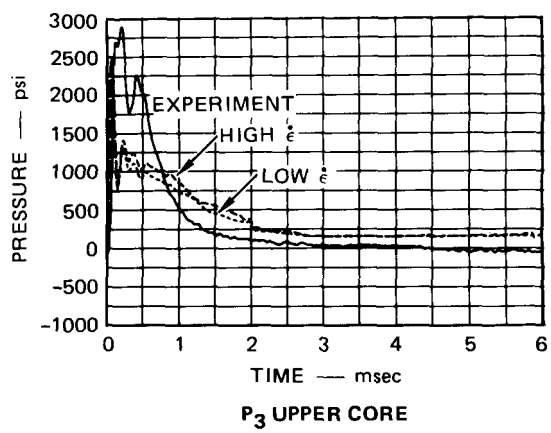

P_3 UPPER CORE

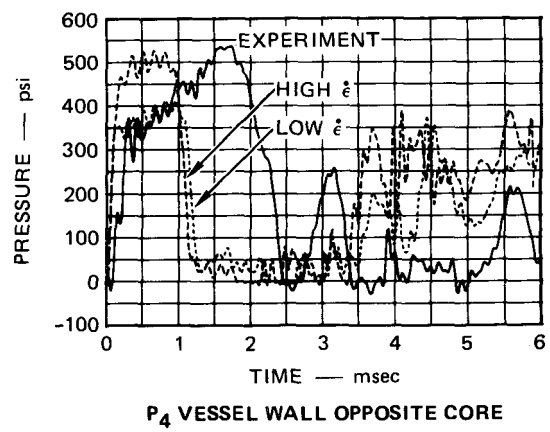

P_4 VESSEL WALL OPPOSITE CORE

MA-3929-256

FIGURE 26 COMPARISON OF SM 2 PRESSURE RECORDS WITH GE REXCO RESULTS

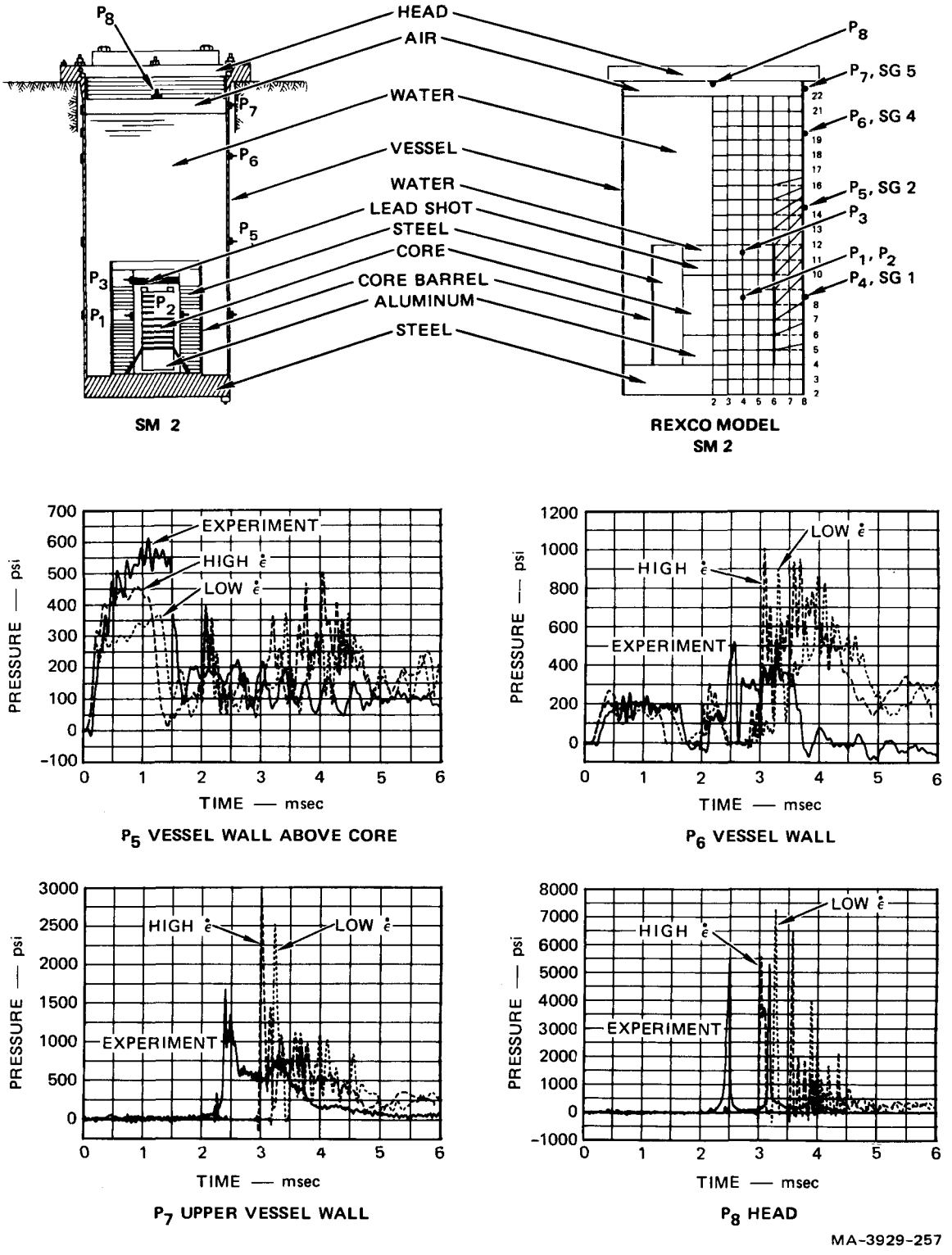

FIGURE 26 COMPARISON OF SM 2 PRESSURE RECORDS WITH GE REXCO RESULTS (Concluded)

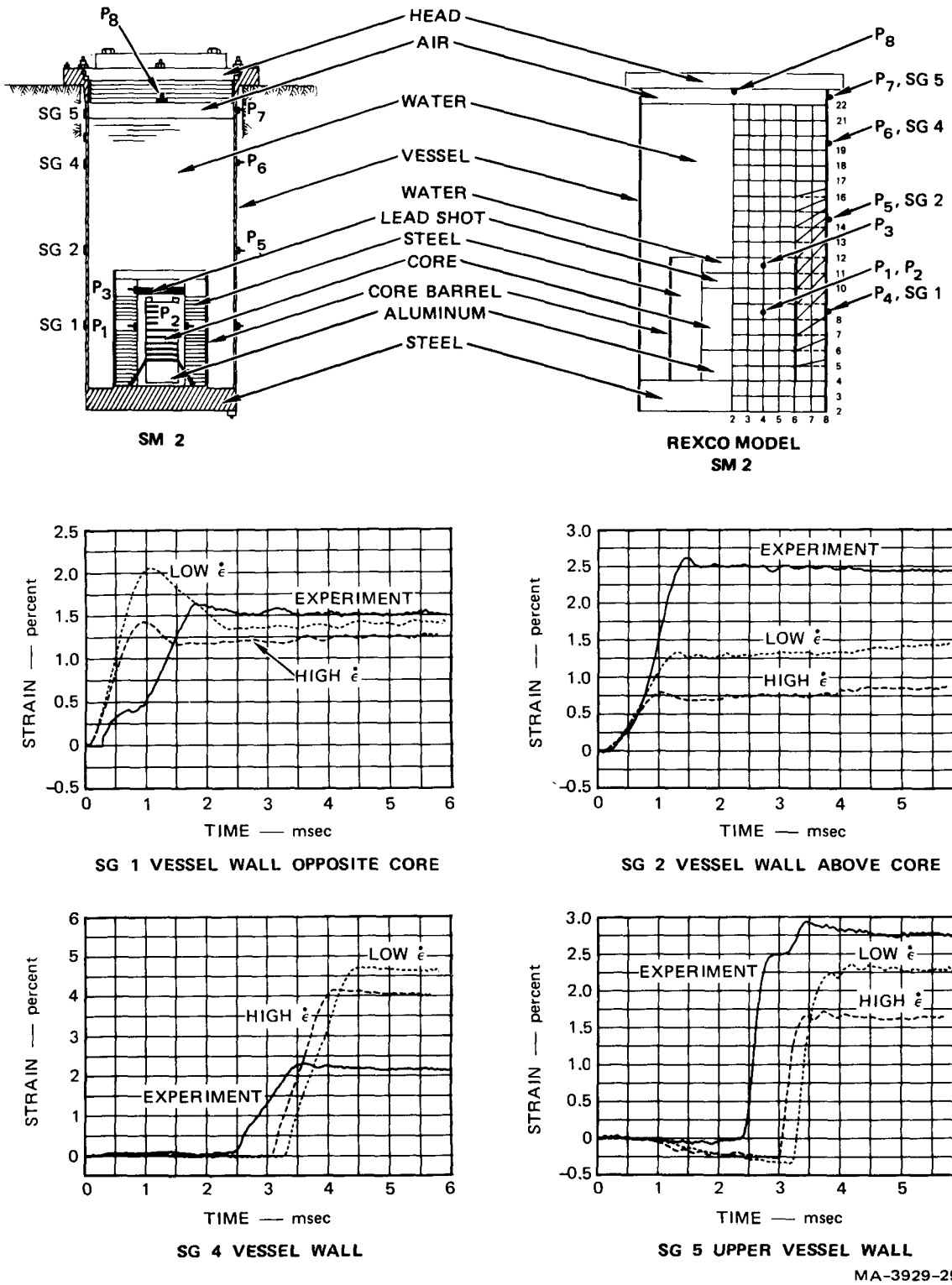

FIGURE 27 COMPARISON OF SM 2 STRAIN RECORDS WITH GE REXCO RESULTS

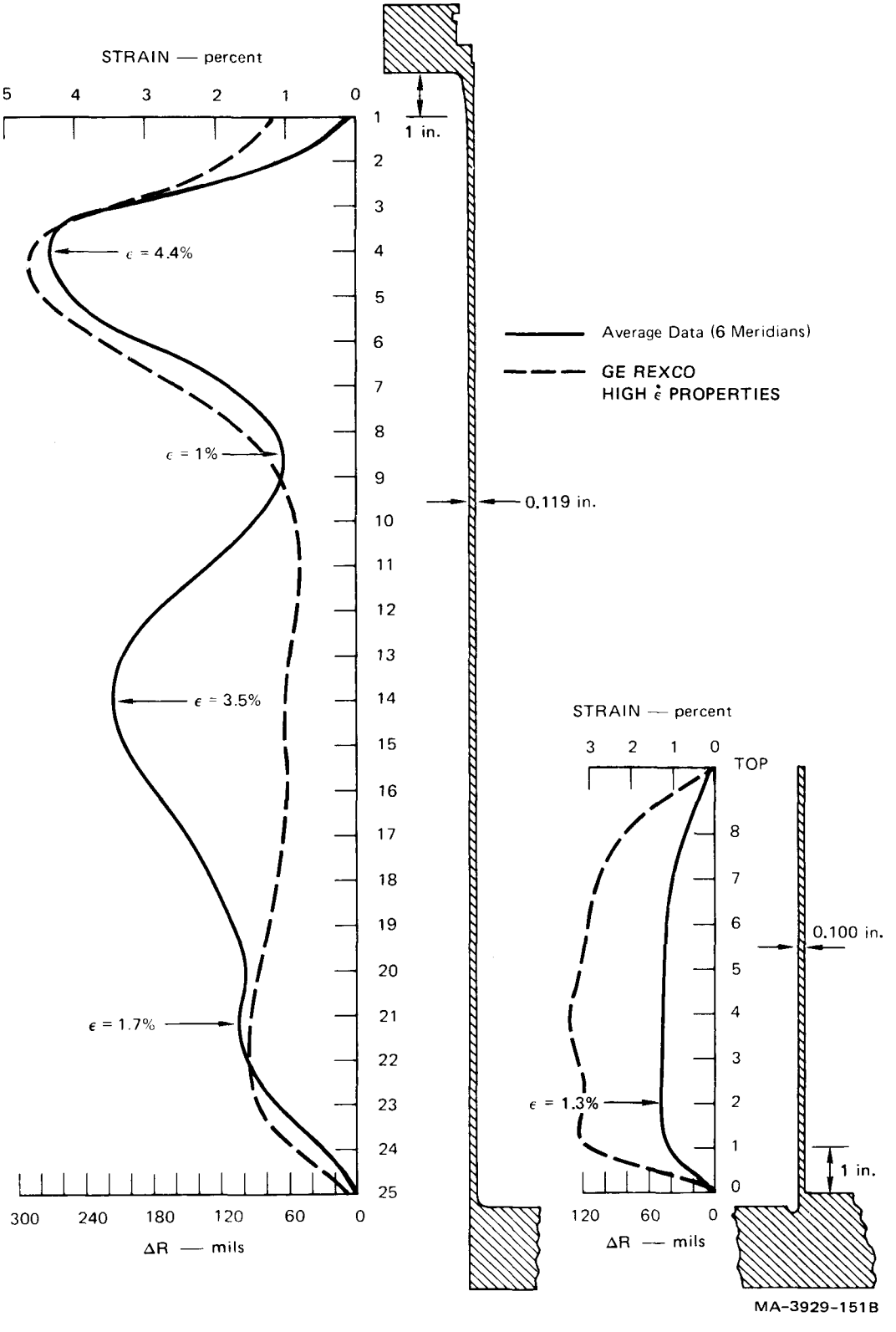

FIGURE 28 COMPARISON OF FINAL DEFORMED SHAPES: SM 2 EXPERIMENT VERSUS GE REXCO

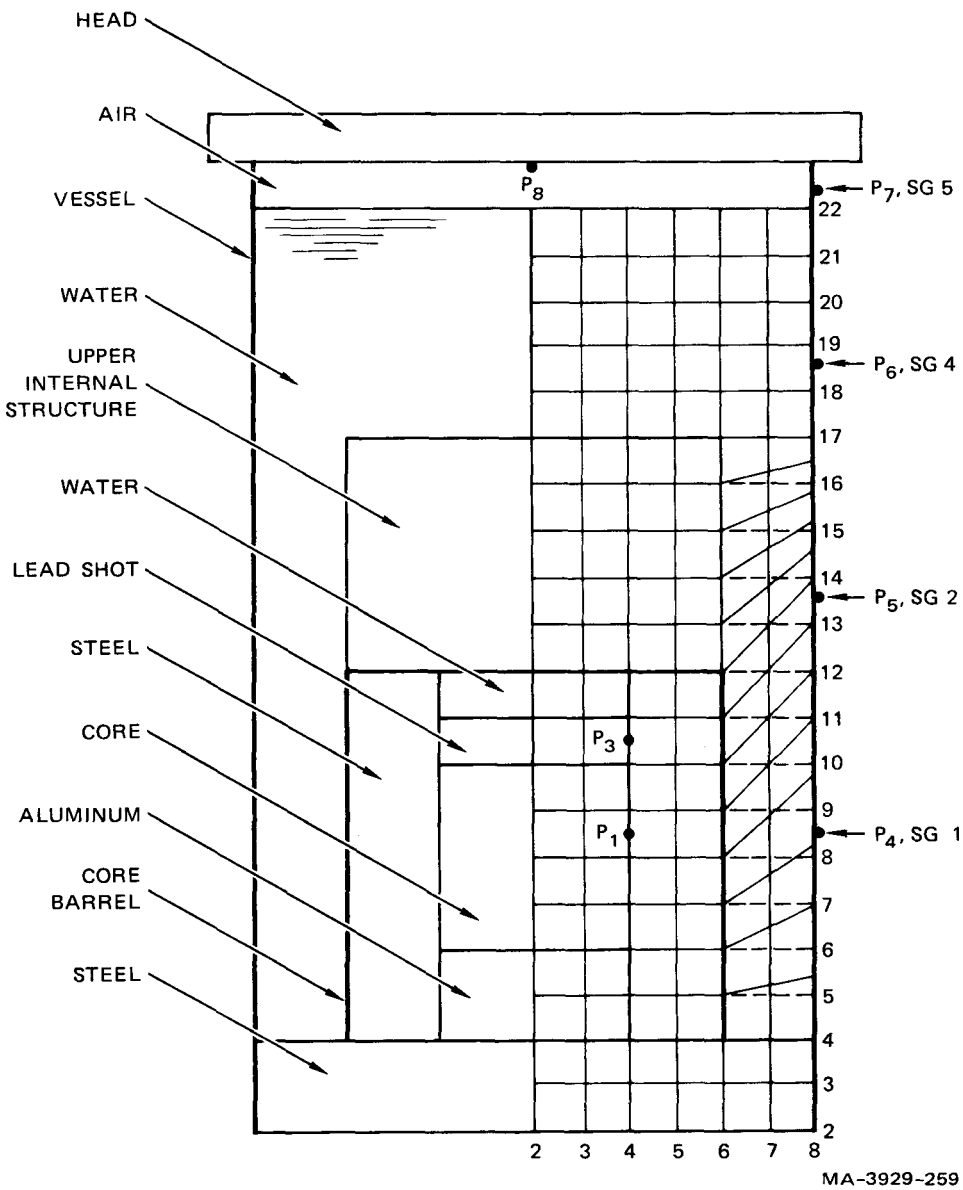

FIGURE 29 ZONE LAYOUT FOR SM 3 GE REXCO MODEL

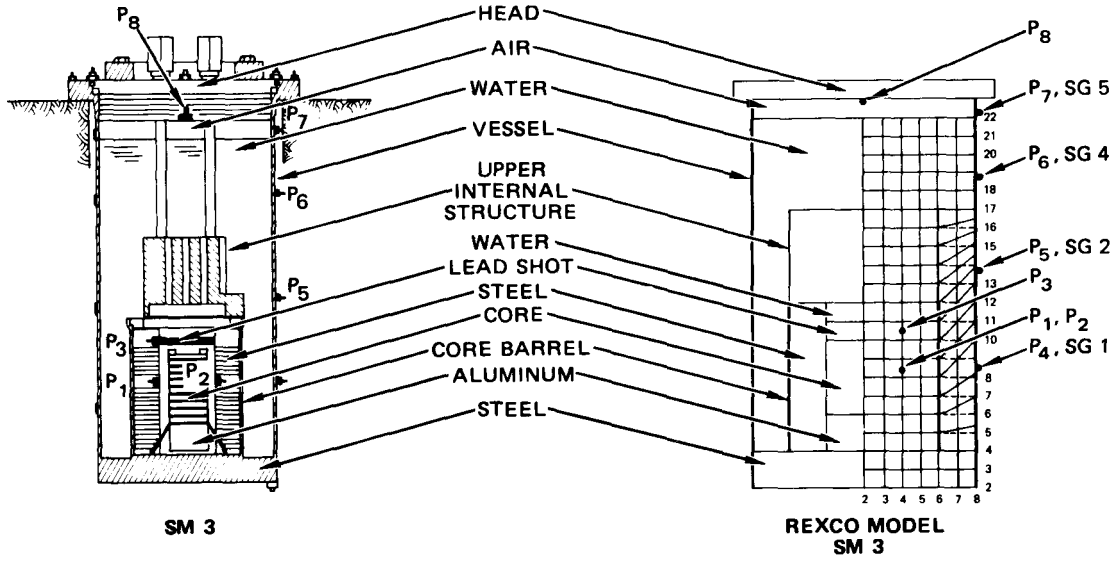

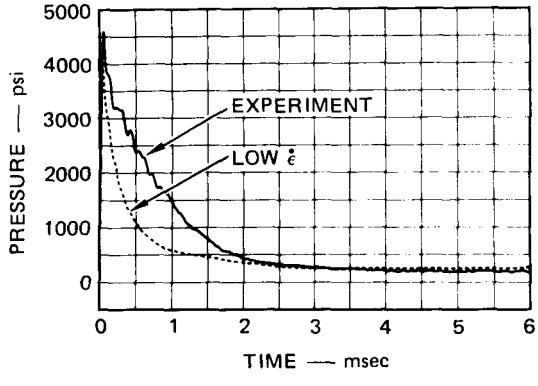

P_1 CORE

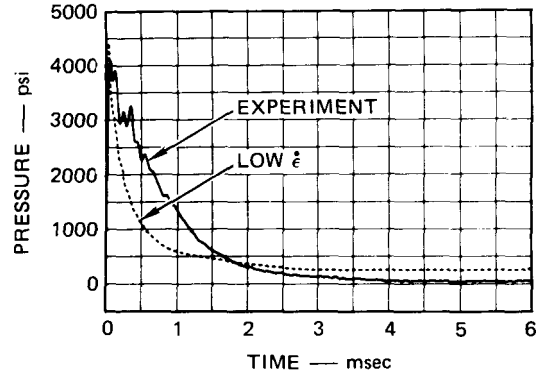

P_2 CORE

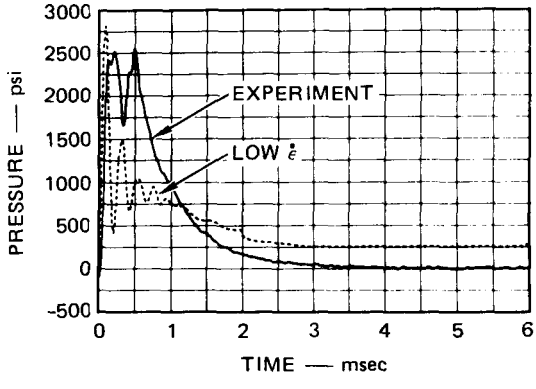

P_3 UPPER CORE

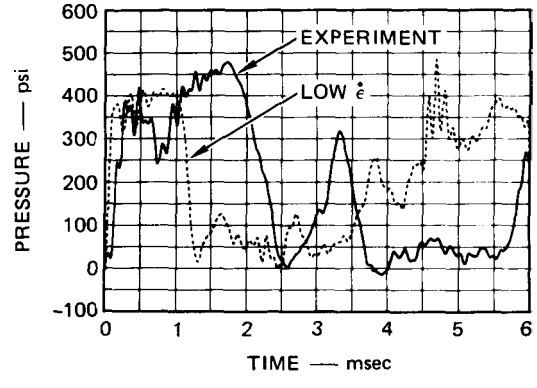

P_4 VESSEL WALL OPPOSITE CORE

MA-3929-260

FIGURE 30 COMPARISON OF SM 3 PRESSURE RECORDS WITH GE REXCO RESULTS

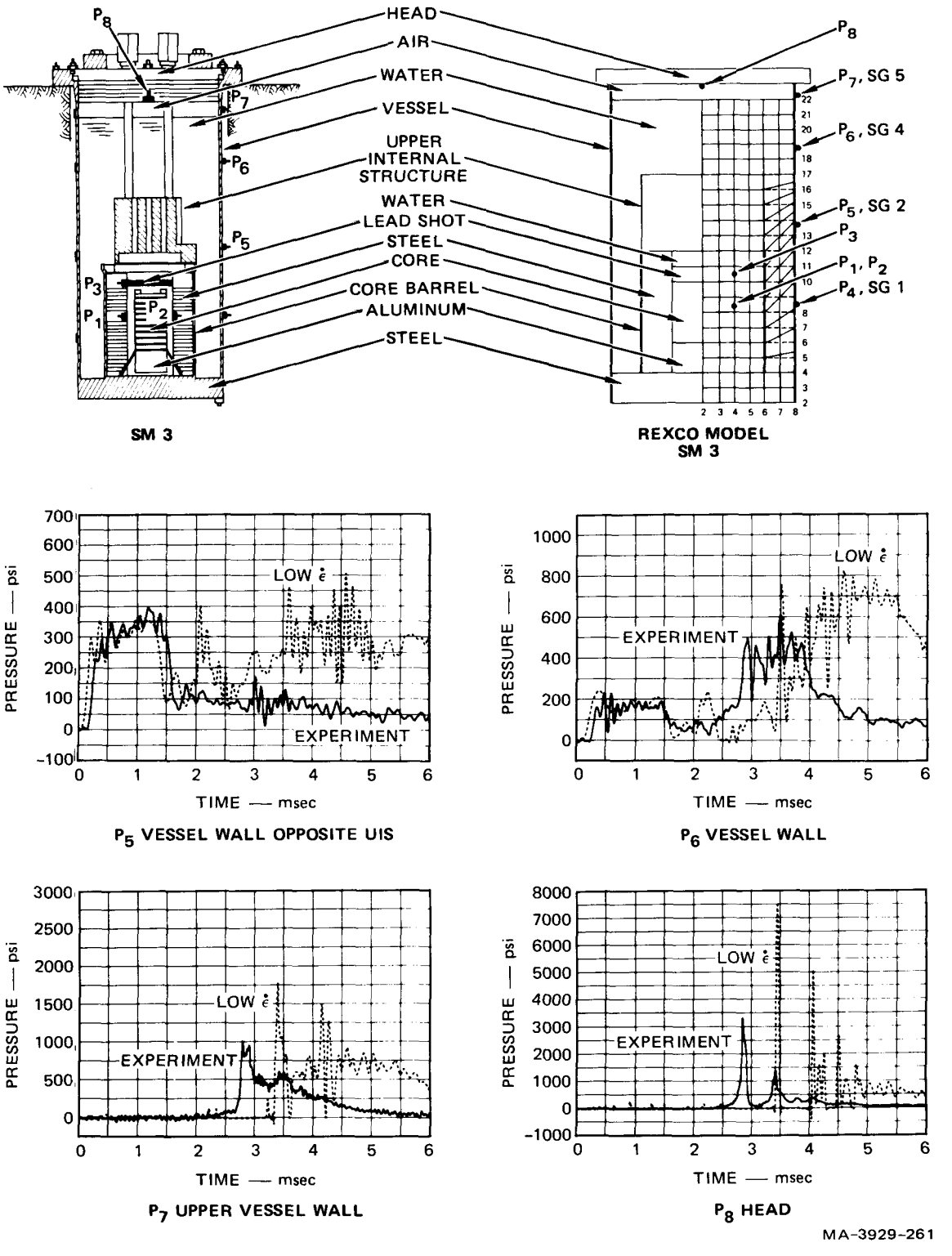

FIGURE 30 COMPARISON OF SM 3 PRESSURE RECORDS WITH GE REXCO RESULTS (Concluded)

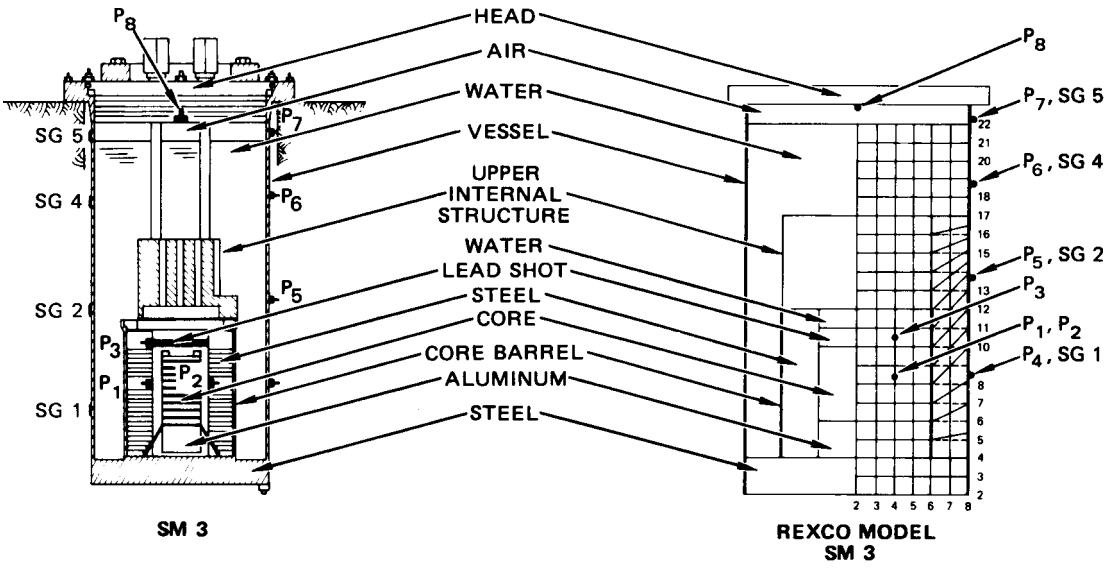

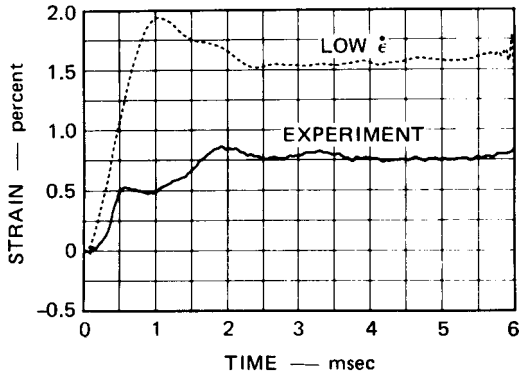

SG 1 VESSEL WALL OPPOSITE CORE

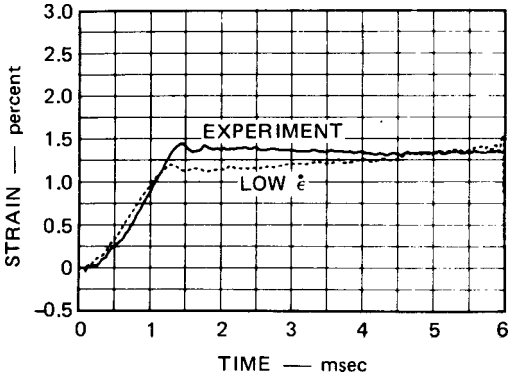

SG 2 VESSEL WALL OPPOSITE UIS

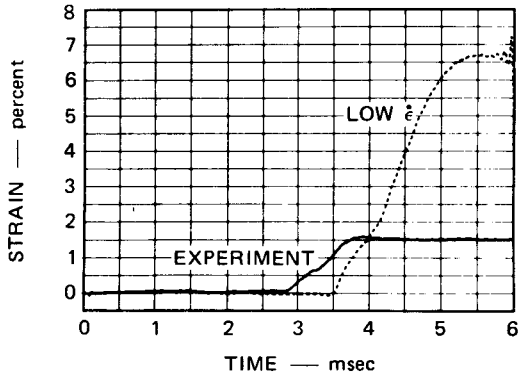

SG 4 VESSEL WALL

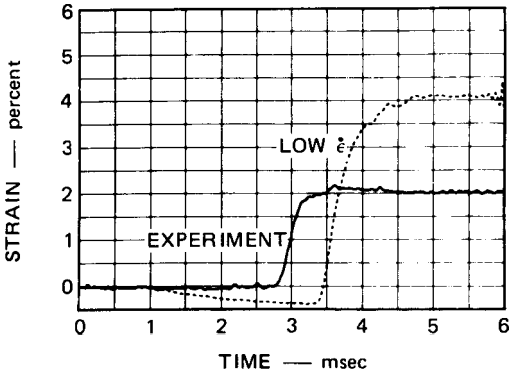

SG 5 UPPER VESSEL WALL

MA-3929-262

FIGURE 31 COMPARISON OF SM 3 STRAIN RECORDS WITH GE REXCO RESULTS

water. The experiments show that the presence of the UIS reduces slug velocity and impact pressure by about 32%. Since the GE REXCO calculations do not show these reductions the UIS is not modeled correctly in REXCO.

3. Comparison of SM 4 and SM 5 Response

Figure 32 shows the zone layout for the GE REXCO model for SM 4 and SM 5 [11]. Two GE REXCO calculations were carried out for this model, one with high and the other with low strain rate properties for the Ni 200 core barrel, thermal liner, and vessel wall. Figures 33 and 34 compare the experimental results with the two GE REXCO calculations for SM 5. In general, the calculations made with the high strain rate properties agree better with the experiments.

Figure 35 compares the final deformed shape of the vessel wall and the calculated deformed shape. There are significant differences between the GE REXCO results and the experiment, particularly, in the lower vessel opposite the core barrel and below the core support ring. The larger calculated radial displacements here are the result of larger pressures in these areas. The larger pressure between the core barrel and vessel wall is caused by the more rapid expansion of the core barrel. The larger pressure in the lower vessel is caused by an overestimation of the downward deformation of the core support structure, which compresses the fluid below the platform. A large downward displacement on the core support platform would result in large inward forces on the core support ring where it attaches to the vessel wall. The final calculated deformed shape shows this effect. Evidently, the core support structure in the calculations was not as stiff as the one in the model. This would account for the large difference between the experimental and the calculated response in the lower vessel.

The larger upper vessel deformation calculated for the GE REXCO model reflects inadequate modeling of the UIS, as discussed in the SM 3 comparisons.

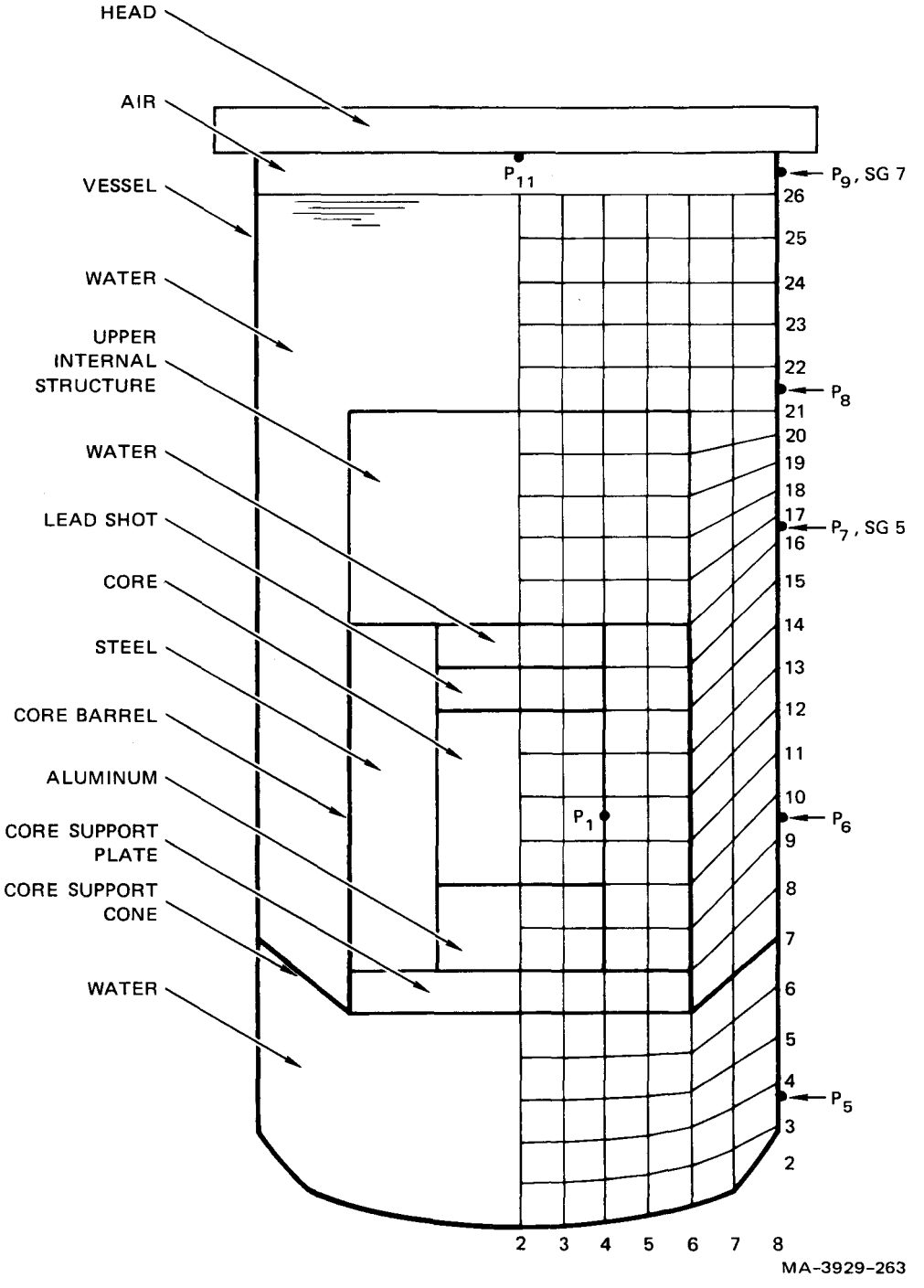

FIGURE 32 ZONE LAYOUT FOR SM 4 AND SM 5 GE REXCO MODEL

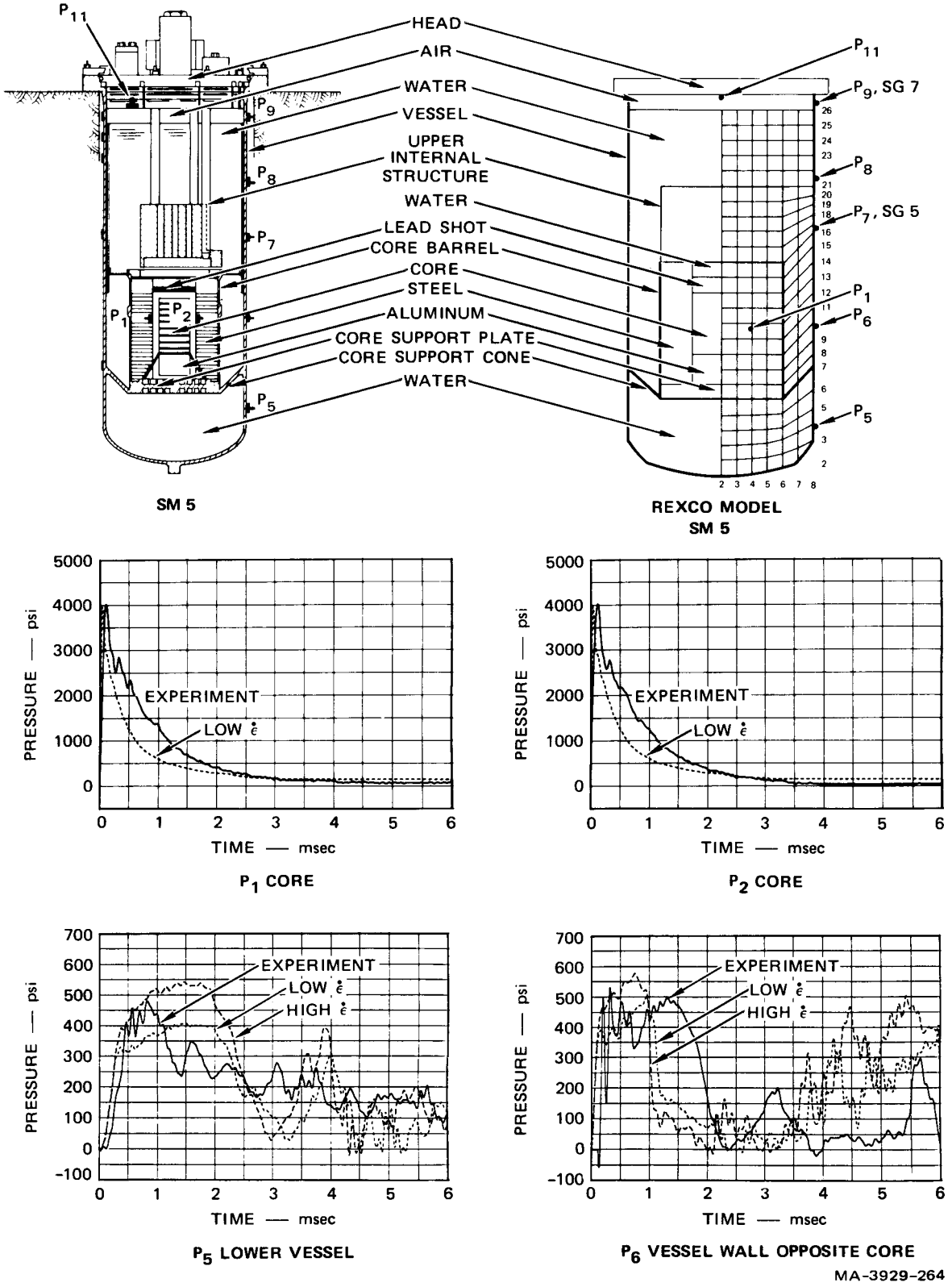

FIGURE 33 COMPARISON OF SM 5 PRESSURE RECORDS WITH GE REXCO RESULTS

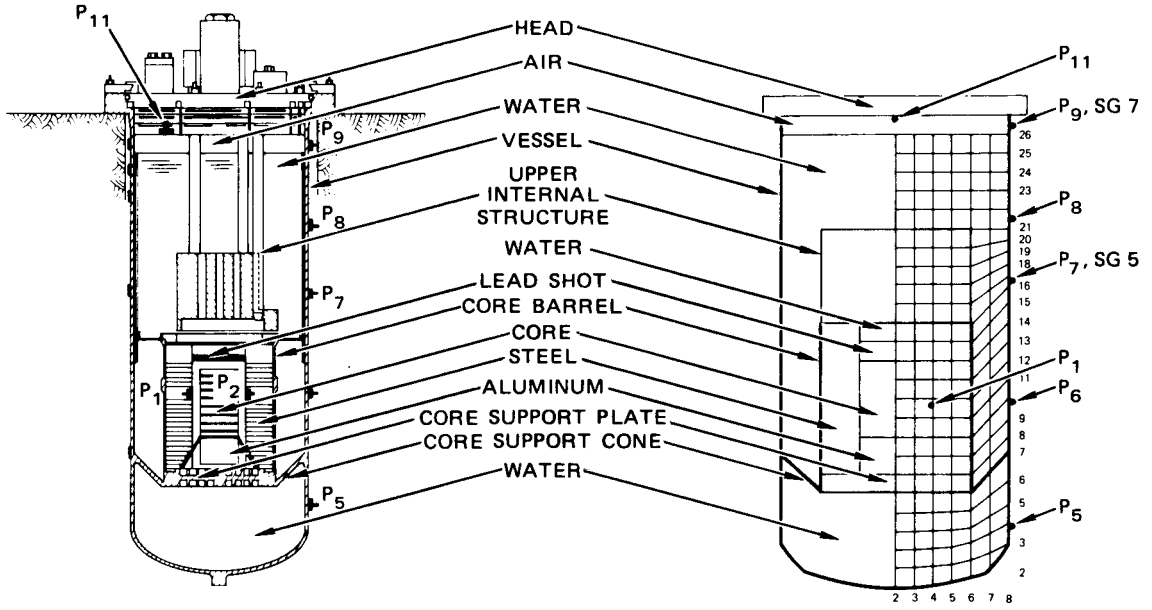

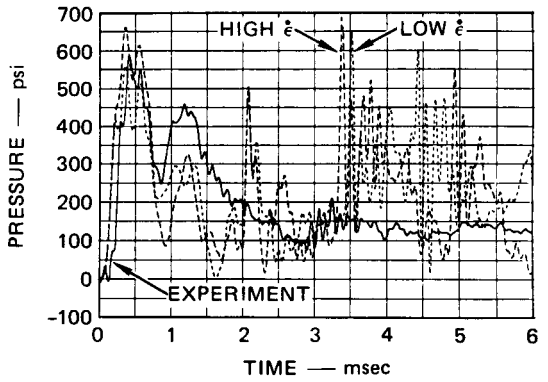

P_7 VESSEL WALL OPPOSITE UIS

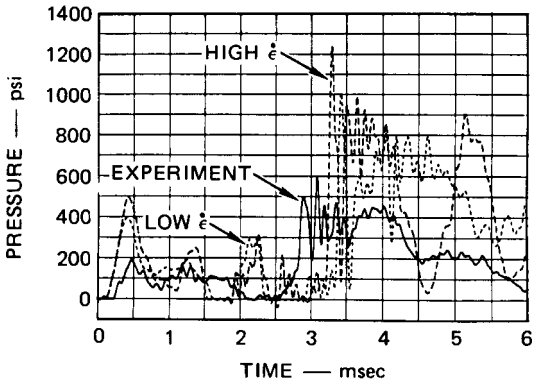

P_8 VESSEL WALL

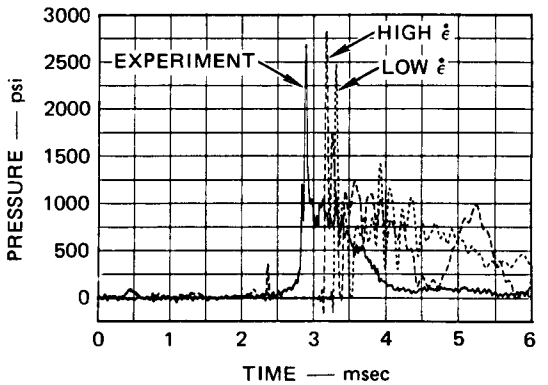

P_9 UPPER VESSEL WALL

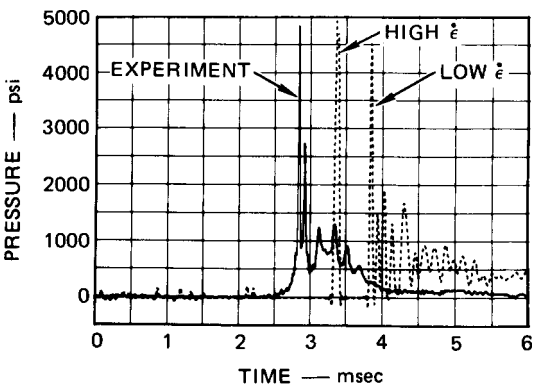

P_{11} HEAD

MA-3929-265

FIGURE 33 COMPARISON OF SM 5 PRESSURE RECORDS WITH GE REXCO RESULTS (Concluded)

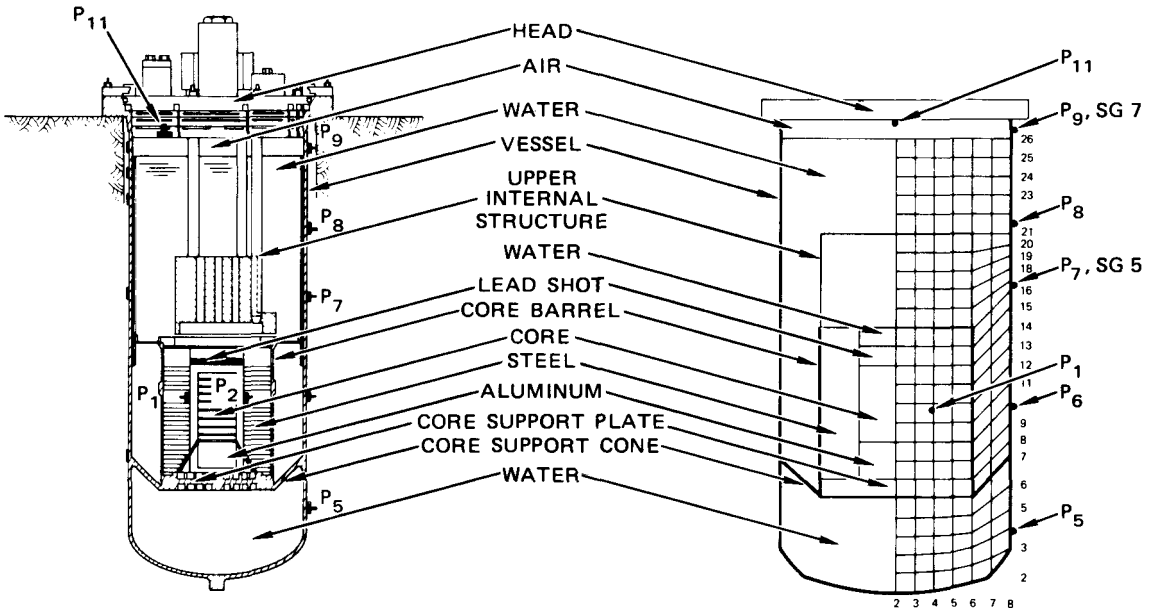

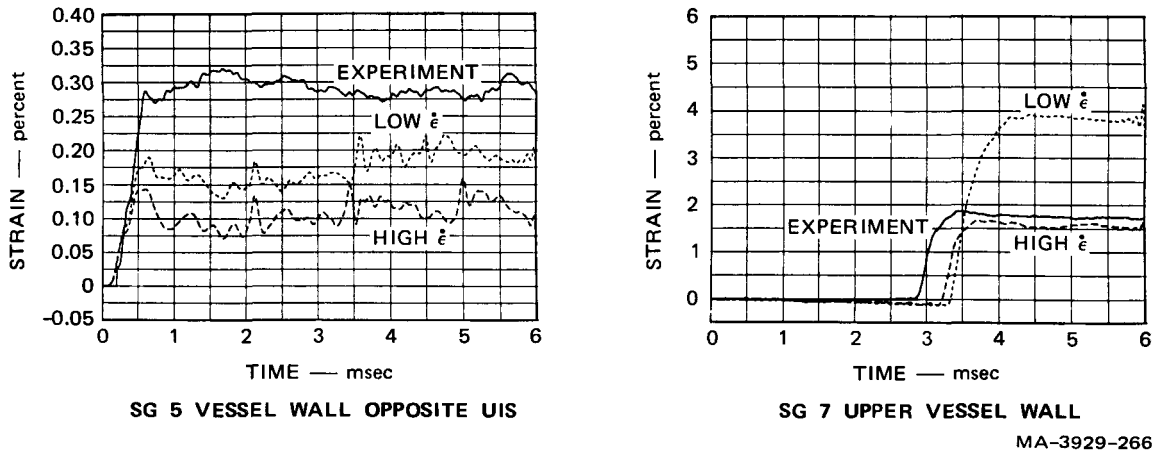

FIGURE 34 COMPARISON OF SM 5 STRAIN RECORDS WITH GE REXCO RESULTS

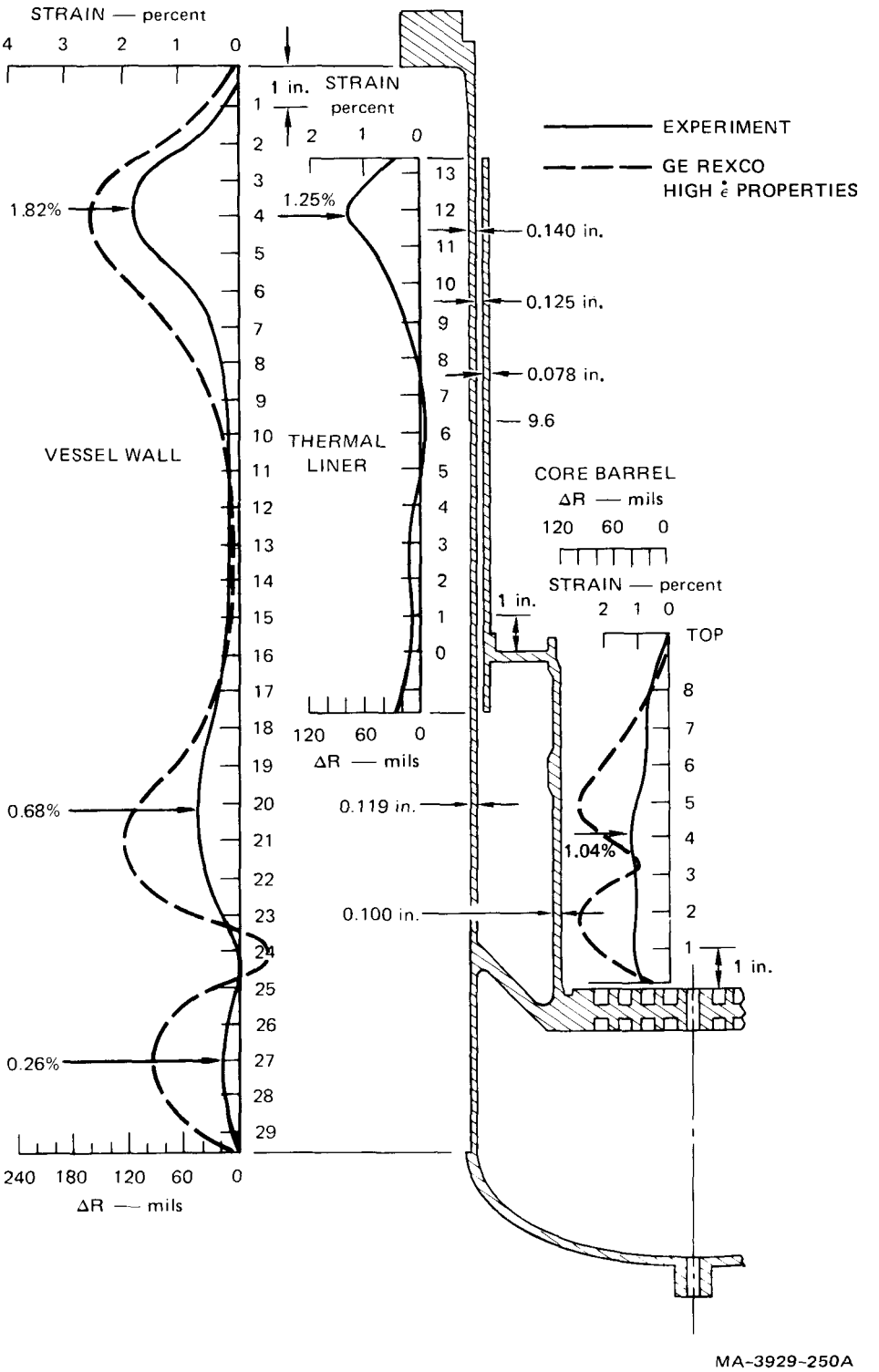

FIGURE 35 COMPARISON OF FINAL DEFORMED SHAPES, SM 5 EXPERIMENT VERSUS GE REXCO

Blank Page

VI SUMMARY AND DISCUSSION

This section summarizes the overall results of the experimental program. The primary conclusions of the program are reviewed and the comparisons of the model response for all dynamic experiments are discussed.

A. Observations

1. Head Response - A Qualitative Evaluation

The main objective of this program was to assess the response of the head assembly of the 1/20-scale CRBR models to slug impact loading. None of the heads on the four models tested dynamically exhibited any mode of failure. In fact, except for some slight plastic deformation of the lead mass bolted to the head of SM 2, no plastic deformation occurred in any of the components that make up the head. This includes the three plugs, the shear rings, shear ring bearing surfaces, shear ring grooves, vessel flange, shielding, and simulated components bolted to the head. Some small amount of damage was done to parts of the shear ring grooves and some of the shear ring segments in an effort to remove the tighter shear rings from the shear ring grooves. (Shear rings were press-fitted into the shear ring grooves.) This damage consisted of scratches or indentations from the use of thin blades and punches and obviously was not related to dynamic response.

To evaluate the displacement of the head during slug impact loading, a linear potentiometer displacement gage (linipot) was mounted next to accelerometer A_6 on the edge of the intermediate rotating plug of SM 5. It was positioned near the point of expected maximum head displacement based on static load-deflection tests of the three-plug head.* However, because of the composite construction of the head and shielding

*See Appendix A.

and because of the relatively narrow gaps between plugs (less than 0.1 inch), the individual plugs could not rotate as much as the three-plug head model without shielding tested in the static loading experiment (SM 1). As the individual plugs of SM 5 displace upwards, they rotate, closing the gap between the shielding layers and strongly resisting further doming of the head. Based on the initial gap size, the maximum upward diplacement that can occur before the gap is closed is calculated to be 0.062 inch at the point where the linipot was placed. The maximum displacement measured by the linipot is 0.060 inch and agrees well with the calculations. We conclude that the shielding on the LRP and IRP came into contact and prevented further doming of the head.

2. Head Response - A Quantitative Evaluation

Head response to a single slug impact load parameter such as peak pressure or impulse is difficult to evaluate because the CRBR head can respond in three distinct and separate modes during the slug impact loading. The three modes are: (1) upward motion of the head due to the thrust of the core pressure acting on the UIS and to compression of the cover gas, which lifts the IRP and closes the gap between shear rings and shear ring bearing surfaces; (2) doming of the three-piece head under slug impact loading until the gaps between the shields are closed, and (3) shear ring resistance to long duration loads. Each of these modes has a characteritic duration during which only a portion of the slug impact load is important. The characteristic time for Mode 1 is the time it takes to close the gap between the shear rings and the shear ring bearing surface. The characteristic time for Mode 2 is the time it takes to close the gap between the plug shielding due to head doming, and the characteristic time for Mode 3 is the response time of a system consisting of a rigid head resited by the stiffness of the shear rings.

Figure 36 shows a simple schematic of the CRBR head, shielding, and UIS. During the first response mode, the IRP is driven upward by the thrust from the core pressure acting on the UIS. The IRP is lifted as a free body until the gap between the LRP shear ring and IRP bearing surface is closed. Then the LRP is lifted until the shear ring gap between the LRP and the vessel flange is closed. The impact velocity of the IRP onto the shear ring surface of the LRP is low (around 4 ft/sec), ensuring an elastic collision. Because the combined mass of the LRP, the SRP, and the UIS is slightly greater than the mass of the LRP, the LRP is accelerated to nearly twice the impact velocity while the IRP, SRP, and UIS are nearly brought to rest. From this time until slug impact, the LRP bounces back and forth between the outer flange shear ring and the IRP bearing surface. An analysis of this reverberation shows that the plugs are not necessarily seated against their respective bearing surfaces when slug impact occurs.

During the second mode of head response, the head domes under slug impact loading. To provide a check on head displacement, an analysis was performed using an equivalent single-degree-of-freedom system [12]. This analysis is summarized in Appendix H. The three-piece head structure was approximated by a symmetrical three-piece plate with hinges representing the shear rings (see Figure H.1). The stiffness of the head included the stiffnesses of the three shield plates bolted to the underside of the head. For the dynamic single-degree-of-freedome analysis, the symmetric three-piece head was replaced by a one-piece simply supported plate that had the same load-deflection characteristics as the three-piece plate.

The slug impact load is approximated as a spike impulse having a peak pressure of about 4000 psi and lasting about 200 μsec (I = 0.026 bar-sec), followed by a triangular load with a sudden rise to about 1200 psi and then a linear decay to a very low pressure in 1.2 msec. The spike portion of the slug impact load gives the head an initial velocity of about 10 ft/sec. The triangular portion of the load causes the center of the

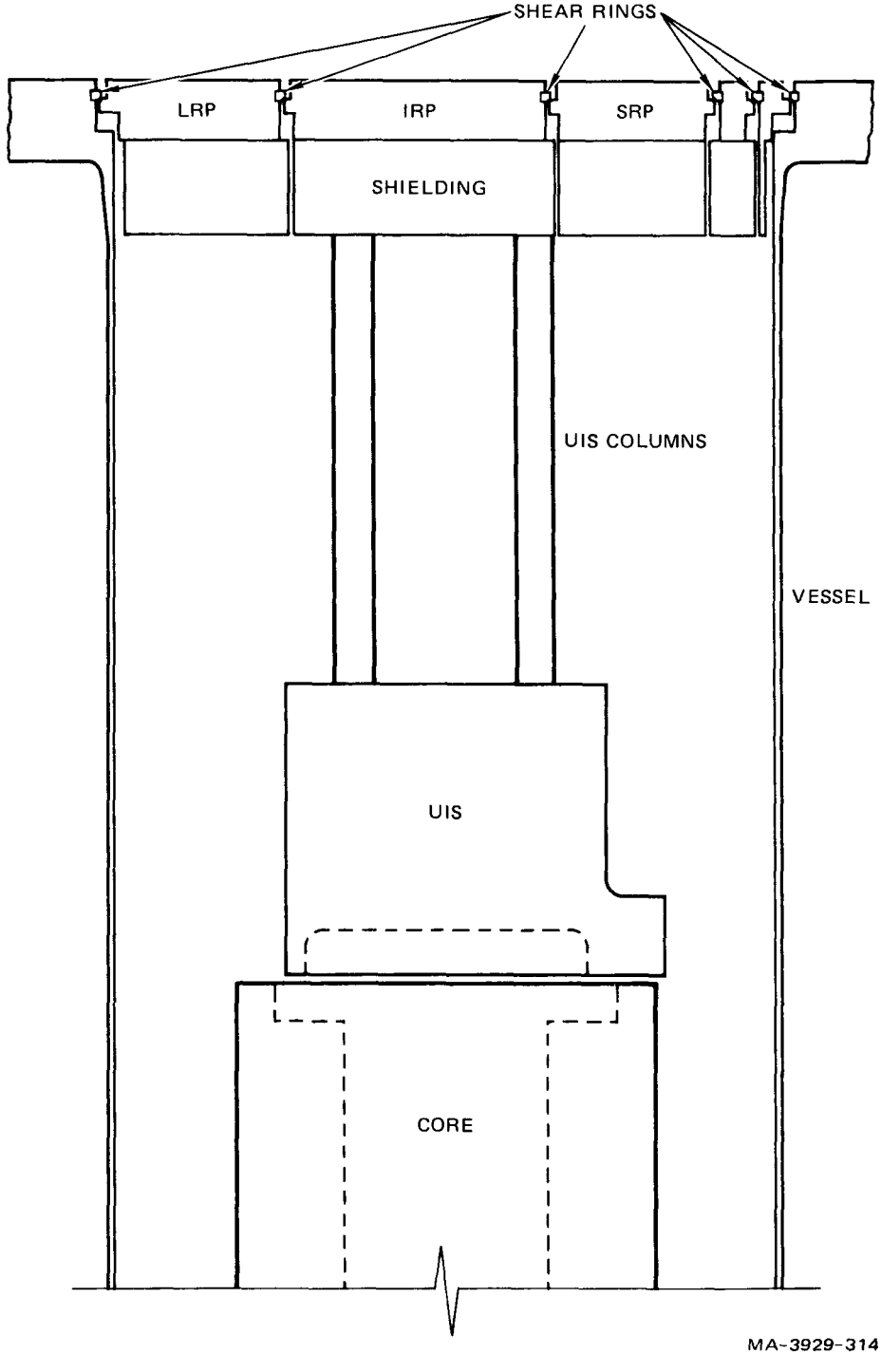

FIGURE 36 SCHEMATIC OF CRBR STRUCTURE

head to deflect about 102 mils (an elastic deflection); the area where the linipot is located (near the shear ring between the IRP and LRP about 3.0 inches out from the center of the head) is deflected about 50 mils. This peak displacement occurs about 680 μsec after slug impact. Both the amplitude and time of this displacement agree well with the measurements (55 mils about 700 μsec after slug impact).

This analysis verifies our assumption that the head domes upward until the gap between shield plates is just closed. The maximum force per unit length transmitted through the large diameter shear ring during this response was 6285 lb/in, much less than the yield load of the rings (11,900 lb/in).

During the third mode of head response, the shear rings carry the load from the residual pressure inside the reactor (<100 psi). This load (<300 lb/in) is much lower than the yield load of the rings. This analysis reinforces the conclusion that the entire head response from shear ring impact to head doming to long duration loading of the shear rings was elastic as observed in the experiments.

3. Vessel Response

All four of the dynamically tested models exhibited the same two phases of response: the first, before slug impact and the second, after slug impact. The first phase, resulting from bubble expansion, was confined to the lower vessel wall and compression and buckling of the UIS columns. Vessel wall deformation was limited to a region extending from the lower vessel structure (SM 4 and SM 5) to a point just above the UIS. Based on strain gage records, this phase is complete before slug impact occurs; no further radial expansion or UIS column buckling occurs in this region from the reflected pressure wave produced by slug impact. The second phase of response, limited to the upper region of the vessel, includes the radial expansion of the vessel wall from the vessel flange down to

just above the UIS. Deformations are produced by the reflected slug impact pressure wave that travels back down into the model. Since this wave is attenuated rapidly by radial expansion of the upper vessel wall and by interaction with the bubble, it has little or no effect on the response of the lower vessel. Dividing the vessel response into two distinctly separate phases simplifies evaluation of overall response and gives a clearer picture of the energy absorbing mechanisms that take place in the models.

Because of the thermal liner inside the more complex models SM 4 and SM 5, these models were significantly stiffer (about 79% more) than the single vessel wall design of the simple models SM 2 and SM 3. The increased stiffness from the thermal liner is the effect of added wall thickness alone. Posttest examination of the vessel and thermal liner showed that the two shells moved together, maintaining the small water-filled gap between the vessel wall and the thermal liner. The peak pressure* in this gap is about 450 psi and very near the yield pressure of the 0.140 inch-thick vessel wall (430 psi). The combined yield pressure of the vessel wall and the thermal liner is 670 psi. The 240-psi difference in yield pressures is very near the yield pressure of the 0.078-inch-thick thermal liner (about 250 psi). It may be assumed, then, that the pressure from slug impact acting on the inside of the thermal liner at the P_8 location is about 670 psi.

4. Core Barrel Response

The core structure of all models was designed to provide the proper radial areal density of the internal core structure, to provide the proper hoop stiffness of the core barrel, and to allow radial expansion of the internal core mass without hoop resistance. These requirements were met by using segmented steel rings that were stacked in the core to provide the proper areal density. The radial saw cuts in each ring prevent

*P_8 on SM 5, Figure D.25, Appendix D.

hoop forces. Stacking a series of thin segmented rings permits differential motion of the rings and allows axial bending modes of the core barrel. The core barrel alone carries the hoop forces generated by the core pressures.

REXCO predicts that there will be a large difference between peak and posttest core barrel strains (6.4% compared with 3.6%).* It is possible that the net inward pressure on the core barrel drives the core barrel inward, thus reducing the peak strain to a strain consistent with the posttest measurements. The GE REXCO calculations bear out this theory by showing a reduction in the core barrel strain.

5. UIS Response

The overall effect of the UIS is to reduce the slug velocity, thereby lowering the slug kinetic energy. This reduction amounts to about 32% in velocity and about 53% in kinetic energy. The reduction in axial kinetic energy is caused by a partial redirection of the gas flow from the core by the UIS and conversion of some gas work into radial and turbulent kinetic energy.

B. Summary Data

Table 7 lists the peaks of all the records gathered on the dynamic experiments. For completeness, the slug impact velocity (IV) is also listed. Because of high pressure spikes caused by local compression of the cover gas, the peak head pressures are difficult to compare. Far more useful for comparision are calculations of slug impact pressure using the slug impact velocities and evaluation of the impulsive load on the head.

*Based on calculations using the high-strain-rate properties of N_i 200 in SM 2.

Table 7

SUMMARY OF DATA FROM SM 2, SM 3, SM 4, AND SM 5

Gage No.					Peaks			
SM 2	SM 3	SM 4	SM 5	Location	SM 2	SM 3	SM 4	SM 5
P_1	P_1	P_1	P_1	Core	3300 psi	4600 psi	4200 psi	4000 psi
P_2	P_2	P_2	P_2	Core	3750 psi	4100 psi	3700 psi	4000 psi
P_3	P_3			Upper core	2900 psi	2600 psi		
			P_3	Lower UIS				1620 psi
			P_4	Upper UIS				690 psi
			P_5	Lower vessel				480 psi
P_4	P_4	P_3	P_6	Vessel wall at core	540 psi	480 psi	575 psi	530 psi
P_5	P_5	P_4	P_7	Vessel wall at UIS	570 psi	400 psi	610 psi	590 psi
P_6	P_6		P_8	Vessel wall	530 psi	520 psi		595 psi
P_7	P_7	P_5	P_9	Upper vessel wall	1650 psi	1000 psi	2700 psi	2850 psi
P_8	P_8	P_6	P_{10}	Head (center)[a]	5300 psi	3500 psi	4200 psi	7750 psi
			P_{11}	Head (LRP)[a]				5350 psi
			P_{12}	Head (SRP)[a]				8900 psi
			P_{13}	Head air gap (center)				33 psi
			P_{14}	Flange air gap				500 psi
			P_{15}	Flange ring gap (180^{o})				25 psi
			P_{16}	Flange ring gap (0^{o})				40 psi
			SG1	Core barrel (C)				1.75%[b]
			SG2	Core barrel (A)				---
		SG1	SG3	Core support ring (C)			-0.06%	0.04%
		SG2	SG4	Core support ring (A)			0.06%	0.05%
SG1	SG1			Vessel wall at core (C)	1.62%	0.87%		
SG2	SG2	SG3	SG5	Vessel wall at UIS (C)	2.65%	1.45%	0.08%	0.32%
SG3	SG3	SG4	SG6	Vessel wall at UIS (A)	0.32%	0.53%	0.07%	---
SG4	SG4			Vessel wall	2.30%	1.60%		
SG10		SG10	SG21	Vessel at peak ϵ (C)	4.53%	( )	1.38%	1.95%
SG5	SG5	SG5	SG7	Upper vessel wall (C)	2.90%	2.15%	1.53%	1.87%
SG6	SG6	SG6	SG8	Upper vessel wall (A)	1.03%	0.54%	0.38%	0.40%
			SG9	LRP (θ)				---
			SG10	LRP (R)				---
			SG11	UIS column (Ni200)				-2.0%
			SG12	UIS column (Ni200)				---
			SG13	UIS column (Ni200)				-2.1%
			SG14	UIS column 1 (cap)				-0.04% +0.14%
			SG15	UIS column 2 (cap)				-0.08% +0.11%
			SG16	UIS column 3 (cap)				-0.04% +0.04%
			SG17	UIS column 4 (cap)				-0.05% +0.05%

(Continued)

Table 7 (concluded)

Gage No.					Peaks			
SM 2	SM 3	SM 4	SM 5	Location	SM 2	SM 3	SM 4	SM 5
SG7	SG7	SG7	SG18	Stud 60°	0.16%	0.12%	0.13%	0.08%
SG8	SG8	SG8	SG19	Stud 180°	0.20%	0.08%	0.14%	0.08%
SG9	SG9	SG9	SG20	Stud 300°	0.16%	0.12%	0.13%	0.09%
			A_1	Flange ring (0°)				2100 g
A_1	A_1		A_2	IRP at 0°	1200 g	1200 g		3600 g
			A_3	SRP near IRP (0°)				2600 g
A_2	A_2	A_1	A_4	SRP near IRP (180°)	4800 g	4600 g	3400 g	4500 g
			A_5	IRP near center				3800 g
A_3	A_3	A_2	A_6	IRP near LRP (180°)	1850 g	1300 g	3300 g	3500 g
		A_3	A_7	LRP near IRP (0°)			3200 g	4800 g
			A_8	LRP near edge (180°)				3800 g
			A_9	Flange ring (180°)				3100 g
A_4	A_4		A_{10}	Platform	950 g	1230 g		
			LP1	Next to A_6				62 mils
IV	IV	IV	IV		91.5 ft/sec	62.5 ft/sec	62.4 ft/sec	62.2 ft/sec
				Impact time	2.5 ms	2.9 ms	2.9 ms	2.9 ms

[a] Peak value of spikes; recommend using impulse or slug impact velocity to calculate impact pressure.

[b] gage broke

C. Energy Partitioning

Table 8 summarizes the energy partitioning in the simple and complex models. The values shown in the table are not directly measured in the experiments, but are calculated using the calibrated gas work at slug impact, the total gas work*, and the material properties data, and are based on assumptions about the deformed shape of the model at slug impact. To properly estimate the gas work from the calibration data, allowance must be made for vessel expansion up to slug impact and for vessel expansion after slug impact. Calculation of slug kinetic energy assumes that the entire slug is moving at the impact velocity and that the slug includes all the water above the top of the core and the water and lead shot on top of the diaphragm in the core.

Strain energy is calculated from the deformed shape at the slug impact.† The deformed model is divided into a series of rings (0.5-inch long) where both hoop and axial deformation are considered separately. The strain energy per unit volume of each ring is calculated by integrating the high-strain-rate stress-strain curve to the hoop strain of the ring. This specific energy is multiplied by the volume of the ring, and the energies from each ring are summed to obtain the total strain energy of the model.

Up to the time of slug impact, the estimated energy in entrained and locally accelerated water is the difference between the gas work and the sum of slug kinetic energy and strain energies of the various deformed

*The effect of the UIS on the gas work curve is not known, but it is assumed that the UIS has little effect on the work potential of the explosive source.

†From strain records at key locations on the model.

components in the model. The calculated energy values listed in Table 8 are used to help evaluate qualitatively the similarities and differences in model response and to help determine the mechanisms that are important in deforming a reactor under HCDA loading conditions.

Table 8 shows that the simple model SM 2 without UIS had an excellent energy balance (only 3.5% of the energy was in entrained and locally accelerated water), well within the experimental accuracy of the test. Adding a UIS in SM 3 reduces the slug kinetic energy as well as the strain energy in the model up to slug impact. The net result is that a significant amount of energy (about 48%) is in the form of entrained and locally accelerated water.

Table 8

EVALUATION OF ENERGY PARTITIONING IN SM 2, SM 3, SM 4, AND SM 5

	Energy (kW-sec)				Energy Distribution (%)			
	SM 2	SM 3	SM 4	SM 5	SM 2	SM 3	SM 4	SM 5
Gas work at slug impact	14.4	13.9	13.5	13.6	100	100	100	100
Slug kinetic energy at impact	9.49	4.43	4.15	4.12	65.9	31.8	30.7	30.3
Strain energy at impact								
Core barrel	0.46	0.42	0.24	0.37				
Vessel wall	3.86	1.60	0.20	0.33				
Thermal liner	--	--	0.02	0.02				
UIS columns	--	0.83	0	0.27				
Support platform	--	--	?	?				
Axial strain energy	0.08	0.01	0.01	0.01				
Total strain energy at impact	4.40	2.86	0.47	1.00	30.6	20.6	3.5	7.4
Estimated kinetic energy in entrained and locally accelerated water	0.51	6.61	8.88	8.48	3.5	47.6	65.8	62.3[a]
Total gas work after impact	14.6	14.2	13.8	13.9	100.0	100.0	100.0	100.0
Strain energy after impact								
Core barrel	0.46	0.42	0.24	0.37				
Vessel wall	6.19	3.18	0.83	1.19				
Thermal liner	--	--	0.21	0.24				
Support platform	--	--	?	?				
Axial strain energy	0.25	0.04	0.02	0.02				
Total strain energy after impact	6.90	4.47	1.30	2.09	47.3	31.5	9.4	15.0

[a] Plus reduction in work potential caused by UIS throttling.

REFERENCES

1. Westinghouse - Advanced Reactors Division, "Clinch River Breeder Reactor Plant Project 1977 Technical Progress Report," Section 8 Safety and Licensing, prepared under Contracts E4-76-C-15-2395 and E4-76-C-15-0003.

2. Romander, C. M., D. J. Cagliostro, and D. W. Ploeger, "Static Response of a 1/20-Scale Model of the Clinch River Breeder Reactor Head," Third Technical Report for Energy Research and Development Administration (now DOE), Contract No. AT(04-3)-115 (July 1977).

3. Chang, Y. W., and J. Gvildys, "REXCO-HEP: A Two Dimensional Computer Code for Calculating the Primary System Response in Fast Reactors", ANL Technical Report ANL-75-19, June 1975.

4. De Salvo, G. J., and J. A. Swanson, "ANSYS Engineering Analysis Systems User's Manual," Swanson Analysis System Inc., Elizabeth, Pa., March 1975.

5. Florence, A. L., and G. R. Abrahamson, "Simulation of a Hypothetical Core Disruptive Accident in a Fast Flux Test Facility," SRI Final Report HEDL-SRI-1, prepared for Hanford Engineering Development Laboratory, SRI Project PYD 1109, Contract No. AT(45-1)-2170, (May 1973).

6. Cagliostro, D. J., and C. M. Romander, "Experiments on the Response of Rigid and Flexible Reactor Vessel Models to a Simulated Hypothetical Core Disruptive Accident," Fifth Interim Report to Argonne National Laboratory, SRI Project 1960, Contract No. 31-109-38-2655 (November 1976).

7. Christie, A. M., "Structural Response of CRBRP Scale Models in a Simulated Hypothetical Core Disruptive Accident," Westinghouse, Advanced Reactor Division, Report No. WARD-D-0218 (May 1978).

8. Cagliostro, D. J., and A. L. Florence, "Characterization of an Energy Source for Modeling Hypothetical Core Disruptive Accidents in Nuclear Reactors," First Interim Report to Argonne National Laboratory, SRI Project PYU-1960, Contract No. 31-109-38-2655, (October 1972).

9. Tobin, R. J. and D. J. Cagliostro, "Effects of Vessel Internal Structures on Simulated HCDA Bubble Expansions," Fifth Technical Report from SRI to Department of Energy, Contract EY-76-C-03-0115, in preparation.

10. Joe, B. W., "SM-2 Posttest Analysis of the Effects of Material Strain Rate," Preliminary Information Report GEFR-00287(L), General Electric Company, Sunnyvale, California (October, 1977).

11. Joe, B. W., "Assessment of Deviation from Prototypic Properties in SRI SM-4 1/20-Scale Model," Preliminary Information Report GEFR-00311(L), General Electric Co., Sunnyvale, California (November 1977).

12. Biggs, J. M., "Introduction to Structural Dynamics," McGraw-Hill Book Co., New York, (1964).

Appendix A

STATIC RESPONSE OF A 1/20-SCALE MODEL OF THE CLINCH RIVER BREEDER REACTOR HEAD

A. Introduction

An important step in the evaluation of the structural response of the CRBR head under slug impact loading during an HCDA is to investigate the potential response modes of the head under quasi-static loads. The slow loading times afforded by a quasi-static test allow a systematic and detailed examination of the deformation patterns of the complex, three-piece, rotating plug head of the reactor. Reported here are the results of experiments to determine the static load-deflection properties of the complex head of the CRBR reactor.

B. Objectives

The objectives of this work were to determine the static load-versus-deflection relationship for the plug-shear ring combination for use in computer simulations of dynamic head response and to evaluate the failure mechanisms of the shear rings designed to hold the head together during impact loadings.

C. Approach

A single 1/20-scale model of the CRBR head was loaded using hydrostatic pressure. Figure A.1 shows a plan view and a section view of the model. The head, made from 533-B carbon steel, included the three plugs of the prototypic head, scaled shear rings, and several cutouts on each plug to model the plate stiffness of the prototypic head. The head was bolted to a thick base plate and the space between the base plate and the head was filled with water. O-ring seals, a Viton rubber disc, and a 1100-0 aluminum sheet prevented leakage during the experiment.

The model was instrumented with displacement gages of the linear potentiometer type and pressure transducers of the piezoresistive and piezoelectric types. Displacements and pressures were recorded

continuously on magnetic tape. The head was loaded until failure, that is, until the volume of the fluid reservoir behind the head increased rapidly and the pressure in the reservoir decreased.

D. Summary

The results of our evaluation of the load-deflection data can be summarized as follows:

- The volume of water between the head and base plate increased linearly with pressure up to a pressure of 700 psi (see Figure A.11). The slope of the pressure-volume change curve was 123 psi/in.^{3}. At 700 psi, the head began to yield and the volume increased rapidly with increasing pressure.
- The largest deflection occurred along the axis of symmetry of the head at the joint between the large plug and the intermediate plug nearest the center of the head (see Figure A.5). A peak deflection of 0.416 in. was measured at this point at a pressure of 1160 psi.
- Only the large plug showed large permanent plastic deformation after the test. The other plugs and the outer ring showed little plastic deformation.
- The mechanical process that led to large deformation of the head was the disengagement of the shear ring between the large and the intermediate plug as the large plug deformed plastically. This shear ring gradually slipped off the bearing surface of the intermediate plug as the intermediate plug was pushed up through the large plug. At no point did a shear ring or any bearing surface fail catastrophically. Upon unloading, the head remained locked in the final deformed shape.

E. Experimental Procedures

1. Loading Technique

The three-segment head (Figure A.1) was bolted securely to a thick steel base plate, which in turn was securely fastened to a rigid steel table. The reservoir between the head and the base plate was filled with water and was carefully bled to ensure that no air was trapped inside. The head apparatus was connected to the loading apparatus shown schematically in Figure A.2. The loading apparatus consists of a bottle of high pressure nitrogen, metering valves, a water-filled manostat, and both mechanical and piezoresistive pressure gages. The

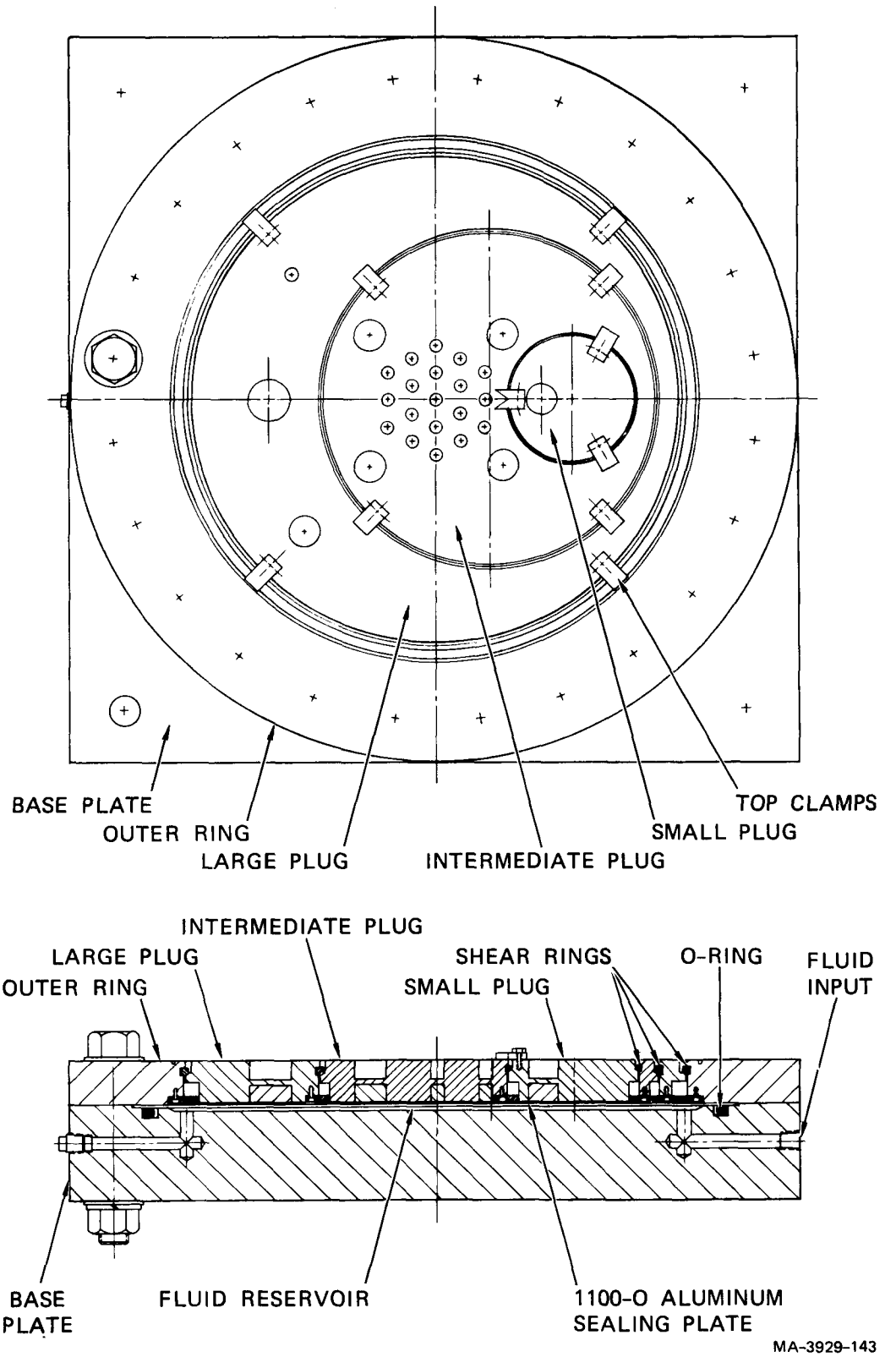

FIGURE A.1 SCHEMATIC OF STATIC VESSEL HEAD APPARATUS, TEST SM 1

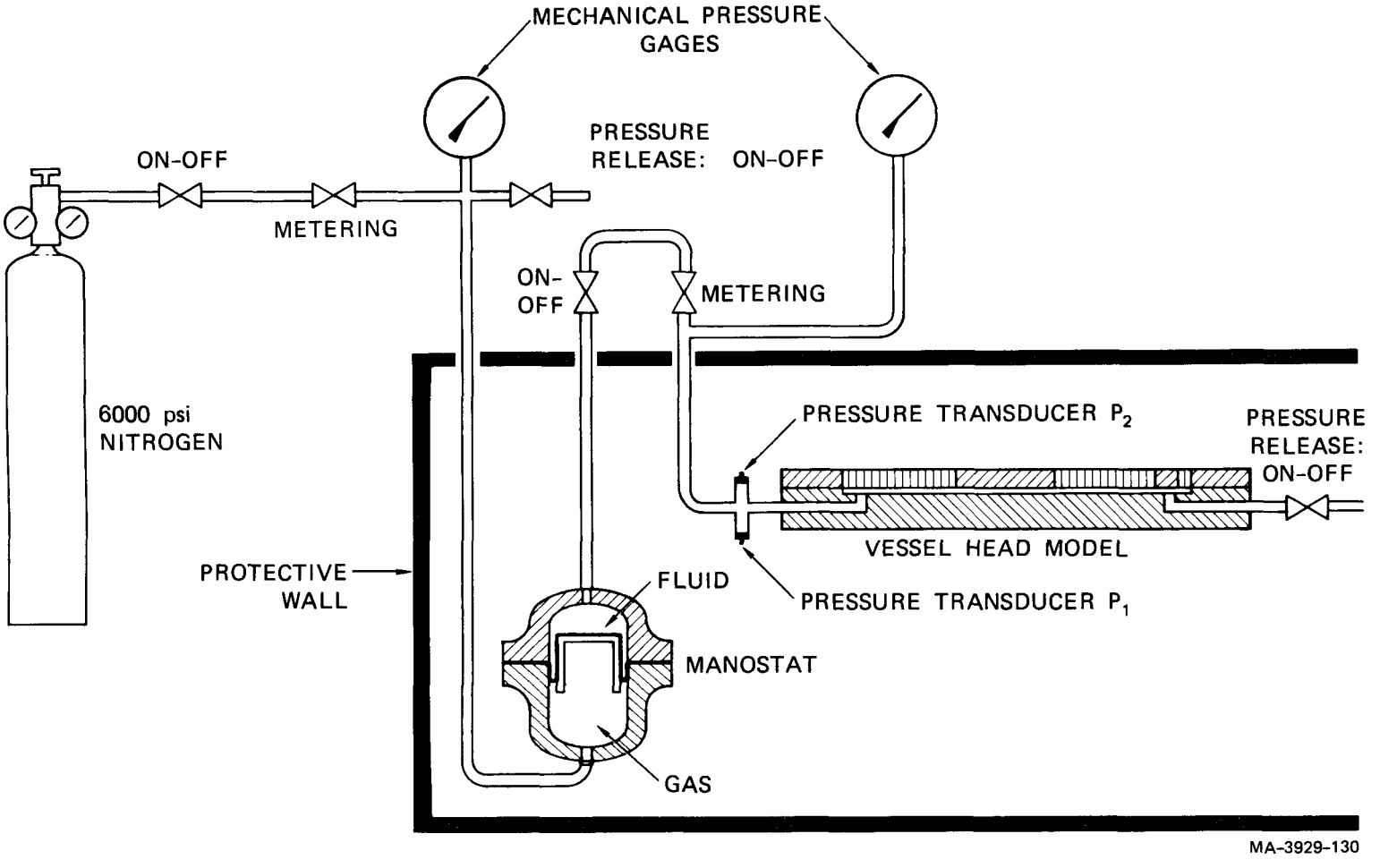

FIGURE A.2 STATIC TEST APPARATUS SCHEMATIC

loading apparatus controls the loading rate of the head while continuously supplying fluid to the expanding head reservoir by controlling the gas flow into as well as the fluid flow out of the manostat. The manostat is a large reservoir divided into two chambers by a flexible diaphragm. As the gas pressure builds up on one side of the diaphragm, an equal fluid pressure builds up on the other. The pressurized fluid is forced into the head reservoir, and the diaphragm in the manostat deforms as the head deforms, forcing more fluid into the head reservoir. The loading rate is controlled primarily by the metering valve that controls gas flow into the manostat. A loading rate of about 150 psi/min was chosen for the static experiment SM 1 based on pretest experiments on dummy heads.

2. Instrumentation

Figure A.3 shows a layout of instrumentation for the static head experiment. Seventeen linear potentiometer displacement gages (linipots)* were used in the experiment. The linipots were attached to rigid beams suspended above the model. The beams were fastened to a support frame to ensure a firm independent base for deflection measurements. Most of the gages could measure a maximum displacement of 0.45 inches with an accuracy of $\pm$0.001 inch. Special conical tips were attached to the linipot rods to accurately position the linipots.

Most of the instrumentation was centered along the primary axis of symmetry of the head. Linipots were placed in pairs on either side of each shear-ring joint along this axis. Other linipots (No. 13 through 16) were positioned to measure the symmetry of response and the tilt of the plugs. A single linipot (No. 17) was positioned to measure the extension of the bolts that secured the head to the base plate.

Two electronic pressure transducers were installed in the fluid supply tube feeding the head to measure head pressure. One of these gages was a piezoelectric gage (CEC Model 1000) with a range of 0 to 5000 $\pm$ 5 psi, and the other was a piezoresistive gage (Kulite Model HKMS-375-2000) with a range of 0 to 2000 $\pm$ 5 psi.

*Model 3273, manufactured by Bourns Instrument Division, Riverside, Calif.

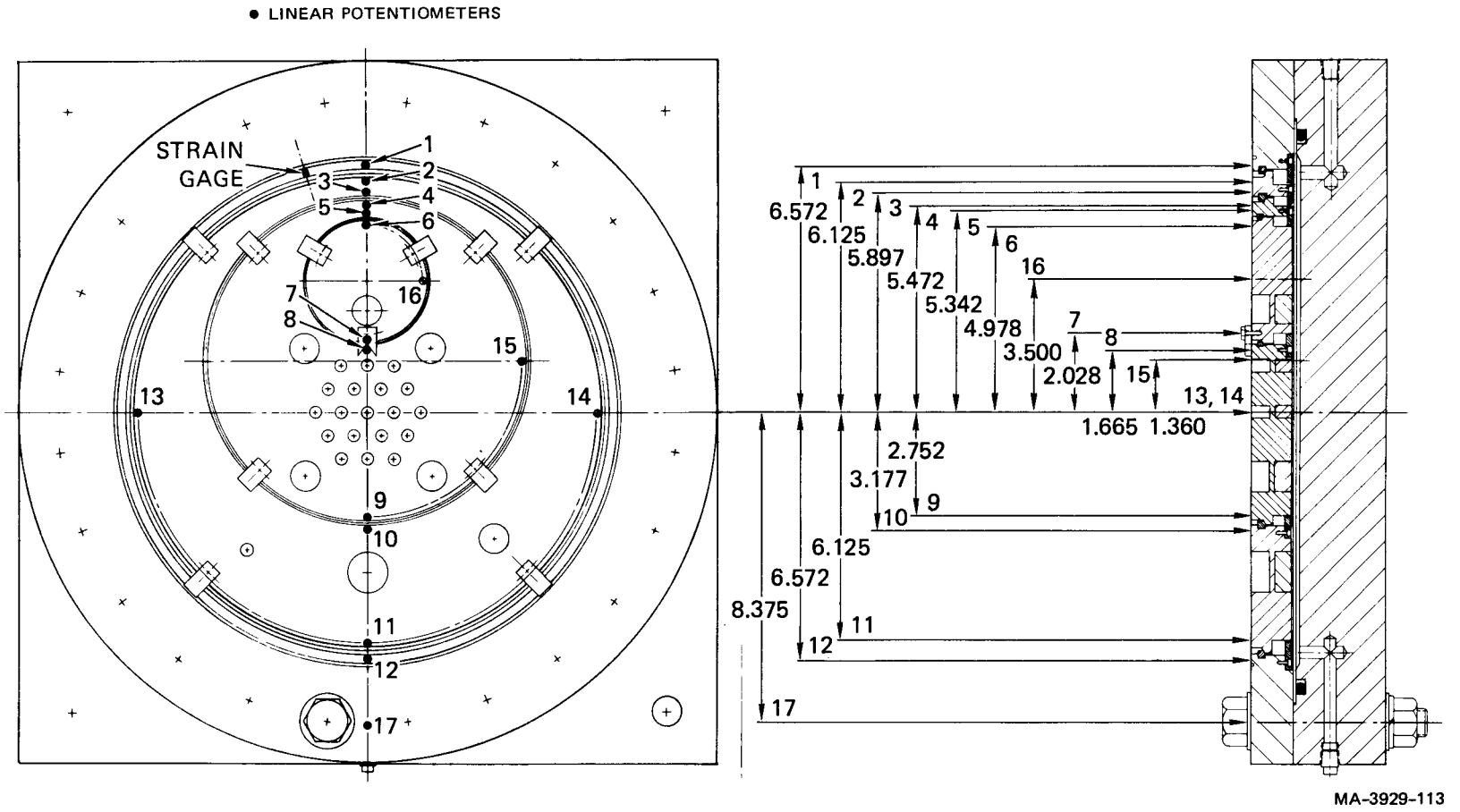

FIGURE A.3 INSTRUMENTATION LAYOUT FOR STATIC TEST SM 1

3. Data Acquisition and Reduction

The output of the pressure transducers and the linipot deflection gages, a total of 23 channels, was recorded directly on magnetic tape using two tape recorders. Each data channel was reproduced on a recording oscillograph, including the timing channel so that the data channels could be synchronized in time. A telereadex machine was used to digitize and punch the data onto computer cards.

From the digitized data, computer plots were made of deflection versus pressure (using the average of the pressure recorded on each tape machine) and shear deflection (the difference in deflection on each side of a shear ring). The deflection-pressure data were compiled in a table and printed by the computer. The elastic stiffness is the inverse of the slope of the linear (elastic) portion of the deflection-pressure curves. The pressure at the elastic limit is the point where the deflection-pressure curve first deviates from a straight line.

F. Results

1. Deformed Shape

Figure A.4 shows photographs of the SM 1 head after the experiment was completed and the linipots were removed. The large plug shows considerable plastic deformation. The other two plugs were virtually undeformed after the test. The large relative displacement between the large and the intermediate plug was caused by disengagement of the shear ring mounted in the large plug from the shear ring bearing surface on the intermediate plug. The intermediate plug was being pushed slowly out through the cutout in the large plug at the time when the test was halted.

Figure A.5 shows profiles of the deformed shape of the head at six successively higher pressures. The profiles were plotted using displacement data taken along the axis of symmetry of the head. The length

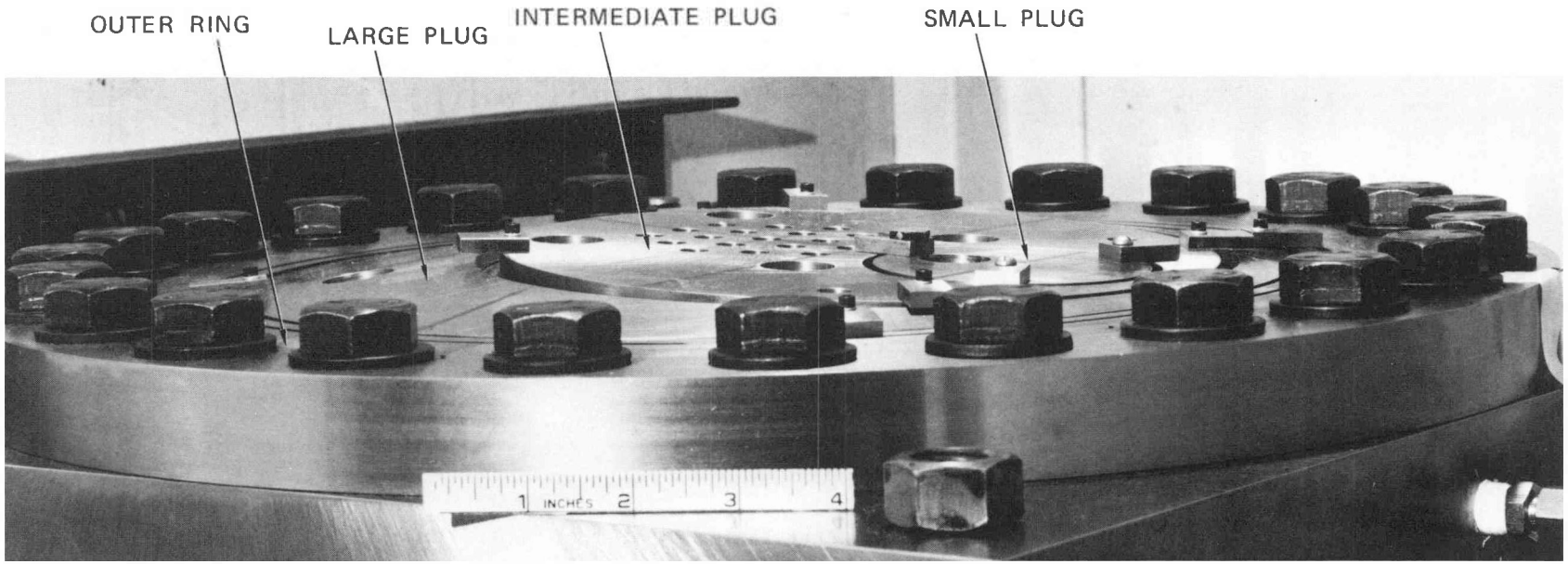

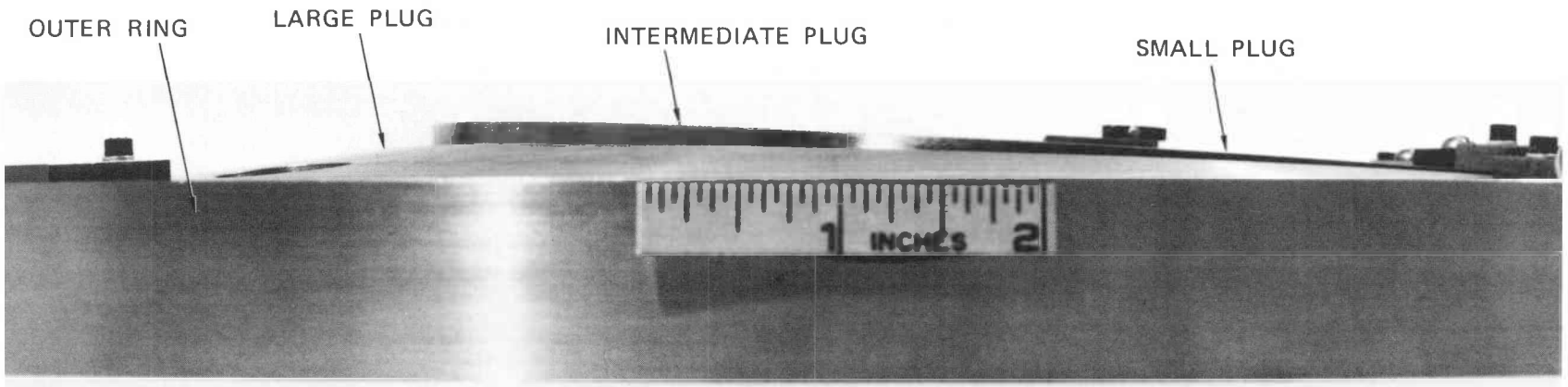

MP-3929-114

FIGURE A.4 DEFORMED SHAPE OF HEAD; STATIC TEST SM 1

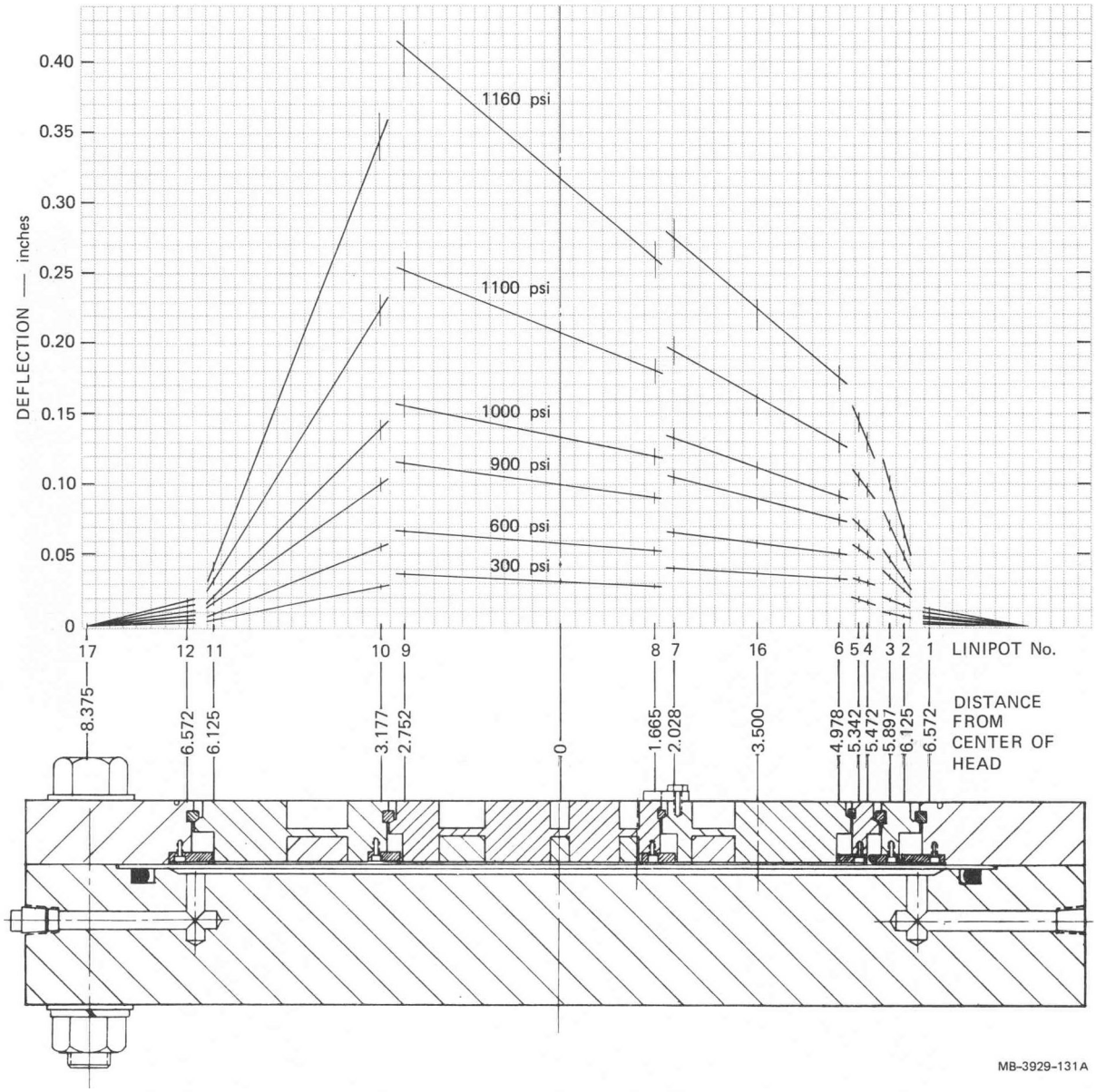

FIGURE A.5 PROFILES OF HEAD AT SIX PRESSURES; STATIC TEST SM 1

of the vertical tick marks at each linipot location represents bounds on the displacement measurements based on a ±5% measurement accuracy.* The large plug shows the most plastic deformation, particularly between displacement gages 10 and 11. Plastic deformation also occurred in the large and intermediate plugs near displacement gages 2, 3, 4, and 5, where the stiffness of the plates was reduced because of the plug cutouts. The small plug remained undeformed throughout the experiment.

2. Shear Ring Response

As mentioned earlier, the head failed because of disengagement of the shear ring between the large and intermediate plugs. This disengagement is gradual and probably begins at about 700 to 800 psi.

Figures A.6, A.7, and A.8 plot shear displacements versus pressure across each shear-ring joint along the axis of symmetry of the head. Some of the plots initially deflect at zero pressure ($\Delta 4 - \Delta 3$, $\Delta 6 - \Delta 5$, $\Delta 7 - \Delta 8$, and shear rings and grooves. An analysis of the effect of these clearances showed that the shear rings could rotate slightly in the shear-ring grooves resulting in displacements equivalent to those measured at zero pressure. The plots in Figures A.6, A.7, and A.8 indicate that the shear displacements were small (about 7 to 20 mils) up to about 700 psi, after which local shear ring distortions and disengagement of the shear rings ($\Delta 9 - \Delta 10$) resulted in rapidly increasing deformation. Below 700 psi, the shear rings nearest the outer edge of the head experienced the largest shear displacements, neglecting initial adjustment of the shear rings at low pressure. This was to be expected, since the shear load per unit length of shear ring increases in proportion to the diameter of the plug. In addition, the largest shear

*Approximately ±2% for gage error and ±3% for record interpretation error.

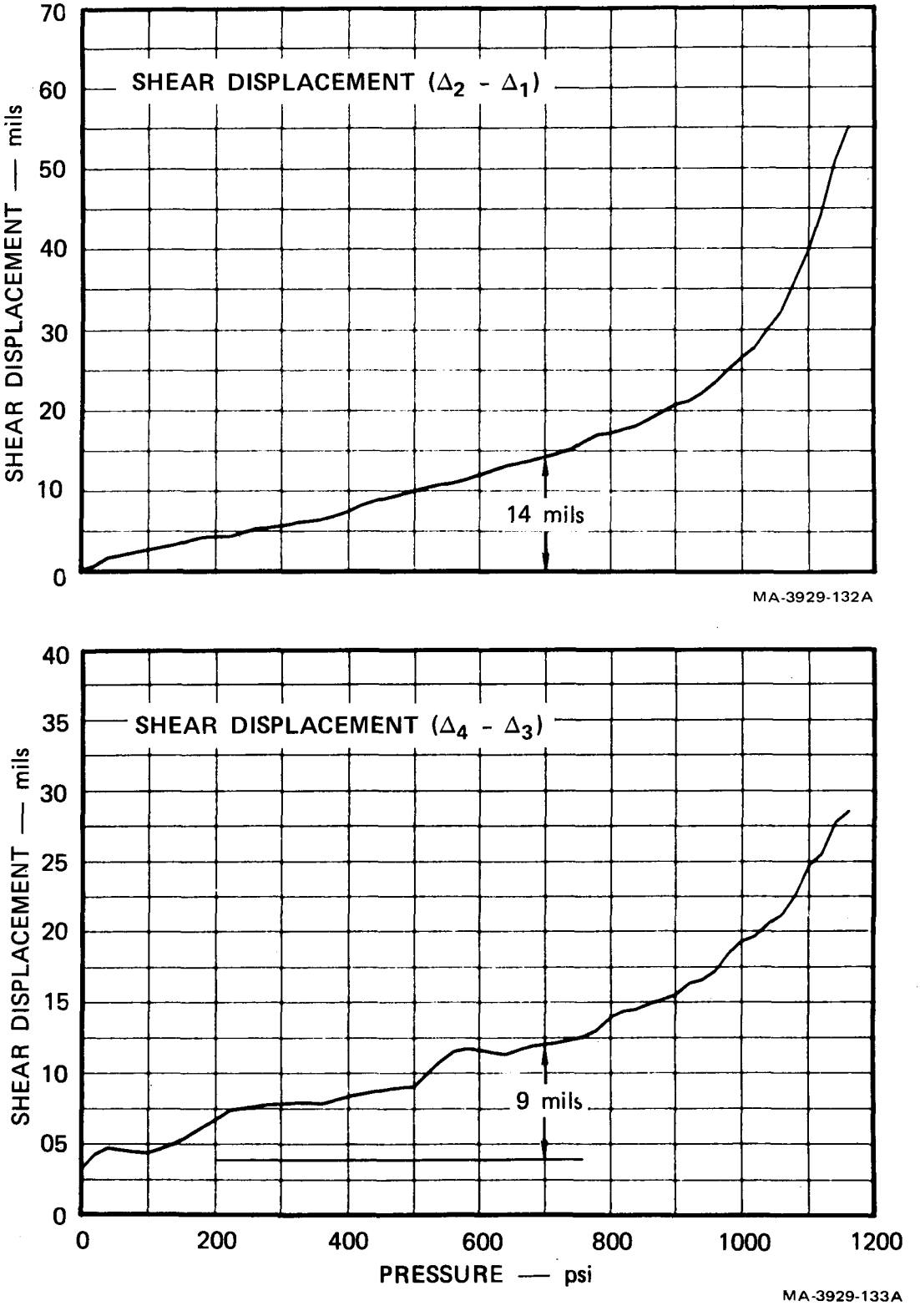

FIGURE A.6 SHEAR DISPLACEMENT VERSUS PRESSURE ($\Delta_2 - \Delta_1$), ($\Delta_4 - \Delta_3$)

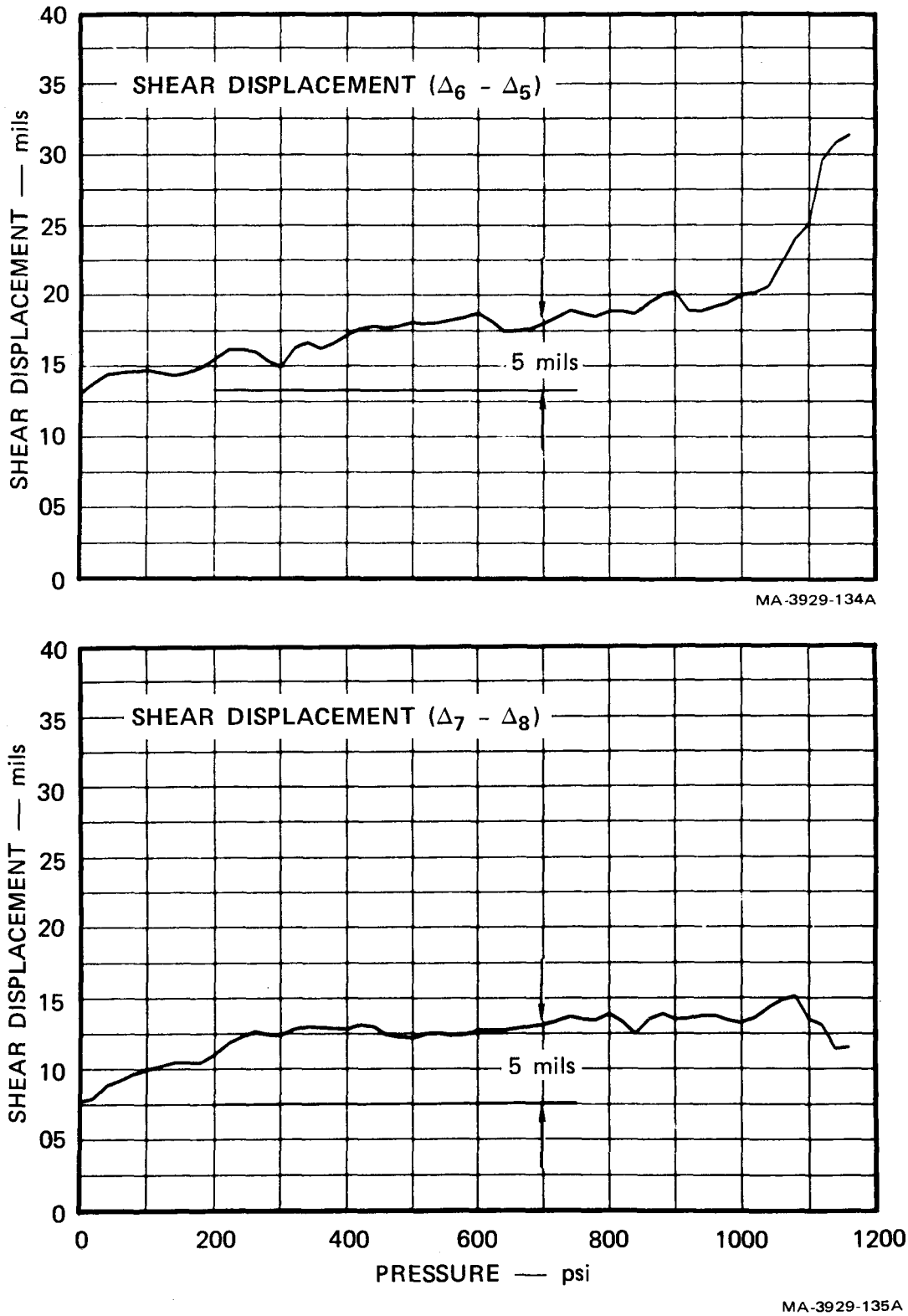

FIGURE A.7 SHEAR DISPLACEMENT VERSUS PRESSURE (Δ_6 – Δ_5), (Δ_7 – Δ_8)

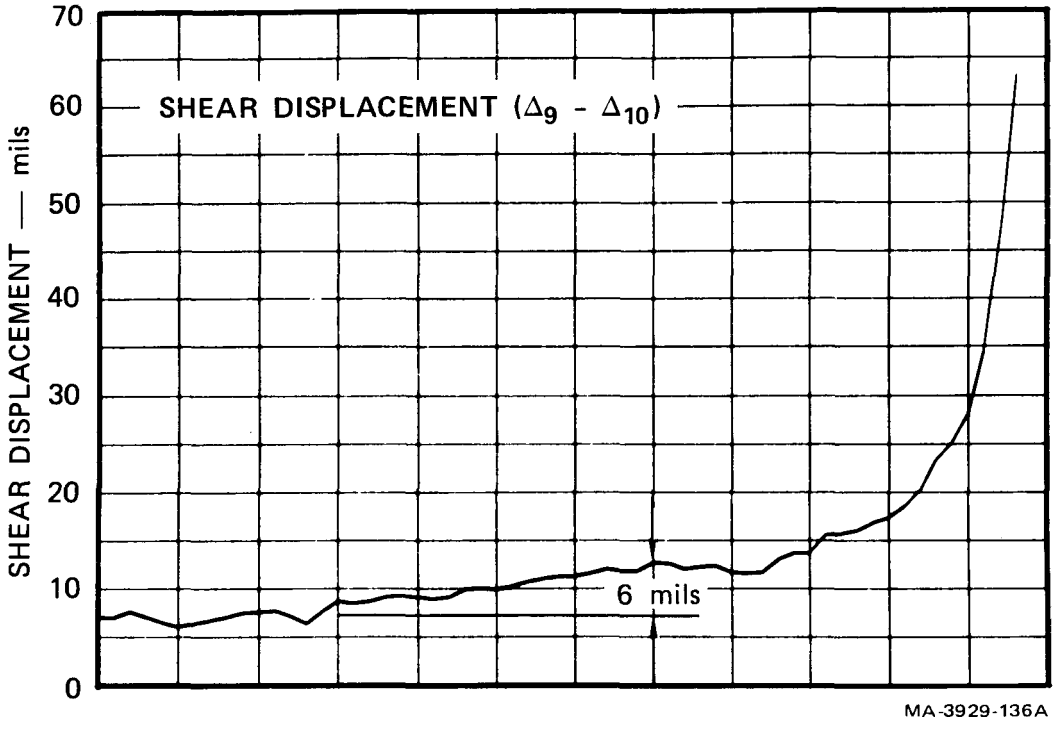

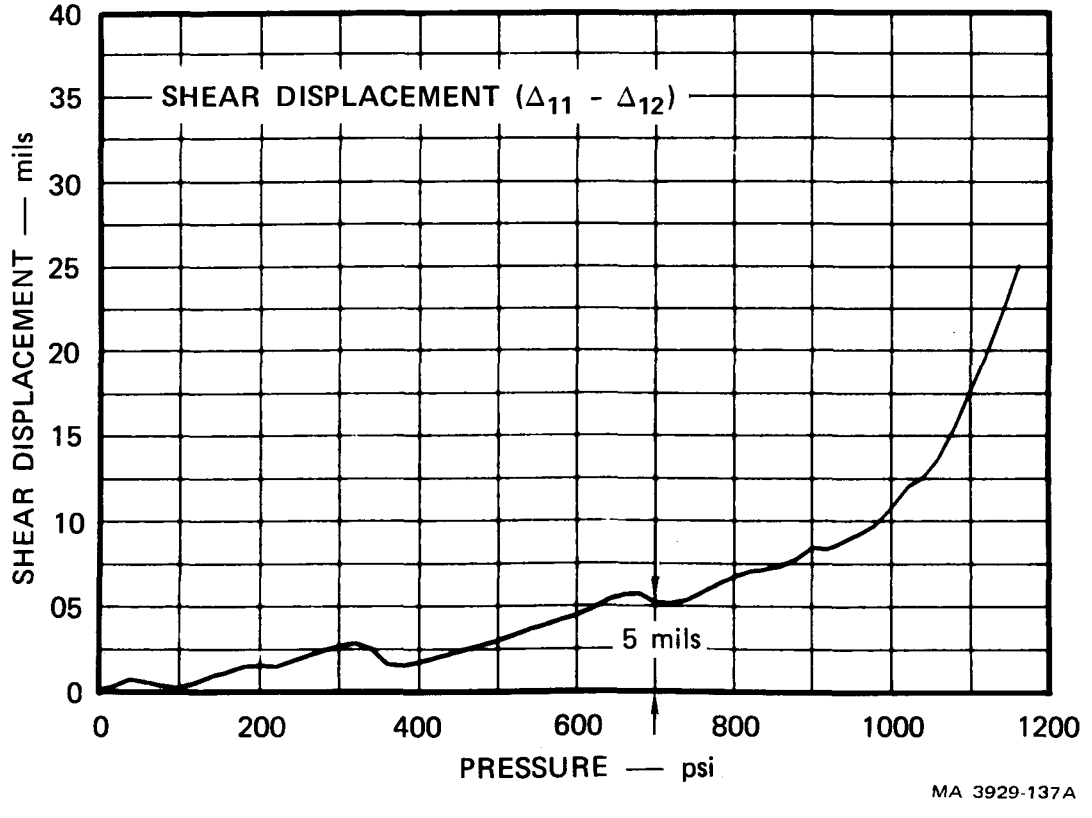

FIGURE A.8 SHEAR DISPLACEMENT VERSUS PRESSURE ($\Delta_9 - \Delta_{10}$), ($\Delta_{11} - \Delta_{12}$)

displacement occurred where the three plugs nest together (the right-hand size of the head in Figure A.4). Here plastic deformation of the head also contributed to the shear displacements.

The shear rings themselves showed no permanent deformation. The shear ring groove in the large plug showed up to 10 mils of permanent deformation along the perimeter where the maximum displacement of the head occurred. This shear ring groove deformation was restricted to the upper lip of the groove. The other shear ring grooves had undergone no permanent deformation. The shear ring bearing surfaces in the large and intermediate plugs showed some local deformation due to crushing of the steel. Deformations from 1 to 8 mils were measured. The smaller deformations occurred on the bearing surface on the large plug while the large deformations occurred on the bearing surface of the intermediate plug near the site of the maximum head displacement and shear ring disengagement. These local crushing deformations were restricted to the outer edge of the shear ring bearing surfaces.

Head Stiffness

Figure A.9 shows load-deflection curves for three locations on the head. These curves, typical of all the load-deflection curves, are nearly linear up to about 700 psi when the head begins to deform nonlinearly because of combined plastic deformation of the large and intermediate plugs and disengagement of the shear ring between the large and intermediate plug. The slope of the linear portion of the load deflection curves is a measure of the local stiffness of the head. Table A.1 lists the elastic limit and local elastic stiffness of the head. The average elastic limit is 700 $\pm$ 50 psi. The elastic stiffness decreases uniformly from 240,000 psi/in. on the outer support ring to 9800 psi/in. on the intermediate plug near the point where the shear ring disengages. The decrease in elastic stiffness is to be expected.

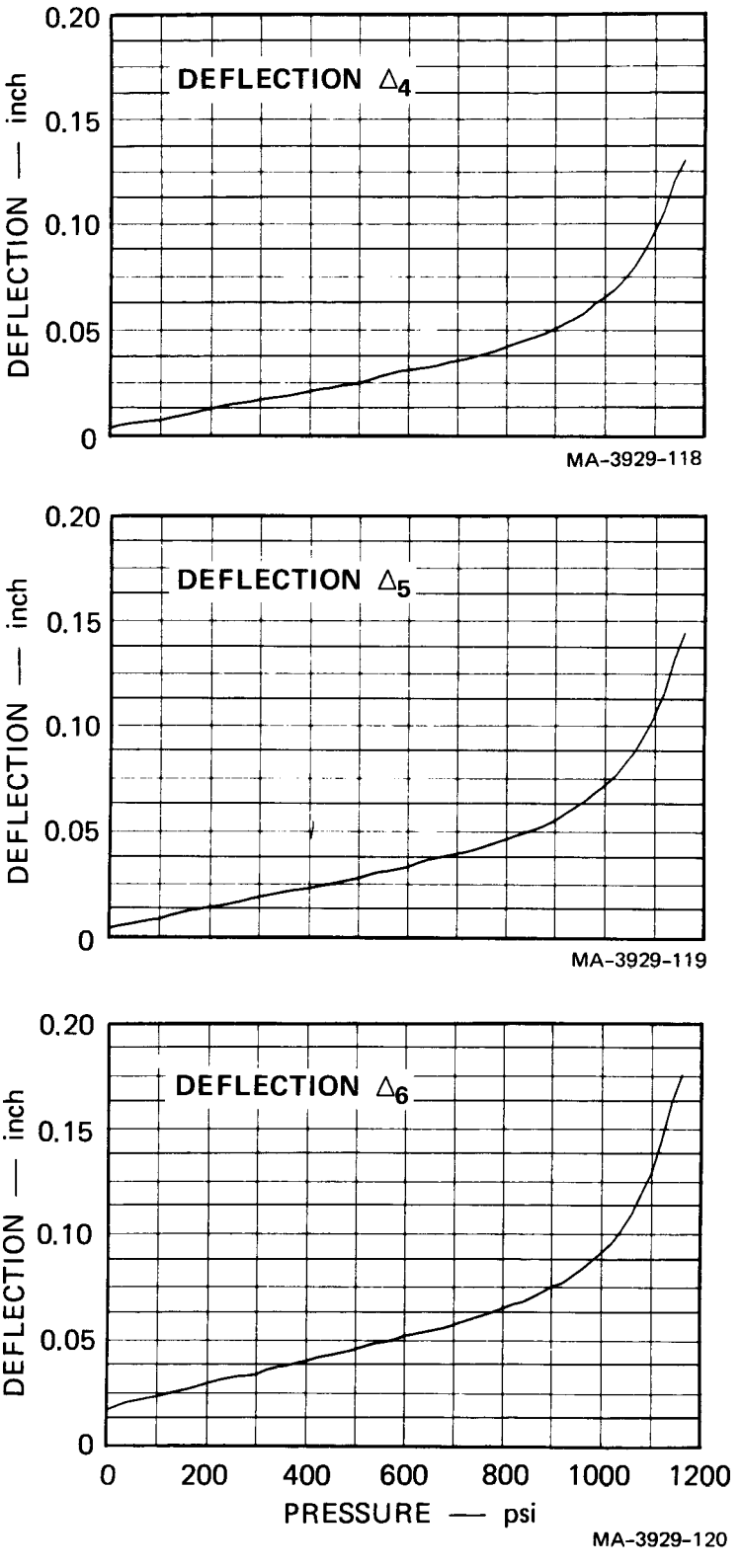

FIGURE A.9 DEFLECTION VERSUS PRESSURE Δ_4, Δ_5, Δ_6

Even for a continuous, simply supported plate, the deflections at a given load increase with distance from the edge.

Another measure of head stiffness is the volume change under the head as a function of the load. This volume change was determined by calculating volume changes based on the deformed profiles shown in Figure A.5. The volume change of each part of the three-piece plug was divided into components, as shown in Figure A.10, to simplify the calculations. Two basic components were considered.

(1) The volume change due to the rigid body motion of each plug with respect to the next larger plug. This volume is assumed to be in the shape of a short truncated cylinder with a crossectional area equal to the area of the plug. The outer ring undergoes no rigid body motion.

(2) The volume change due to the deformation of each plug and the outer ring. This volume is assumed to be in the shape of a conical frustum. The area of the base of the frustum is the area of the plug and the area of the upper plane of the frustum is the area of the next smallest plug.

Figure A.11 shows the final plot of pressure versus volume change for SM 1. The curve indicates a linear elastic stiffness of 123 psi/in.^{3} up to about 700 psi, after which the volume increases nonlinearly. The volume of the deformed head, based on measurements of the deformed 1100-0 aluminum disc used to seal the head (see Figure A.1) was calculated to be 31.6 in.^{3} using the volume components listed above. The final volume of the deformed head, measured by filling the deformed aluminum disc with water, was 30.3 in.^{3}, 4% below the calculated volume.

The initial volume on the volume change-pressure curve is due to deflections of each plug that result from small translations and rotations of the shear rings in their grooves at low pressures.

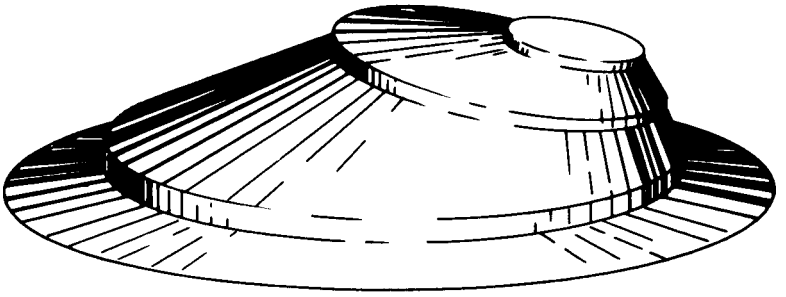

(a) SHAPE OF FLUID RESERVOIR UNDER HEAD (EXAGGERATED)

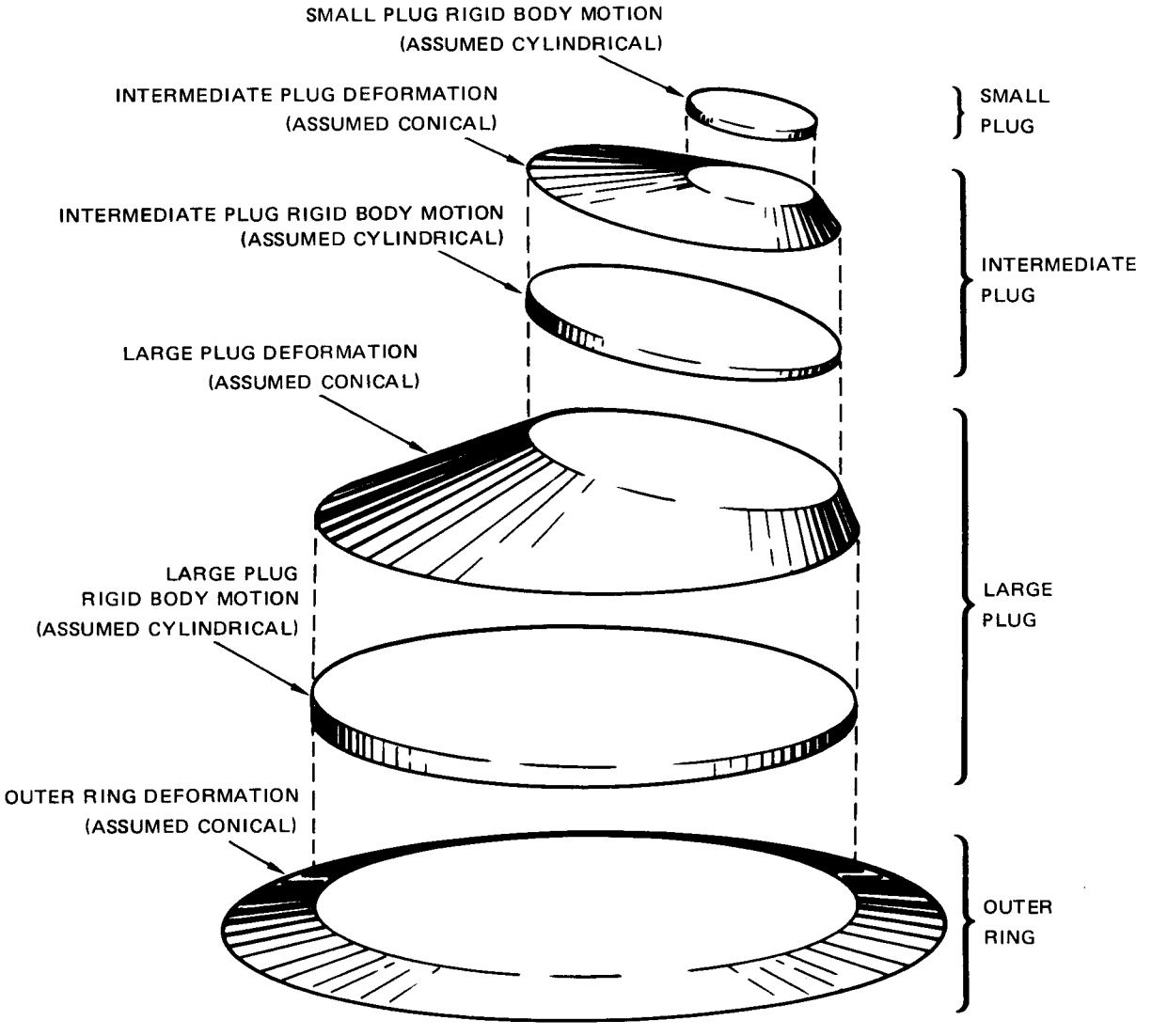

(b) VOLUME COMPONENTS USED IN CALCULATIONS

MA-3929-144

FIGURE A.10 VOLUME COMPONENTS USED IN PRESSURE-VOLUME CHANGE CALCULATIONS

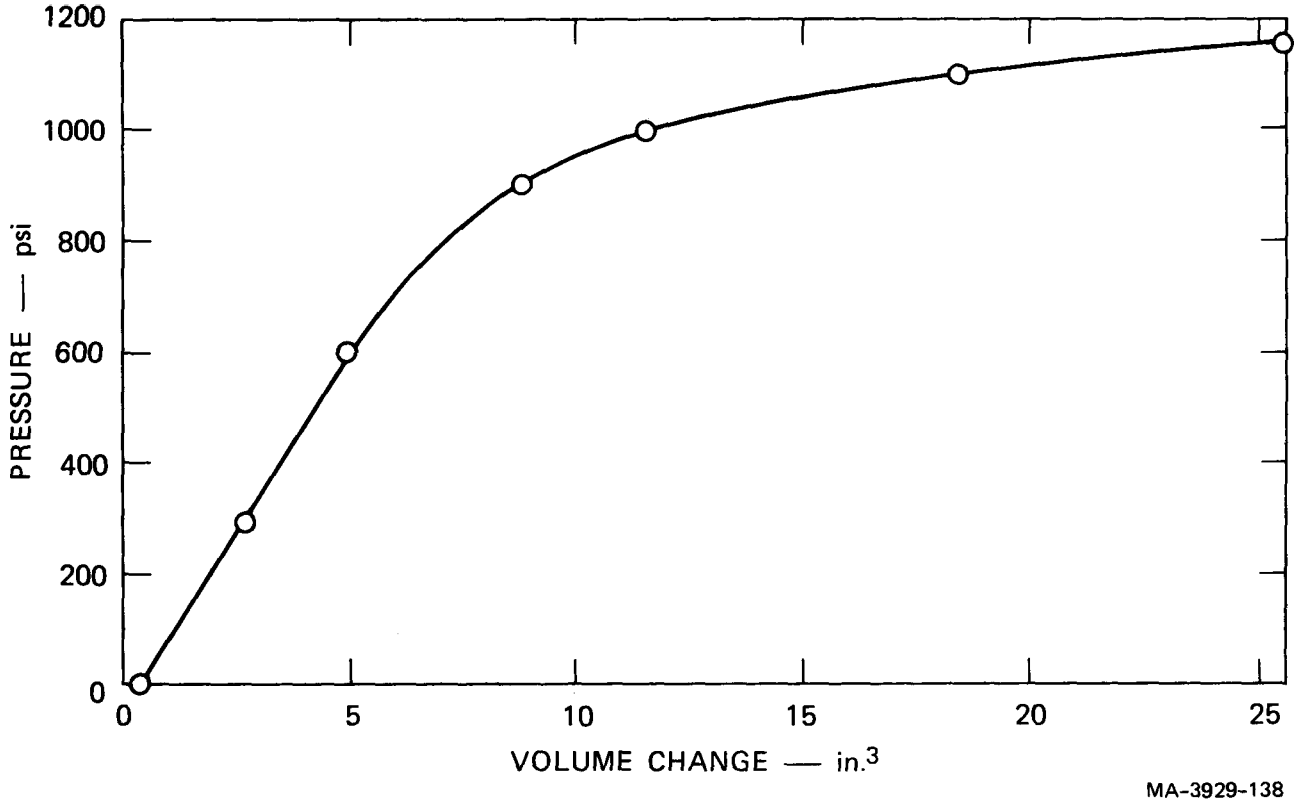

FIGURE A.11 PRESSURE-VOLUME CHANGE RELATION FOR SM 1

Table A1

ELASTIC LIMIT AND ELASTIC STIFFNESS OF SM 1

Location, Δ	Elastic Limit (psi)	Elastic Stiffness (10^4 psi/inch)
1	700	24.0
2	650	4.0
3	700	3.1
4	700	2.1
5	650	2.1
6	700	1.7
7	700	1.2
8	725	1.3
9	675	0.98
10	725	1.1
11	700	8.0
12	700	24.0
14	675	7.0
15	700	1.5
16	800	1.4

Average elastic limit = 700 psi

4. Detailed Restuls of SM 1

Table A.2 lists the deflections recorded for each displacement gage at 20 psi intervals up to 1160 psi. Figures A.12 through A.16 show load-deflection curves for each of the displacement gages. The initial displacements at zero load for some of the gages are caused by initial displacements of the shear rings at low pressures.

Table A.2

HEAD DEFLECTIONS FOR STATIC TEST SM-1

Pressure	Location, Δ (mils)																
(psi)	1	2	3	4	5	6	7	8	9	10	11	12	13	14	15	16	17
0	0	0	0	3	4	17	12	4	7	0	0	0		0	4	16	0
20	0	1	0	5	5	19	15	7	9	2	0	0		0	7	18	0
40	0	2	1	6	6	21	17	8	11	4	1	0		1	9	20	0
60	0	2	2	6	7	21	19	10	13	6	1	1		1	10	21	0
80	0	2	2	7	8	22	21	11	14	8	1	1		1	11	22	0
100	0	3	3	7	9	23	23	13	16	10	2	1		2	12	23	0
120	0	3	4	8	10	25	24	14	18	11	2	1		2	14	25	0
140	0	3	4	9	12	26	26	15	20	13	2	1		2	15	27	0
160	0	4	5	11	13	27	28	17	22	15	2	1		3	16	28	0
180	0	4	6	12	13	28	29	19	25	17	3	1		3	17	29	0
200	0	5	6	13	14	30	32	21	27	19	3	1		3	18	31	0
220	1	5	7	14	15	31	34	22	29	21	3	2		4	20	32	0
240	1	6	7	15	16	32	36	24	30	23	3	2		4	21	33	0
260	1	6	8	16	17	33	38	25	31	25	4	2		4	22	34	0
280	1	7	9	16	18	33	39	27	34	26	4	2		4	23	35	0
300	2	7	9	17	19	34	41	28	37	28	4	2		4	24	37	0
320	2	8	10	18	20	36	43	30	38	30	5	2		5	25	38	0
340	2	8	10	18	21	38	44	31	40	32	5	3		5	27	40	0
360	2	9	11	19	22	38	46	33	43	34	5	4		5	28	41	0
380	2	9	12	20	23	39	47	35	45	36	6	4		6	29	42	0
400	2	10	13	21	23	40	49	36	46	37	6	4		6	31	44	0
420	2	10	13	22	24	42	51	38	49	40	6	4		6	32	46	0
440	2	11	14	23	25	43	53	39	51	42	6	4		7	33	47	0
460	2	12	15	23	26	44	54	41	53	43	7	4		7	35	49	0
480	3	12	15	24	27	45	55	43	55	45	7	4		7	36	50	0
500	3	13	16	25	28	46	57	44	57	47	7	4		7	37	50	0
520	3	13	16	26	30	48	59	46	59	49	7	4		8	39	52	0
540	3	13	17	28	31	49	61	48	61	50	8	4		8	40	53	0
560	3	14	18	29	31	50	62	50	63	52	8	4		8	41	55	0
580	3	14	19	30	32	51	64	52	65	54	8	4		9	43	56	0
600	3	15	19	31	33	52	66	53	67	56	8	4		9	44	58	0
620	3	15	20	32	35	53	68	56	70	58	9	4		9	45	59	0
640	3	16	21	32	37	54	71	58	73	61	9	4		9	47	61	0
660	3	17	22	33	38	55	73	60	74	63	10	4		10	49	62	0
680	4	17	22	34	39	56	75	62	76	65	10	4		10	50	63	0
700	4	18	23	36	40	58	77	64	80	67	10	5		10	52	65	0
720	4	18	24	37	41	59	79	65	82	69	11	6		11	54	67	0
740	4	19	25	38	42	61	81	67	84	72	11	6		11	56	68	0
760	4	20	26	39	44	62	83	70	87	75	12	6		12	58	70	0
780	4	21	27	40	45	64	86	72	90	78	12	6		12	60	72	0
800	4	21	28	42	47	66	89	75	93	81	13	6		13	62	74	0
820	5	22	29	44	48	67	91	78	96	85	13	6		13	65	76	0
840	5	23	31	45	50	68	94	81	99	88	14	6		13	67	79	0
860	5	24	32	47	51	71	97	84	105	92	14	7		14	70	81	0
880	5	25	33	49	53	73	101	87	110	96	15	7		15	73	84	0
900	6	26	35	51	55	76	105	91	114	101	16	7		15	76	87	0
920	6	27	37	53	59	77	110	96	121	106	16	8		16	80	91	0
940	6	29	39	55	61	80	114	100	128	112	17	8		17	84	95	0
960	7	30	41	58	65	84	120	106	136	119	18	9		18	90	100	0
980	7	32	44	62	68	88	126	112	145	128	19	10		19	96	105	0
1000	7	34	46	66	72	92	133	119	156	138	20	10		20	102	110	0
1020	8	36	50	70	76	96	141	128	169	150	22	10		22	111	117	0
1040	9	39	54	75	82	103	151	137	184	163	24	11		24	121	124	0
1060	10	42	59	80	88	110	163	148	202	179	26	13		26	132	133	0
1080	10	46	65	88	96	120	179	164	226	201	29	14		29	146	144	0
1100	10	50	72	97	105	130	195	181	252	224	32	14		32	162	157	0
1120	11	56	81	107	116	145	217	204	289	255	35	15		35	184	174	0
1140	12	63	93	121	132	163	247	236	347	300	39	17		39	215	198	0
1160	13	68	102	131	145	176	275	263	410	347	43	17		44	244	221	0

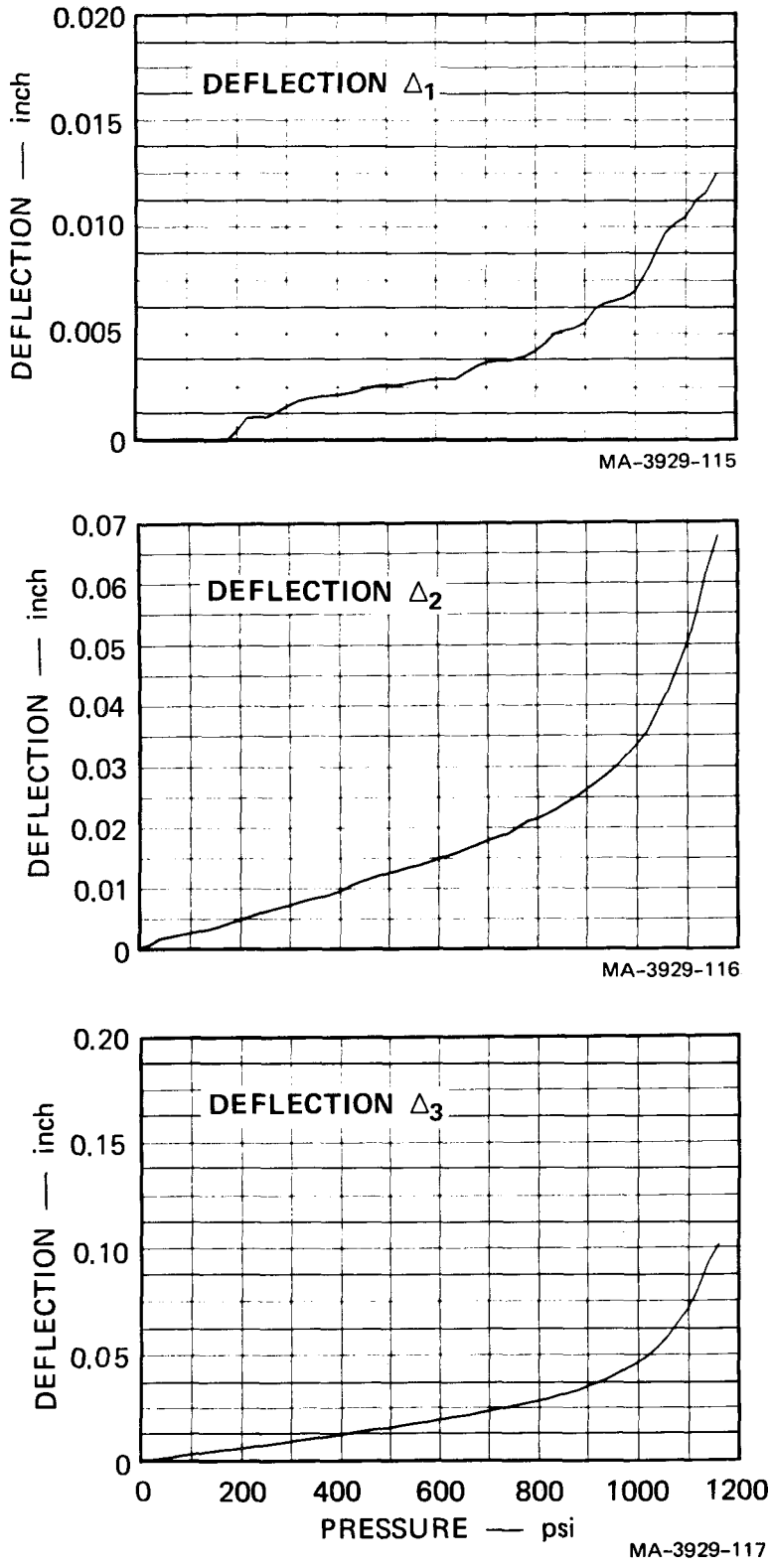

FIGURE A.12 DEFLECTION VERSUS PRESSURE Δ_1, Δ_2, Δ_3

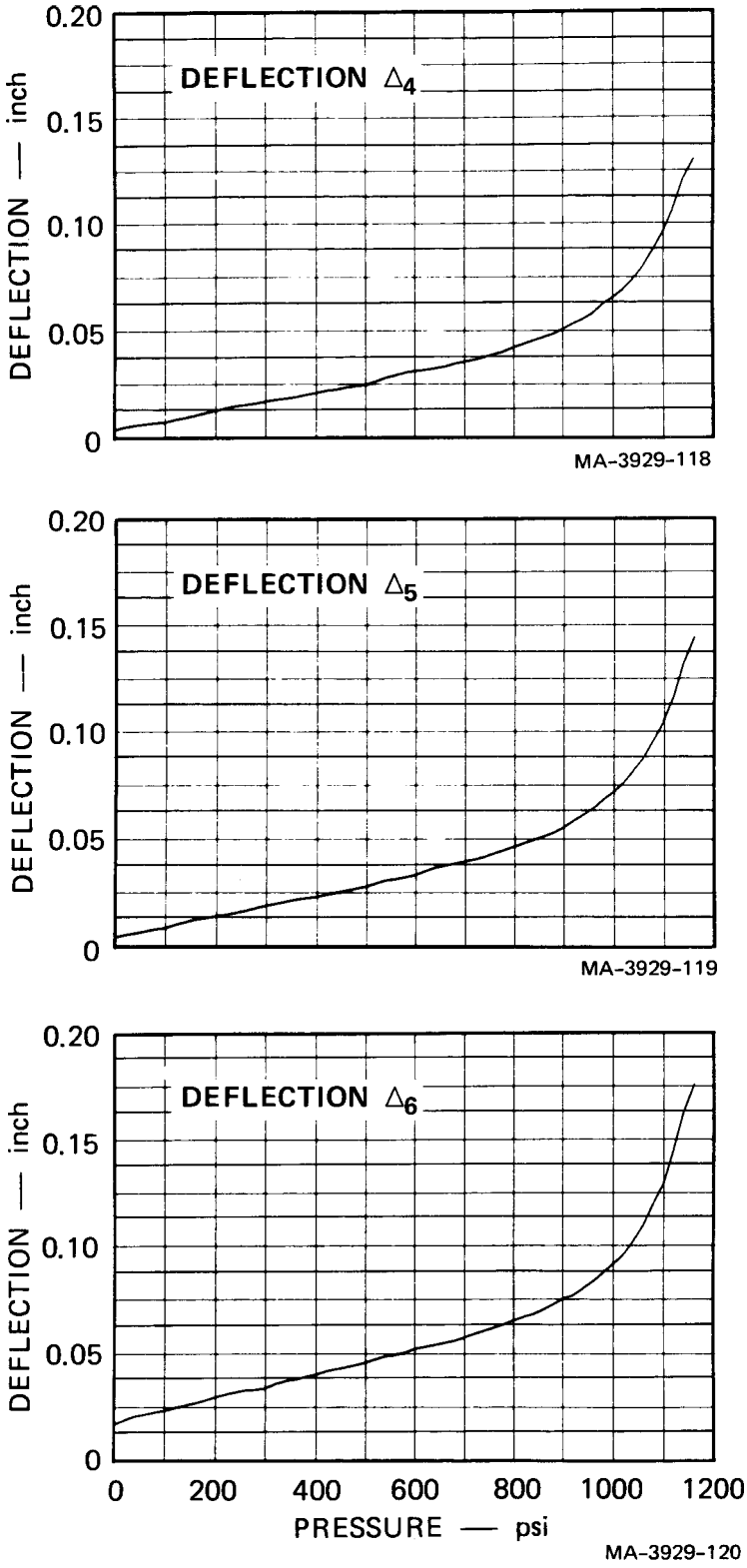

FIGURE A.13 DEFLECTION VERSUS PRESSURE Δ_4, Δ_5, Δ_6

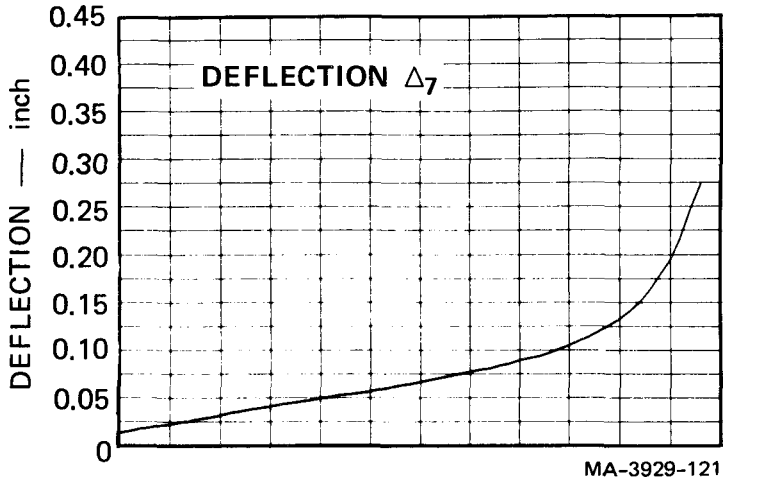

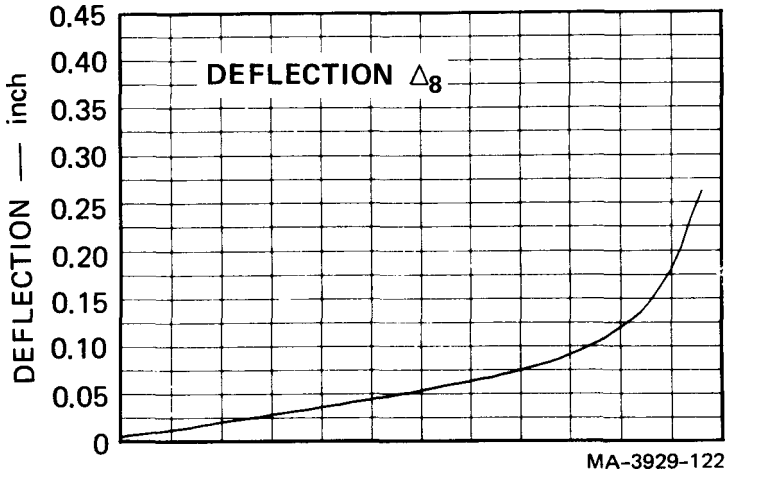

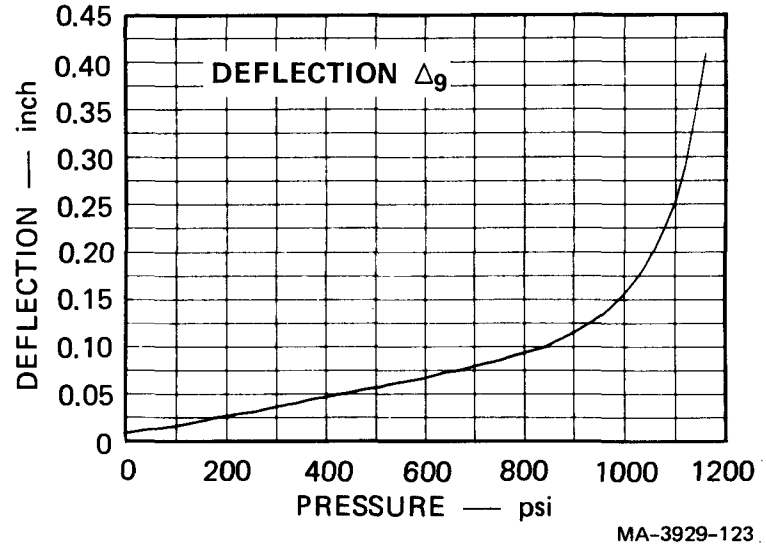

FIGURE A.14 DEFLECTION VERSUS PRESSURE Δ_7, Δ_8, Δ_9

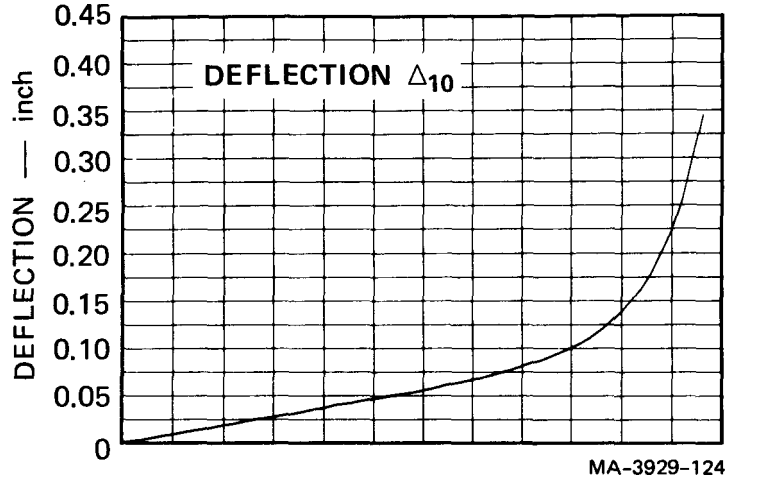

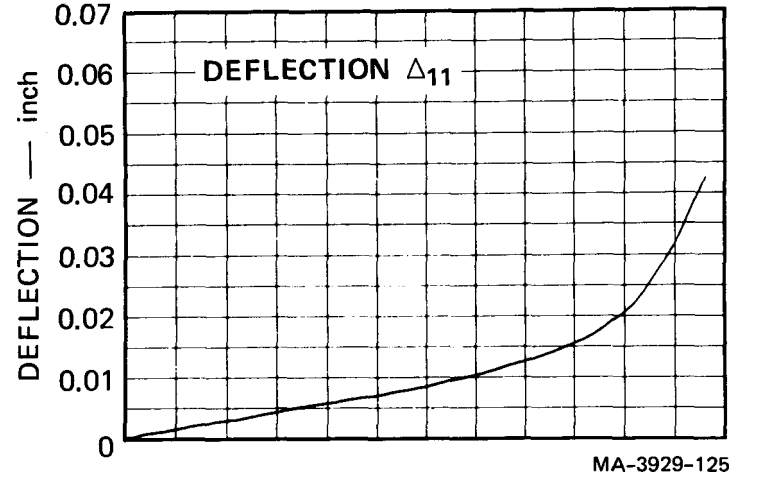

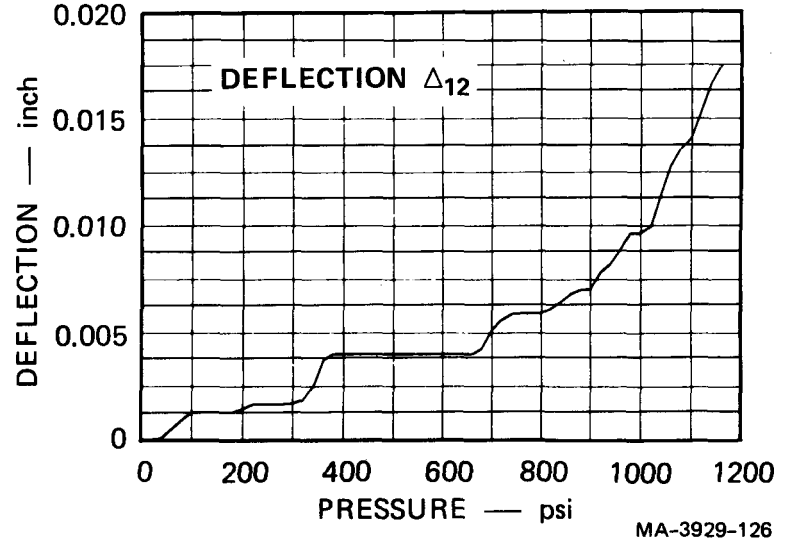

FIGURE A.15 DEFLECTION VERSUS PRESSURE Δ_{10}, Δ_{11}, Δ_{12}

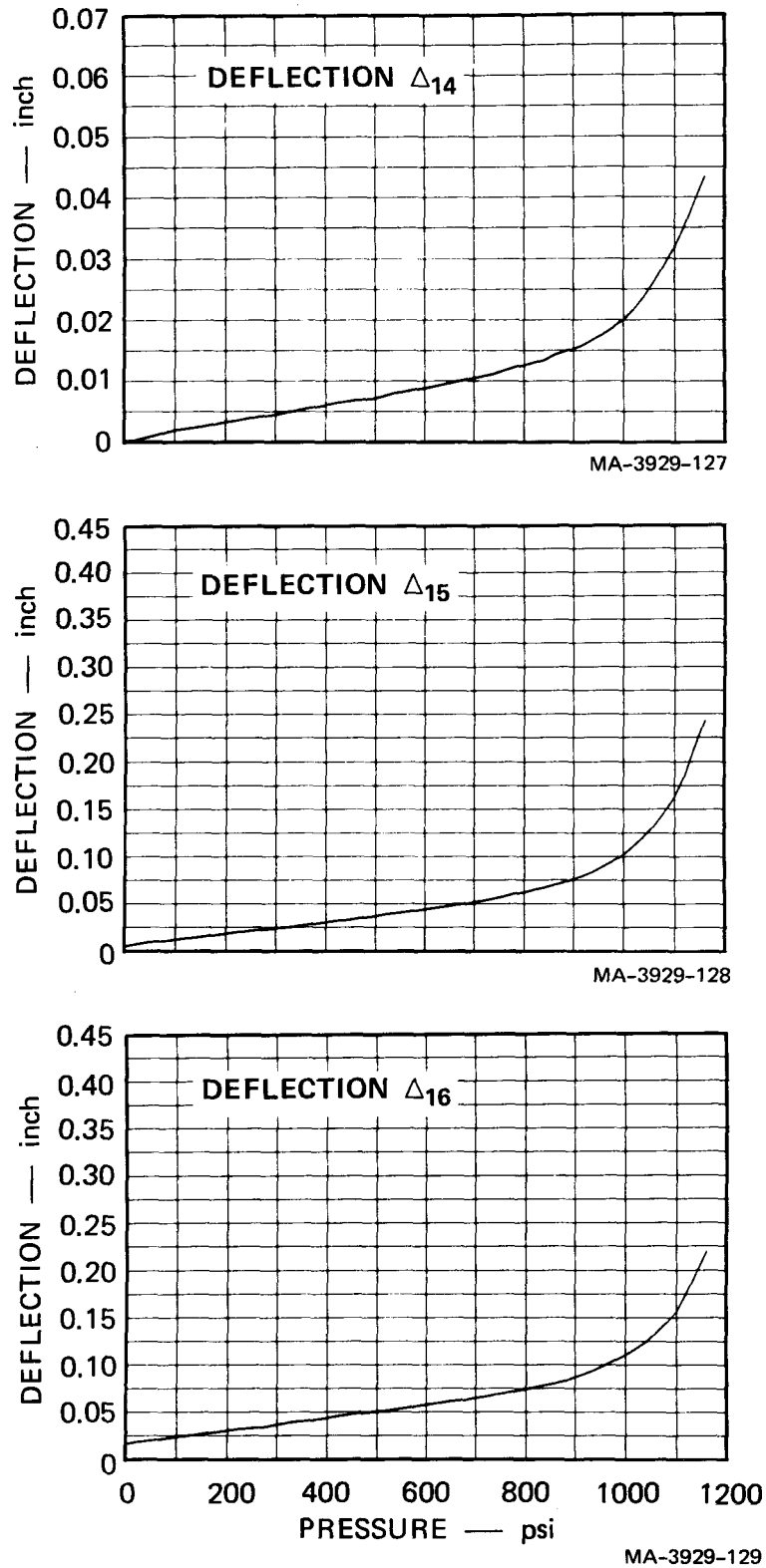

FIGURE A.16 DEFLECTION VERSUS PRESSURE Δ_{14}, Δ_{15}, Δ_{16}

Appendix B

MATERIAL PROPERTIES OF CRBR MODELS

A. Introduction

The reasons for performing stress-strain tests on samples of the material used to fabricate the 1/20-scale models of the CRBR were:

(1) To demonstrate that the materials in the models simulate the stress-strain properties of the prototypic materials at reactor operating temperatures.

(2) To provide reliable material property data that could be used in pre- and posttest analysis.

In the scale models, 533-B carbon steel simulates the 508 carbon steel cover material, and Ni 200 simulates the 304 stainless steel vessel wall, core barrel, and core support platform materials.

This appendix describes the stress-strain tests, which were performed at both low and high strain rates. Low strain rate tests were performed as part of a quality assurance program to ensure that proper materials were being used and that proper annealing procedures were being followed on completed models. High strain rate tests were performed to provide more accurate data for use in computer analysis of the models and to assess the strain rate sensitivity of the materials.

B. Material Properties of Ni 200

1. Low Strain Rate Test Procedures

Low strain rate tests for Ni 200 were performed on specimens cut from the sheet stock used to fabricate the vessel walls and core barrels of the model and from billets of the material used to fabricate the core support platforms of SM 4 and SM 5. Sufficient specimens were prepared to allow for initial preassembly stress-strain tests and for archive specimens. Each batch of specimens went through the heat treating

cycle with the corresponding models to ensure that the tensile specimens and the models experienced the same heat treatment. Figure B.1 shows a schematic drawing of a tensile specimen. Low strain rate tests were performed on an Instron testing machine. Crosshead speed was 0.05 in./min and resulted in a nominal strain rate of 0.83×10^{-3} sec^{-1}.

2. Low Strain Rate Properties of Ni 200

Figure B.2 shows pre- and posttest stress-strain curves for the Ni 200 used to fabricate various components of the models. Reasonably good agreement between pre- and posttest stress-strain properties were noted for the vessel and core barrel materials. The higher strength of the posttest core support platform material is unexplained except that Ni 200 is known for its inconsistent properties from batch to batch. For this reason pre- and posttest stress-strain tests must be performed to ensure reliable material property data for structural response analysis.

3. High Strain Rate Properties of Ni 200

High strain rate tests were performed by Terra Tek, Incorporated,* on samples of Ni 200 cut from the sheets and billets used to fabricate the vessel walls, core barrels, and core support platforms of the CRBR models. The test procedure employed by Terra Tek provided a strain rate of about 100 sec^{-1}. For comparison, peak strain rates measured on the vessel wall of the 1/20-scale models was about 50 sec^{-1}. Results of the high strain rate tests are therefore more appropriate for use in computer analysis of the models.

Figure B.3 shows comparative stress-strain curves for the vessel walls, core barrels, and core support platforms of the CRBR models. The Ni 200 stress-strain properties at high strain rate (solid line) agree very well with the 304 stainless steel properties at $1000^{o}F$ (line with dots). Even the quasi-static Ni 200 stress-strain curves (dashed line) agree fairly well with the high strain rate curves.

---

*Salt Lake City, Utah

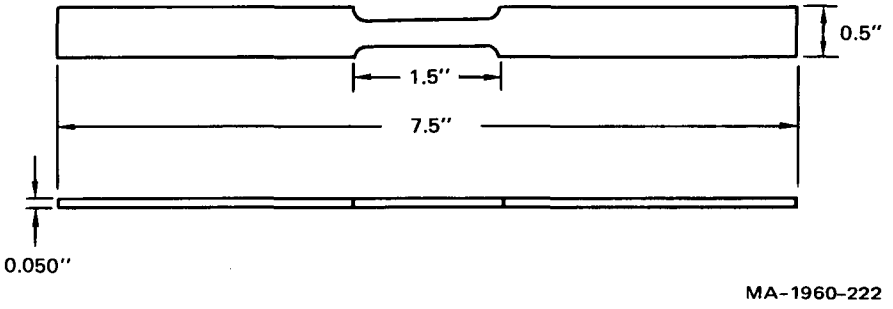

FIGURE B.1 TENSILE SPECIMEN FOR Ni 200 STRESS-STRAIN TEST

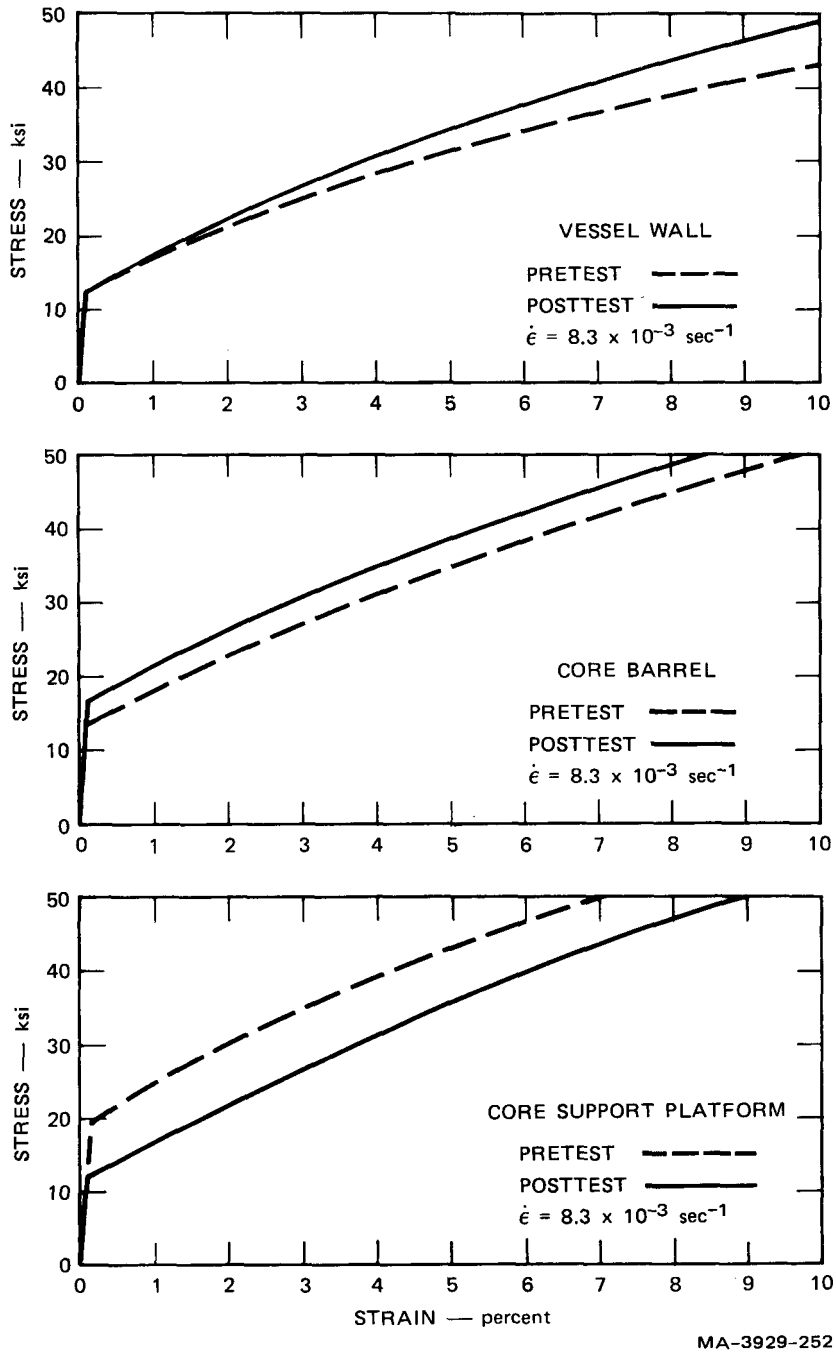

FIGURE B.2 LOW STRAIN RATE MATERIAL PROPERTIES OF Ni 200

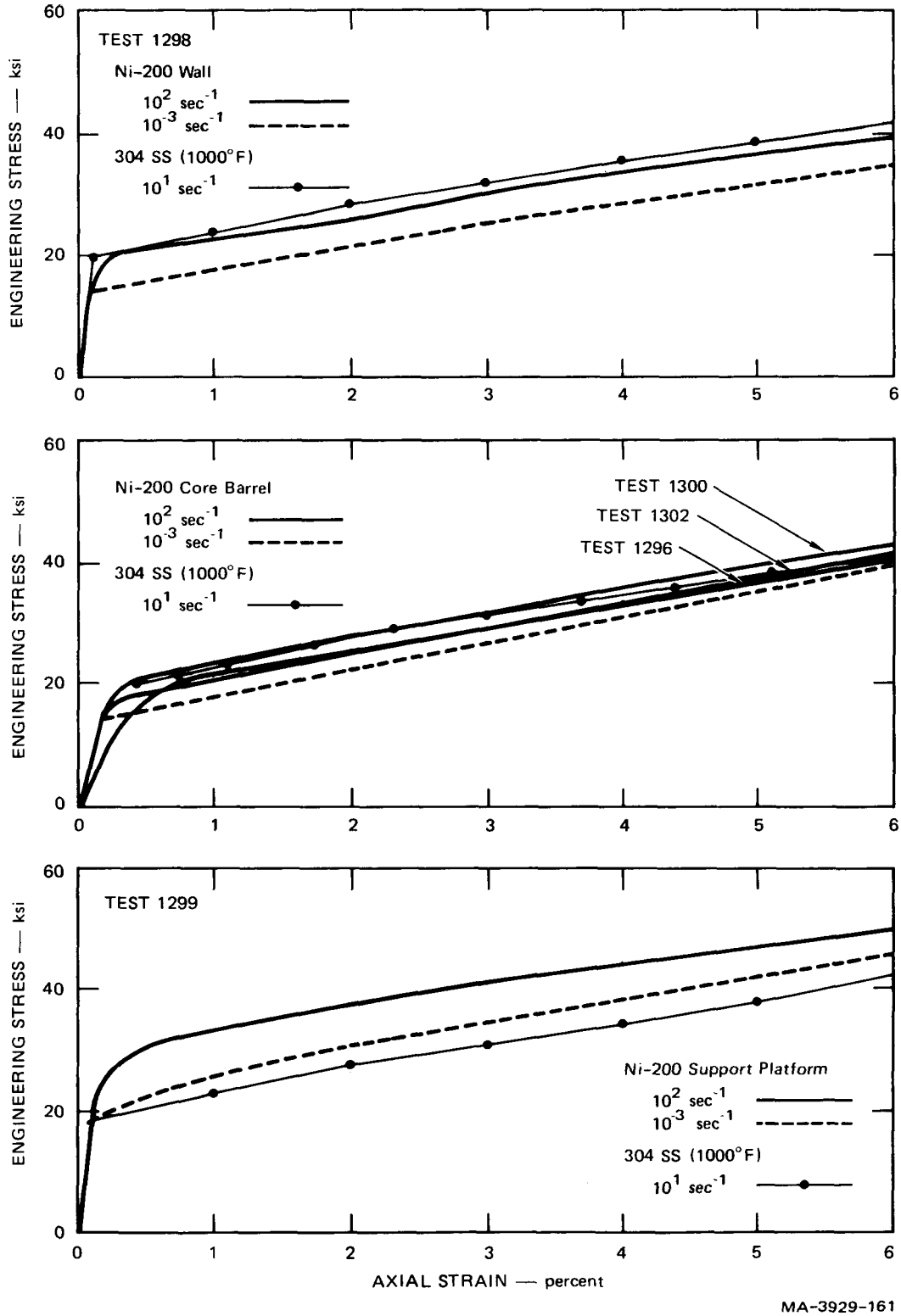

FIGURE B.3 STRESS-STRAIN PROPERTIES OF Ni 200 AND 304 STAINLESS STEEL

C. Material Properties of 533-B Carbon Steel

Low and high strain rate tests were performed on 533-B carbon steel, the material used to fabricate the heads of the CRBR models. Terra Tek, Incorporated, performed these tests. Figure B.4 shows the low strain rate ($\dot{\varepsilon}$ = 0.5 sec^{-1}) stress-strain curves for 533-B carbon steel. Figure B.5 demonstrates the strain rate insensitivity of 533-B carbon steel up to a strain rate of 100 sec^{-1}. Since the maximum strain rates predicted in the experiments (Ref. 10) are about 50 sec^{-1}, stress-strain rate effects are negligible in the experiments.

D. Material Properties of UIS Column Material

Figure B.6 shows low strain rate stress-strain curves for the Ni 200 material used for the UIS columns of SM 3 and SM 5. These curves are based on tests where the strain rate is about 0.8 x 10^{-3} sec^{-1}. The columns of SM 3 were annealed for 60 min at 1300^{o}F, while the columns of SM 5 were annealed for 30 min at 1300^{o}F as prescribed. The stress-strain curve for SM 5 columns lies uniformly above the stress-strain curve for SM 3 columns by about 21 kpsi. Even though the columns for SM 3 were not annealed to specification, the stress-strain properties for these columns is closer to the properties of the prototypic column material.

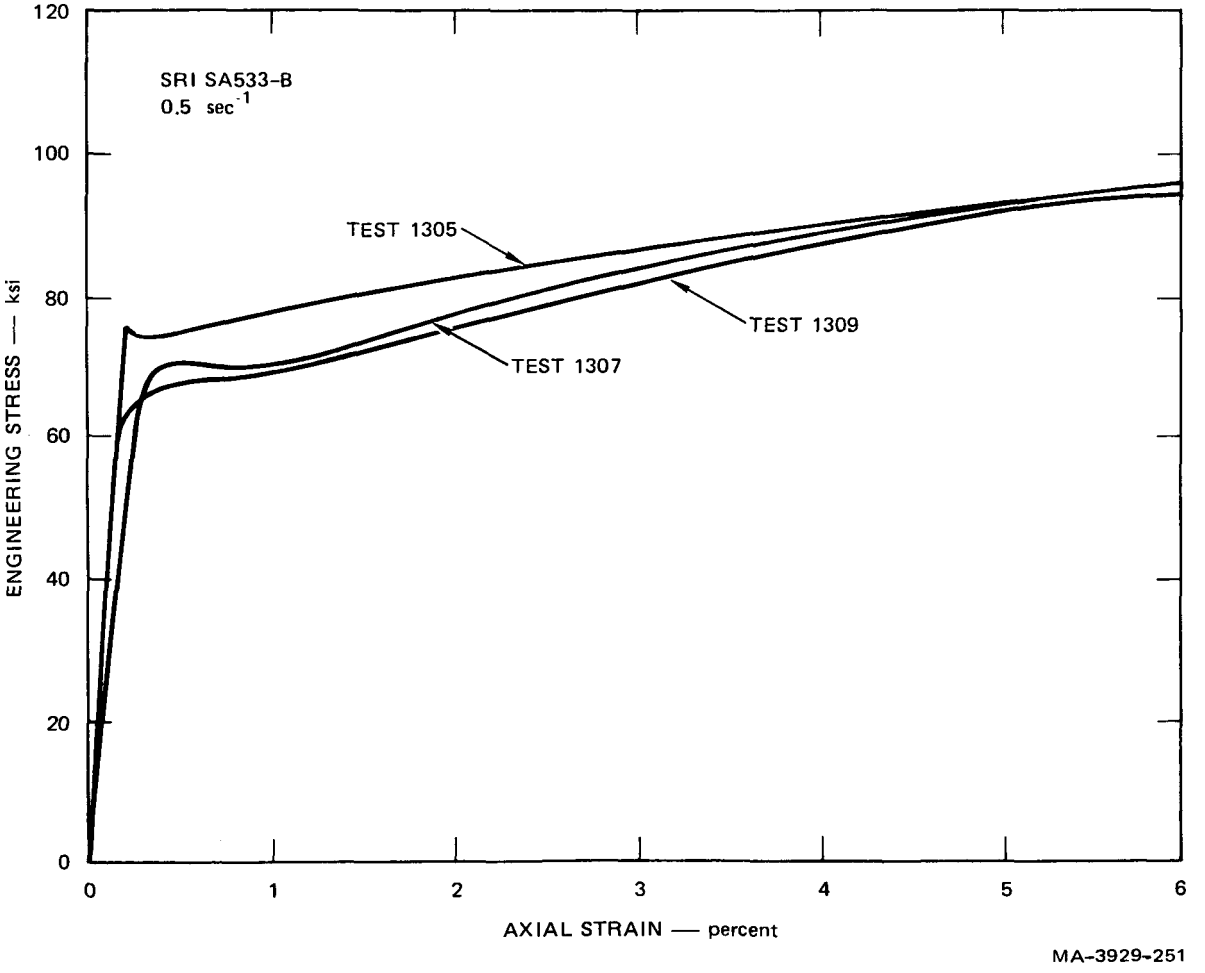

FIGURE B.4 STRESS-STRAIN CURVES FOR 533-B CLASS 1 CARBON STEEL

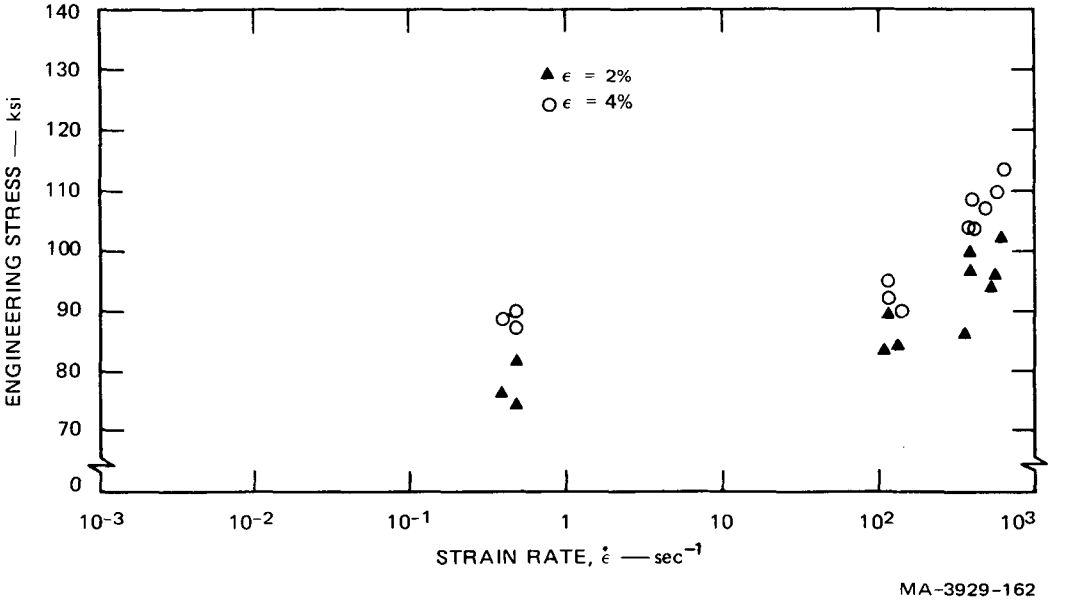

FIGURE B.5 STRAIN RATE EFFECTS IN 533-B CLASS 1 CARBON STEEL

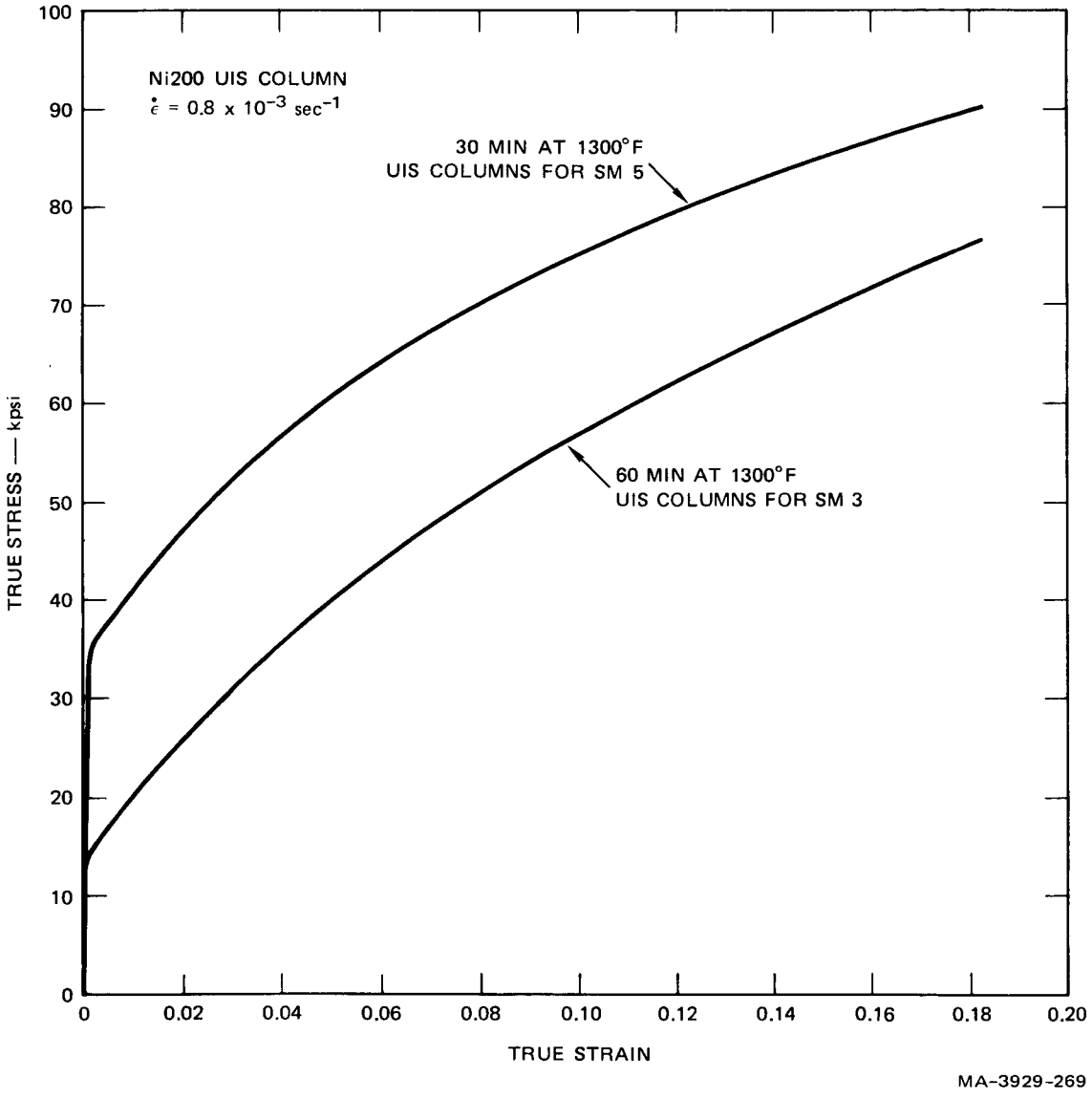

FIGURE B.6 LOW STRAIN RATE PROPERTIES FOR Ni 200 UIS COLUMN MATERIAL

Appendix C

ENERGY SOURCE CALIBRATION

A. Calibration Experiments

Twenty calibration experiments were performed in the apparatus shown in Figure C.1. The apparatus consists of a rigid core barrel, a thick-walled steel cylinder, and a thick core support plate, all carefully designed to simulate a rigid 1/20-scale model of the CRBR primary containment vessel (12.15-in. ID). The low-density 90/10 PETN-microsphere explosive used to simulate the 661 MW-sec HCDA is placed in a steel canister that suppresses shock waves from the explosive. The canister is bolted into the core structure and a Mylar diaphragm is bonded inside the core barrel at a prescribed location to provide a known initial volume for the detonation products. The 90/10 explosive was tested over a range of charge masses and initial volumes to determine the appropriate source to simulate the SMBDB. Table C.1 lists the twenty experiments.

B. Instrumentation

1. Pressure Transducers

Four pressure transducers were used to measure pressures in the core. The transducers were piezoelectric pressure gages (PCB Model 113A03/61) with a natural frequency of 450 kHz and a rise time of 1 μsec. Two transducers were mounted in the center portion of the core barrel to measure the source pressure, and two were mounted in the core barrel above the Mylar diaphragm to measure the water pressure in the core before the detonation products expanded out of the core barrel. This gage also recorded the approximate pressure that would act on the upper internal structure.

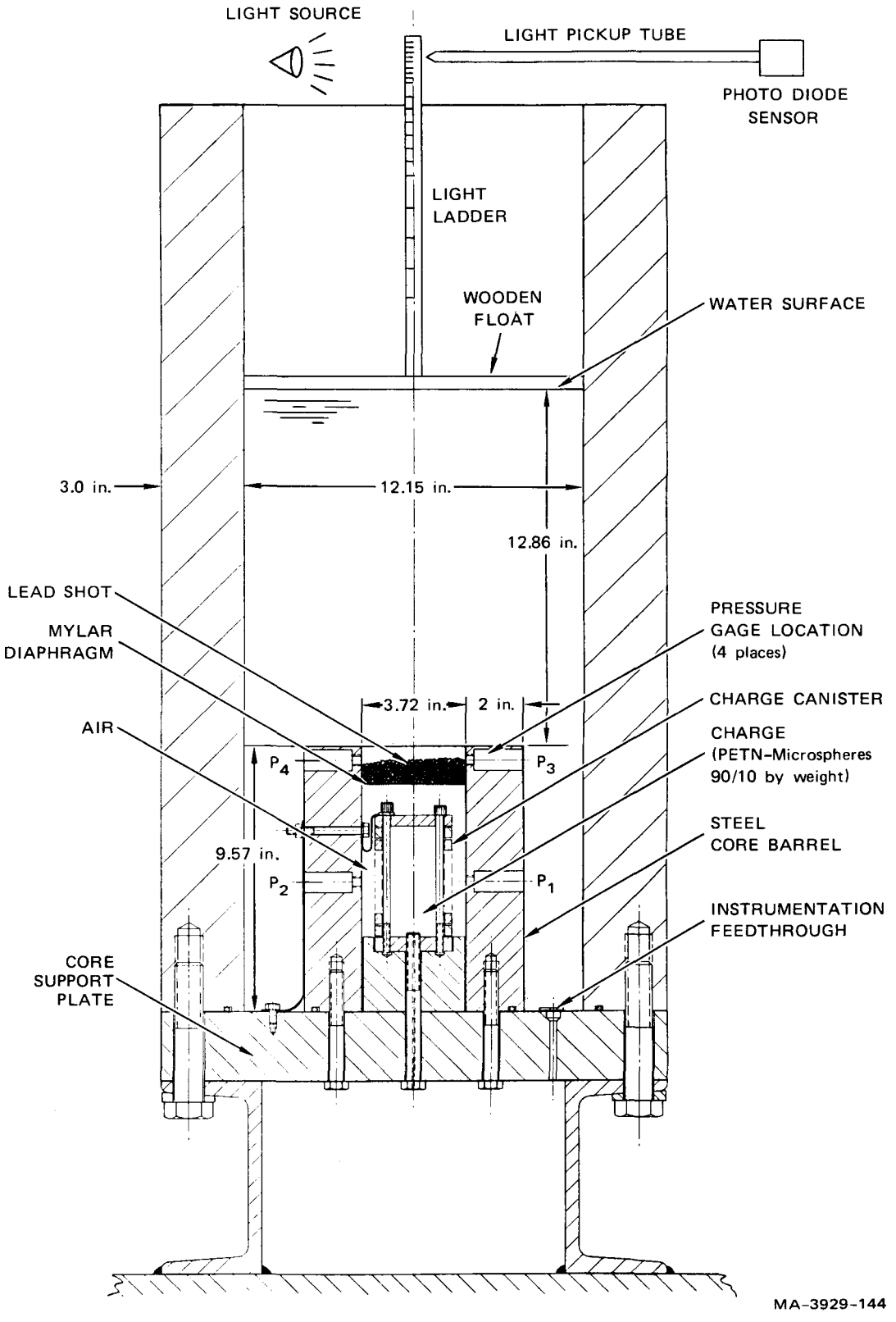

FIGURE C.1 SCHEMATIC OF CALIBRATION TEST APPARATUS

Table C.1

SUMMARY OF CALIBRATION EXPERIMENTS

Test No.	Charge[a] Mass (g)	Initial Volume (cm^3)	Peak Pressure (bars)	Gas Work at Cover Gas Volume (kW-sec)
CRBR-C-1[b]	--	--	--	--
CRBR-C-2	19.6	651	335	17.1
CRBR-C-3	19.6	651	--	--
CRBR-C-4	19.6	1028	--	--
CRBR-C-5	19.6	1028	360	17.1
CRBR-C-6	19.6	651	282	--
CRBR-C-7	19.6	854	296	10.5
CRBR-C-8	19.6	854	296	10.5
CRBR-C-9	19.6	651	327	13.2
CRBR-C-10	26.0	962	372	17.2
CRBR-C-11	26.0	962	375	18.0
CRBR-C-12	23.0	776	375	15.2
CRBR-C-13	23.0	776	375	14.5
CRBR-C-14	20.7	962	282	17.1
CRBR-C-15	20.7	962	275	16.5
CRBR-C-16	20.7	962	305	16.5
CRBR-C-17	19.7	962	265	12.8
CRBR-C-18	19.7	962	260	12.9
CRBR-C-19	19.7	962	265	14.0
CRBR-C-20	19.7	962	260	13.2

[a] PETN-microspheres (90/10 by weight)

[b] Noise check

2. Light Ladder Apparatus

The light ladder apparatus was used to measure slug displacement. The apparatus consists of a split, hollow aluminum tube (the ladder) attached to a 1/2 in.-thick, 12-in.-dia wooden float. Thin (0.010 in.) slits are precisely cut into the metal tube, and a light source behind the light ladder illuminites the slits. A Lucite light-guide tube connected to a LED photodiode is positioned near the light ladder so that it can distinguish the light from one slit it a time. As the ladder moves, successive slits pass the Lucite tube. The alternate light and dark intervals produce distinct voltage peaks when sensed by the LED photodiode. Knowing the distances between slits ind the time interval between voltage peaks, we can calculate a displacement-time history of slug motion. For these experiments, the slit spacings were: 11 slits on 0.050-in. centers, followed by 10 slits on 0.1-in. centers, followed by 15 slits on 0.2 in. centers, followed by 12 slits on 0.5 in. centers. The light pipe (Lucite tube) is centered initiilly on the first slit by adjusting it to produce maximum photodiode voltage. During early motion, the first 20 closely spaced slits give high displacement-time resolution. It is possible to follow a total of 10.5 in. of motion with this slit arrangement.

3. Recording System

Data from each experiment were recorded on oscilloscopes and on high-speed magnetic tape. The oscilloscopes were Tektronix 543B models with a frequency response of 33 MHz. The tape records were made on two Bell and Howell 3700B tape recorders, which record at 120 in./sec and are set up for an 80-kHz frequency response. A visual record of the data wis made from the magnetic tape record by playing the tapes back through a recording oscillograph (Visicorder Model 5-124), which reproduces the tape recorder signals on light-sensitive paper.

C. Data Analysis

The data analysis technique combines the core pressure data with the gas volume change to obtain pressure-volume change relationships for the energy source.

The gas volume change at any time is the sum of the volume displaced by the water surface, the increase in volume of the vessel, and the compression of the water. The volume displaced by the water surface is determined from the light ladder data, whereas the increase in volume of the vessel is negligible because of its relatively thick walls.

The contribution of the compression of the water is calculated by using a two-stage analytical model. In Stage 1, the fluid motion is described by a conical wave emanating from the core upward to the free surface. Approximating the motion of this conical mass of fluid by the spherical flow of an infinite compressible fluid caused by an expanding spherical gas bubble, the gas-water interface displacement is

$$y(t) = \frac{1}{\rho c} \int_0^t p(\tau)\, d\tau + \frac{1}{\rho a} \int_0^t I(\tau) d\tau$$

where $y(t)$ = interface radial displacement

ρ = density of fluid

$p(\tau)$ = pressure history in core

c = sound speed in fluid

a = bubble radius

I = impulse at the interface; $I(\tau) = \int_0^t p(\tau)\, d\tau$

An approximation to the volume change due to compression is therefore

$$\Delta V_c = Ay$$

where A is the cross-sectional area of the core.

The expansion of the bubble is terminated in this analytical model at a time t_1, the time required for a wave in the water to travel from the source to the surface and back to the source.

Stage 2 commences at a time t_2 greater than t_1. Time t_2 is the time at which pressure at the vessel wall just above the core becomes

approximately equal to the core pressure. Time t_2 is estimated for these experiments based on previous experiments of this type. These two pressures stay equal so that for $t > t_2$, a quasi-static analytical model suggests itself in which the pressure outside the core and the pressure below the core top behave similarly. Above the core top, the pressure distribution is approximated by a linear drop to atmospheric pressure at the free surface. With this linear pressure distribution, the gas volume increase due to compressibility is $\Delta V_c = P/K$, where P is the average pressure in the fluid above the core and K is the fluid bulk modulus. During the transition time from t_1 to t_2, ΔV_c is approximated by a linear relationship. For the 1/20-scale models tested here, it was assumed that $t_1 = t_2$ so no linear interpolation was required.

Figure C.2 shows a schematic description of the technique for obtaining the pressure-volume change relationship. Figure C.2(a) shows the pressure-time history in the core. Figure C.2(b) shows the gas volume increase-time history. Note the two components of gas volume increase: ΔV_c, the volume due to compressibility, and ΔV_s is, the volume increase due to upward slug motion (ΔV_v = vessel volume increase = 0).

The two records, Figure C.2(a) and C.2(b), are combined to obtain Figure C.2(c), the desired pressure-volume change relationship.

D. Experimental Reproducibility

Figure C.3 compares the pressure-time and water surface-time history for the four final calibration experiments. The pressure-time histories in Figure C.3(a) are each the average of the two pressure records in the core. The records are reproducible to $\pm$5% at high pressure and $\pm$50% at low pressures. The water surface-time histories in Figure C.3(b) are very reproducible, about $\pm$2% throughout the record.

To obtain the average pressure-volume change curve described in the next section, these pressure and water surface records were averaged to obtain single pressure- and water surface-time histories. The average gas work-volume change curve was obtained by integrating the average pressure-volume change curve.

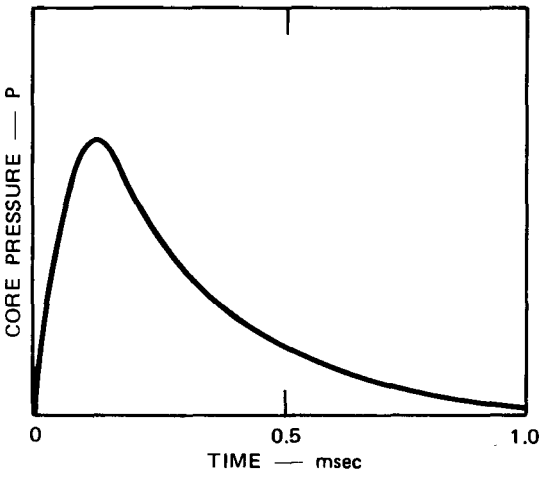

(a) PRESSURE-TIME HISTORY IN THE CORE

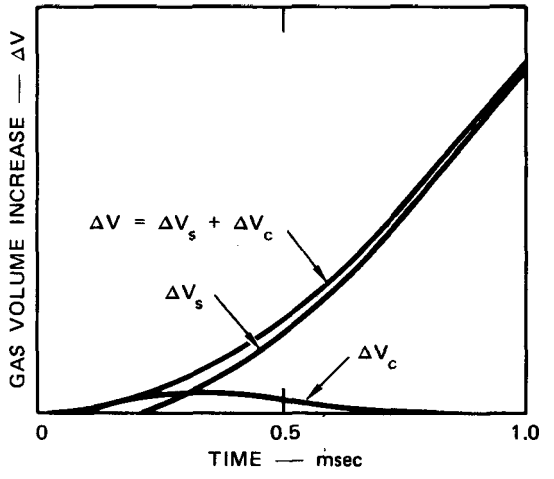

(b) GAS VOLUME INCREASE-TIME HISTORY

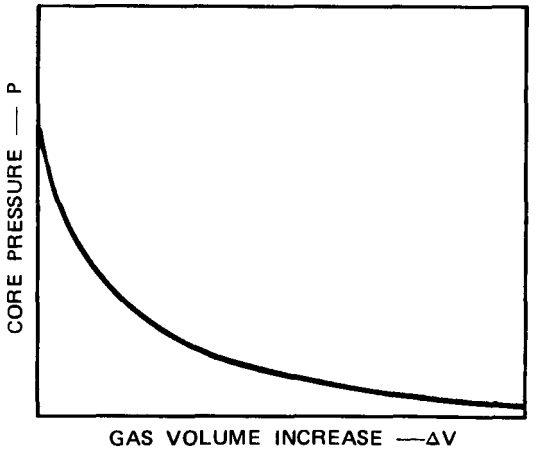

(c) PRESSURE-VOLUME CHANGE

MA-1960-243

FIGURE C.2 PRESSURE-VOLUME CHANGE RELATIONSHIP FROM PRESSURE AND DISPLACEMENT HISTORIES

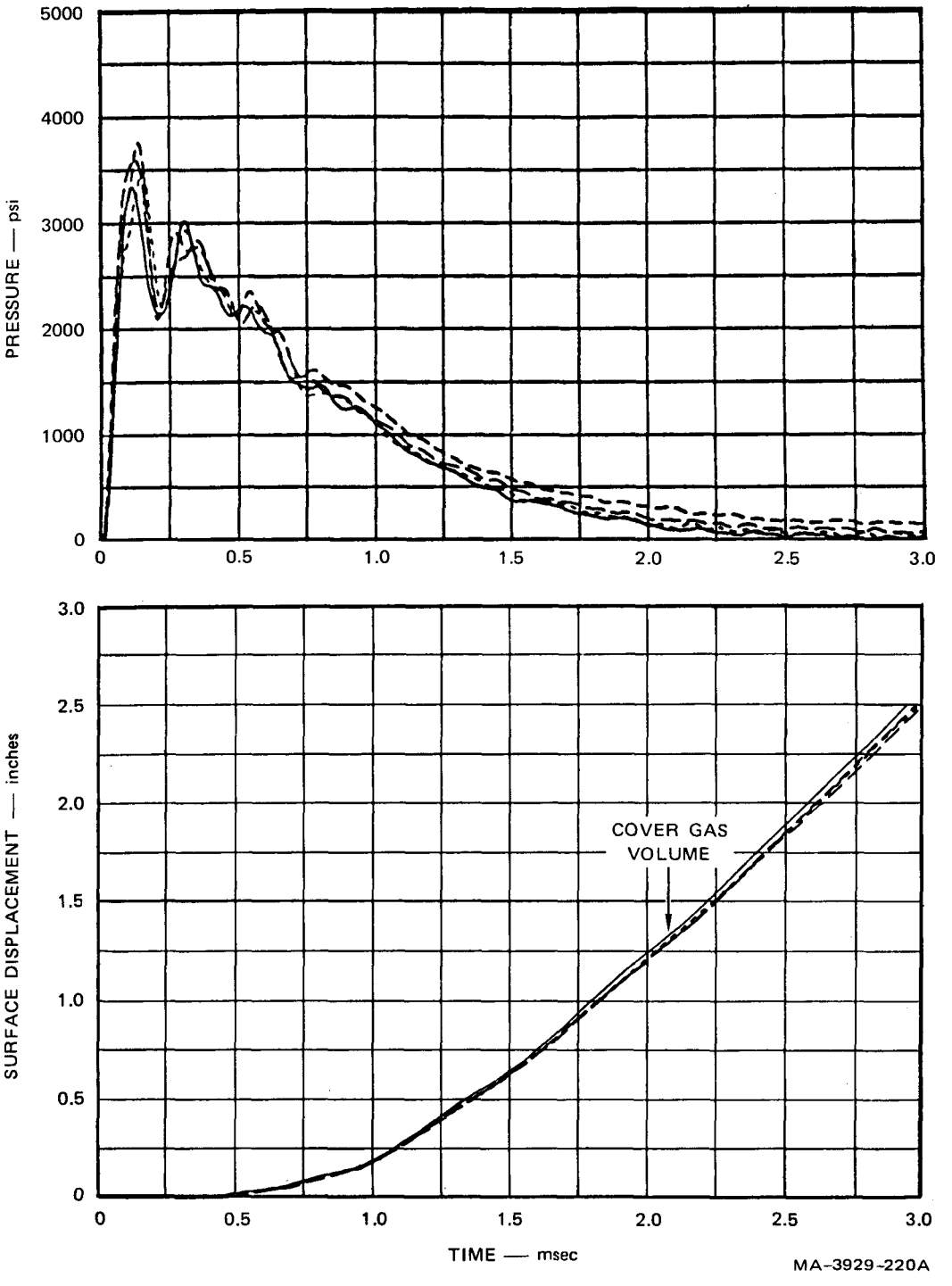

FIGURE C.3 REPRODUCIBILITY OF CALIBRATION TEST DATA

E. Pressure-Volume Change and Gas Work-Volume Change Relationships

Figure C.4 shows the pressure-volume change and gas work-volume change relationships obtained by averaging the final four calibration tests. Also shown is the pressure-volume change and gas work-volume change curve of the SMBDB (dashed line). The shaded band on the experimental results represents the spread in the experimental data. At low volume change (high pressure), the spread is very small. At cover gas volume, the spread is about $\pm$25% for pressure and about $\pm$5% for gas work.

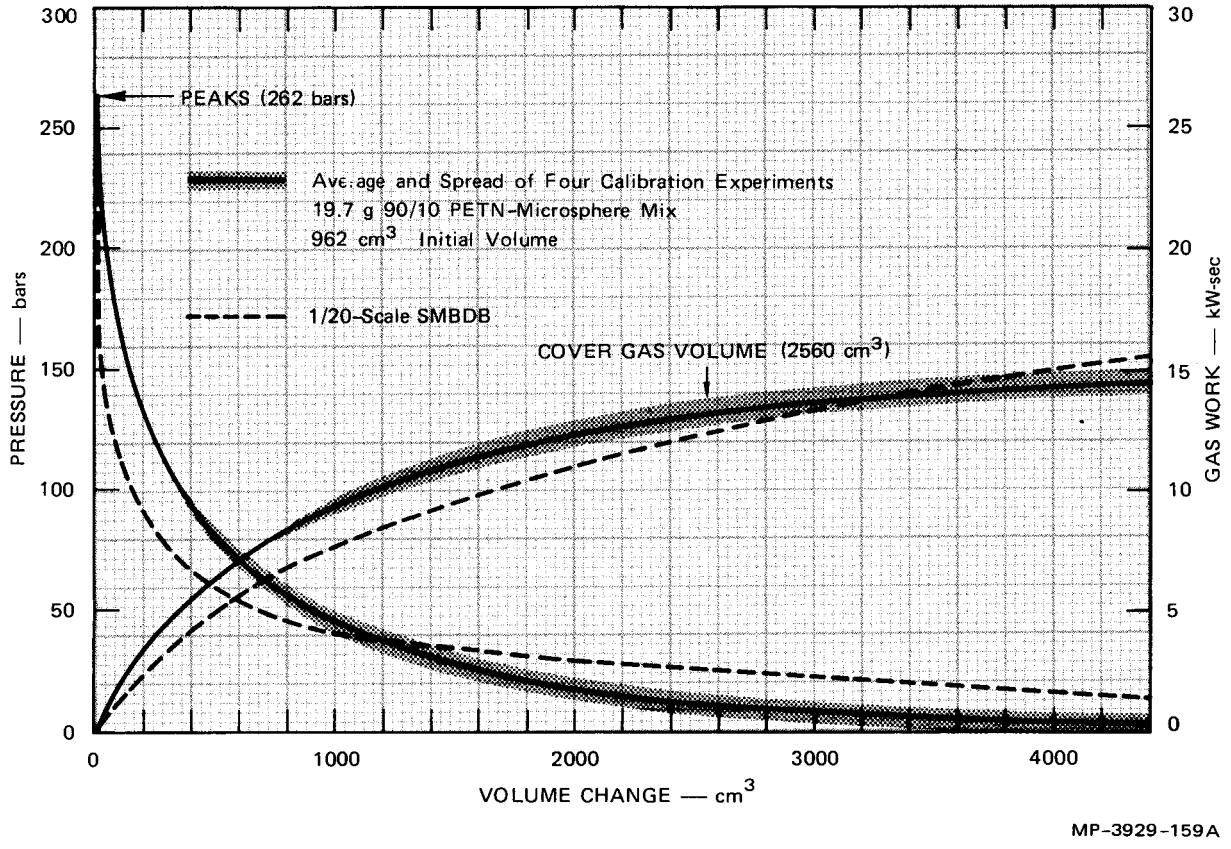

FIGURE C.4 PRESSURE-VOLUME CHANGE AND GAS WORK VOLUME CHANGE RELATIONSHIPS FOR EXPLOSIVE ENERGY SOURCE AND SMBDB LOADING

Appendix D

EXPERIMENTAL DATA

This appendix presents detailed experimental data for each of the dynamic CRBR experiments. The data sections for each experiment are organized as follows: First, a schematic drawing of the model for each experiment is shown. The schematic shows important dimensions, gage locations, and materials for the model. The second figure in each data section is a comprehensive, detailed foldout drawing of the model, including the precise dimensions of the model and such details as head mass, gage mounting designs, precise location of gages, and the mass and construction details of the core structure. The third to fifth figures give complete sets of pressure, strain, and acceleration records for each experiment. The records have been digitally filtered* and cover 10 msec of the model response (9 msec on SM 5). The schematic drawing of the model in the upper left corner of each figure shows the gage layout for the records presented in that figure. These records are followed by a figure showing the water surface history of the slug. The data from each water surface gage are plotted for 4 msec, which includes slug impact time. The impact velocity is also listed in this figure. The seventh figure in each set shows the final deformed shape profile for each model. The figure shows the average of six profiles made around the circumference of each vessel, thermal liner, and core barrel. The spread in the data is shown. For comparison, the long-time permanent strain measured by the strain gages is plotted at appropriate points along the profile. Peak deformed shape strains are also pointed out in this figure. Tables listing the vessel deformations are also given.

---

*See Table E.3 in Appendix E for filter cutoff frequencies.

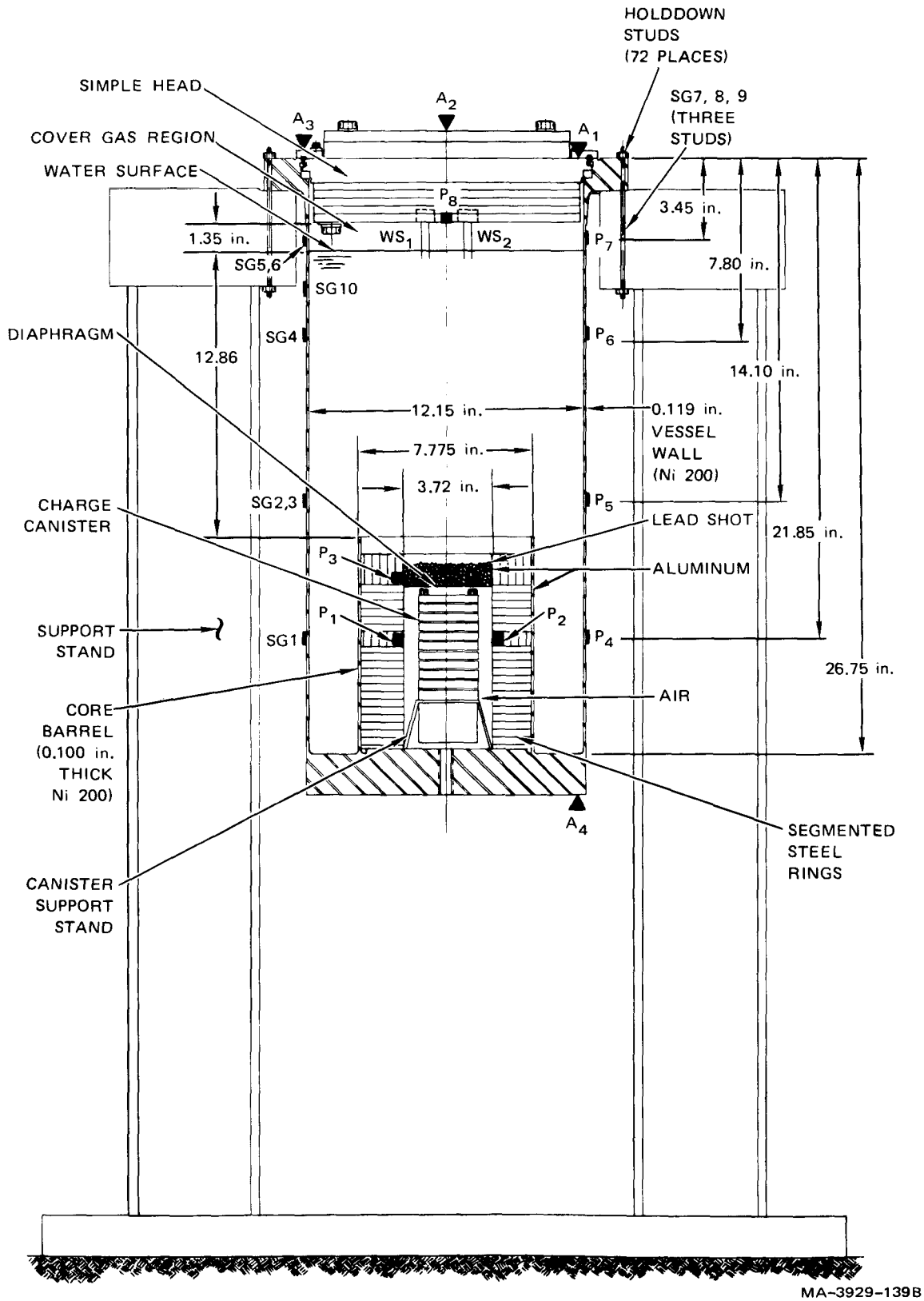

FIGURE D.1 SM 2 WITH INSTRUMENTATION

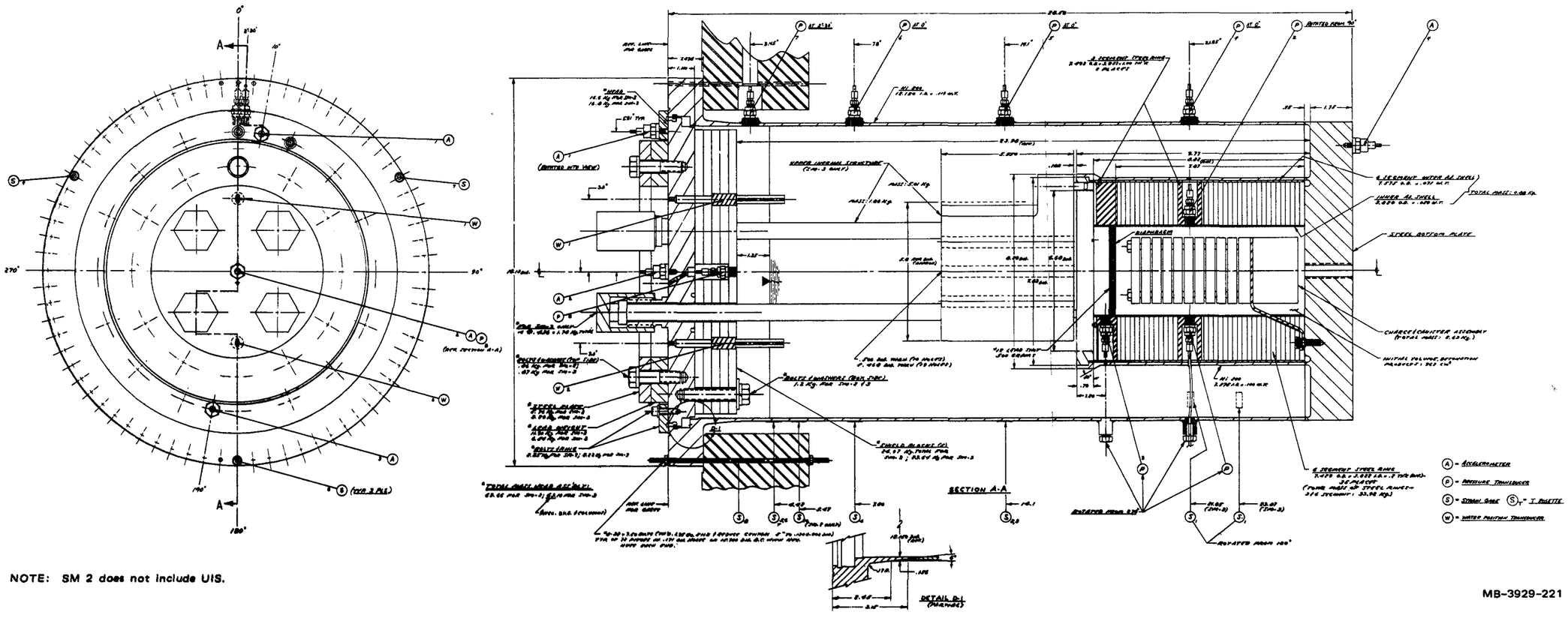

NOTE: SM 2 does not include UIS.

MB-3929-221

FIGURE D.2 DETAILED CROSS SECTION OF SM 2

Blank Page

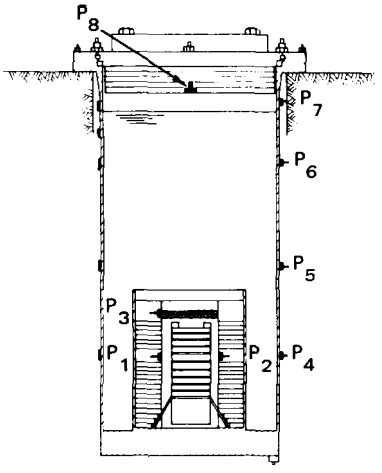

SM 2

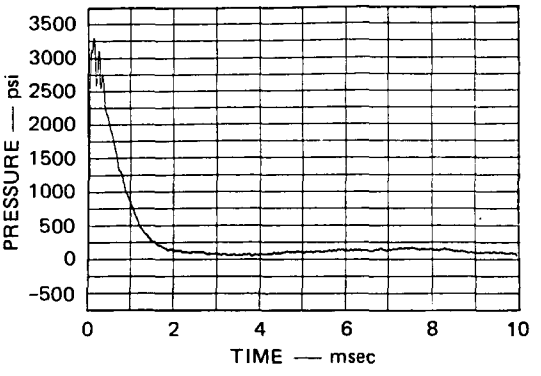

P_1 CORE

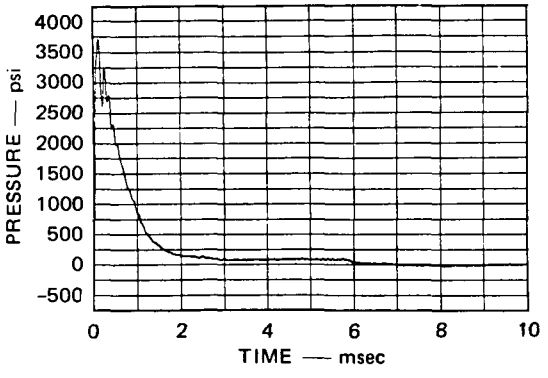

P_2 CORE

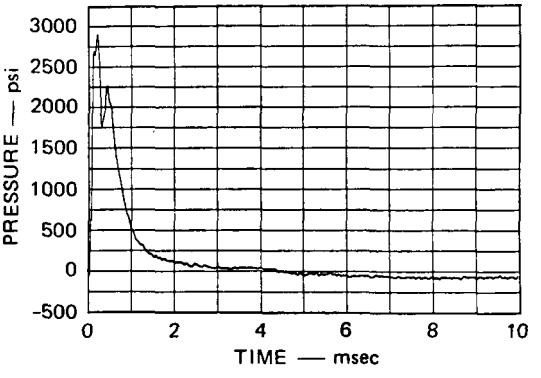

P_3 UPPER CORE

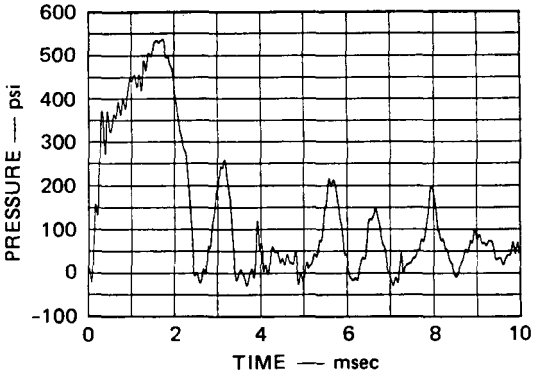

P_4 VESSEL WALL AT CORE

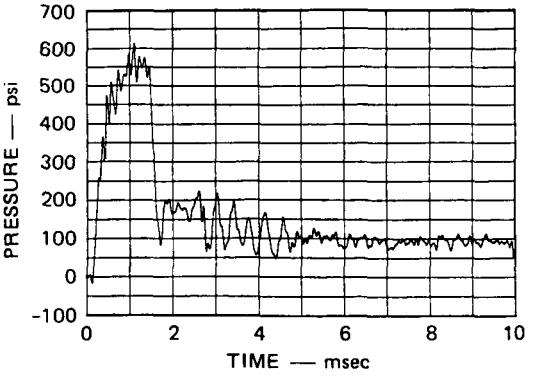

P_5 SODIUM OUTLET NOZZLE

MA-3929-222

FIGURE D.3 PRESSURE RECORDS FOR SM 2

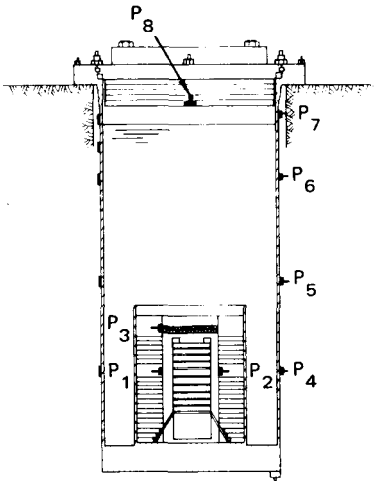

SM 2

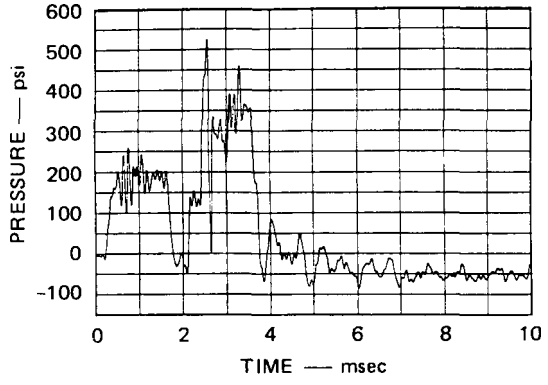

P_6 VESSEL WALL

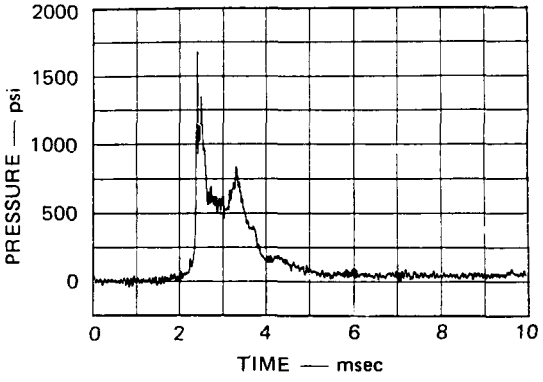

P_7 UPPER VESSEL WALL

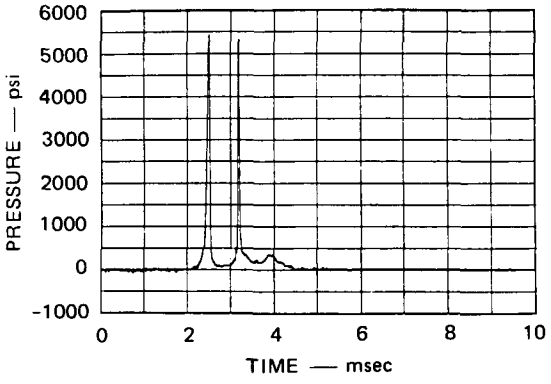

P_8 HEAD

MA-3929-223

FIGURE D.3 PRESSURE RECORDS FOR SM 2 (Concluded)

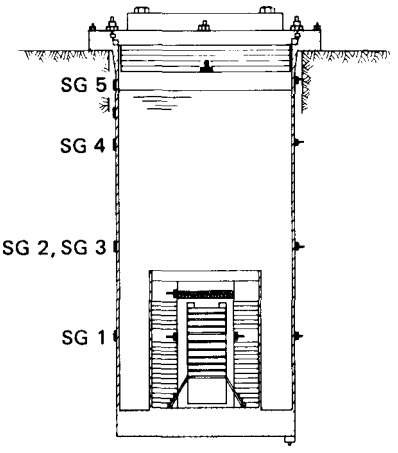

SM 2

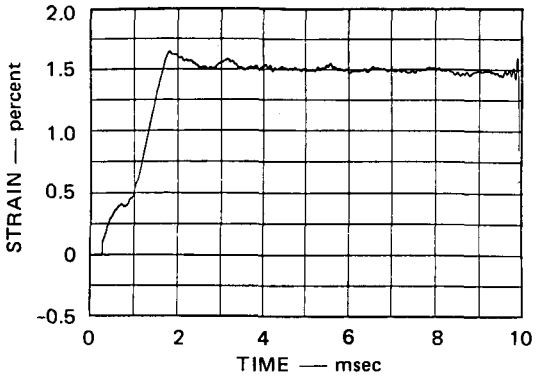

SG 1 VESSEL WALL AT CORE BARREL (C)

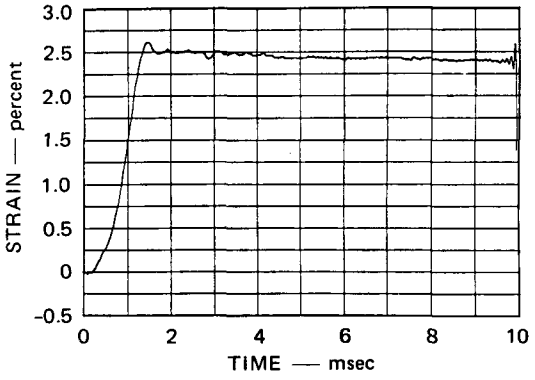

SG 2 VESSEL WALL AT UIS (C) (SODIUM OUTLET NOZZLE)

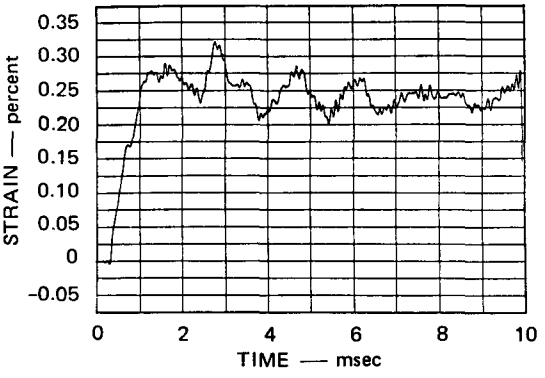

SG 3 VESSEL WALL AT UIS (A)

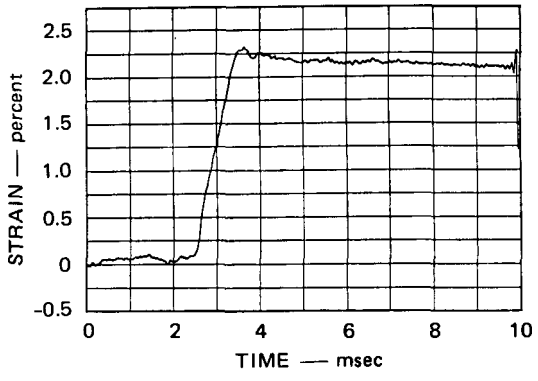

SG 4 VESSEL WALL (C)

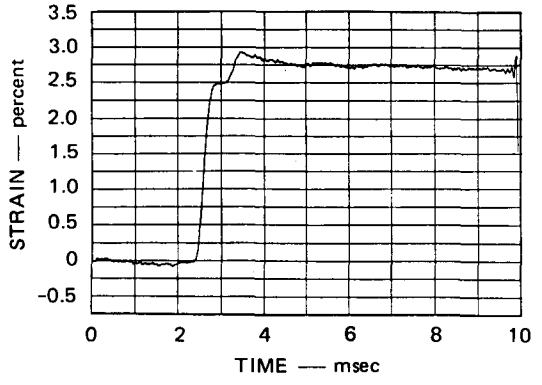

SG 5 UPPER VESSEL WALL (C)

MA-3929-224

FIGURE D.4 STRAIN RECORDS FOR SM 2

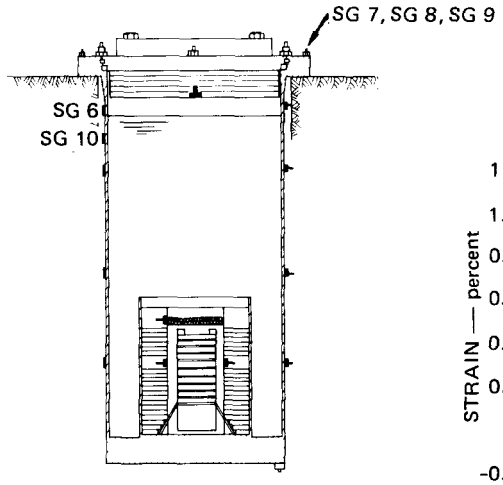

SM 2

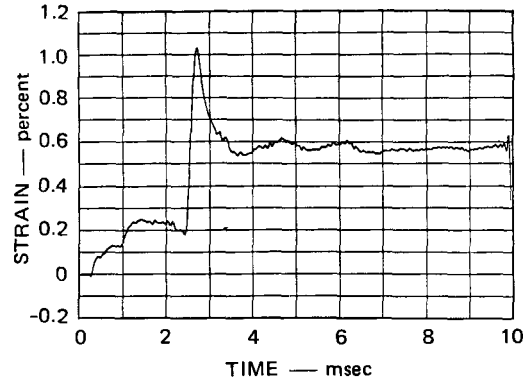

SG 6 UPPER VESSEL WALL (A)

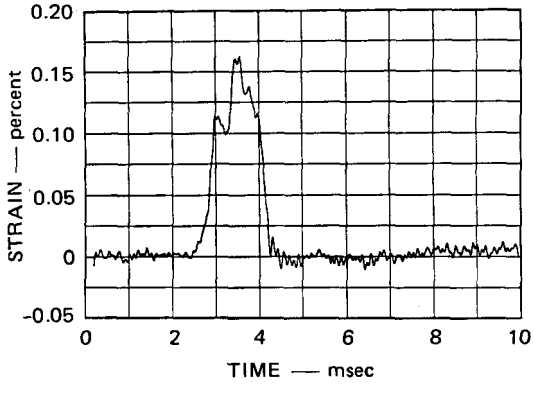

SG 7 STUD AT 60°

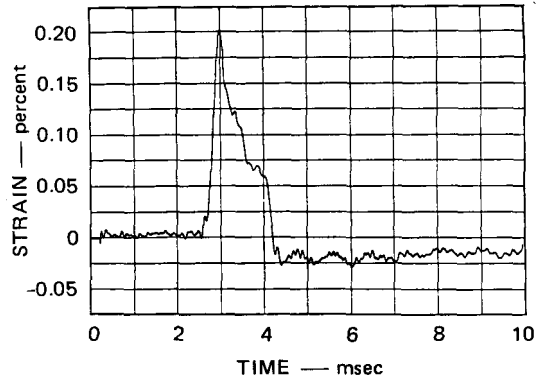

SG 8 STUD AT 180°

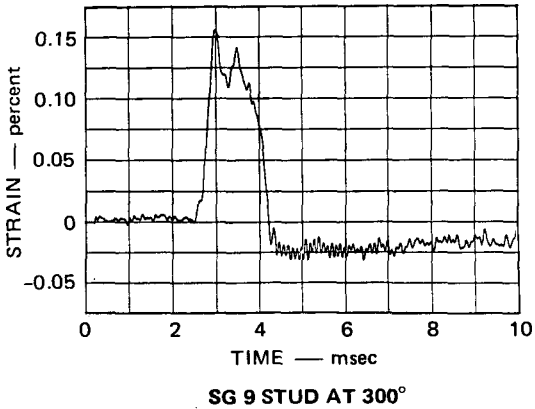

SG 9 STUD AT 300°

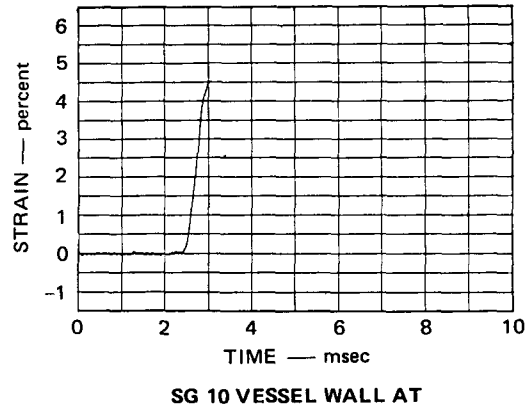

SG 10 VESSEL WALL AT PEAK DEFORMATION

MA-3929-225

FIGURE D.4 STRAIN RECORDS FOR SM 2 (Concluded)

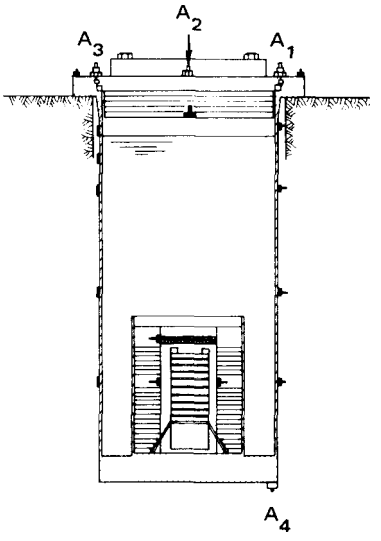

SM 2

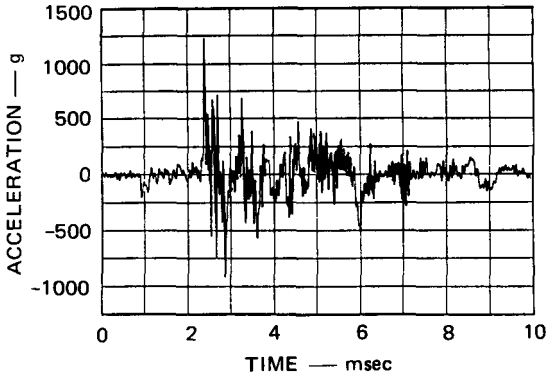

A_1 HEAD EDGE

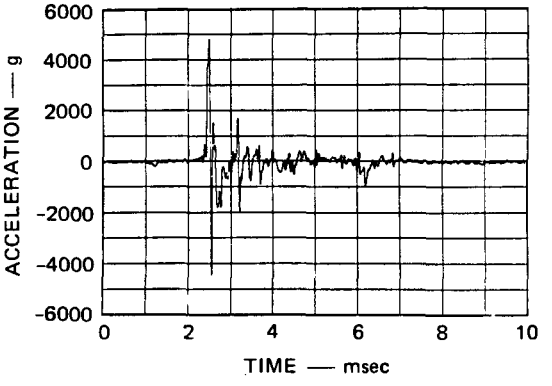

A_2 HEAD CENTER

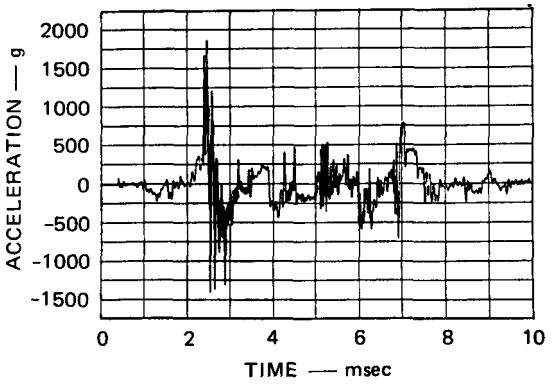

A_3 HEAD EDGE

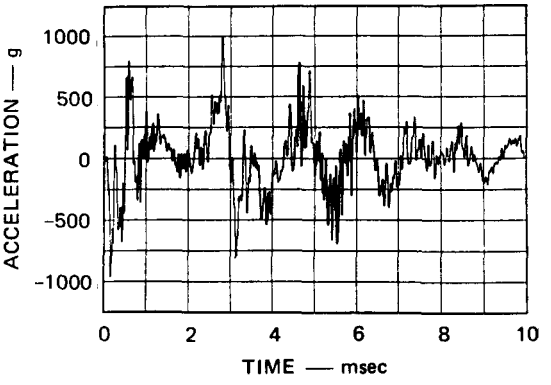

A_4 PLATFORM

MA-3929-226

FIGURE D.5 ACCELEROMETER RECORDS FOR SM 2

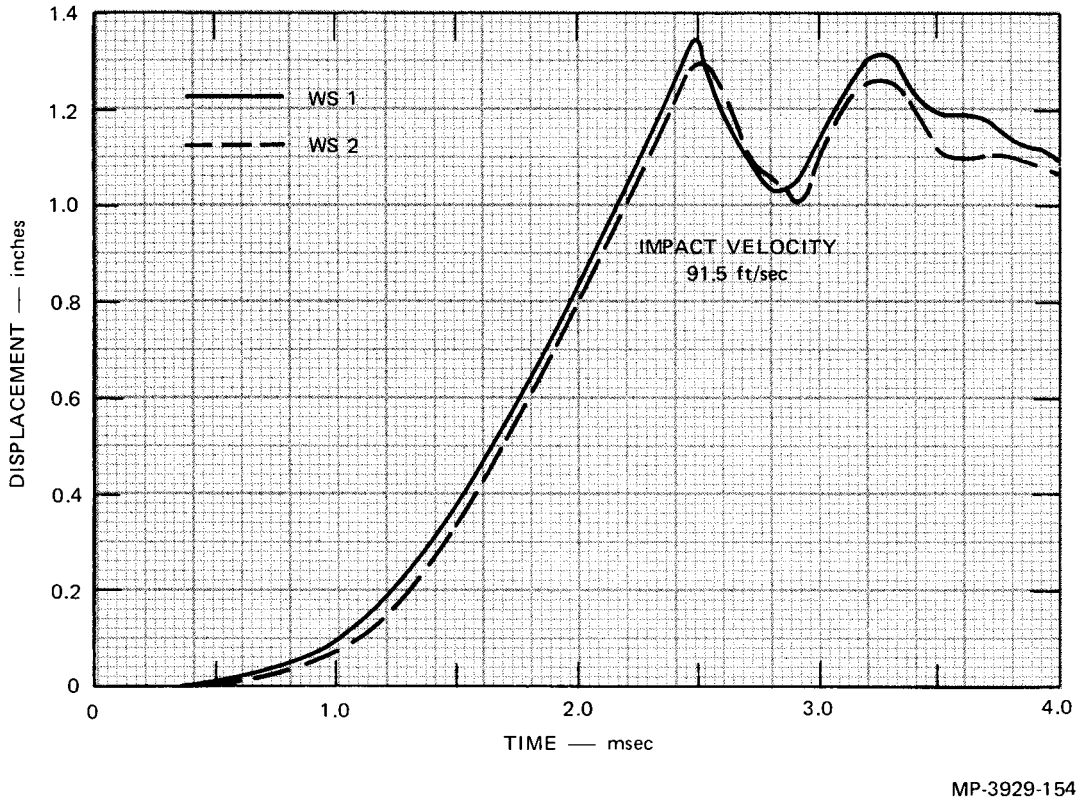

FIGURE D.6 WATER SURFACE DISPLACEMENT FOR SM 2

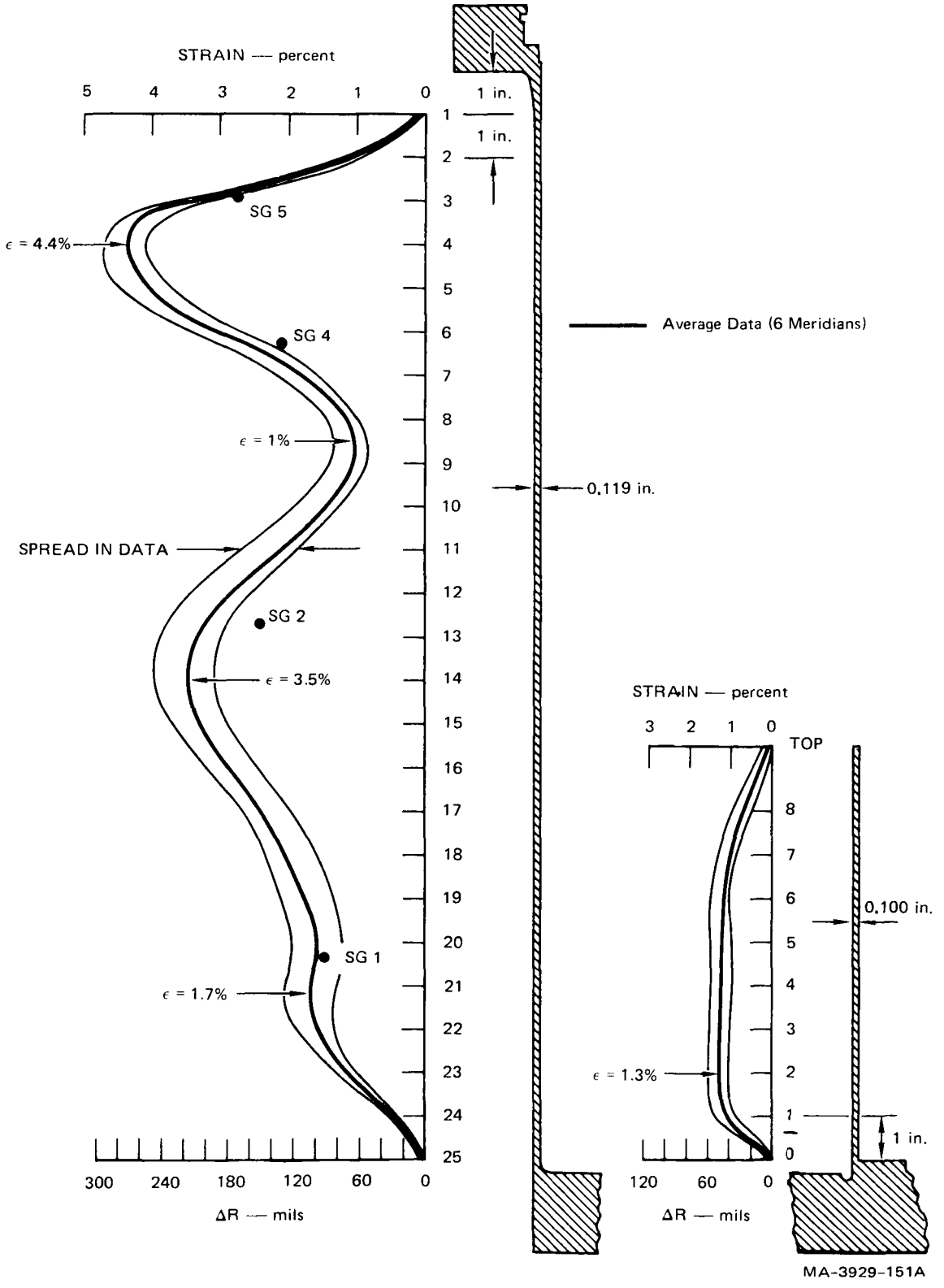

FIGURE D.7 DEFORMED SHAPE PROFILE: SM 2

Table D.1

RADIAL DISPLACEMENTS OF THE VESSEL WALL OF SM 2

Point[a]	Meridian 1	2	3	4	5	6	Average
1	3.5[b]	6.0	5.5	3.0	7.5	6.5	5.4
2	-	69.5	63.5	75.0	66.5	54.0	65.7
3	189.5	218.0	214.5	203.5	203.0	208.5	206.2
4	256.5	275.5	292.0	273.5	259.0	277.0	272.3
5	229.5	253.0	279.0	260.5	239.5	249.5	251.9
6	-	186.0	216.5	193.0	174.0	178.5	189.6
7	93.5	115.5	135.5	114.5	105.0	111.5	112.4
8	71.0	68.0	89.0	64.0	62.5	71.0	70.9
9	63.0	59.5	88.0	56.0	54.0	68.0	64.8
10	86.0	82.5	119.5	86.0	78.0	93.5	90.9
11	126.5	120.5	171.5	131.5	117.5	132.0	131.0
12	172.5	160.5	214.5	176.5	159.5	172.5	176.0
13	-	193.5	241.0	207.5	188.5	202.5	206.6
14	219.5	207.0	247.0	217.5	191.0	214.0	216.0
15	209.5	199.0	230.0	208.0	180.5	211.0	206.4
16	188.5	174.5	199.0	183.0	153.5	190.5	181.5
17	164.0	144.5	164.5	-	122.5	164.0	151.9
18	146.0	118.0	138.0	127.5	98.0	139.0	127.8
19	134.0	100.0	118.0	110.0	84.0	123.0	111.6
20	-	93.5	107.5	-	75.0	115.0	97.8
21	125.5	94.0	108.5	96.0	80.5	126.0	105.3
22	117.0	91.5	105.5	91.5	81.0	104.0	98.4
23	80.0	65.0	75.5	69.0	62.0	71.5	70.5
24	34.5	29.5	29.0	34.5	26.0	31.5	30.9
25	2.5	1.5	2.5	4.5	2.0	4.0	2.9

[a] See Figure D.7 for axial position location

[b] Displacements in mils

Note: Average radius of model is 6.198 in.

Table D.2

RADIAL DISPLACEMENTS OF THE CORE BARREL OF SM 2

Point[a]	Meridian 1	2	3	4	5	6	Average
0	16.0[b]	10.5	14.0	11.5	11.5	8.5	12.0
1	52.5	35.0	48.5	39.0	42.0	43.5	43.4
2	58.5	40.0	55.5	46.0	47.5	47.5	49.2
3	58.0	38.5	53.0	48.0	45.0	44.0	47.8
4	57.5	36.0	51.0	51.0	44.5	44.0	47.4
5	57.5	37.5	48.5	45.5	44.0	37.5	45.1
6	57.0	40.0	45.5	44.0	43.0	40.0	44.9
7	50.5	35.5	39.5	34.0	37.0	36.5	38.9
8	36.5	30.0	20.5	18.0	20.0	30.0	25.9
TOP	2.0	5.5	-3.0	0.0	1.5	6.5	2.4

[a] See Figure D.7 for axial position locations.

[b] Displacements in mils.

Note: Average radius of model is 3.838 in.

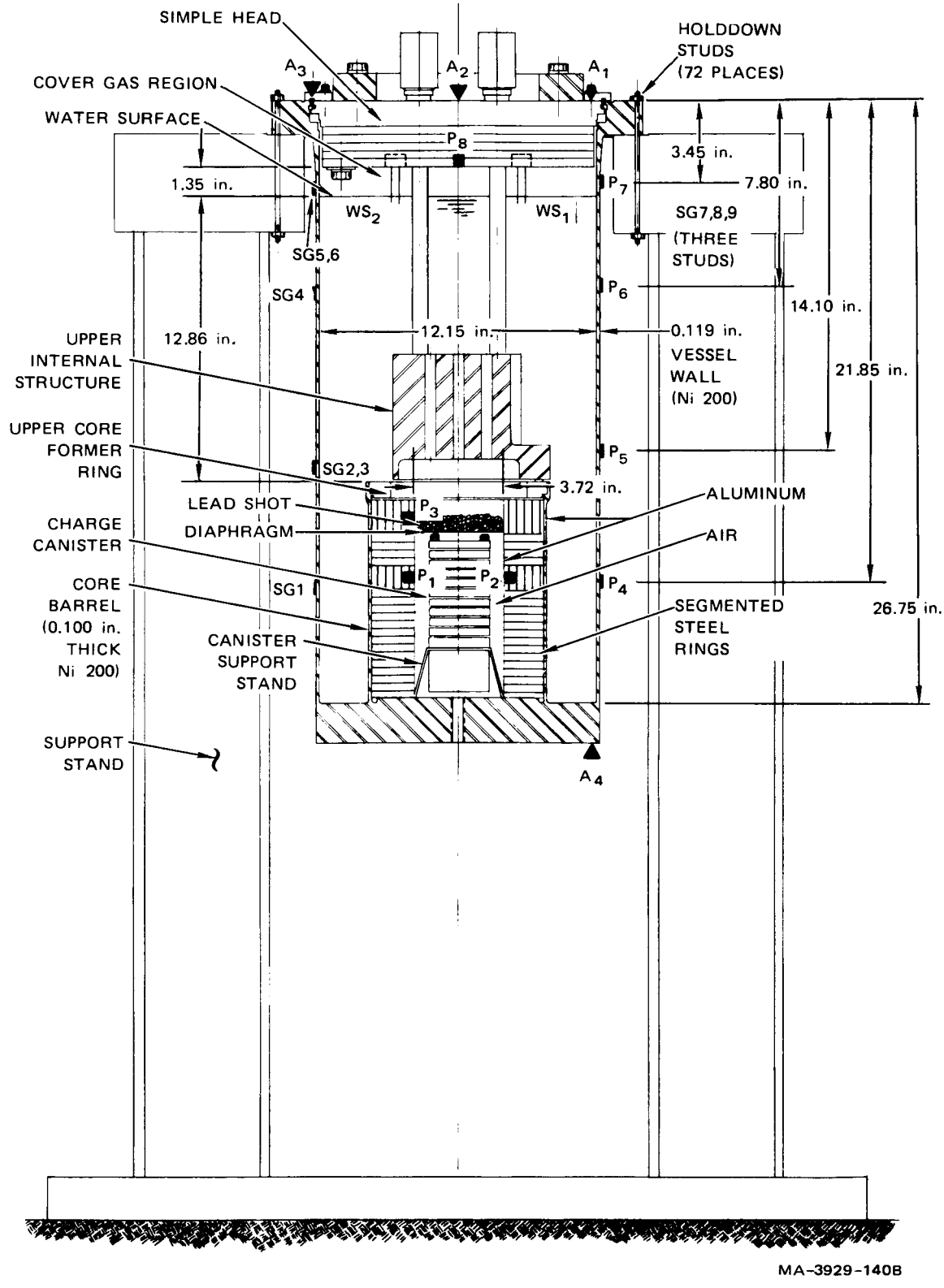

FIGURE D.8 SM 3 WITH INSTRUMENTATION

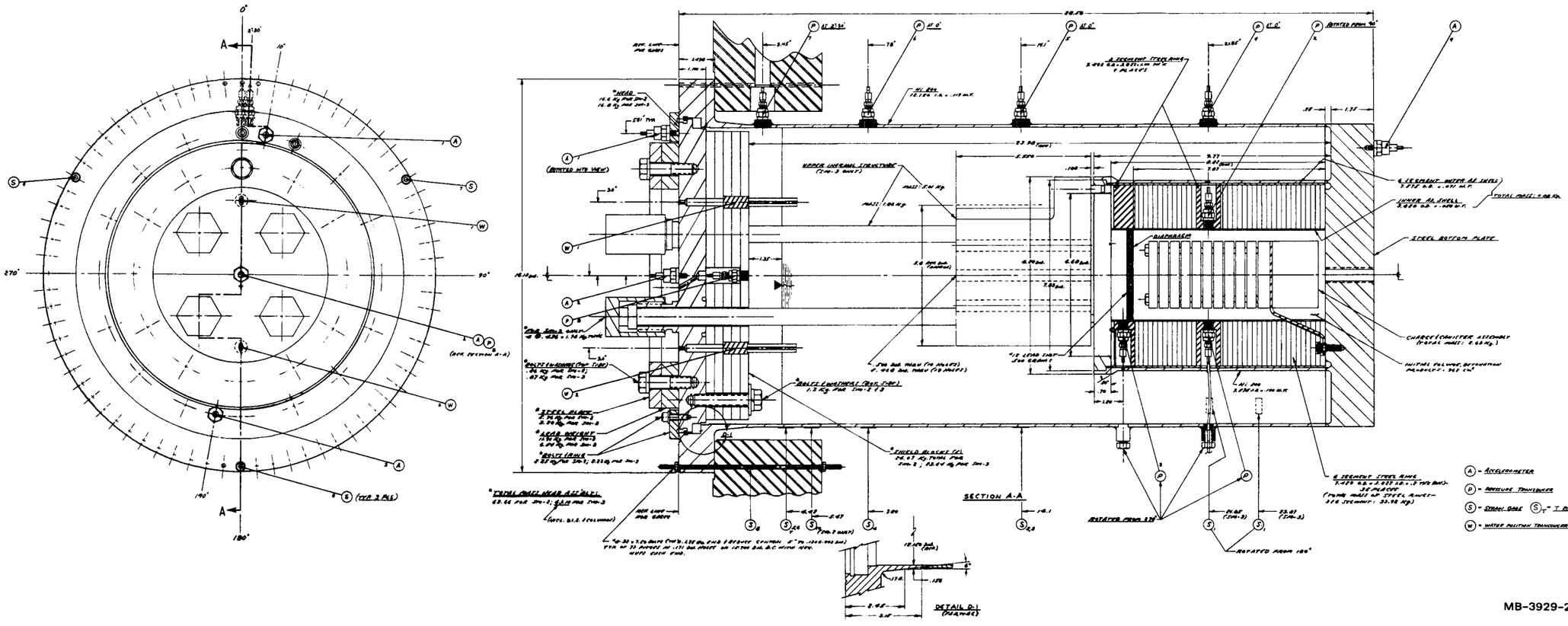

MB-3929-221

FIGURE D.9 DETAILED CROSS SECTION OF SM 3

Blank Page

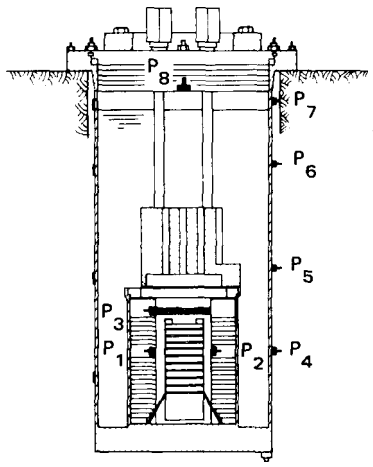

SM 3

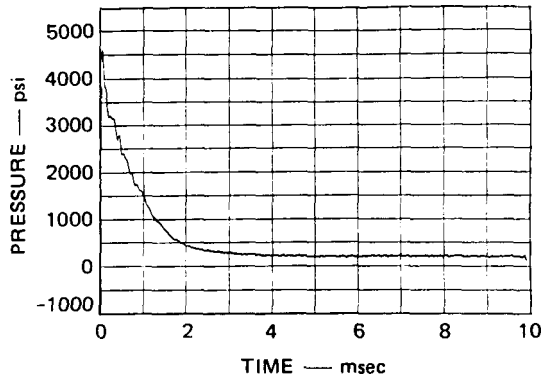

P_1 CORE

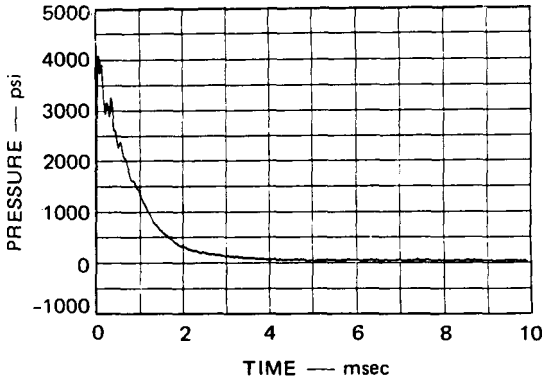

P_2 CORE

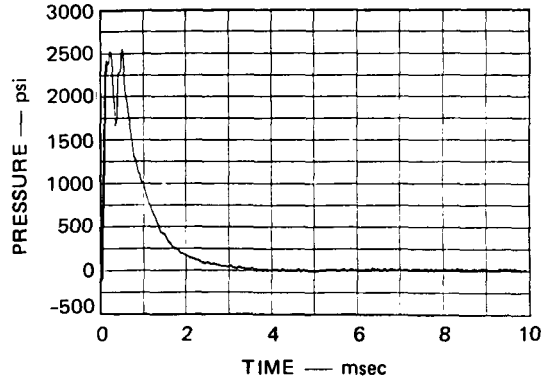

P_3 UPPER CORE

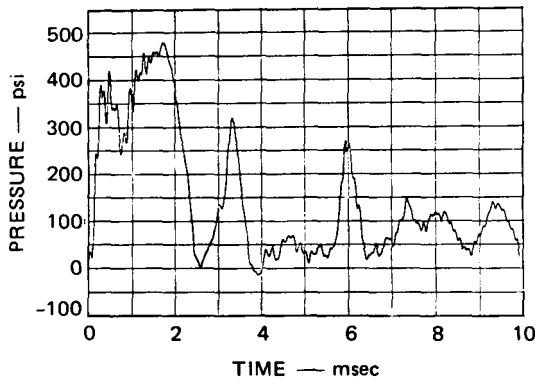

P_4 VESSEL WALL AT CORE

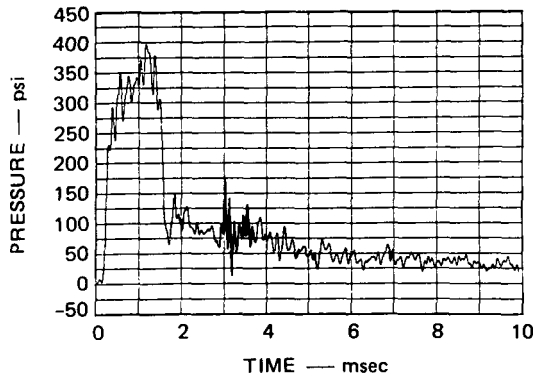

P_5 SODIUM OUTLET NOZZLE

MA-3929-227

FIGURE D.10 PRESSURE RECORDS FOR SM 3

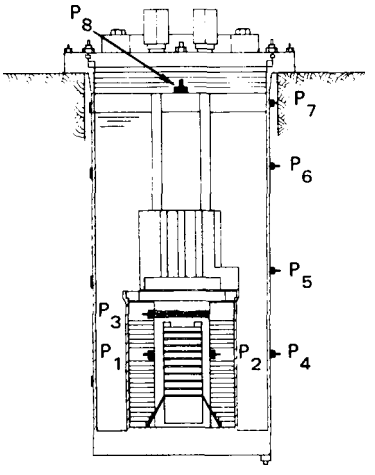

SM 3

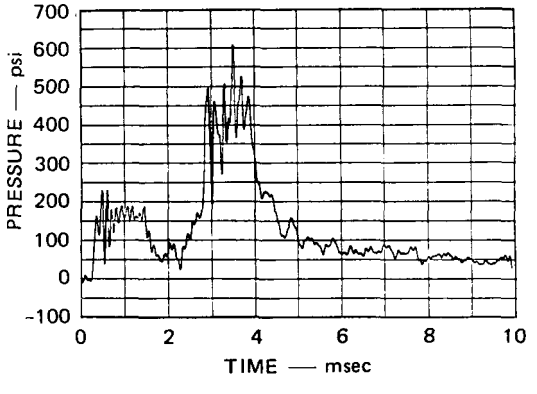

P_6 VESSEL WALL

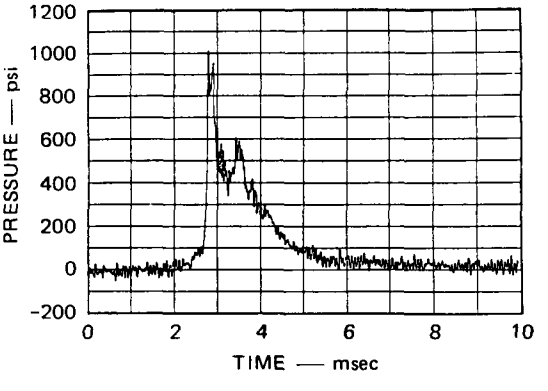

P_7 UPPER VESSEL WALL

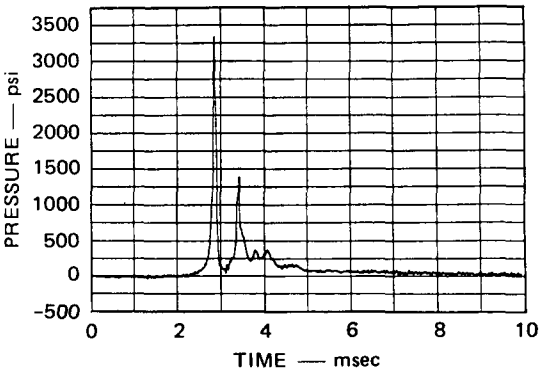

P_8 HEAD

MA-3929-228

FIGURE D.10 PRESSURE RECORDS FOR SM 3 (Concluded)

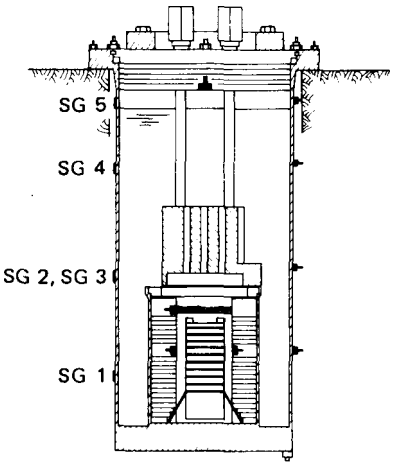

SM 3

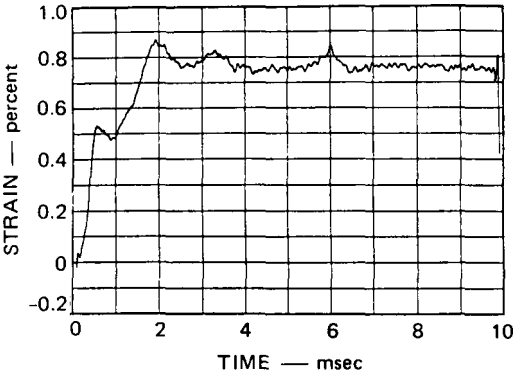

SG 1 VESSEL WALL AT CORE BARREL (C)

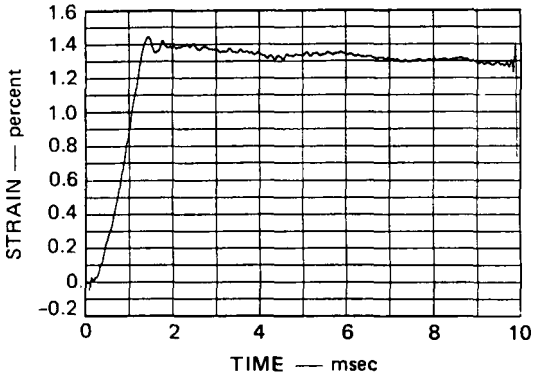

SG 2 VESSEL WALL AT UIS (C) (SODIUM OUTLET NOZZLE)

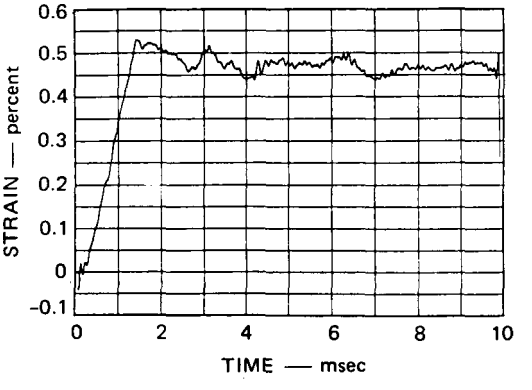

SG 3 VESSEL WALL AT UIS (A)

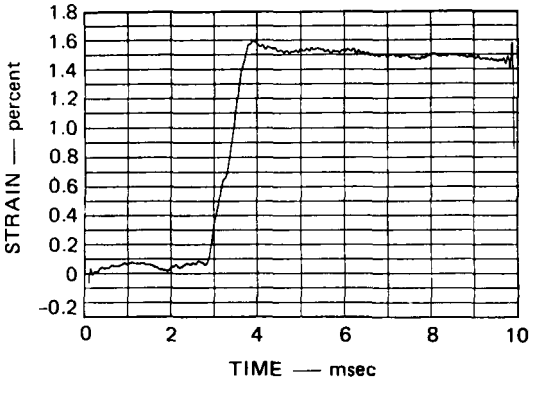

SG 4 VESSEL WALL (C)

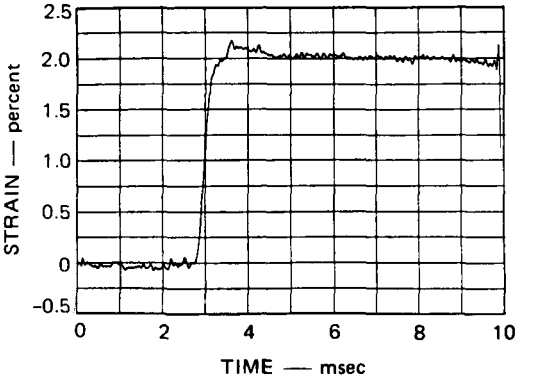

SG 5 UPPER VESSEL WALL (C)

MA-3929-229

FIGURE D.11 STRAIN RECORDS FOR SM 3

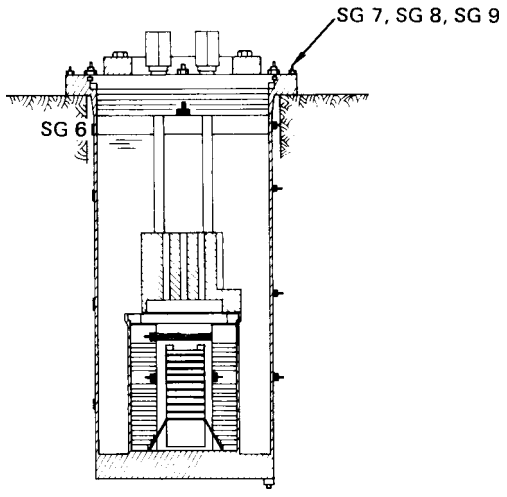

SM 3

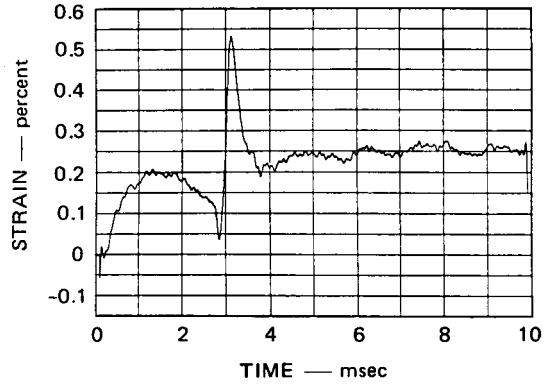

SG 6 UPPER VESSEL WALL (A)

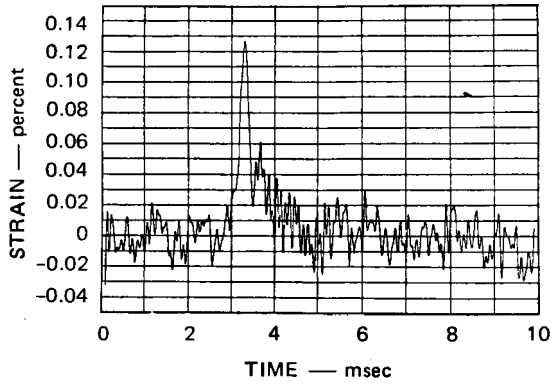

SG 7 STUD AT 60°

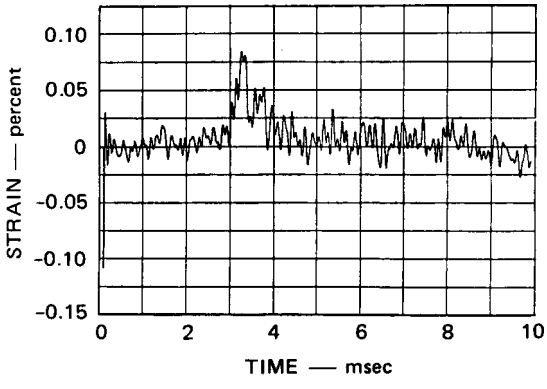

SG 8 STUD AT 180°

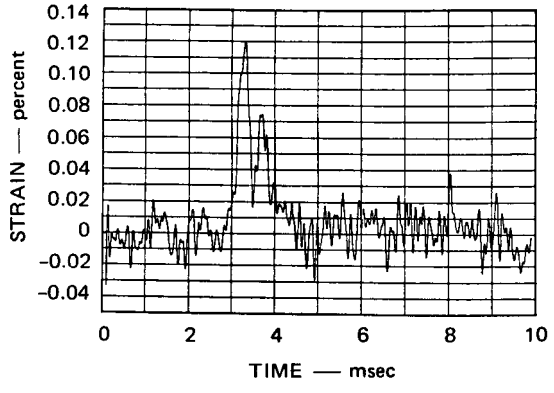

SG 9 STUD AT 300°

MA-3929-230

FIGURE D.11 STRAIN RECORDS FOR SM 3 (Concluded)

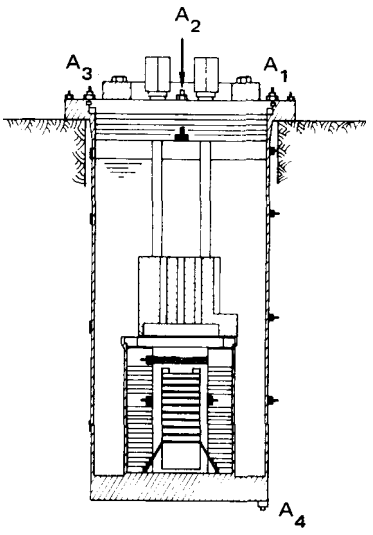

SM 3

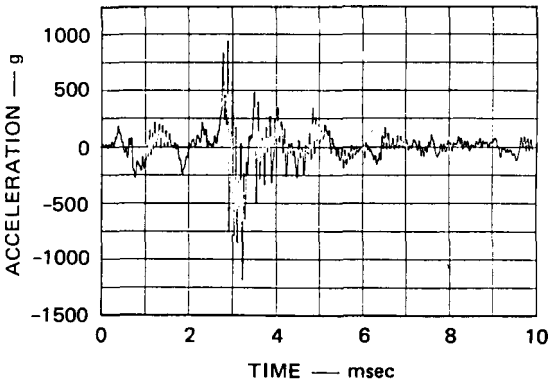

A_1 HEAD EDGE

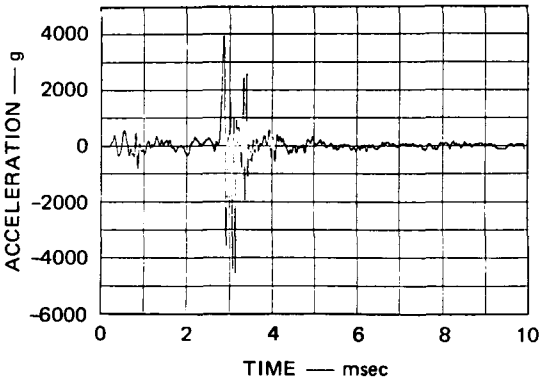

A_2 HEAD CENTER

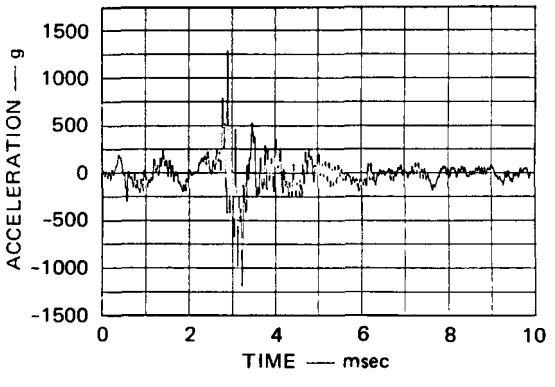

A_3 HEAD EDGE

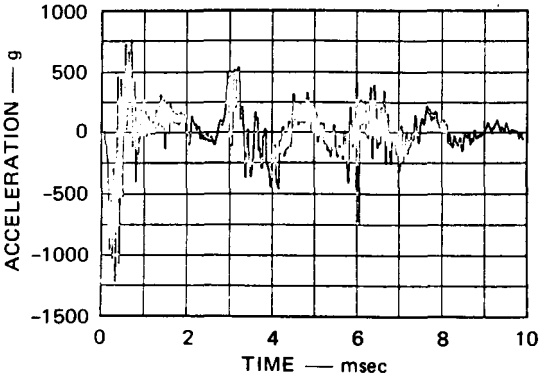

A_4 PLATFORM

MA-3929-231

FIGURE D.12 ACCELEROMETER RECORDS FOR SM 3

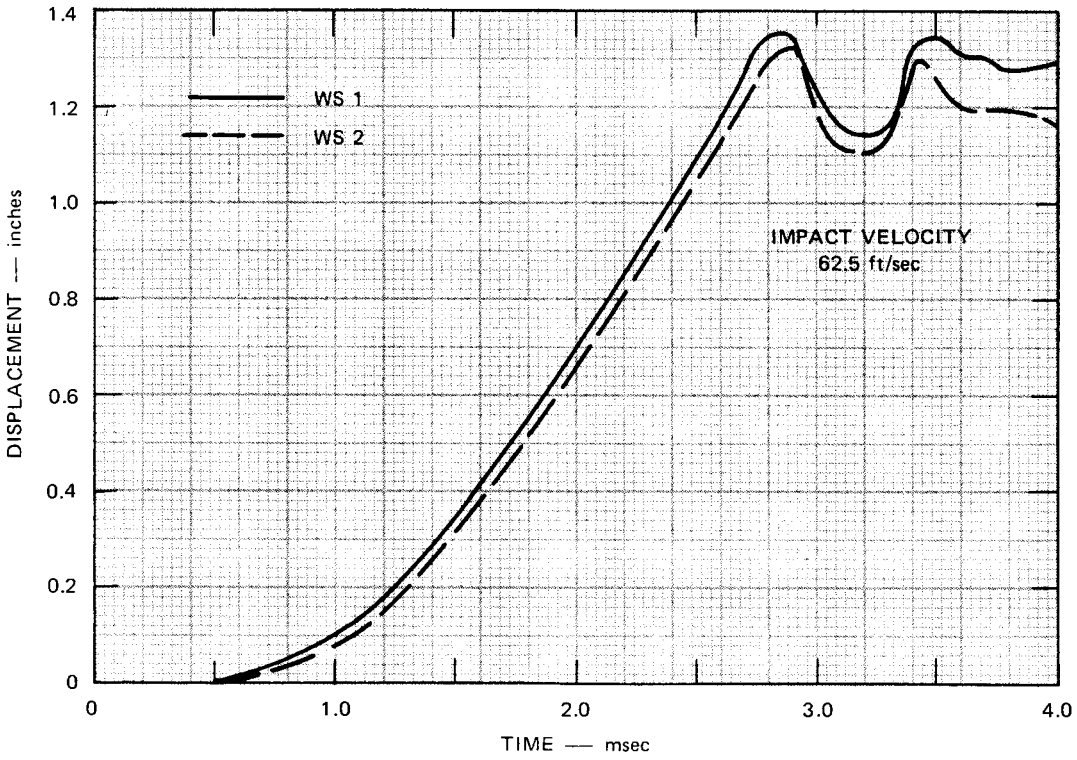

MP-3929-155

FIGURE D.13 WATER SURFACE DISPLACEMENT FOR SM 3

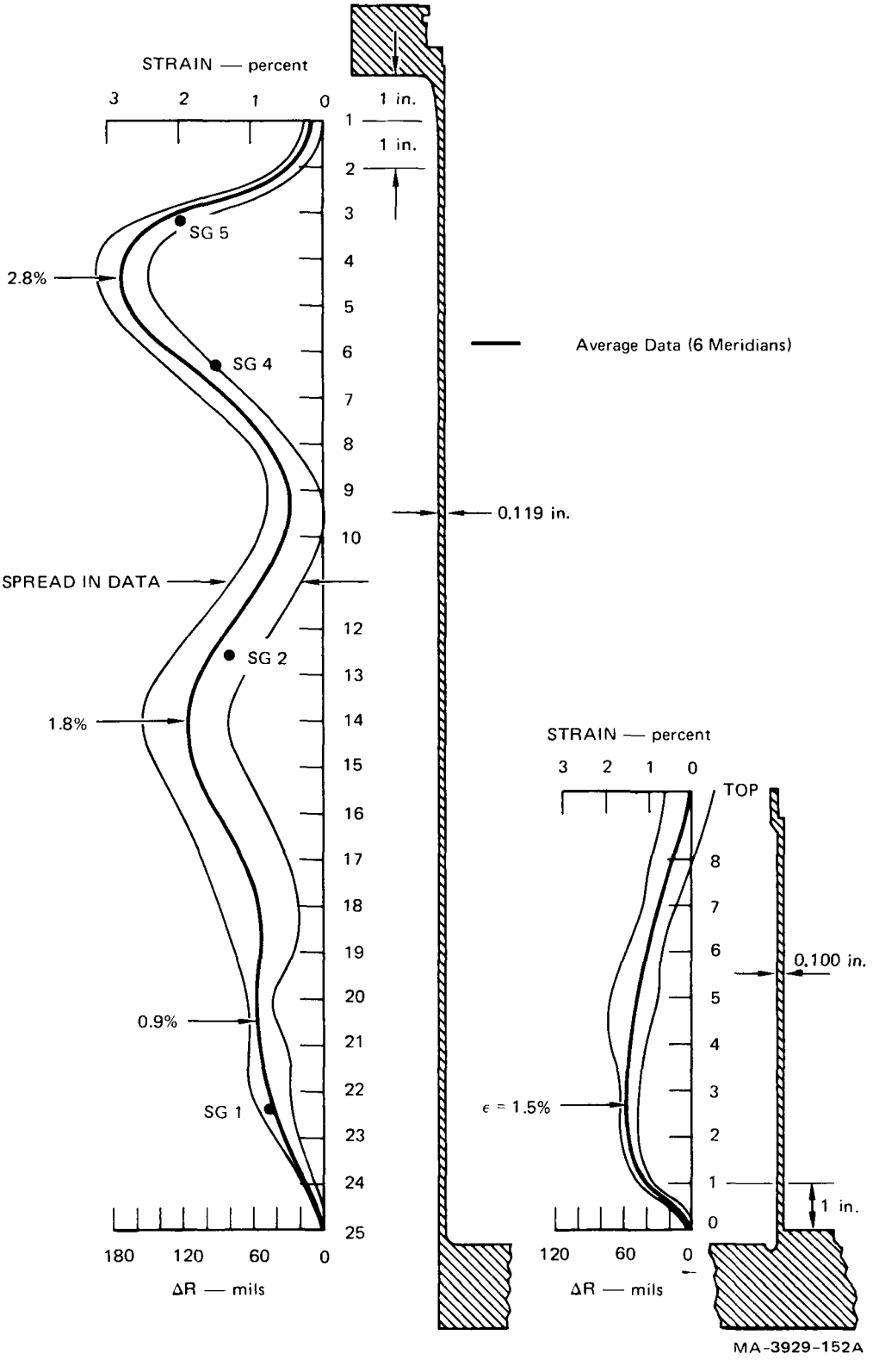

FIGURE D.14 DEFORMED SHAPE PROFILE, SM 3

Table D.3

RADIAL DISPLACEMENTS OF THE VESSEL WALL OF SM 3

Point[a]	Meridian 1	2	3	4	5	6	Average
1	8.0[b]	4.0	0.0	5.5	4.5	1.0	3.8
2	-	24.5	12.5	25.0	32.5	27.5	24.4
3	130.0	123.5	102.0	118.0	137.0	130.0	123.4
4	173.0	172.0	146.5	149.5	195.0	184.0	170.0
5	164.0	161.0	144.5	137.0	189.0	179.5	162.5
6	-	128.0	114.5	105.5	151.0	137.5	127.3
7	72.5	86.0	76.5	61.0	103.5	86.5	81.0
8	36.0	50.5	44.5	24.5	60.0	50.0	44.3
9	21.0	33.5	26.0	0.0	43.0	37.5	26.8
10	24.5	39.5	28.0	2.5	57.0	48.0	33.3
11	41.5	57.5	44.0	17.5	77.0	74.0	51.9
12	67.0	79.0	66.0	43.0	103.0	107.0	77.5
13	-	102.5	88.5	67.0	126.5	139.5	104.8
14	104.5	120.0	96.5	78.0	130.5	154.5	114.0
15	100.0	122.0	85.0	64.0	121.5	145.0	106.3
16	80.5	106.0	67.0	46.5	100.5	121.5	87.0
17	62.5	81.5	53.0	-	74.0	105.0	94.0
18	54.5	67.5	45.5	20.0	60.5	89.0	56.2
19	55.0	62.5	41.5	25.0	60.5	75.0	53.3
20	-	63.5	40.0	-	64.0	65.0	58.1
21	59.5	62.0	40.5	29.0	63.0	60.0	52.3
22	56.5	50.5	37.0	28.0	58.0	51.0	46.8
23	43.5	33.5	27.0	18.0	40.5	35.5	33.0
24	15.0	9.5	9.0	8.0	11.0	15.0	11.3
25	0.0	-4.0	-3.5	0.0	-1.5	-2.0	-1.8

[a]See Figure D.14 for axial locations. of points.

[b]Dissplacements in mils.

Note: Average radius of model is 6.185 in.

Table D.4

RADIAL DISPLACEMENTS OF THE CORE BARREL OF SM 3

Point[a]	Meridian 1	2	3	4	5	6	Average
0	8.0[b]	4.5	9.5	10.0	8.0	3.5	7.3
1	38.5	36.0	43.5	38.5	44.0	33.0	38.9
2	50.0	47.5	60.5	56.0	61.0	45.0	53.3
3	43.5	42.5	59.0	59.5	61.5	42.0	51.3
4	42.0	42.0	63.0	70.0	65.5	38.0	53.4
5	35.0	31.5	59.5	70.0	64.0	27.0	47.8
6	26.5	28.5	50.0	52.0	50.0	26.0	38.8
7	14.0	21.0	41.5	42.0	39.5	16.5	29.1
8	-1.5	10.5	26.5	33.0	20.5	1.0	15.0
TOP	-21.0	-7.0	13.5	21.5	4.0	-18.0	-1.2

[a] See Figure D.14 for axial position locations.

[b] Displacement in mils.

Note: Average radius of model 3.838 in.

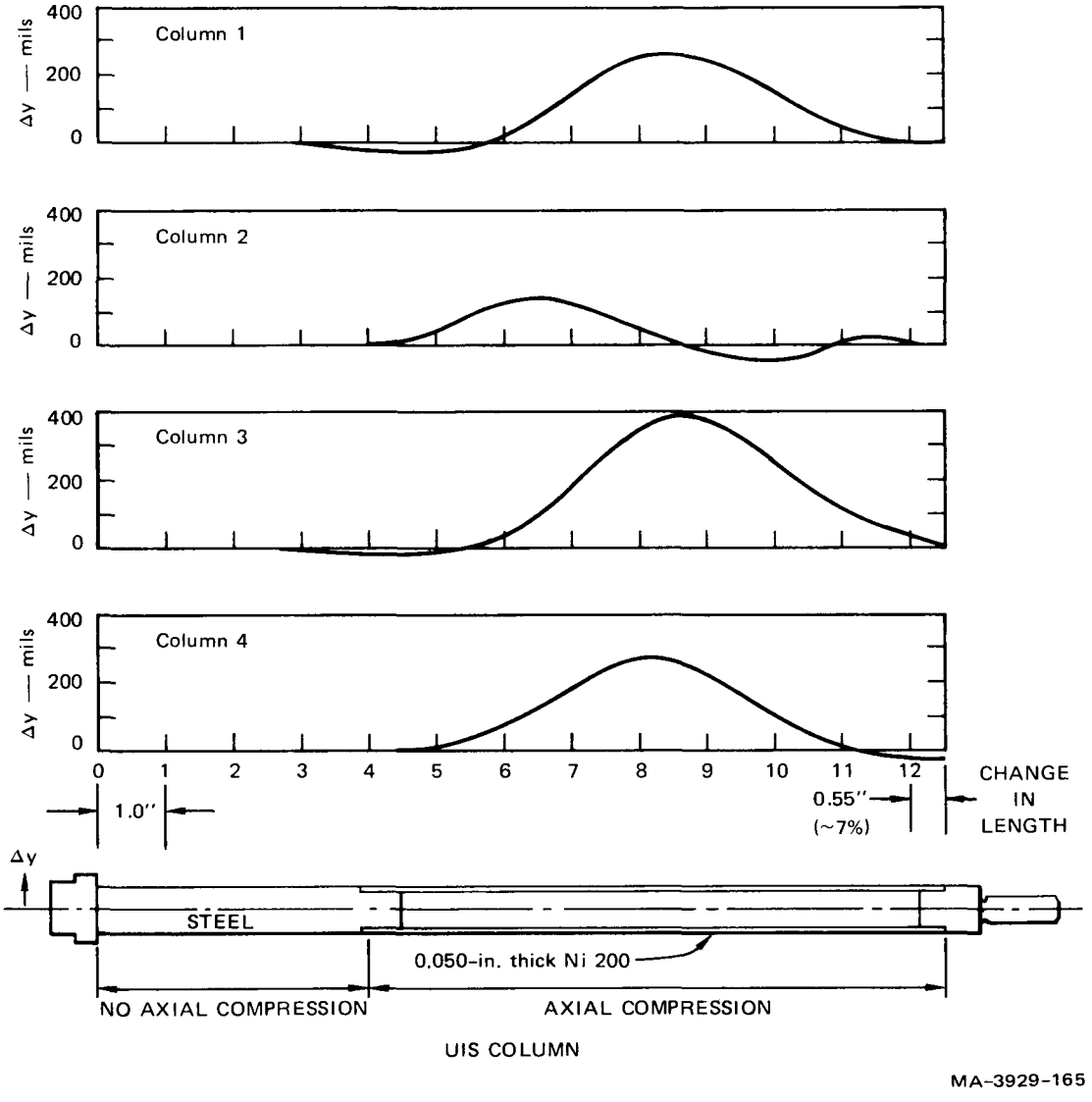

FIGURE D.15 DEFORMED SHAPE PROFILES OF SM 3 UIS COLUMNS

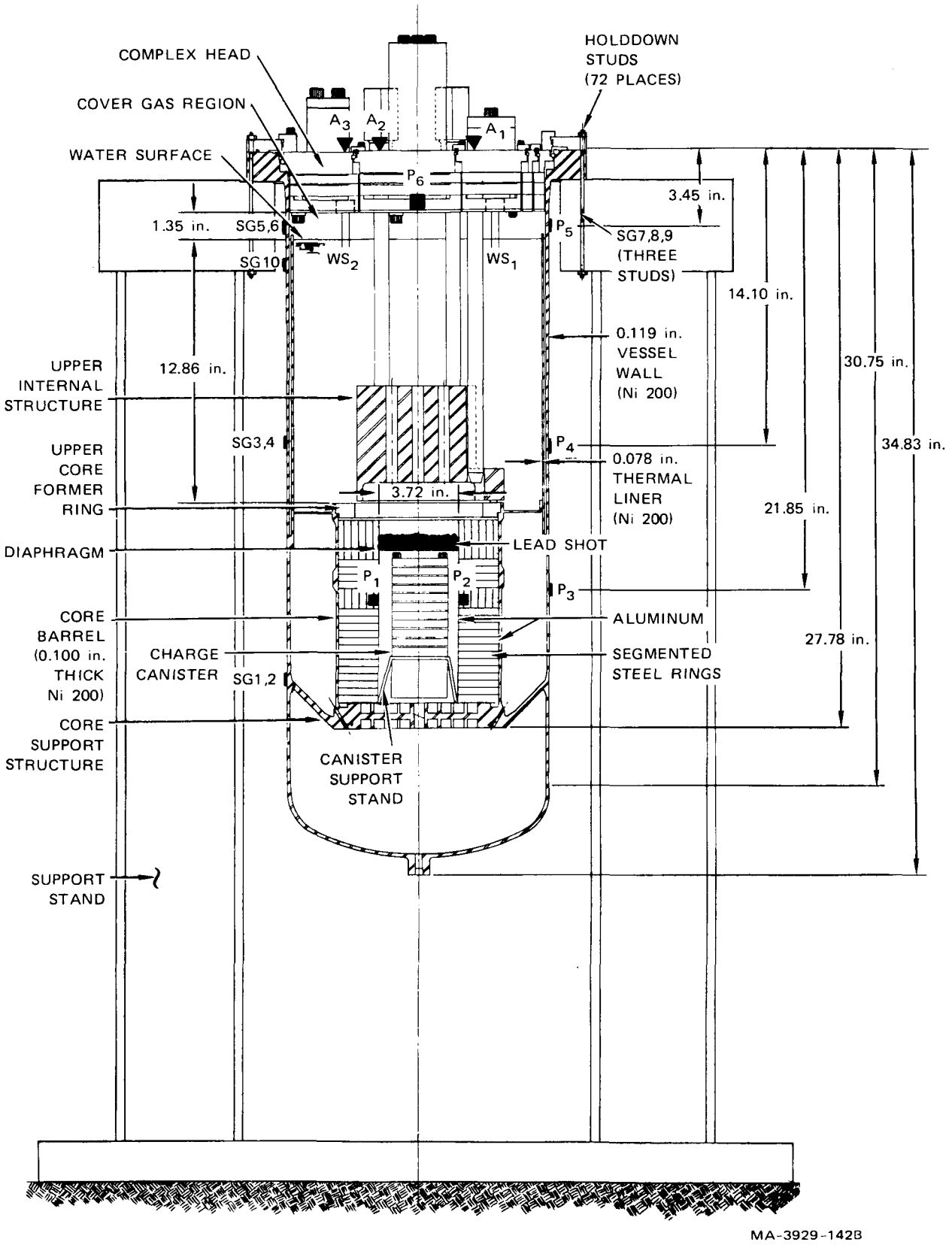

FIGURE D.16 SM 4 WITH INSTRUMENTATION

Blank Page

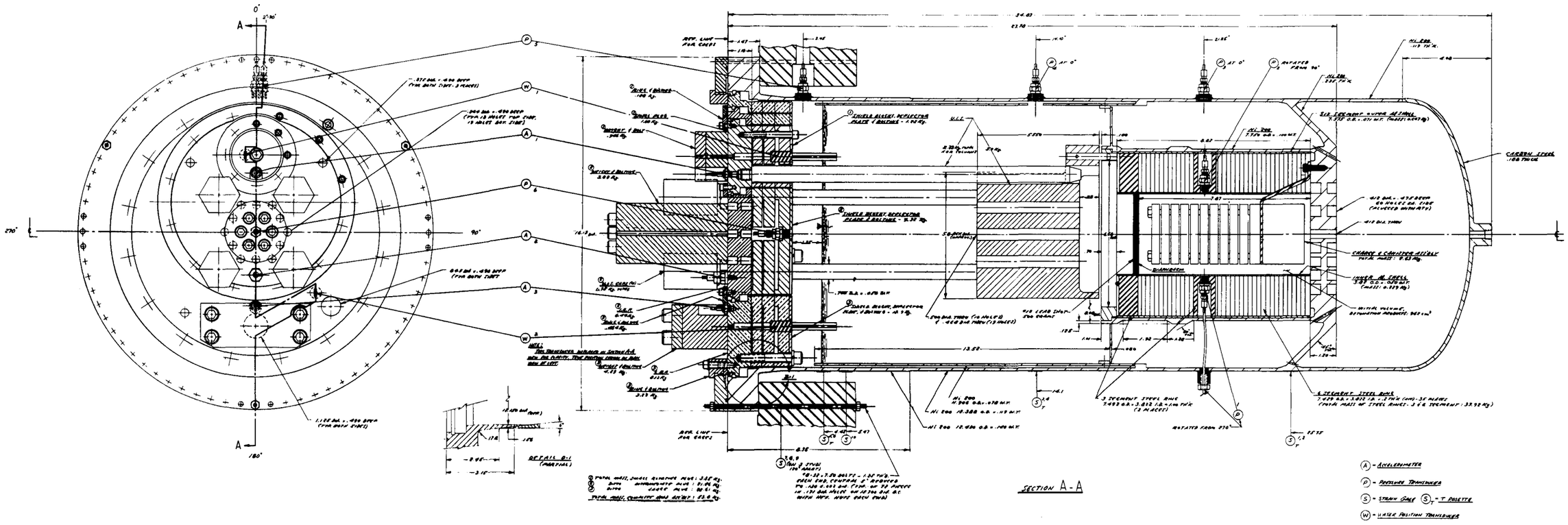

MB-3929-232

FIGURE D.17 DETAILED CROSS SECTION OF SM 4

Blank Page

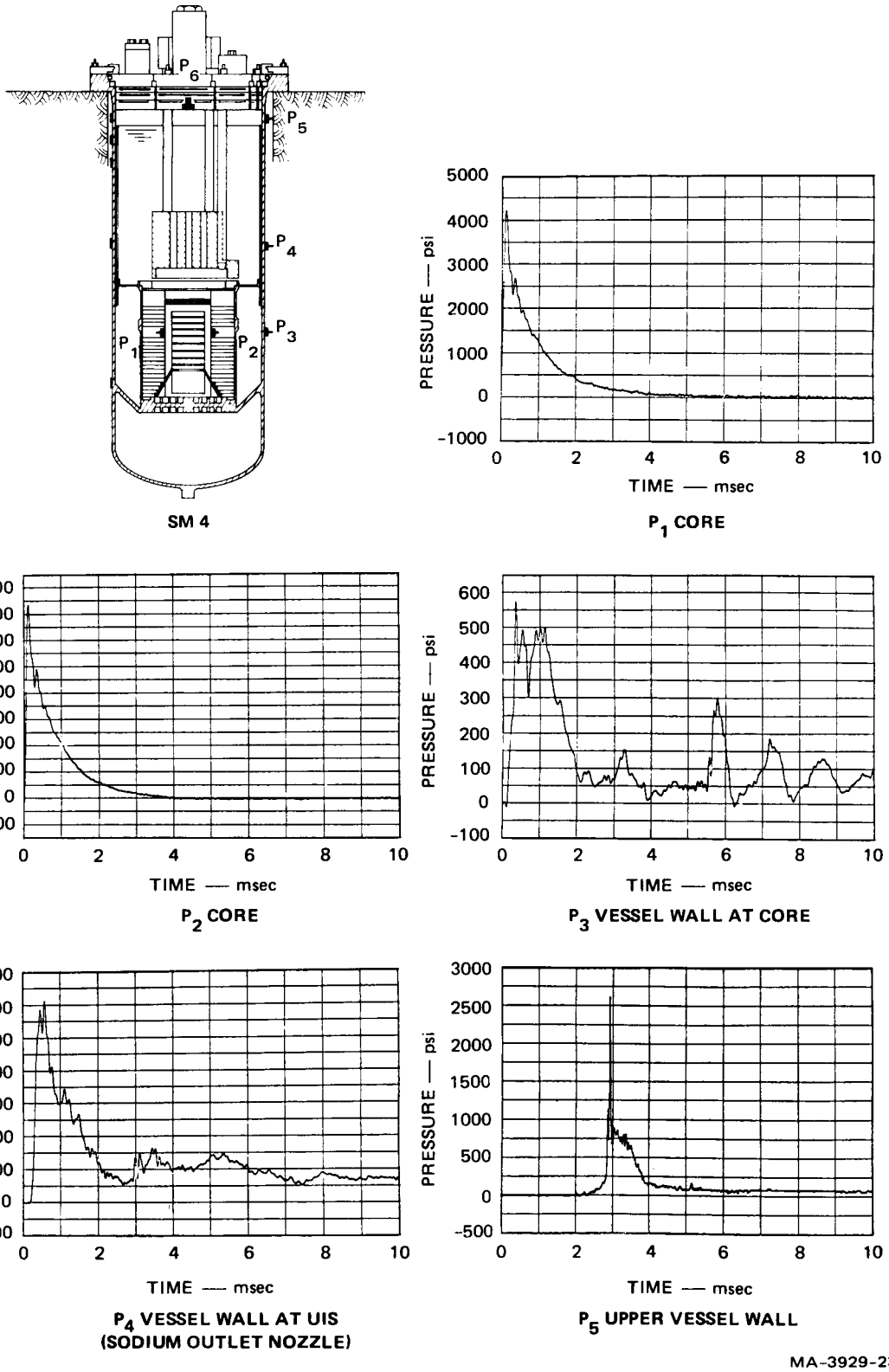

FIGURE D.18 PRESSURE RECORDS FOR SM 4

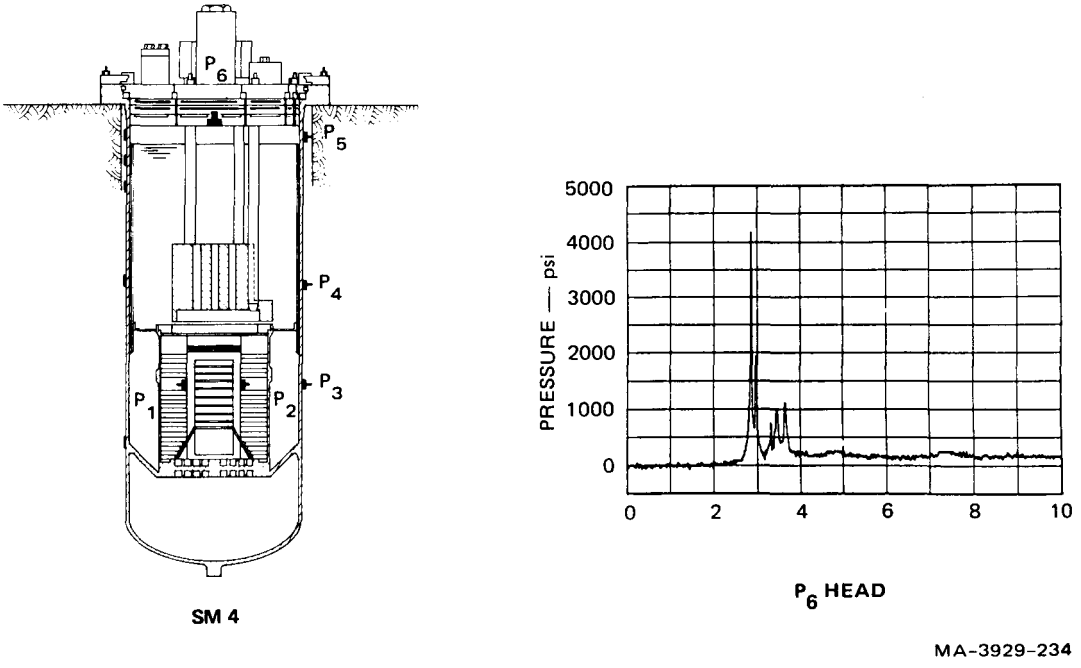

FIGURE D.18 PRESSURE RECORDS FOR SM 4 (Concluded)

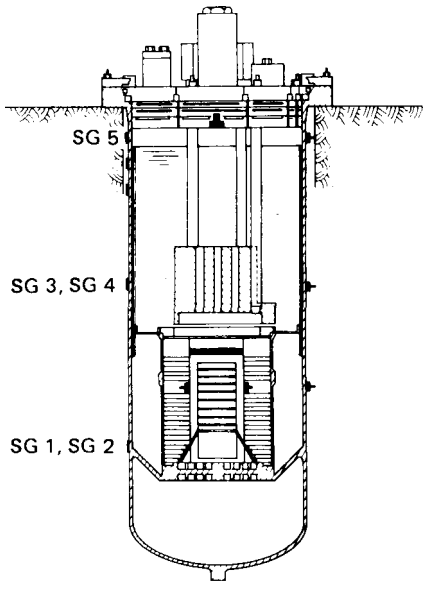

SM 4

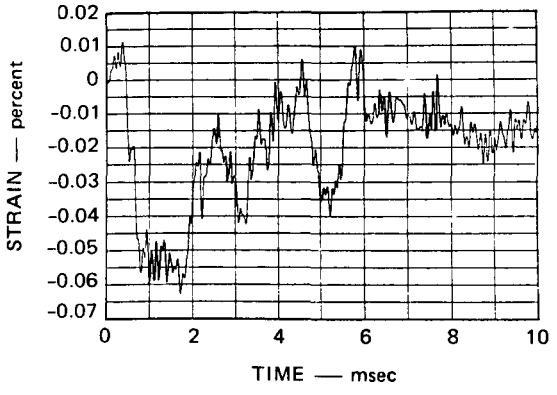

SG 1 CORE SUPPORT RING (C)

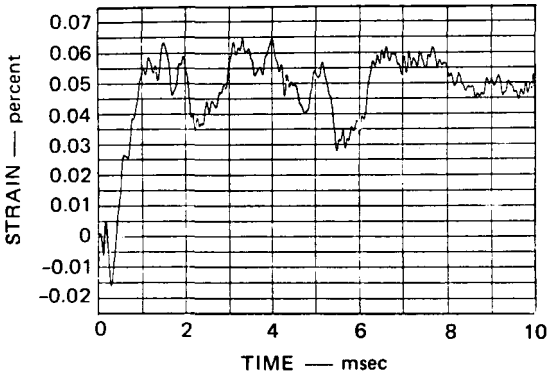

SG 2 CORE SUPPORT RING (A)

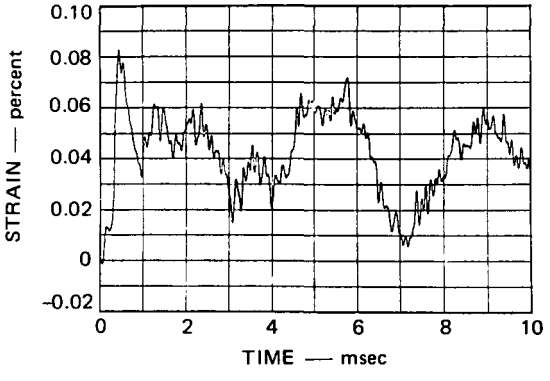

SG 3 VESSEL WALL AT UIS (C)
(SODIUM OUTLET NOZZLE)

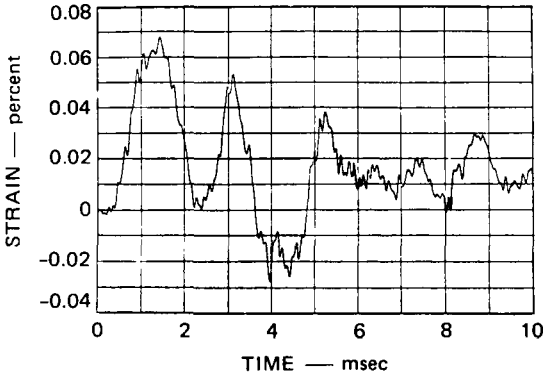

SG 4 VESSEL WALL AT UIS (A)
(SODIUM OUTLET NOZZLE)

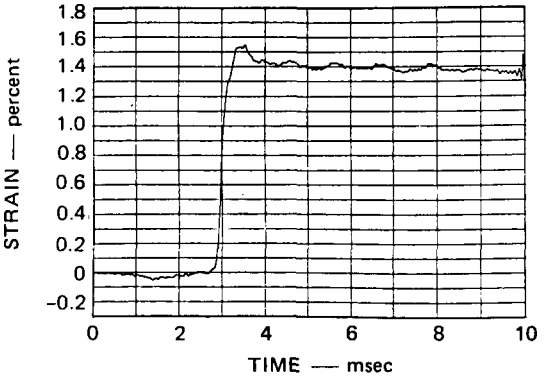

SG 5 UPPER VESSEL WALL (C)

MA-3929-235

FIGURE D.19 STRAIN RECORDS FOR SM 4

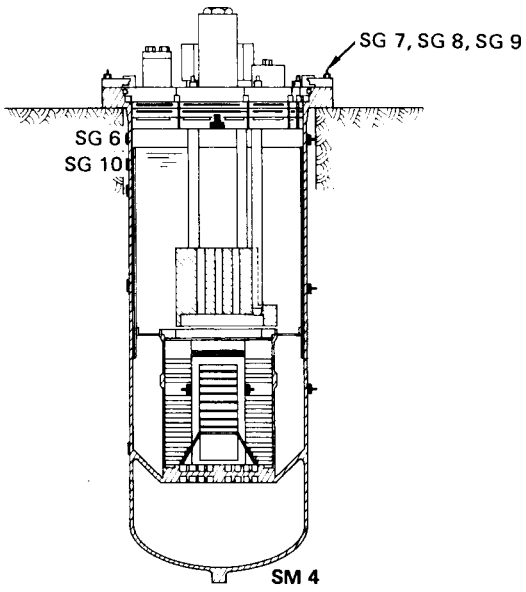

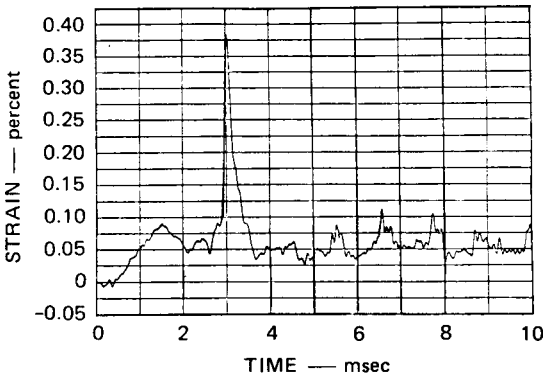

SG 6 UPPER VESSEL WALL (A)

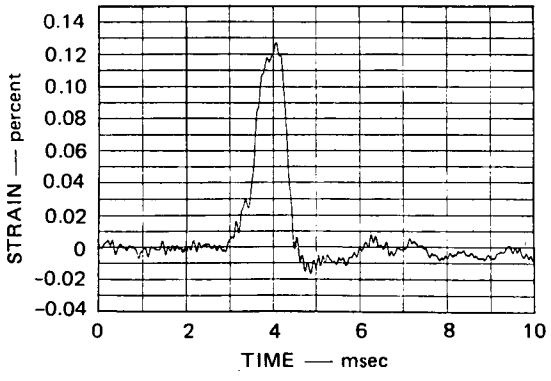

SG 7 STUD AT 60°

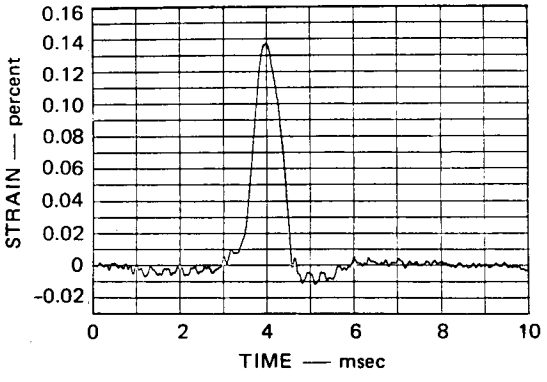

SG 8 STUD AT 180°

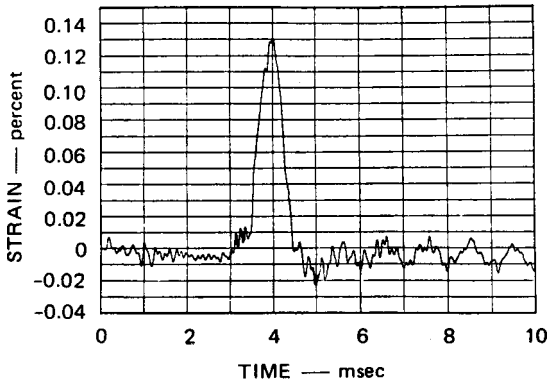

SG 9 STUD AT 300°

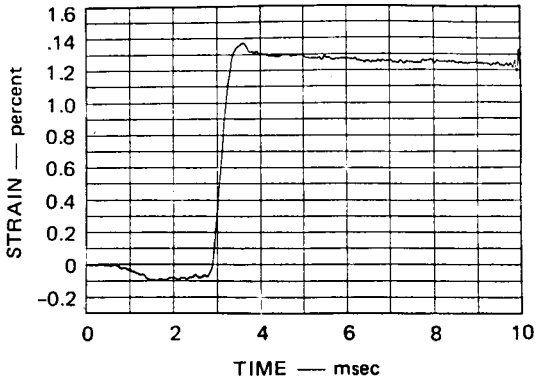

SG 10 VESSEL WALL AT PEAK DEFORMATION

MA-3929-236

FIGURE D.19 STRAIN RECORDS FOR SM 4 (Concluded)

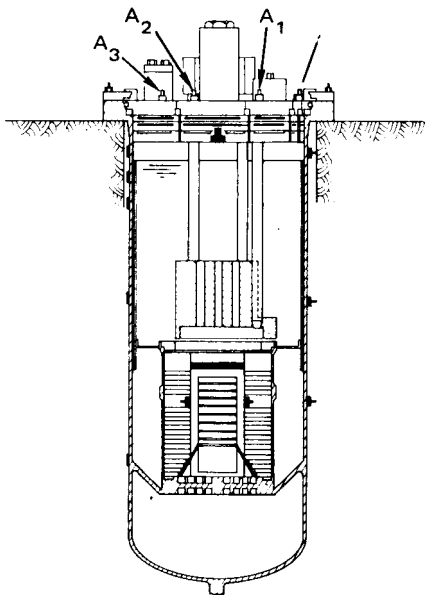

SM 4

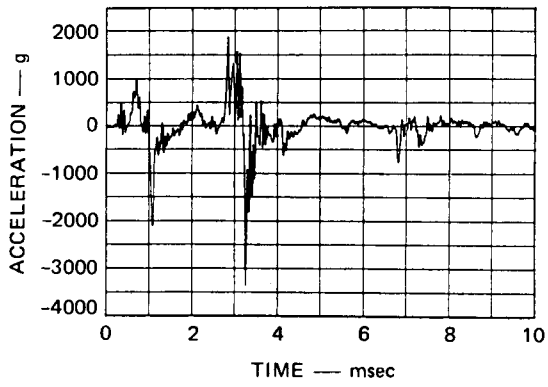

A_1 LRP EDGE

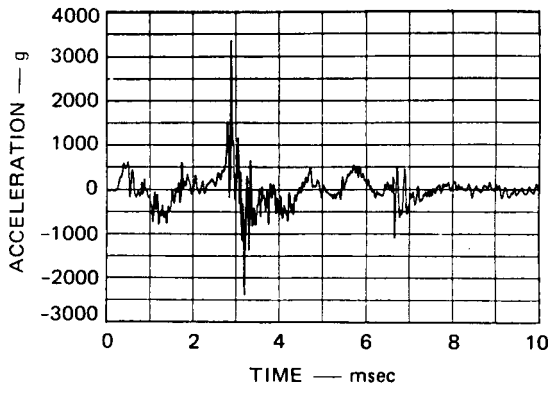

A_2 SRP

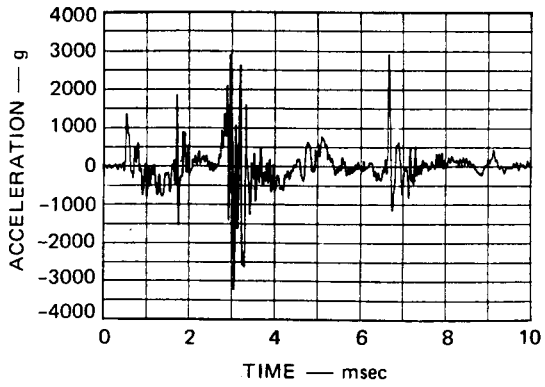

A_3 IRP EDGE

MA-3929-237

FIGURE D.20 ACCELEROMETER RECORDS FOR SM 4

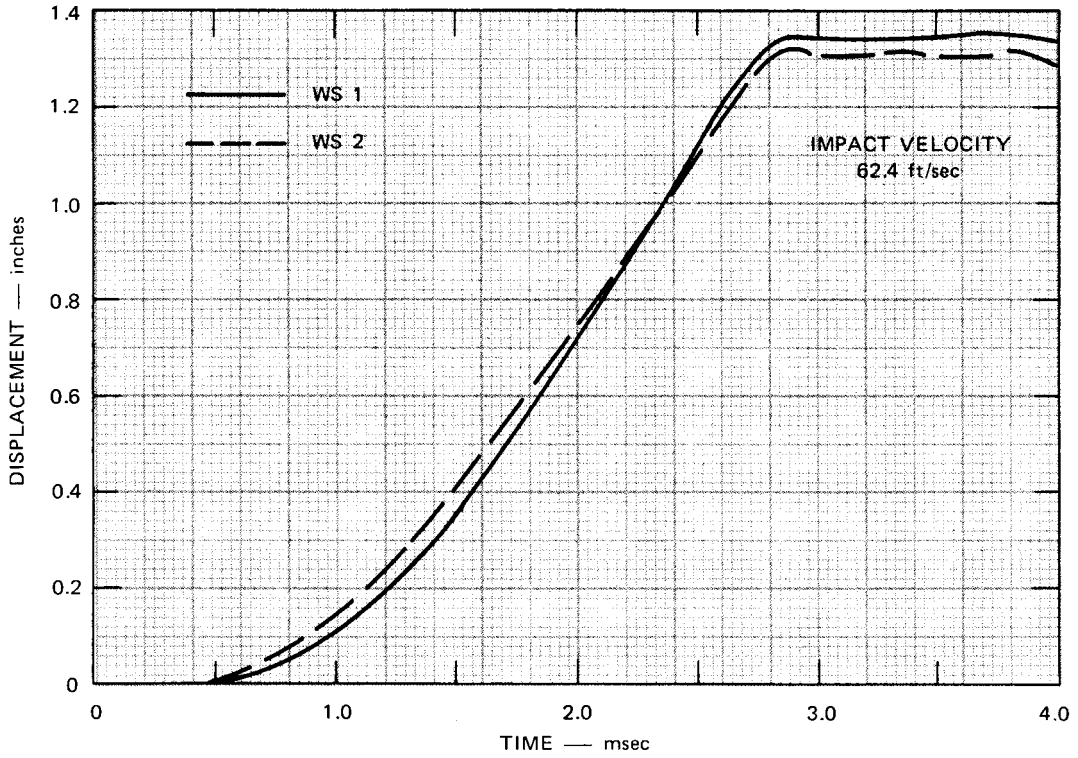

FIGURE D.21 WATER SURFACE DISPLACEMENT FOR SM 4

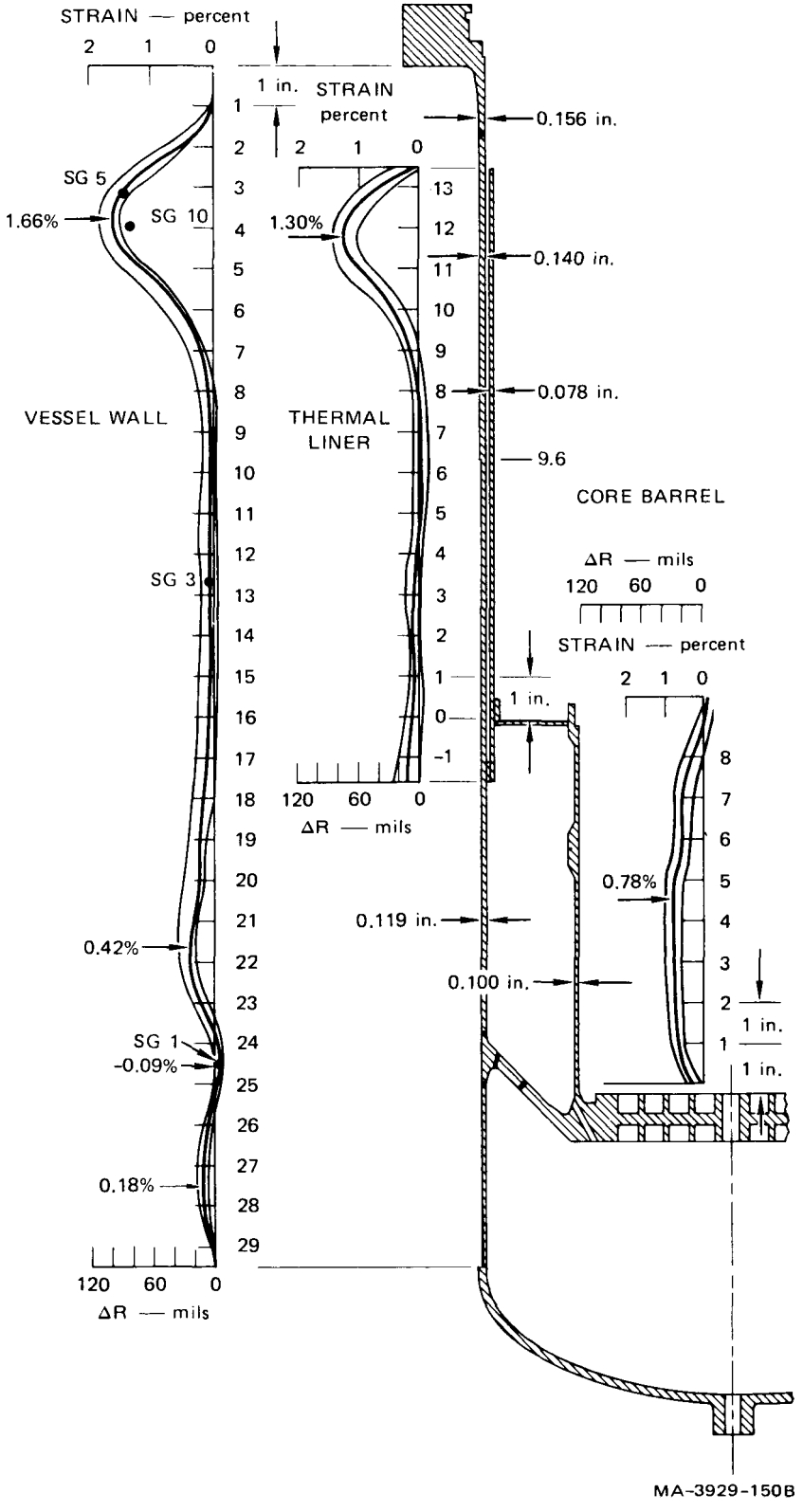

FIGURE D.22 DEFORMED SHAPE PROFILE, SM 4

Table D.5

RADIAL DISPLACEMENTS OF THE VESSEL WALL OF SM 4

Point[a]	Meridian 1	2	3	4	5	6	Average
1	1.5[b]	4.0	4.5	-0.5	1.0	3.5	2.4
2	-	37.0	37.5	23.5	32.5	38.0	33.7
3	89.0	90.0	80.5	72.5	78.0	95.0	84.3
4	102.0	106.0	94.0	94.0	90.5	100.5	97.5
5	73.0	74.5	64.0	64.0	62.0	70.5	68.0
6	40.5	40.0	29.5	29.0	33.5	39.5	35.4
7	21.5	19.5	10.5	8.0	13.5	21.0	15.7
8	12.0	10.5	2.5	-0.5	3.0	10.5	6.4
9	10.0	8.5	4.0	-1.0	0.0	7.5	4.9
10	9.5	6.0	4.5	-0.5	-2.0	7.0	4.1
11	9.5	4.5	5.0	0.0	-3.0	6.0	3.7
12	11.0	4.5	6.0	1.0	-2.0	5.0	4.3
13	-	5.0	8.0	3.0	-3.0	4.0	3.4
14	8.0	5.5	7.5	4.5	-2.0	4.5	4.7
15	7.5	4.0	6.5	5.5	-1.0	5.0	4.6
16	7.5	4.5	8.5	9.5	0.0	5.0	5.9
17	8.5	5.5	11.0	15.0	0.0	5.5	7.6
18	9.0	10.0	17.5	23.0	1.0	7.0	11.3
19	11.0	14.5	22.0	32.0	3.5	7.5	15.1
20	-	19.0	23.0	-	8.5	10.0	15.2
21	-	25.0	27.0	-	19.5	15.5	21.8
22	22.0	26.0	29.0	32.0	21.0	21.5	25.3
23	11.5	11.5	12.5	15.0	21.0	13.0	14.1
24	-2.5	-2.5	-4.0	-2.5	-4.0	-2.5	-6.0
25	-	-	-	-	-	-	-
26	4.0	5.5	5.0	3.0	7.0	4.5	4.9
27	10.0	13.5	12.0	10.0	14.0	8.0	11.3
28	12.0	12.5	11.5	11.5	13.5	7.5	11.4
29	4.5	2.0	1.5	3.0	5.5	2.5	3.2

[a] See Figure D.22 for axial location of points.

[b] Displacement in mils.

Note: Average radius of model 6.166 in.

Table D.6

RADIAL DISPLACEMENTS OF THE THERMAL LINER OF SM 4

Point[a]	Meridian 1	2	3	4	5	6	Average
1	8.5[b]	5.0	9.0	3.5	1.5	-3.0	4.1
2	9.0	6.0	9.0	1.5	4.5	-4.5	4.3
3	11.0	4.5	8.0	-1.0	5.5	-6.5	3.6
4	9.5	1.5	6.5	-4.5	6.5	-10.0	1.6
5	5.0	-1.5	1.5	-7.0	3.0	-14.0	-2.2
6	-0.5	-2.0	0.5	-8.0	3.5	-10.0	-2.8
7	0.0	-1.0	-0.5	-7.5	3.5	-3.5	-1.5
8	2.5	-0.5	0.5	-5.5	4.5	0.5	0.4
9	8.0	5.0	11.5	4.0	5.5	12.0	7.7
10	23.0	25.0	30.0	19.5	18.5	36.5	25.4
11	48.0	57.5	56.5	46.0	44.0	95.5	57.9
12	76.0	80.0	76.0	60.5	62.0	88.0	73.8
13	46.5	41.0	34.5	24.5	24.0	53.0	37.3
TOP	10.5	7.5	0.0	-6.0	-6.5	26.5	5.4

[a] See Figure D.22 for axial location of points.

[b] Displacement in mils.

Note: Average radius of model is 5.914 inches.

Table D.7

RADIAL DISPLACEMENTS OF THE CORE BARREL OF SM 4

Point[a]	Meridian 1	2	3	4	5	6	Average
0	16.0[b]		18.5	12.0	19.0	15.5	16.5
1	27.5	26.0	27.0	21.5	30.5	22.5	25.9
2	30.5	24.0	29.5	25.5	29.0	21.5	26.7
3	30.0	24.0	30.0	27.5	30.0	21.0	27.1
4	30.5	24.0	32.5	37.5	32.0	21.0	29.6
5	32.5	18.0	33.0	36.0	32.0	21.5	28.9
6	23.5	17.0	24.0	22.5	25.0	17.5	21.5
7	23.5	18.0	23.5	19.0	24.5	17.5	21.0
8	10.5	9.0	10.0	10.0	12.5	8.0	9.8
TOP	-3.5	-3.0	-2.0	-2.5	-2.0	-1.5	-2.4

[a] See Figure D.22 for axial location of points.

[b] Displacement in mils.

Note: Average radius of model 3.836 in.

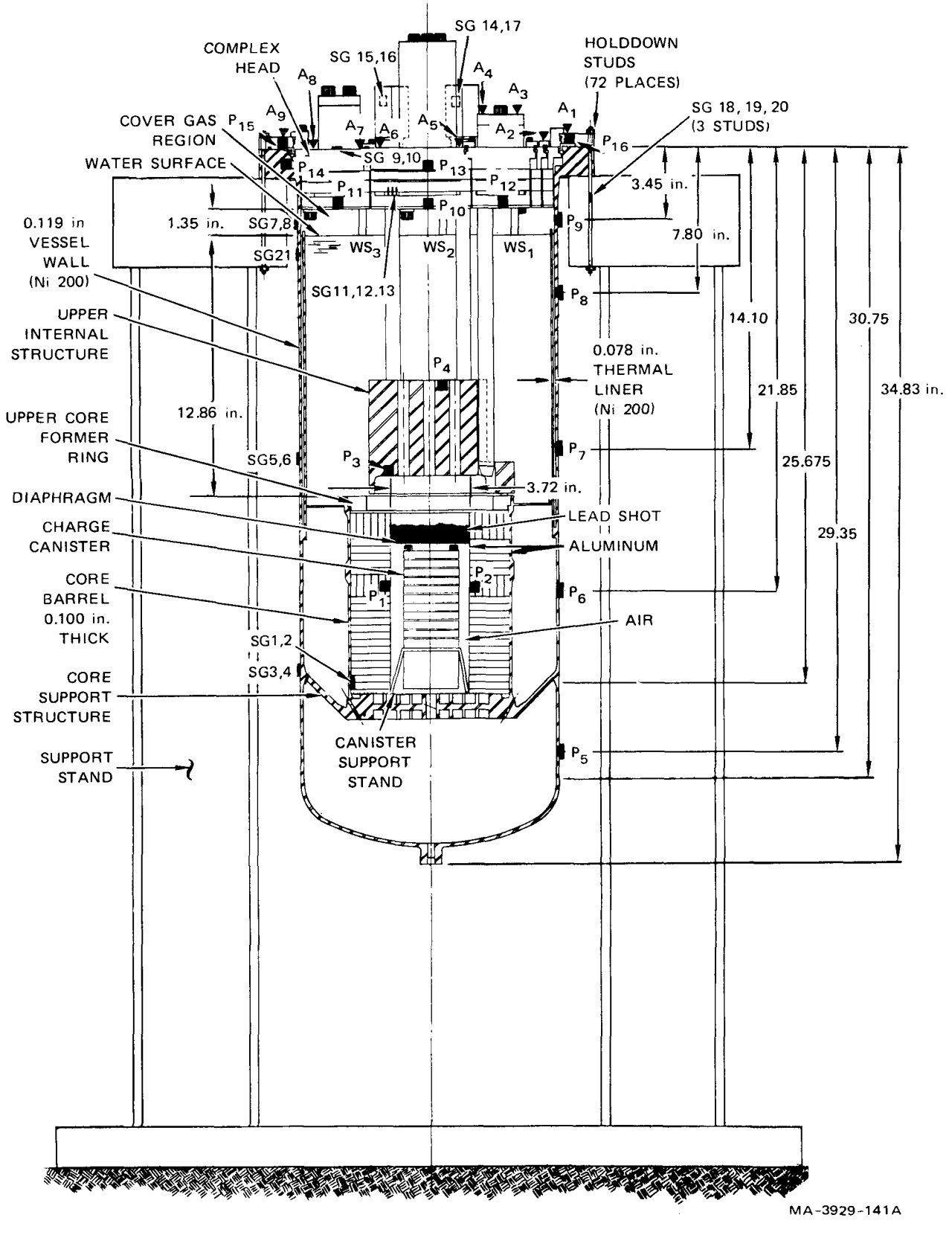

FIGURE D.23 SM 5 WITH INSTRUMENTATION

Blank Page

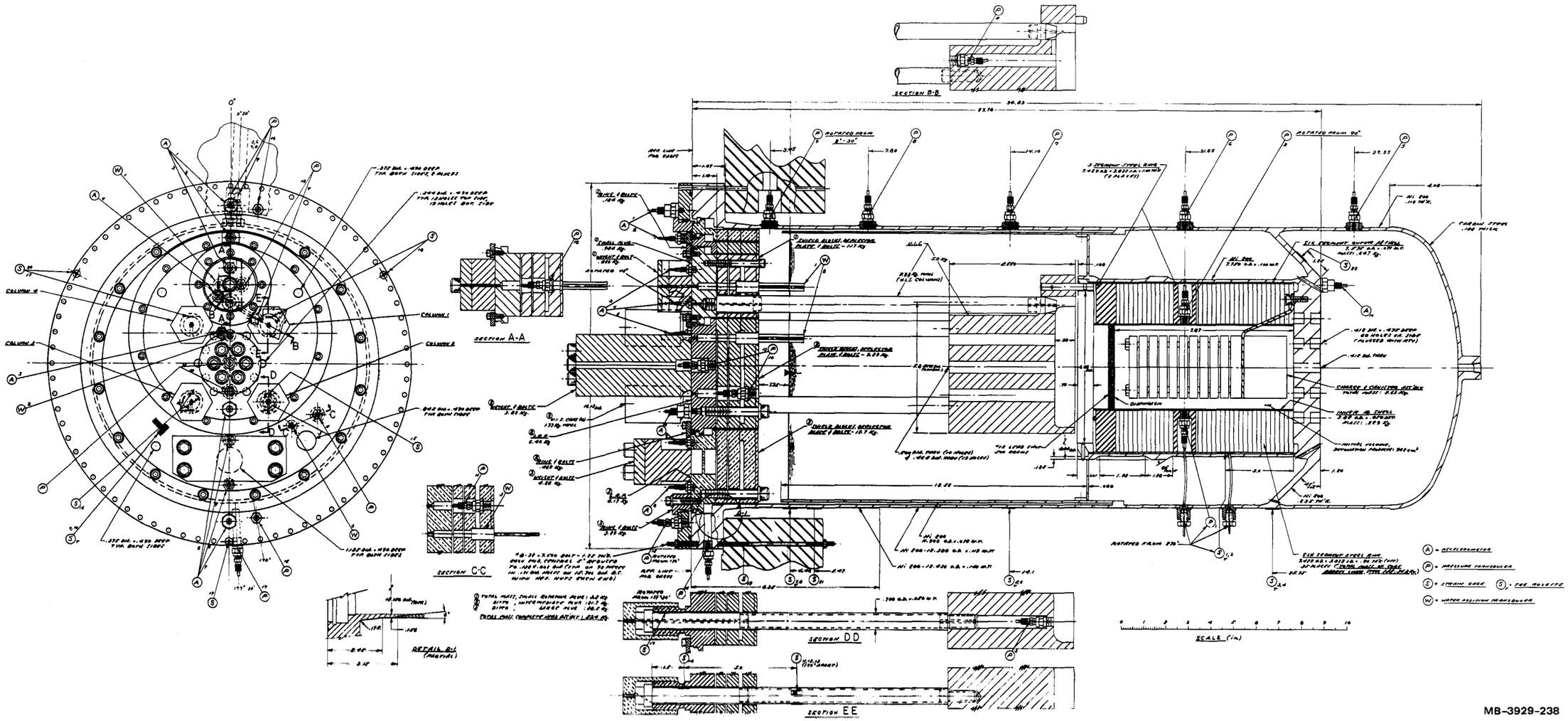

MB-3929-238

FIGURE D.24 DETAILED CROSS SECTION OF SM 5

Blank Page

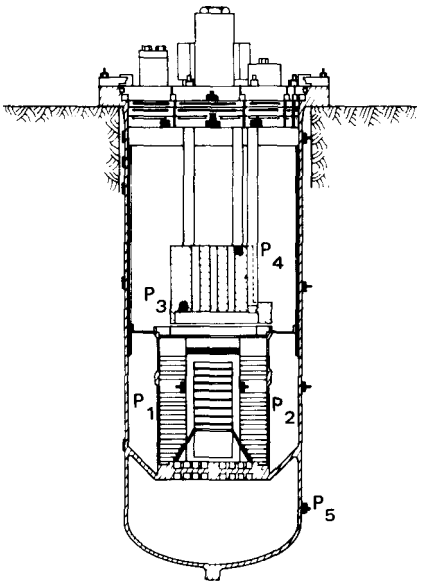

SM 5

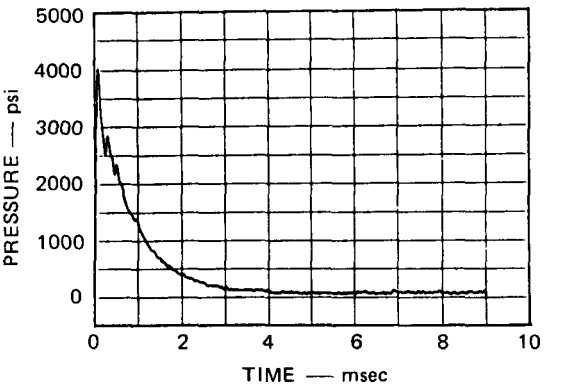

P_1 CORE

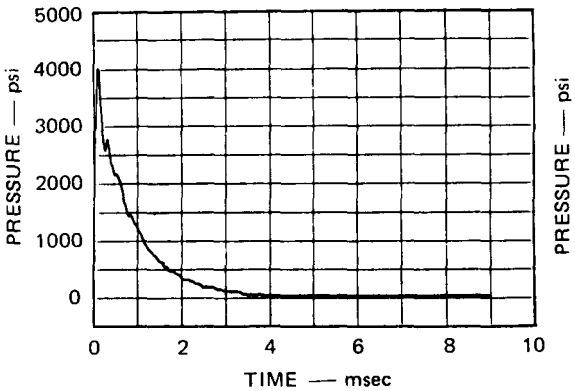

P_2 CORE

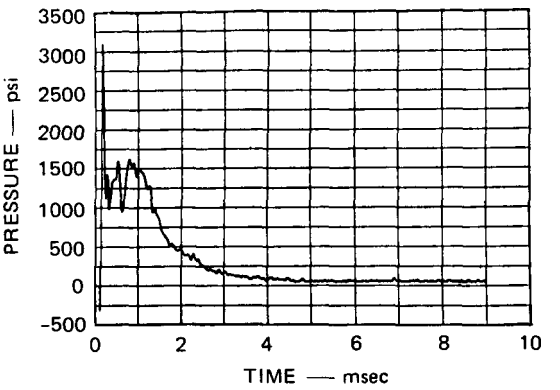

P_3 LOWER UIS

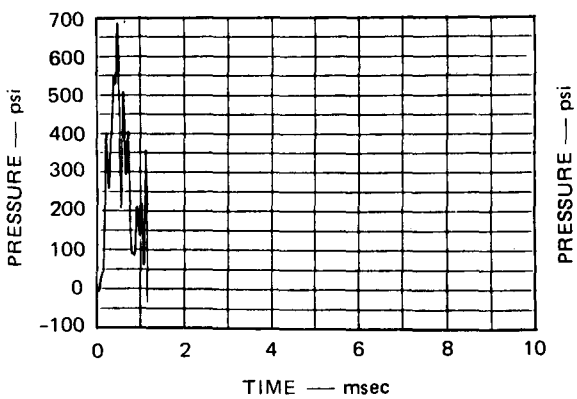

P_4 UPPER UIS

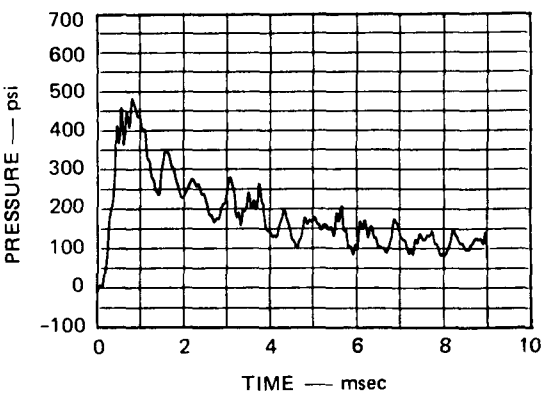

P_5 LOWER VESSEL

MA-3929-239

FIGURE D.25 PRESSURE RECORDS FOR SM 5

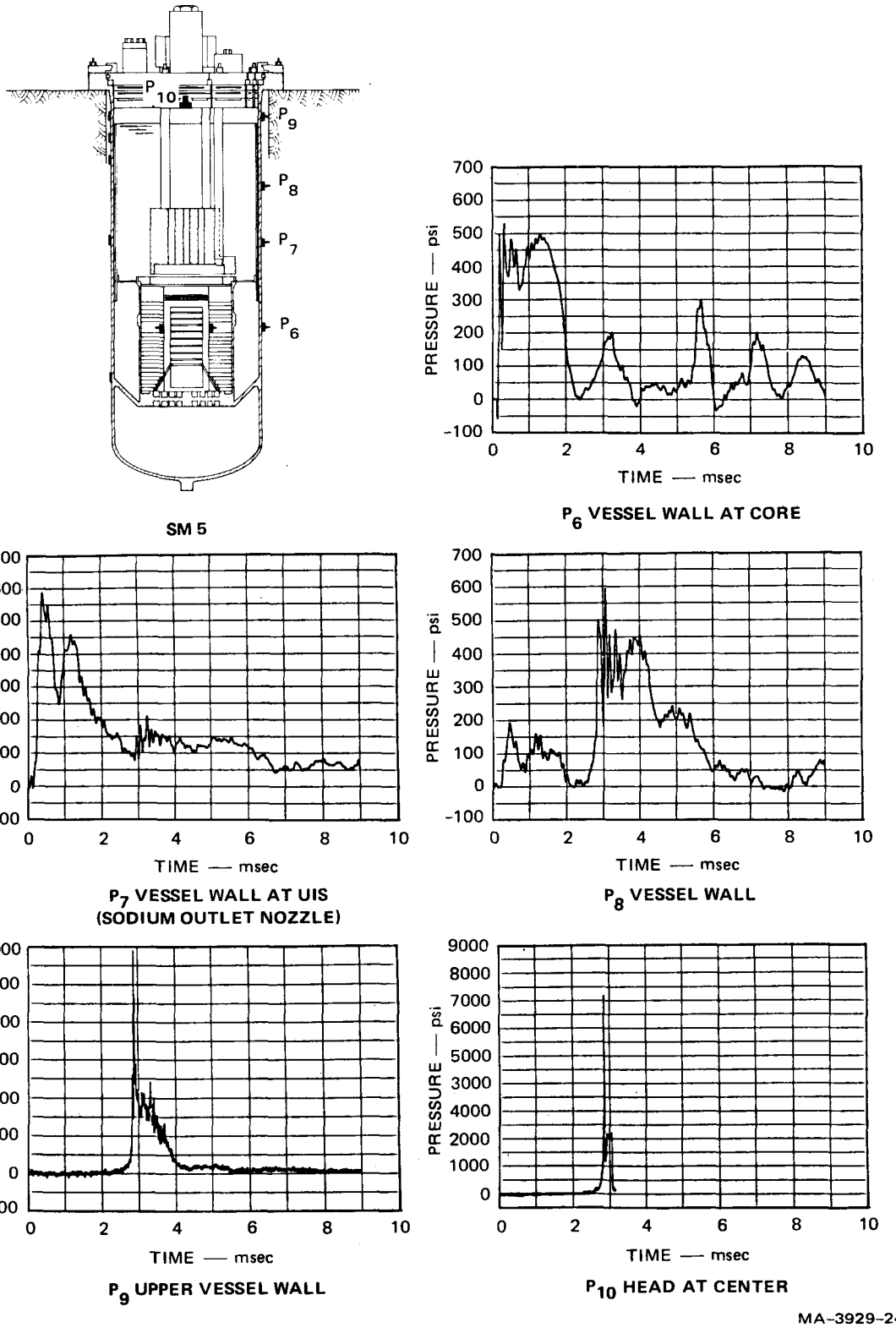

FIGURE D.25 PRESSURE RECORDS FOR SM 5 (Continued)

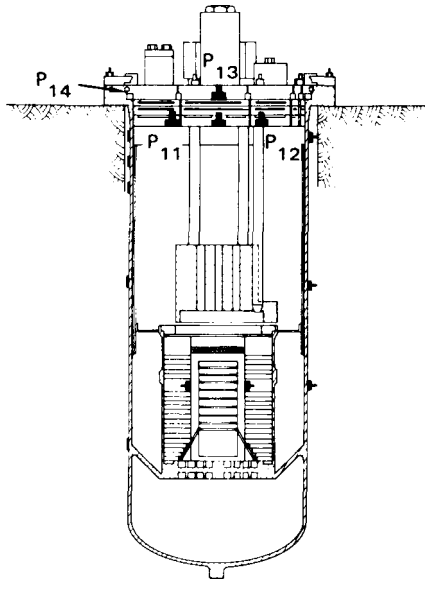

SM 5

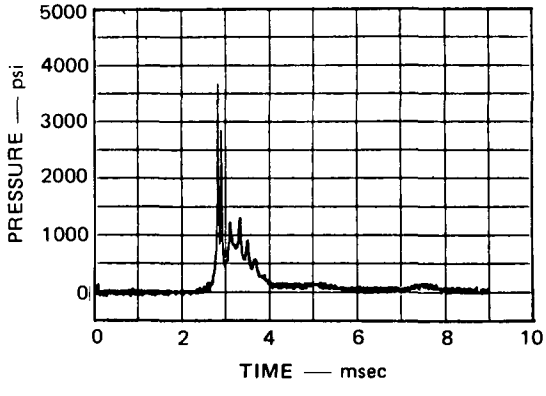

P_{11} HEAD—LRP

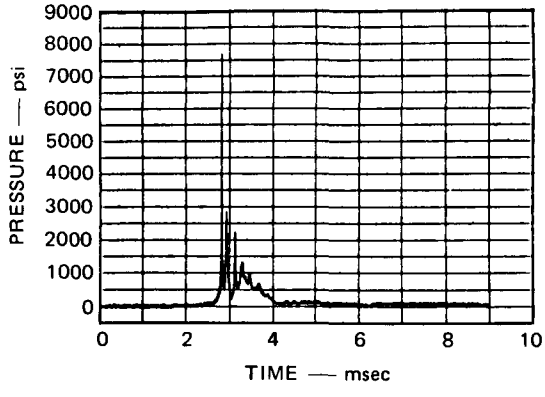

P_{12} HEAD—SRP

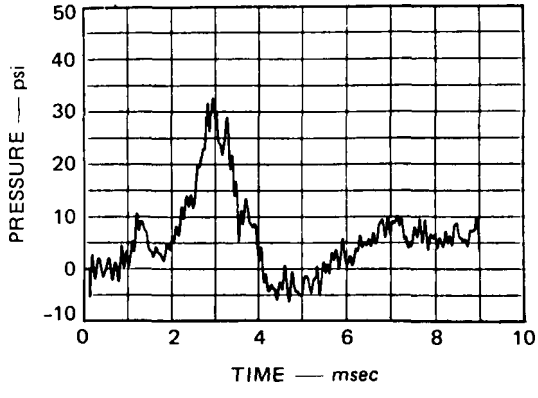

P_{13} HEAD—AIR GAP AT CENTER

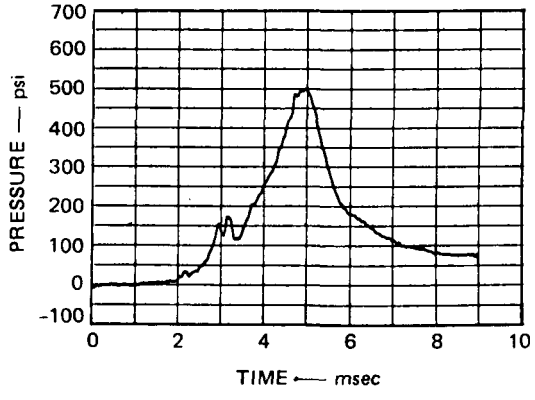

P_{14} FLANGE—AIR GAP

MA-3929-241

FIGURE D.25 PRESSURE RECORDS FOR SM 5 (Continued)

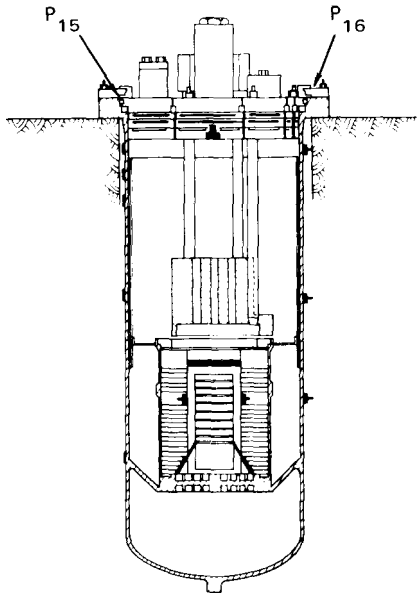

SM 5

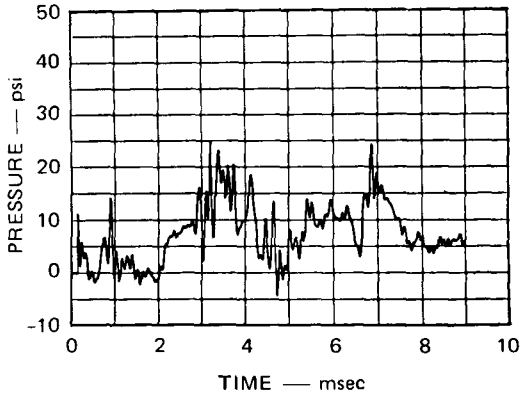

P_{15} FLANGE RING AIR GAP (180°)

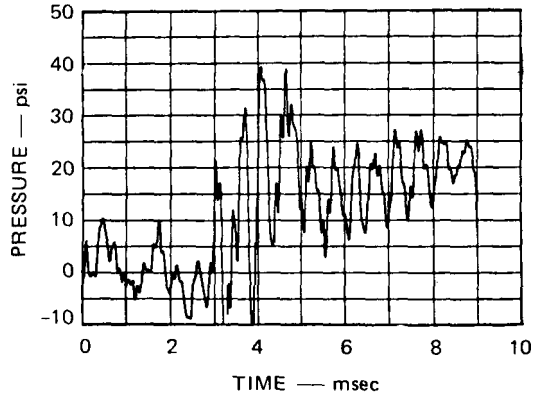

P_{16} FLANGE RING AIR GAP (0°)

MA-3929-242

FIGURE D.25 PRESSURE RECORDS FOR SM 5 (Concluded)

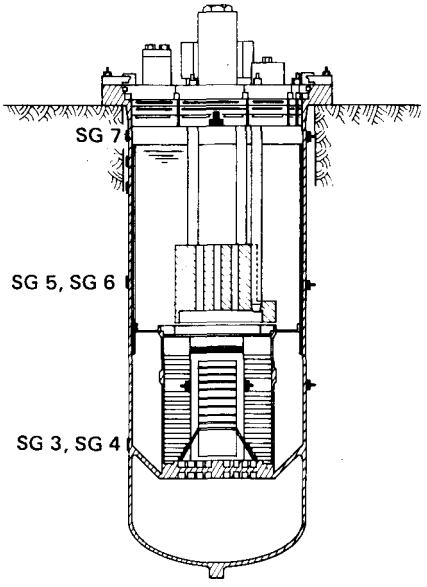

SM 5

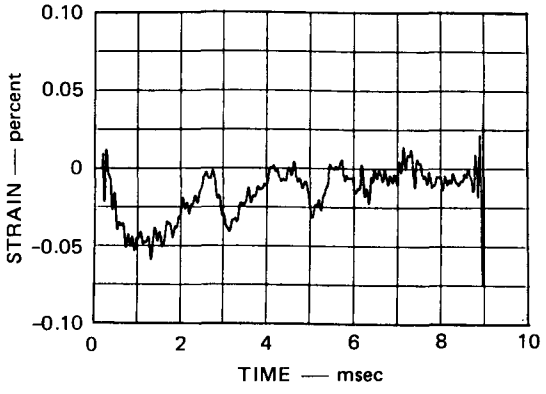

SG 3 CORE SUPPORT RING (C)

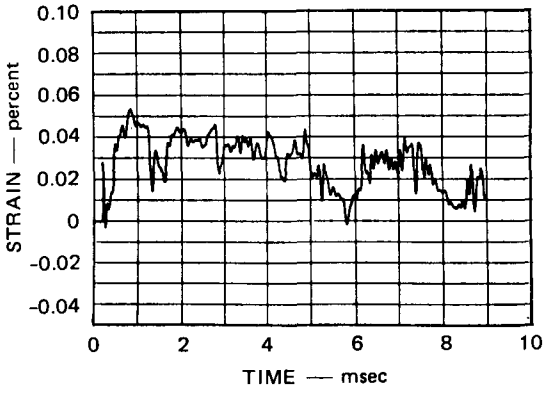

SG 4 CORE SUPPORT RING (A)

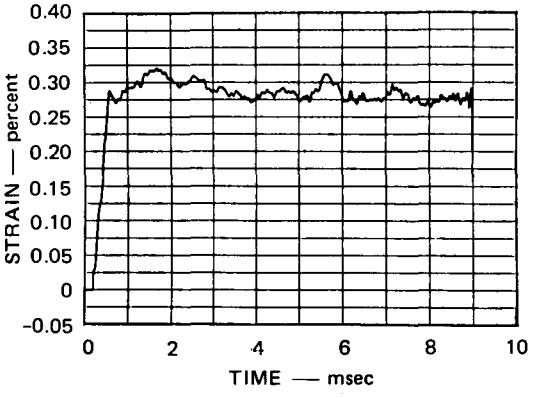

SG 5 VESSEL WALL AT UIS (C)
(SODIUM OUTLET NOZZLE)

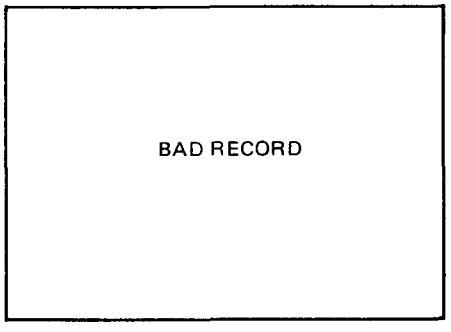

SM 6 VESSEL WALL AT UIS (A)
(SODIUM OUTLET NOZZLE)

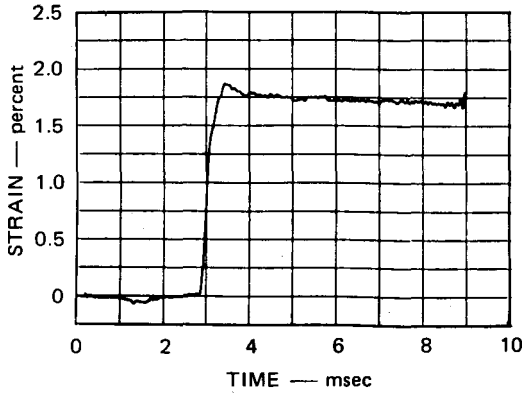

SG 7 UPPER VESSEL WALL (C)

MA-3929-243

FIGURE D.26 STRAIN RECORDS FOR SM 5

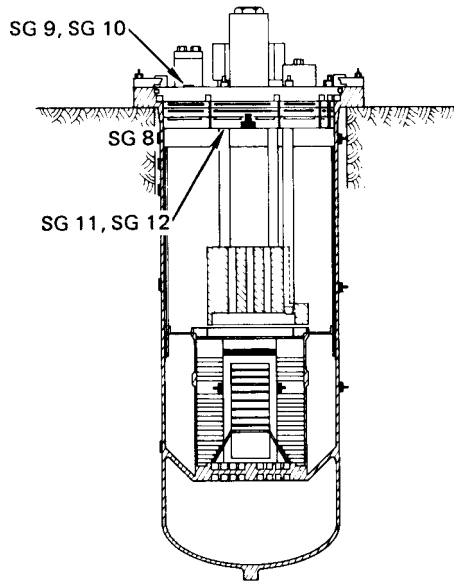

SM 5

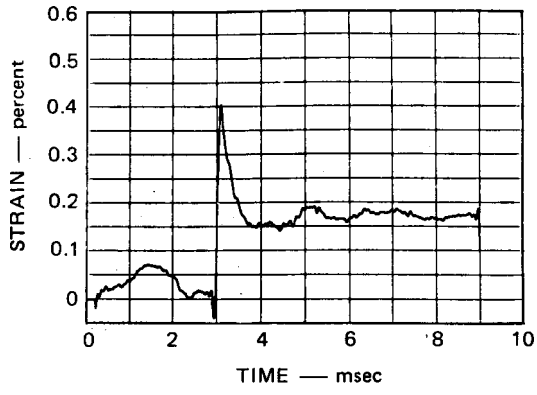

SG 8 UPPER VESSEL WALL (A)

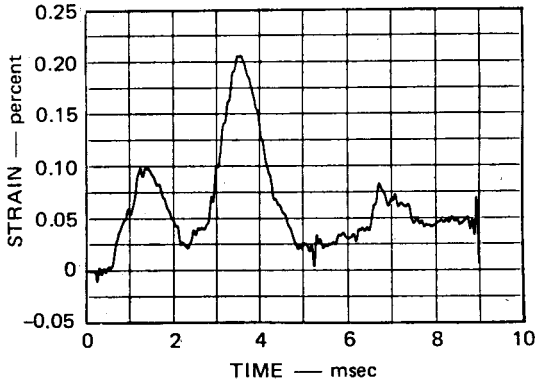

SG 9 LRP (θ)

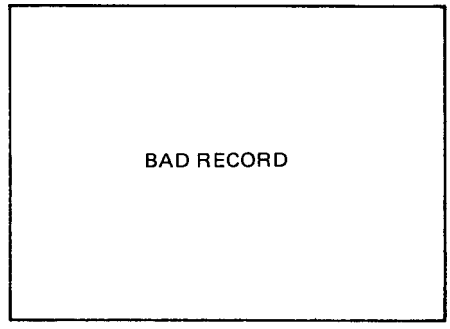

SG 10 LRP (R)

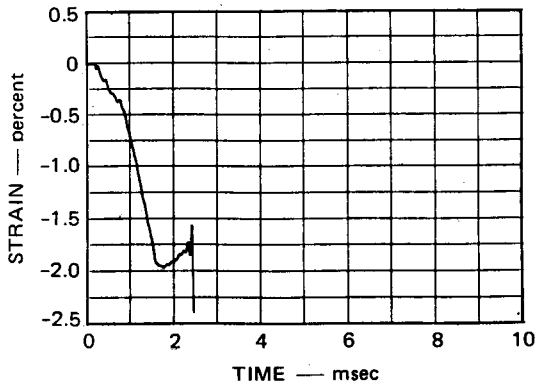

SG 11 UIS COLUMN 1 (A)

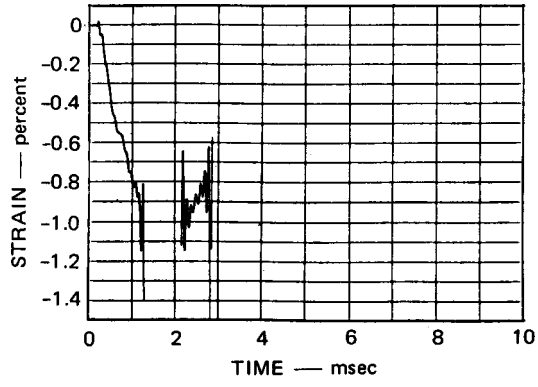

SG 12 UIS COLUMN 1 (A)

MA-3929-244

FIGURE D.26 PRESSURE RECORDS FOR SM 5 (Continued)

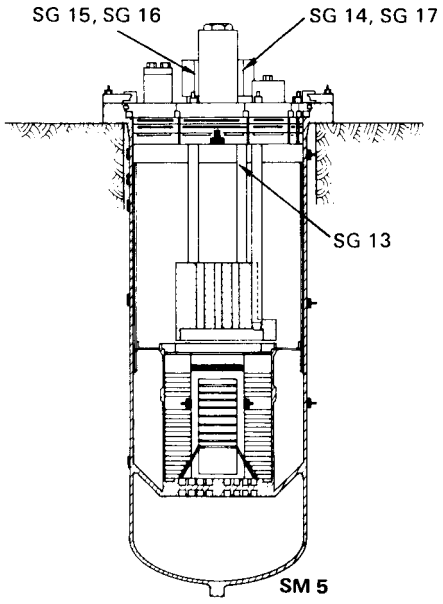

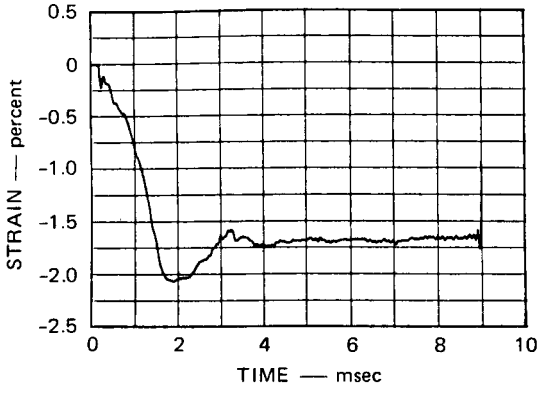

SG 13 UIS COLUMN 1 (A)

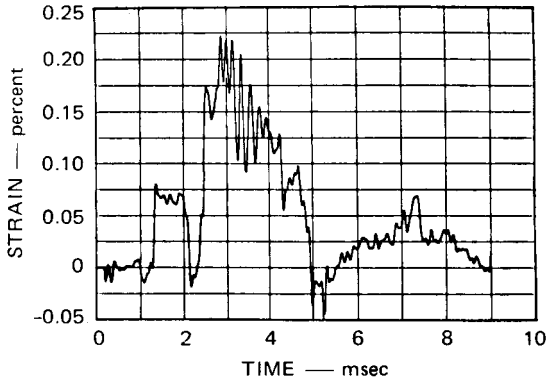

SG 14 UIS COLUMN 1 (TOP)

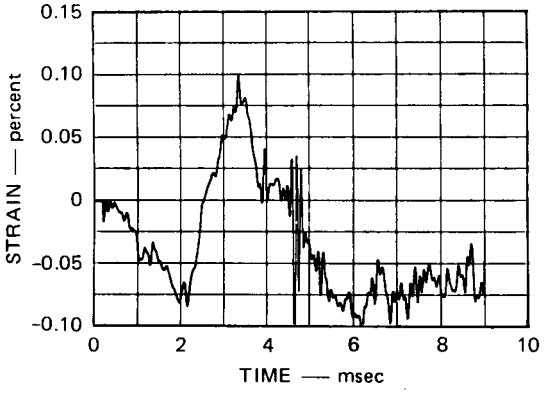

SG 15 UIS COLUMN 2 (TOP)

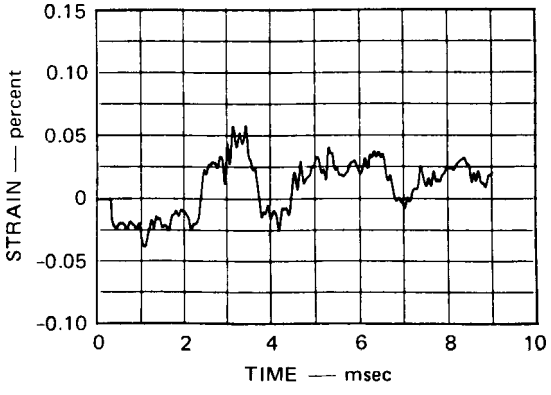

SG 16 UIS COLUMN 3 (TOP)

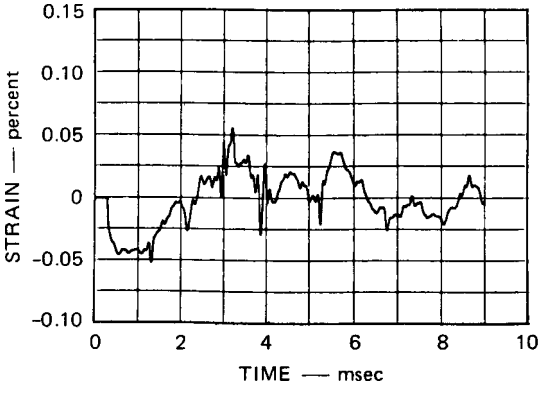

SG 17 UIS COLUMN 4 (TOP)

MA-3929-245

FIGURE D.26 STRAIN RECORDS FOR SM 5 (Continued)

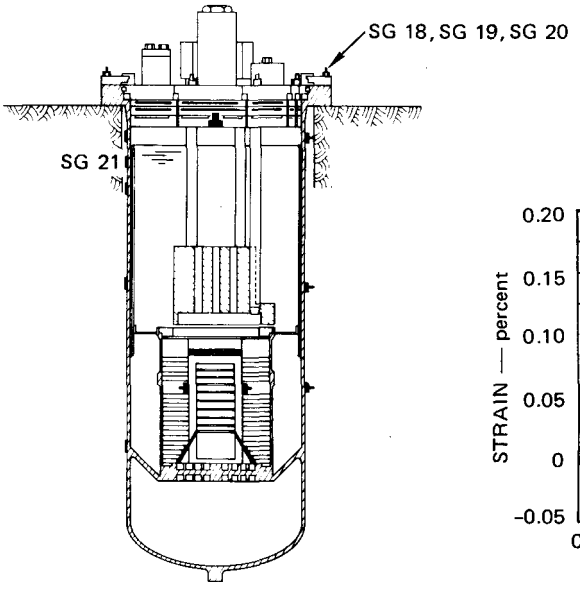

SM 5

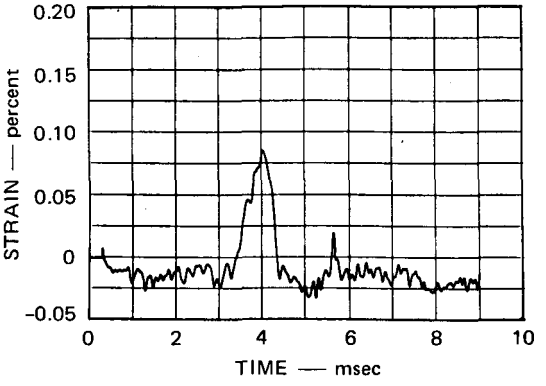

SG 18 STUD (60°)

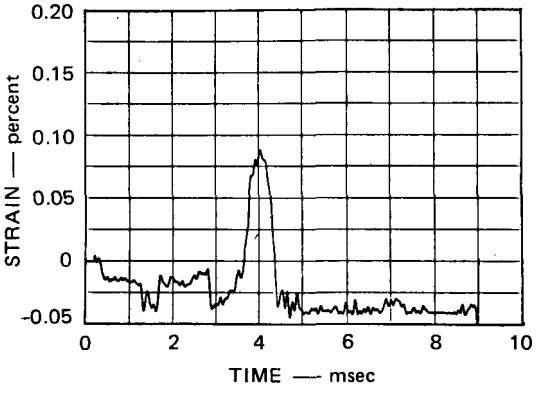

SG 19 STUD (180°)

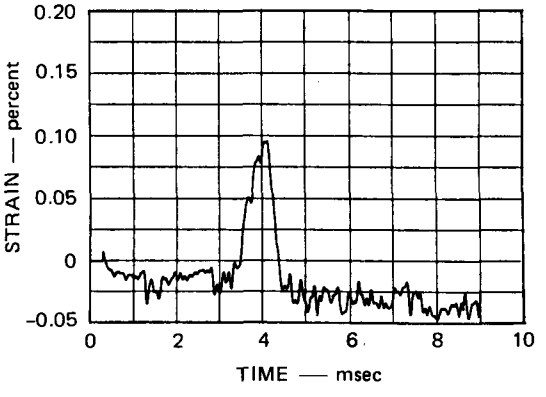

SG 20 STUD (300°)

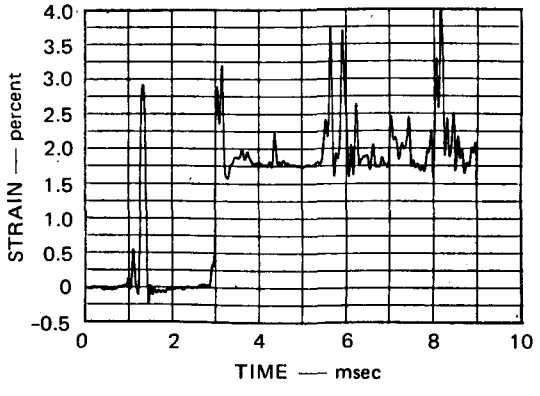

SG 21 VESSEL WALL AT PEAK

MA-3929-246

FIGURE D.26 STRAIN RECORDS FOR SM 5 (Concluded)

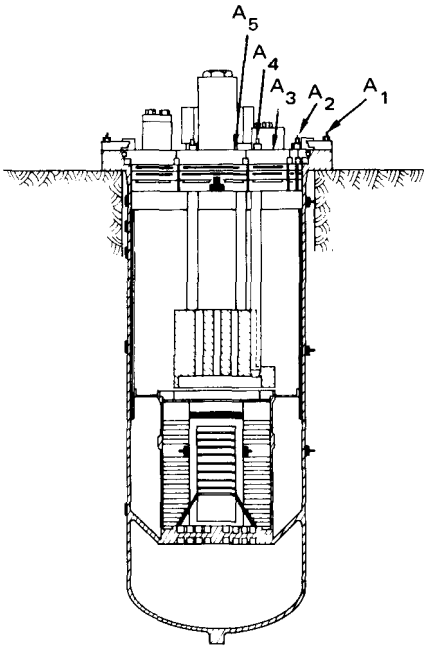

SM 5

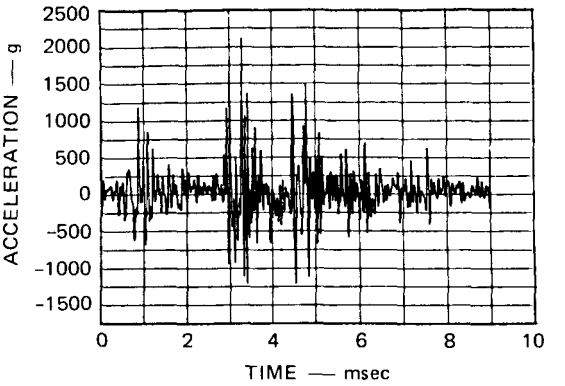

A_1 FLANGE RING 0°

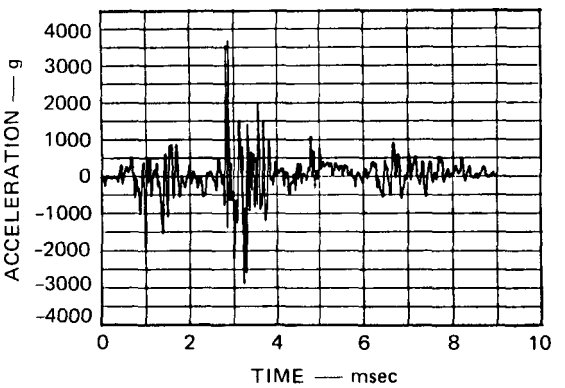

A_2 IRP AT 0°

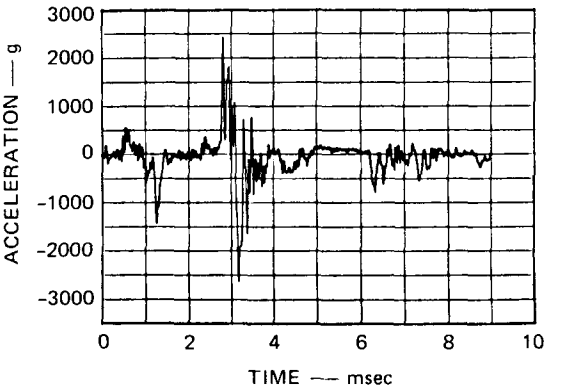

A_3 SRP NEAR IRP 0°

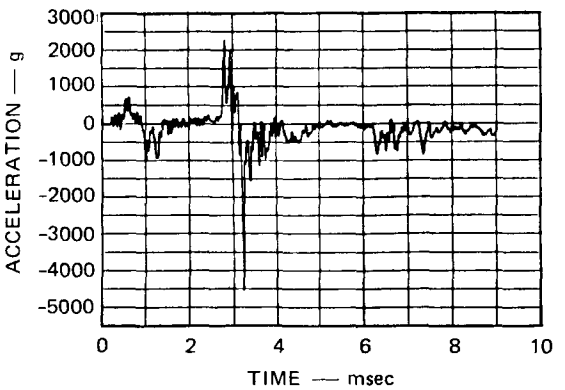

A_4 SRP NEAR IRP 180°

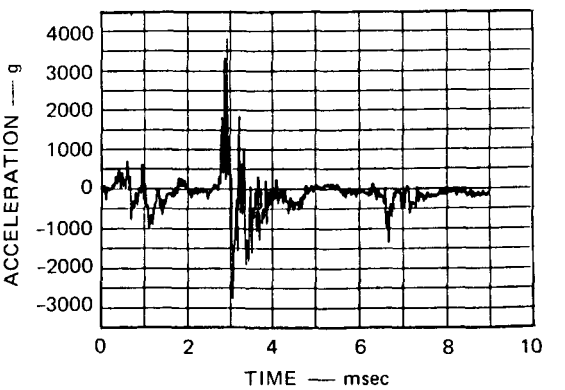

A_5 IRP NEAR CENTER

MA-3929-247

FIGURE D.27 ACCELEROMETER RECORDS FOR SM 5

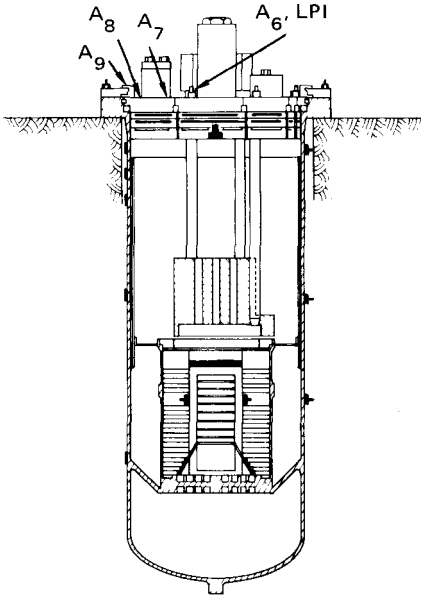

SM 5

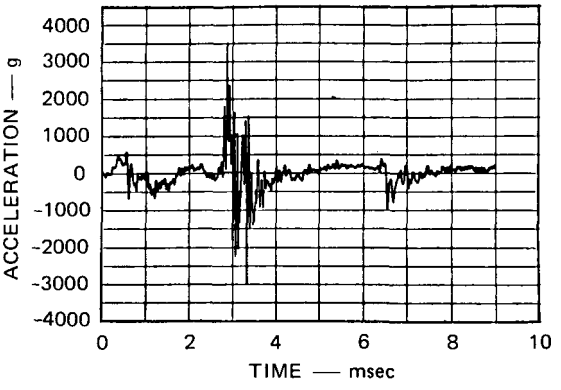

A_6 IRP NEAR LRP -180°

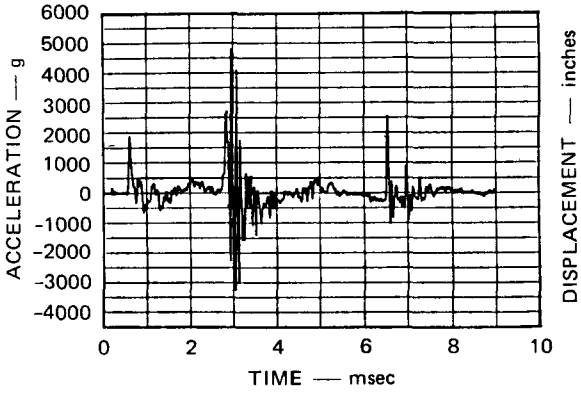

A_7 LRP NEAR IRP

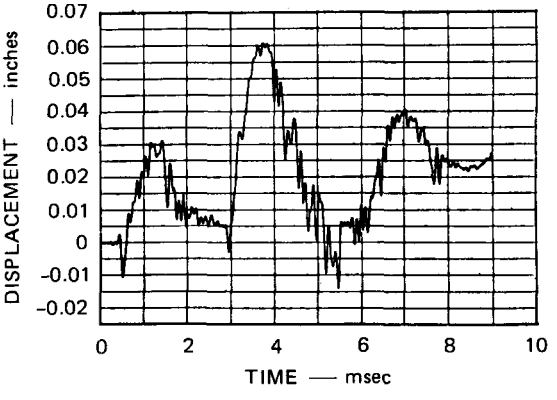

LPI NEXT TO A_6

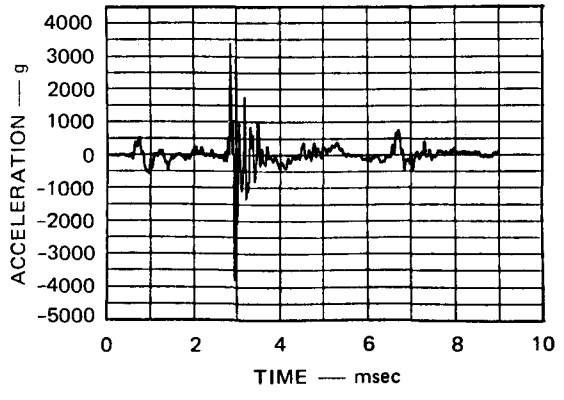

A_8 LRP NEAR EDGE

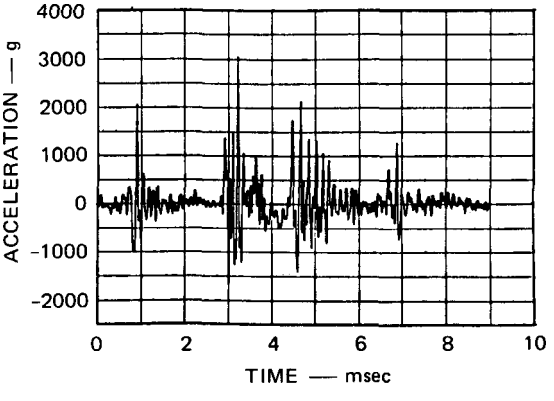

A_9 FLANGE RING 180°

MA-3929-248

FIGURE D.27 ACCELEROMETER RECORDS FOR SM 5 (Concluded)

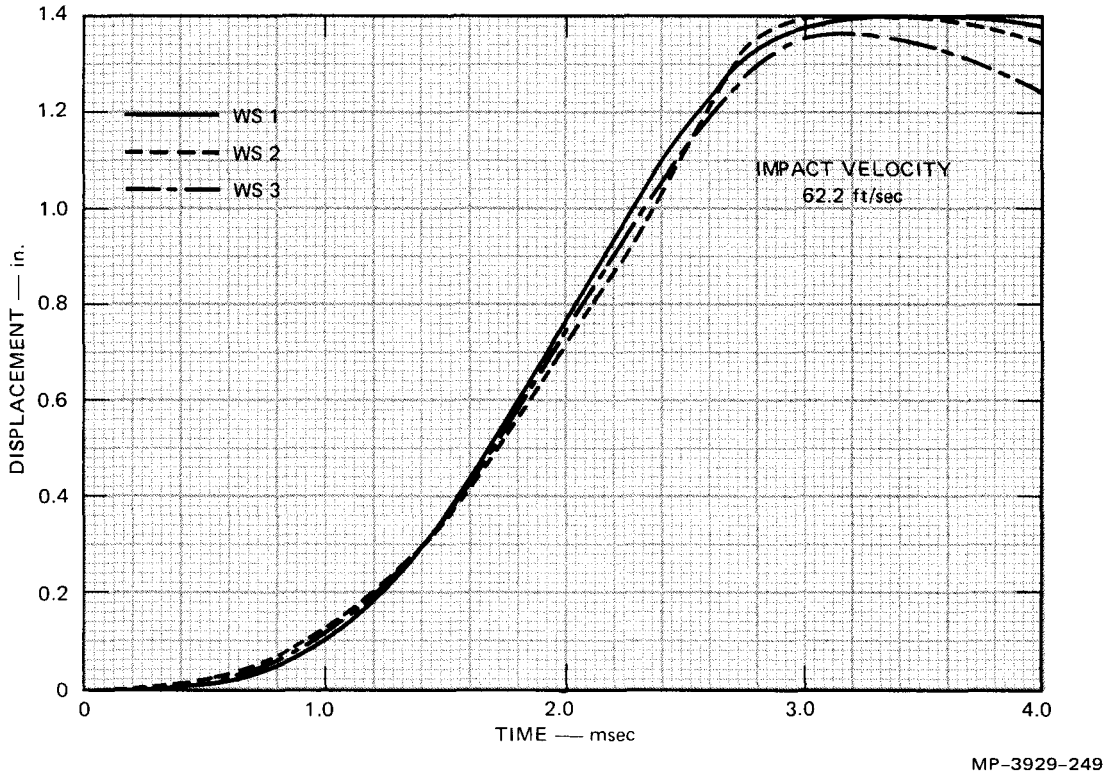

FIGURE D.28 WATER SURFACE DISPLACEMENT FOR SM 5

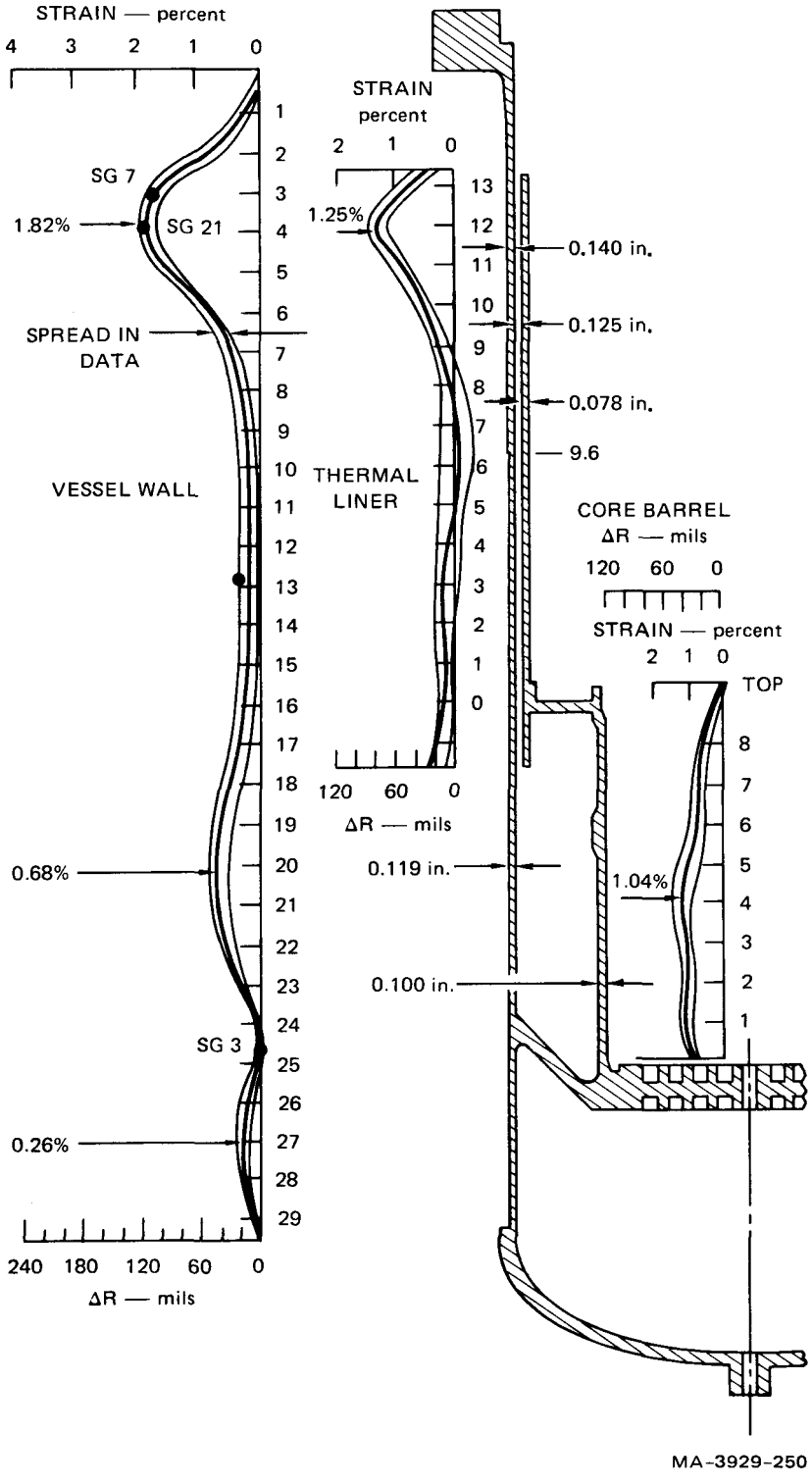

FIGURE D.29 DEFORMED SHAPE PROFILE FOR SM 5

Table D.8

RADIAL DISPLACEMENT OF THE VESSEL WALL OF SM 5

Point[a]	Meridian 1	2	3	4	5	6	Average
1	4.5[b]	7.5	1.0	1.5	3.5	7.5	4.25
2	-	42.5	35.0	36.0	37.5	42.5	38.70
3	102.0	95.0	88.0	91.5	88.0	92.0	92.75
4	119.0	118.5	111.0	109.0	104.0	106.0	111.25
5	94.5	91.0	89.5	87.5	81.5	83.5	87.92
6	-	50.5	51.5	47.5	48.0	45.5	48.60
7	34.5	25.5	23.5	21.0	24.0	24.5	25.50
8	25.0	16.5	12.0	12.5	15.0	17.0	16.33
9	22.0	13.0	8.0	7.0	11.0	13.5	12.42
10	18.5	9.5	4.5	3.0	7.5	12.0	9.17
11	16.0	6.0	2.0	0	5.5	11.0	6.75
12	19.0	5.5	1.5	0.5	5.5	11.5	7.25
13	-	6.0	2.0	2.0	6.0	12.5	5.70
14	17.0	6.5	2.0	5.0	6.5	14.0	8.50
15	17.5	7.0	3.0	7.5	9.0	17.5	10.25
16	20.0	10.0	4.5	11.0	13.0	21.5	13.33
17	24.0	15.5	10.0	15.5	16.0	26.0	17.83
18	36.0	25.0	18.5	30.0	27.5	35.0	28.67
19	45.0	34.5	27.0	40.5	35.5	45.5	38.17
20	-	40.0	31.0	-	40.0	50.0	40.25
21	44.0	39.5	29.5	40.0	38.0	48.0	39.83
22	31.0	29.5	21.5	-	26.5	34.0	28.50
23	12.5	10.5	7.5	12.0	7.5	10.5	10.08
24	-2.0	-1.5	-1.0	-0.5	-0.5	-1.0	-1.08
25	-	-	-	-	-	-	-
26	4.0	7.5	7.5	3.0	10.5	6.5	6.5
27	8.5	18.5	19.5	9.5	24.0	13.0	15.50
28	-	15.0	19.0	10.0	20.0	11.0	15.00
29	4.5	4.5	5.5	3.0	5.5	3.0	4.33

[a]See Figure D.29 for axial location of points.

[b]Displacement in mils.

Note: Average radius of model is 6.148 inches.

Table D.9

RADIAL DISPLACEMENT OF THE THERMAL LINER OF SM 5

Point[a]	Meridian 1	2	3	4	5	6	Average
1	12.5[b]	-1.0	3.5	4.5	2.5	7.0	4.83
2	14.0	-0.5	3.0	2.5	3.5	5.0	4.58
3	16.5	-2.0	1.5	-2.0	2.0	3.5	3.25
4	17.0	-4.5	-0.5	-6.5	1.0	2.0	1.42
5	14.5	-6.5	-4.0	-10.5	0	0	-1.08
6	11.5	-7.5	-6.5	-20.0	-1.5	-3.5	-4.58
7	10.0	-6.0	-5.0	-22.0	0.5	-3.0	-4.25
8	10.0	-2.5	-1.5	-13.5	2.5	2.5	-0.42
9	18.0	7.0	8.0	2.0	12.0	10.0	9.50
10	39.0	29.0	27.5	26.5	35.0	27.0	30.67
11	60.5	59.0	52.5	52.0	61.5	56.0	56.92
12	75.0	81.0	70.0	68.5	76.0	74.0	74.08
13	52.0	49.0	44.0	44.0	45.5	46.5	46.83
TOP	23.5	13.5	6.5	10.0	18.5	12.5	14.08

[a] See Figure D.29 for axial location of points.

[b] Displacement in mils.

Note: Average radius of model is 5.912 inches.

Table D.10

RADIAL DISPLACEMENT OF THE CORE BARREL OF SM 5

Point[a]	Meridian 1	2	3	4	5	6	Average
0	30.5[b]	28.5	28.0	27.5	27.0	24.5	27.67
1	38.5	38.0	41.0	36.0	38.0	30.5	37.00
2	41.5	33.5	41.0	36.5	41.0	29.5	37.17
3	36.5	35.0	44.0	7.0[c]	46.0	29.5	38.20
4	39.6	29.0	49.0	48.0	47.5	32.0	40.83
5	39.5	20.0	41.0	45.5	41.5	24.0	35.25
6	24.0	19.0	29.0	28.5	29.5	20.5	25.08
7	25.0	21.0	30.5	23.5	30.0	23.0	25.50
8	12.5	15.0	21.5	15.5	18.5	11.0	15.67
TOP	-3.0	-2.0	-1.0	1.0	-2.0	-4.0	-1.83

[a]See Figure D.29 for axial location of points.

[b]Displacements in mils.

[c]Data point not used.

Note: Average radius of model is 3.836 inches.

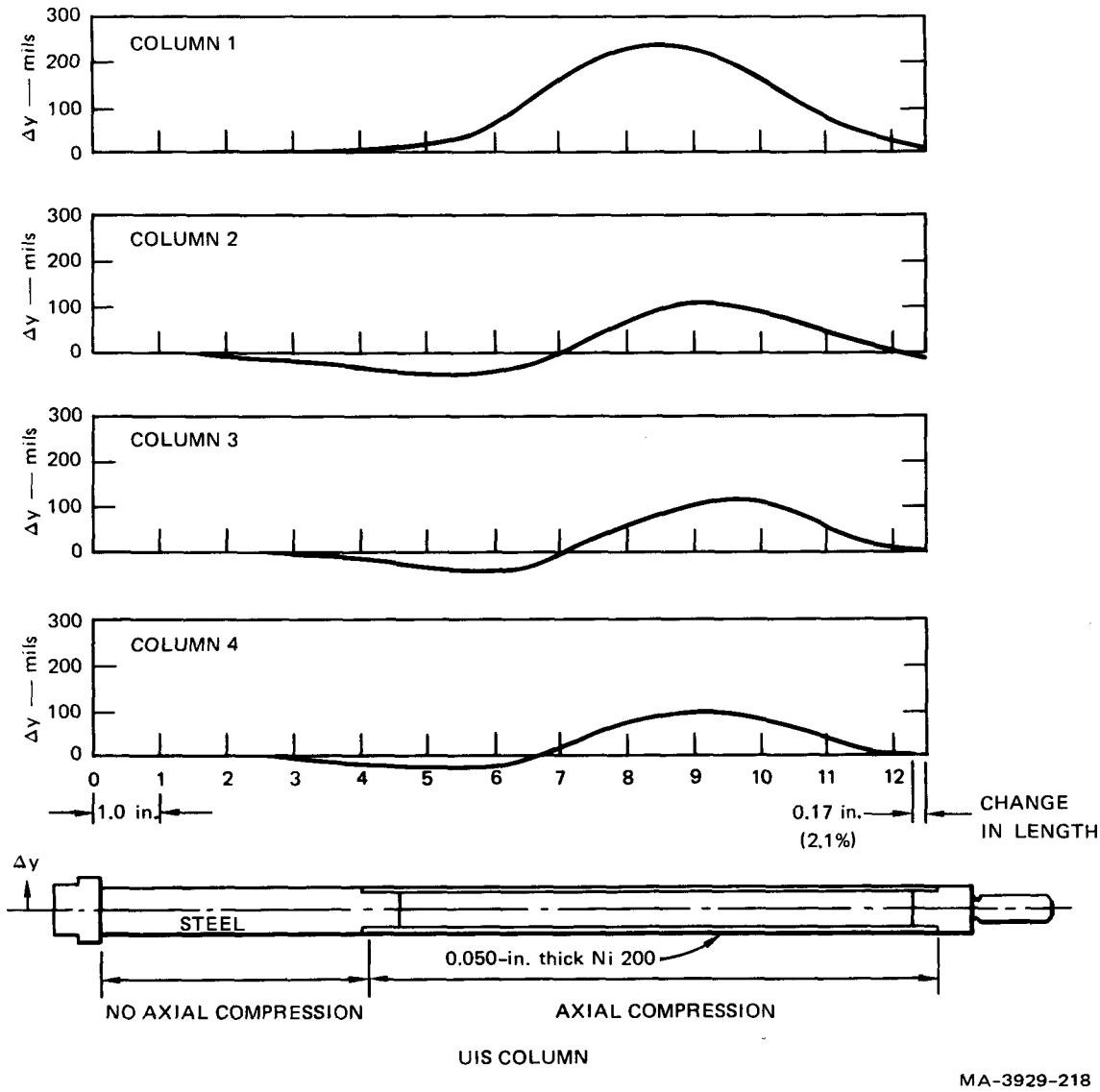

FIGURE D.30 DEFORMED SHAPE PROFILE OF SM 5 UIS COLUMNS

Appendix E

DATA ANALYSIS

In the choice and development of data recording and processing techniques, it is important to consider all structural response frequencies to ensure that important modes are not filtered out of the data by either the recording system (transducers, signal conditioning, and tape recorder), the playback system (tape recorder, analog-to-digital converter) or the selection of cutoff frequencies for the digital filters. Table E.1 lists the important wave transit times and structural response frequencies for SM 2. Response times and wave transit times for the other simple models are similar.

Table E.2 lists the cutoff frequencies of the recording and playback equipment along with the cutoff frequency of the analog-to-digital (A/D) converter and the frequency response of the pressure and accelerometer transducers. The recording and digitizing frequencies are much higher than any of the structural response frequencies, so no important structural response modes are filtered out during the recording and playback of the data. The natural frequencies of the transducers are also much higher than any structural response frequency. However, shock loading can excite these transducers at high frequencies, resulting in an apparent noisy signal. Special digital filters were used on the digitized data to eliminate the high frequency noise from the records.

The digital filter program "filters" digital data in a manner analogous to electronic filtering of analog data. The method of filter-simulation is based on a numerical technique called the Fast Fourier Transform (FFT). Because the FFT has properties similar to those of a Fourier integral transform, the program also provides a power spectrum of the unfiltered and filtered signal.

Table E.1

RESPONSE FREQUENCIES FOR SM MODELS

Item	Key Dimension (inches)	Waves Period[a] (m sec)	Waves Frequency (Hz)
Vessel (length)	25	0.260	3,850
Head (thickness)	2.9	0.030	33,333
Platform (thickness)	2.0	0.020	50,000
Slug	12.9	0.430	2,325
Water between core barrel and vessel wall	2.1	0.070	14,285
		Structural Response	
Vessel (hoop mode)	12.15	0.198	5,030
Vessel (axial mode)	25	1.703	587
Head (SM 2)	2.9	0.298	3,354
Head (SM 4)	2.9	2.710	369
Platform	2.0	0.310	3,219

[a]Round Trip

Table E.2

FREQUENCY RESPONSE OF INSTRUMENTATION

Instrument	Frequency Response (Hz)	Useful Frequency Range (Hz)
Tape recorder	80,000	60,000
Visicorder[a]	133,000	100,000
A/D sampler	80,000	80,000
Pressure gages	90,000[b]	90,000[c]
Accelerometers	16,000[b]	16,000[c]

[a] For tape playback speed reduction of 32:1.

[b] Natural frequency.

[c] 1/5 of natural frequency.

A sample of the digital filtering process is shown in Figure E.1. Figure E.1(a) is the digitized input waveform, an accelerometer record from SM 5. The record contains noise, which may be from ringing of the accelerometer and its mount. The number of data points (N) in the input waveform is 2048, and the points are evenly spaced over a sampling interval of 12.8 ms (6.25 μsec per sample).

Figure E.1(b) is the FFT of the sampled data. The spectrum represented in Figure E.1(b) is an approximation of the coefficients of the ordinary Fourier Transform of the continuous waveform.* An estimate of the Fourier Coefficients is given by F.C. = 2 x FFT coef $\sqrt{N}$ for $\omega \neq 0$, and F.C.= FFT coef/$\sqrt{N}$ for $\omega = o$. The spectrum in Figure E.1(b) shows the high frequency noise especially around 70 kHz, which is near the resonant frequency of the gage.

The data are filtered by multiplying the FFT of the input waveform by an attenuation characteristic. The characteristic now in the program simulates a low pass filter with no attenuation below a specified cutoff frequency (COF) and with attenuation at a specified rate (db/octave) bove the cutoff frequency. Figure E.1(c) shows the attenuated spectrum for a COF of 16 kHz** and an attenuation rate of 60 db/octave above 16 kHz. Figure E.1(d) is the inverse of the transform of the attenuated signal (the filtered record) showing the effect of filtering. Most of the high frequency content has been removed leaving a record that more clearly represents the response of the structure. All of the data on the simple model experiments were digitally filtered with the technique described above. Table E.3 lists the cutoff frequencies used on each gage record. In general, pressure and strain records were filtered at 10 kHz; accelerometer records at 16 kHz. The cutoff frequency for filtering pressure and strain records was selected to eliminate background noise from the records and still be high enough to ensure that

---

*The spectrum band width is limited to N/2T.

**The linear response range of the accelerometer is limited to 1/5 of the natural frequency of the gage, which is 80 kHz; 1/5 of 80 kHz is 16 kHz.

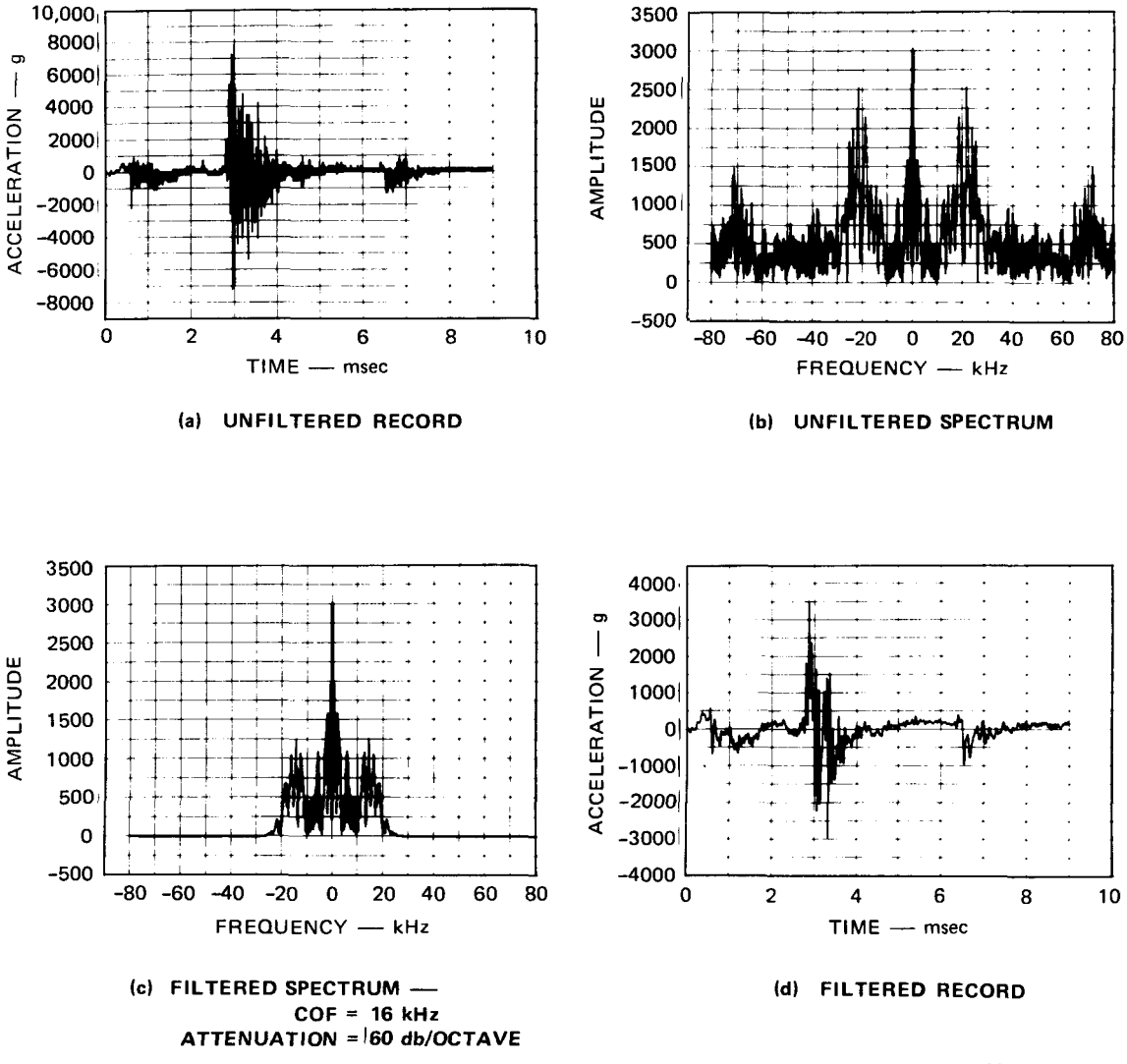

FIGURE E.1 SAMPLE OF DIGITAL FILTERING SEQUENCE

Records are for A6 on SM 5

important structural response modes were not attenuated by the filter. On selected pressure records on the cover and the upper vessel wall, the cutoff frequency was raised to 25 kHz or 50 kHz to preserve the spike loading from slug impact. Figure E.2 shows examples of the unfiltered and filtered pressure, strain, and accelerometer records.

Table E.3

DIGITAL FILTER CUT OFF FREQUENCIES FOR TEST DATA

Gage No.					Filter Frequency--kHz			
SM 2	SM 3	SM 4	SM 5	Location	SM 2	SM 3	SM 4	SM 5
P_1	P_1	P_1	P_1	Core	10	10	10	10
P_2	P_2	P_2	P_2	Core	10	10	10	10
P_3	P_3			Upper core	10	10		
			P_3	Lower UIS				10
			P_4	Upper UIS				10
			P_5	Lower vessel				10
P_4	P_4	P_3	P_5	Vessel wall at core	10	10	10	10
P_5	P_3	P_4	P_7	Vessel wall at UIS	10	10	10	10
P_6	P_6		P_8	Vessel wall	10	10	10	10
P_7	P_7	P_5	P_8	Upper vessel wall	25	25	25	25
P_8	P_8	P_6	P_{10}	Head (center)	25	25	25	50
			P_{11}	Head (LRP)				50
			P_{12}	Head (SRP)				50
			P_{13}	Head air gap (center)				10
			P_{14}	Flange air gap				10
			P_{15}	Flange ring gap (180°)				10
			P_{16}	Flange ring gap (0°)				10
			SG1	Core barrel (C)				-
			SG2	Core barrel (A)				-
		SG1	SG3	Core support ring (C)			10	10
		SG2	SG4	Core support ring (A)			10	10
SG1	SG1			Vessel wall at core (C)	10	10		
SG2	SG2	SG3	SG5	Vessel wall at UIS (C)	10	10	10	10
SG3	SG3	SG4	SG6	Vessel wall at UIS (A)	10	10	10	-
SG4	SG4			Vessel wall	10	10		
SG10		SG10	SG21	Vessel at peak ε (C)	10		10	10
SG5	SG5	SG5	SG7	Upper vessel wall (C)	10	10	10	10
SG6	SG6	SG6	SG8	Upper vessel wall (A)	10	10	10	10
			SG9	LRP (θ)				-
			SG10	LRP (R)				-
			SG11	UIS column (Ni200)				10
			SG12	UIS column (Ni200)				-
			SG13	UIS column (Ni200)				10
			SG14	UIS column 1 (cap)				10
			SG15	UIS column 2 (cap)				10
			SG16	UIS column 3 (cap)				10
			SG17	UIS column 4 (cap)				10

(Continued)

Table E.3 (Concluded)

Gage No.					Filter Frequeincy kHz			
SM 2	SM 3	SM 4	SM 5	Location	SM 2	SM 3	SM 4	SM 5
SG7	SG7	SG7	SG18	Stud 60^{o}	10	10	10	10
SG8	SG8	SG8	SG19	Stud 180^{o}	10	10	10	10
SG9	SG9	SG9	SG20	Stud 300^{o}	10	10	10	10
			A_1	Flange ring (0^{o})				16
A_1	A_1		A_2	IRP at 0^{o}	16	16		16
			A_3	SRP near IRP (0^{o})				16
A_2	A_2	A_1	A_4	SRP near IRP (180^{o})	16	16	16	16
			A_5	IRP near center				16
A_3	A_3	A_2	A_6	IRP near LRP (180^{o})	16	16	16	16
		A_3	A_7	LRP near IRP (0^{o})			16	16
			A_8	LRP near edge (180^{o})				16
			A_9	Flange ring (180^{o})				16
A_4	A_4		A_{10}	Platform	16	16		16
			LP1	Next to A_6				10
IV	IV	IV	IV					
				Impact time				

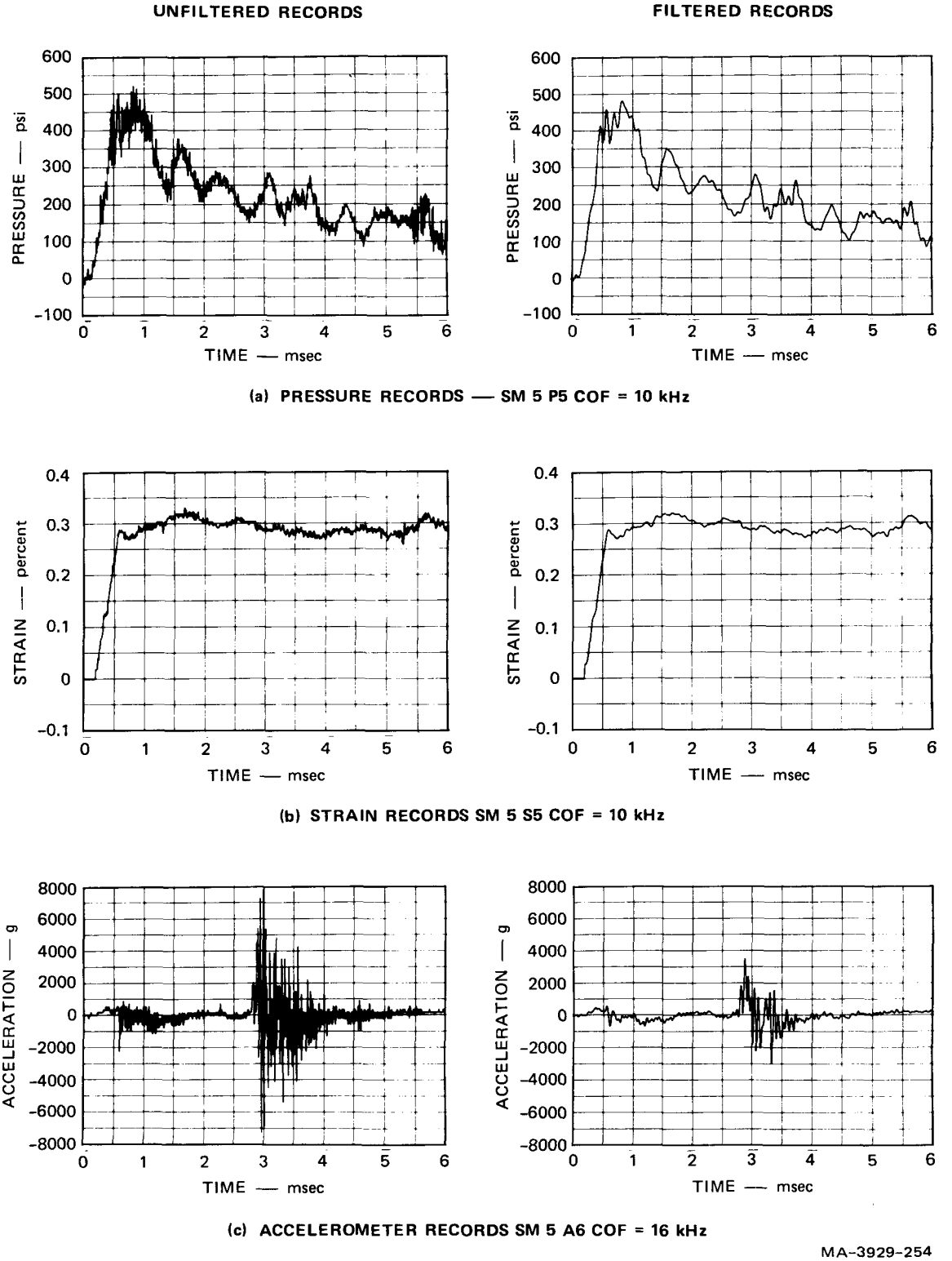

FIGURE E.2 SAMPLES OF UNFILTERED AND FILTERED RECORDS

Appendix F

EXPERIMENTAL ACCURACY

To establish experimental accuracy, one must consider the accuracy of both instrumentation and interpretation of the experimental work. The accuracy of individual gages is determined based on repeated calibration of the gages. In addition, the accuracy of the recording, playback, and digitization equipment is evaluated. Together, these establish the instrumentation accuracy. The reproducibility of individual experiments is considered to establish bounds on such information as the material properties of the models, the energy release from the explosive as measured by the pressure-volume change relationships obtained during calibration tests and simple model tests, and pre- and posttest measurement of weights and dimensions of the models. These establish the interpretation accuracy.

Table F.1 lists the instrumentation accuracy for gages and recording equipment. This information is based on repeated use and calibration of the individual gages and on an overall evaluation of the recording system.

Table F.2 lists the bounds on data obtained from supportive experiments that affect the overall evaluation of the accuracy of the simple model experiments.

Table F.1

ACCURACY OF INSTRUMENTATION

System	Error Band[a]	Devices Considered
Pressure gages[b]	±2%	Gages, calibration system
Strain gages[c]	±2%	Gages
Accelerometers[d]	±5%	Gages, calibration system
Water surface gages[e]	±5%	Gages, calibration system, data reduction system
Linear displacement gages[e]	±2%	Calibration system
Light ladder[f]	±5%	Machining process, data reduction system
Tape recorder scale[g]	±3%	Electronic support equipment
A/D scale[h]	±2%	Sampler, computer system

[a] Errors in systems when noise levels negligible

[b] Based on several pre- and posttest measurements of gage factor

[c] Based on precision of gage factor and on final measurements in simple geometries

[d] Based on factory specifications

[e] Based on calibration records

[f] Based on slit spacing and data interpretation

[g] Based on manufacturer's specifications. Tape system checked before experiment series

[h] Average data read to ±2 counts out of 100 counts

Table F.2

BOUNDS ON EXPERIMENT EVALUATION

Experiment	Error Band	Systems Evaluated
Material property tests	±10%	Testing machine, extensometer, heat treating process
Pressure-volume change	± 5%	Pressure gages, light ladder, water displacement gage, analysis of records
Pre- and posttest dimensions	± 2%	Measuring devices, tolerances on models, out-of-roundness

Appendix G

SCALING

Table G.1 lists the applications of scale factors for geometrical scaling to various quantities relevant to scale model experiments. Note, that several key quantities (density, velocity, pressure, stress, and strain) are unaffected by geometric scaling. Other quantities like strain rate and acceleration do not scale directly with geometric scaling. Quantities that are affected by strain rate or gravity do not scale.

Table G.1

APPLICATION OF SCALE FACTORS[a]

Quantity	Prototype Quantity / Model Quantity	Example $\lambda = 20$
Length	λ	20
Area	λ^2	400
Volume	λ^3	8000
Mass	λ^3	8000
Density	1	1
Time	λ	20
Displacement	λ	20
Velocity	1	1
Acceleration	$1/\lambda$	1/20
Pressure	1	1
Stress	1	1
Strain	1	1
Force	λ^2	400
Spring Constant	λ	20
Frequency	$1/\lambda$	1/20

[a]Scale Factor: λ - Prototype Dimension/Model Dimension

Appendix H

ANALYSIS OF CRBR HEAD DISPLACEMENT

A primary objective of this program was to evaluate the response of the CRBR head under simulated slug impact loading from a HCDA. The experiments showed that the head responded elastically to slug impact loading from a simulated 661 MW-sec HCDA and demonstrated that the shear rings are able to keep the three-piece head of the CRBR intact. To provide more insight into the deformations produced in the head by slug impact loading and to evaluate the peak loads carried by the shear rings during a 661 MW-sec HCDA, we performed a simple dynamic response analysis of the head.

The objectives of this analysis were to: (1) determine the peak displacement of the head and the peak displacement at the shear ring joint between the large rotating plug (LRP) and the intermediate rotating plug (IRP) during slug impact; (2) determine the response time of the three-piece head of the 1/20-scale CRBR models; (3) determine if sufficient head displacement occurred to cause the joints between the plugs in the head to "lock"; (4) determine the peak shear ring forces under slug impact loading; and (5) determine the static load-deflection properties of the composite three-piece head including shielding.

The approach for this analysis was to first develop a symmetrical three-piece model of the CRBR head that had the same load-deflection properties as the asymmetric CRBR head. A check of this model is provided by comparing calculated quantities with data from the SM 1 test. The symmetric three-piece head was then replaced by a simply supported one-piece plate having the same load-deflection properties as the CRBR head including shielding. Next, the motion of the head under slug impact loading was calculated, using an equivalent single-degree-of-freedom (SDOF) system to simplify the analysis. Finally, the peak load carried

by the shear rings was calculated from the peak reaction forces from the SDOF analysis.

A. Static Load-Deflection Properties of Composite Head

Static loading experiment SM 1 was performed on a 1/20-scale model of the CRBR head. This model did not include the plates that are bolted to the underside of the head to simulate the shielding. An analysis was made to estimate the load-deflection properties of the composite head, which was approximated by the symmetric three-piece plate shown in Figure H.1. The shear rings were approximated by circular hinges. The loads applied to each plug were approximated by circular line loads applied at or near the hinges. The circular line loads at a hing included the resultant pressure applied uniformly to the next smaller plug and the distributed resultant of the pressure pushing up on the annualr plate. This distribution is required because the shielding does not make contact over the entire surface of each annular plate but rather along its inner and outer perimeter. The bending stiffness of the composite plate is the sum of the bending stiffnesses of the individual layers of the composite plate.

As a simple check on this analytical model, the volume under the head of the SM 1 model was calculated and compared with the measured volume change. Very good agreement was achieved when only the bending stiffness of the single layered head of the SM 1 model was used in the analysis.

The volume change under the layered CRBR head caused by doming of the plugs can be expressed by:

$$V_{total} = \frac{2\pi P_o}{64D} \left(1.03 r_{OI}^6 + 1.89 r_{OL}^6\right) \qquad \text{(H-1)}$$

where P_o is the applied pressure, D is the composite bending stiffness of the head = 4.18×10^6 lb-in, r_{OI} is the radius of the IRP, and r_{OL} is the radius of the LRP. In expression (H-1) there is no component of volume change created by doming of the SRP because it is a rigid body

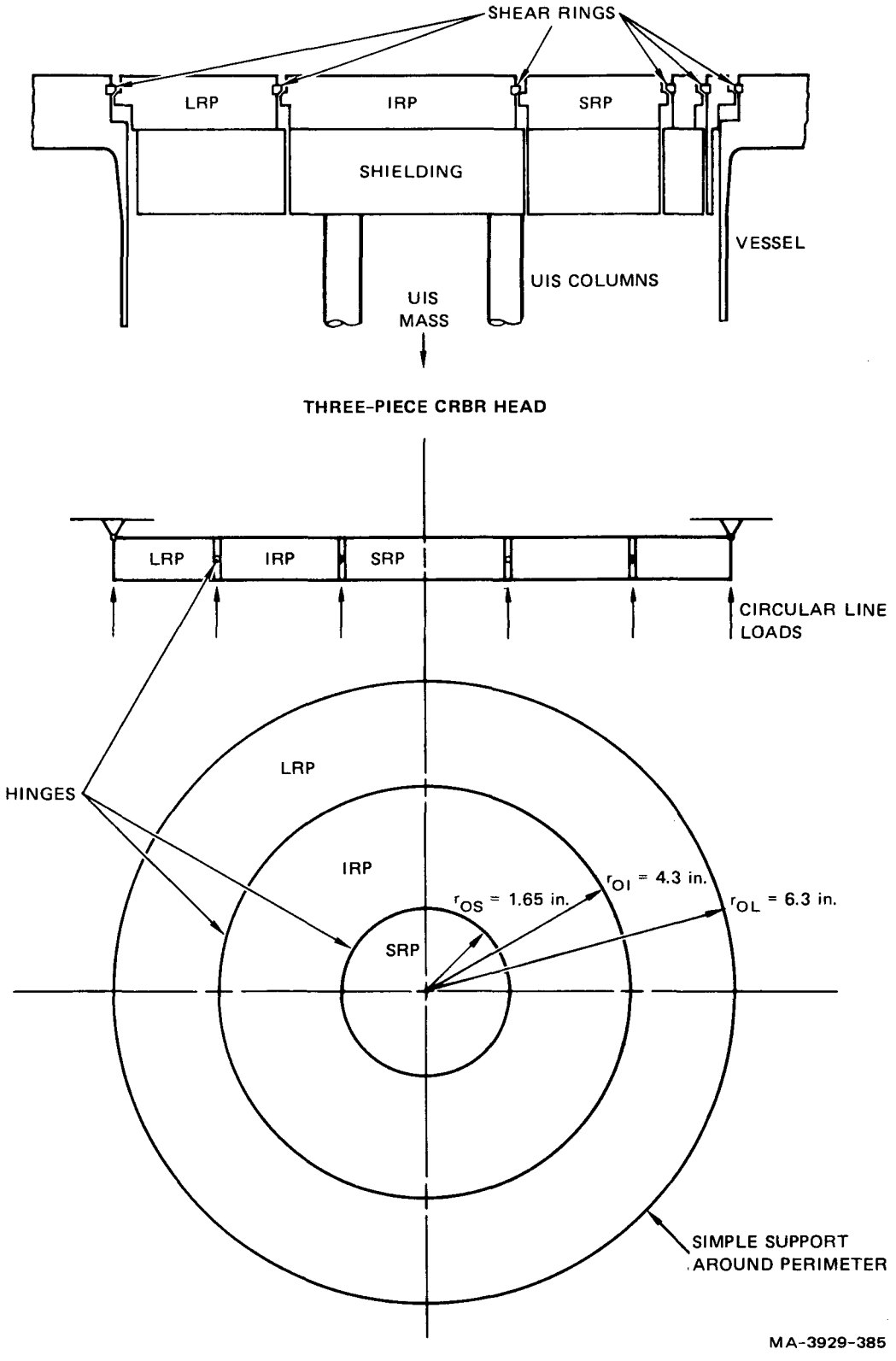

FIGURE H.1 SYMMETRICAL MODEL OF CRBR HEAD

and does not deform. The r_{OI}^6 term is the volume created by the deformation of the IRP, and the r_{OL}^6 term is the volume of the LRP.

To simplify the dynamic response analysis, the complicated three-piece model was replaced by a single simply supported plate that would have the same pressure-displacement and pressure-volume change relationships as the three-piece head. The volume under a uniformly loaded, simply supported plate is:

$$V = \frac{\pi P_o r_{OL}^6}{64 D_{eq}(1 + \nu)} \left[\frac{7 + \nu}{3}\right] \qquad \text{(H-2)}$$

were ν = Poissons ratio (assumed = 0.26) and D_{eq} is the effective bending stiffness of the equivalent plate. This bending stiffness is determined by equating volumes from the three-piece plate and the equivalent one-piece plate.

$$D_{eq} = \frac{D\, r_{OL}^6 \left[\frac{3 + \nu}{2} - \frac{1 + \nu}{3}\right]}{(1 + \nu)[1.03 r_{OI}^6 + 1.89 r_{OL}^6]} = 2.01 \times 10^6 \text{ lb-in} \qquad \text{(H-3)}$$

The displacement of the simple one-piece plate is given by:

$$w(\rho) = \frac{P_o r_{OL}^4}{64 D_{eq}} \left[\frac{2(3 + \nu)}{(1 + \nu)} (1 - \rho^2) - (1 - \rho^4)\right] \qquad \text{(H-4)}$$

and

$$w_{max} = \frac{P_o r_{OL}^4}{64 D_{eq}} \left[\frac{5 + \nu}{1 + \nu}\right] \qquad \text{(H-5)}$$

where $w(\rho)$ is the deflection and $\rho = r/r_{OL}$.

B. Equivalent Single-Degree-of-Freedom Analysis

The dynamic response of the simple plate to a suddenly applied uniform load can be analyzed by solving the differential equation for the equivalent single-degree-of-freedom (SDOF) system. This equation can be stated as:

$$M_e \ddot{x} + K_e x = F_e(t) \tag{H-6}$$

where M_e is the effective mass, K_e is the effective stiffness, and F_e is the effective forcing function of the single-degree-of-freedom system. The effective mass can be calculated from:

$$M_e = \int_A m\phi^2(r,\theta)dA \tag{H-7}$$

where m is the mass per unit area of the plate and $\phi(r,\theta)$ is the mode shape assumed for the displacement of the head. We assume that the head will deform as a simply supported plate under uniform loading. Therefore, combination of equations (H-4) and (H-5) gives:

$$\phi(\rho,\theta) = \frac{w(r)}{w_{max}} = \frac{2(3+\nu)}{(5+\nu)}(1-\rho^2) - \frac{(1+\nu)}{(5+\nu)}(1-\rho^4) \tag{H-8}$$

where $w(\rho)$ is the static deflected shape of the plate, and w_{max} is the maximum deflection at the center of the plate. Substituting equation (H-8) into equation (H-7) and performing the integration gives:

$$M_e = 0.2954\pi r_{OL}^2 m \tag{H-9}$$

Since $\pi r_{OL}^2 m$ is the total mass of the plate M,

$$M_e = 0.2954M \tag{H-10}$$

The effective forcing function is given by

$$F_e(t) = \int_A F(r,\theta,t)\phi(r,\theta)dA \qquad \text{(H-11)}$$

Substituting equation (H-8) into equation (H-11) and performing the integration gives:

$$F_e(t) = 0.4601\pi r_{OL}^2 P_o(t) \qquad \text{(H-12)}$$

Since $P_o(t)$ is uniform over the plate and πr_{OL}^2 is the area of the plate, equation (12) can be reduced to:

$$F_e(t) = 0.4601F(t) \qquad \text{(H-13)}$$

The effective stiffness is defined as:

$$K_e = K_L K \qquad \text{(H-14)}$$

where $K_L = F_e/F$ and K is the stiffness of the plate, which can be expressed by:

$$K = \frac{P_o A}{w_{max}} \qquad \text{(H-15)}$$

where A is the area of the plate and w_{max} is the maximum displacement of the plate. Substitution of (H-5) into (H-15) and using (H-3) gives $K = 2.439 \times 10^6$ lb/in.

The quivalent load factor $K_L = F_e/F = 0.4601$ is obtained from (H-13)

$$K_e = K_L K = (0.4601)(2.439 \times 10^6) = 1.12 \times 10^6 \text{ lb/in} \qquad \text{(H-16)}$$

The natural period of the plate is

$$T = \frac{2\pi r_{OL}^2}{\lambda}\sqrt{\frac{m}{D_{eq}}} = 1.93 \times 10^{-3}\text{sec} \qquad \text{(H-17)}$$

where $\lambda = 4.977$ is a constant for a simply supported plate vibrating in the first mode and m is the mass per unit area of the plate.

The natural period of the effective SDOF is

$$T_e = 2\pi\sqrt{\frac{M_e}{K_e}} = 1.93 \times 10^{-3}\text{sec} \qquad \text{(H-18)}$$

The natural period of the effective SDOF in the same as the real system as it should be.

The equivalent forcing function is an approximation to the slug impact load. The approximation is shown in Figure H.2 and can be characterized as an impulse that gives the head an initial velocity of 122 in/sec (10.2 ft/sec) and a triangular load that has an instantaneous rise and decays to zero when $t_d = 1.2$ msec.

The maximum displacement occurs when $\dot{x} = 0$

$$x = \frac{V_o}{\omega}\sin\omega t + \frac{F_e}{K_e}(1 - \cos\omega t) + \frac{F_e}{K_e t_d}\left(\frac{\sin\omega t}{\omega} - t\right) \qquad \text{(H-19)}$$

$$\dot{x} = V_o\cos\omega t + \frac{\omega F_e}{K_e}\sin\omega t + \frac{F_e}{K_e t_d}(\cos\omega t - 1) \qquad \text{(H-20)}$$

where V_o is the initial velocity and $\omega = \sqrt{\frac{K_e}{M_e}}$.
Solution of (H-20) with $\dot{x} = 0$ gives $t = 0.680$ msec. The maximum displacement at $t = 0.680$ msec is $x = 0.102$ inch. The displacement at the shear ring joint between the LRP and IRP in the symmetric model (Figure H.1) is 0.050 inch. The peak force acting on the shear ring occurs when the displacement reaches a maximum and is equal to $K\,x_{max}$. This force is 2.5×10^5 lb, which corresponds to a stress per unit length of the

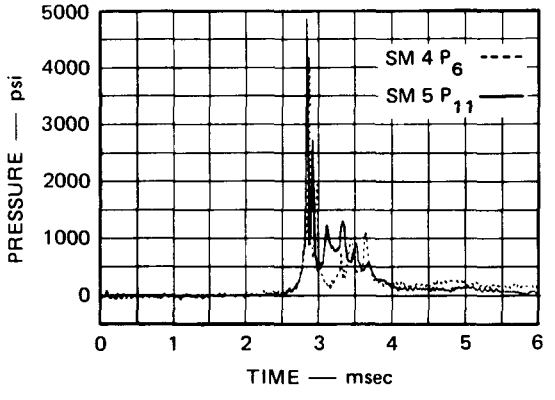

SLUG IMPACT LOAD

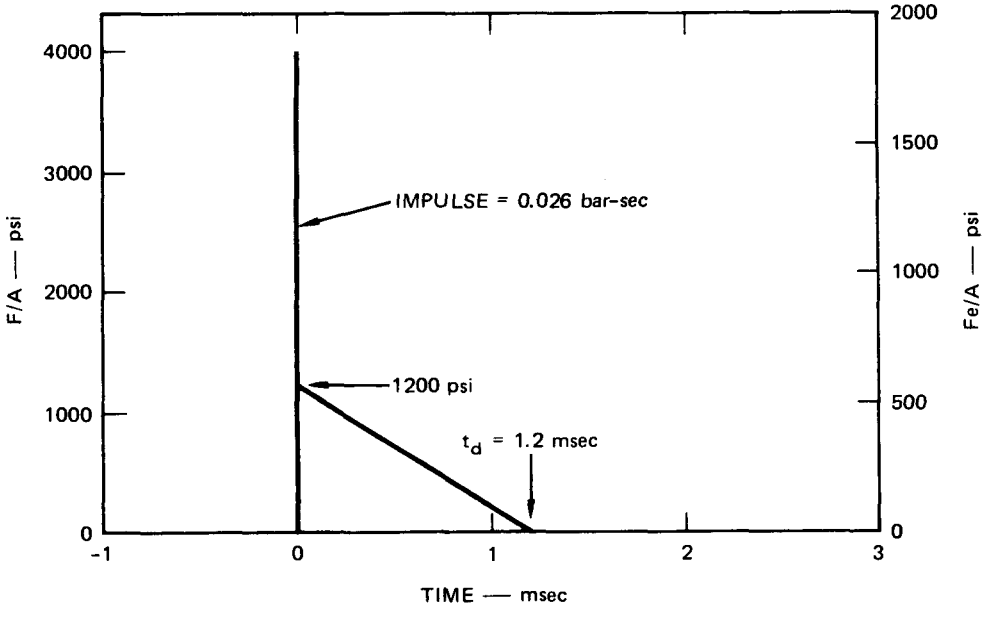

APPROXIMATION TO SLUG IMPACT LOAD

MA-3929-386

FIGURE H.2 EQUIVALENT SLUG IMPACT LOAD

large shear ring of 35.9×10^3 lb/in^2, which is about half of the shear yield stress of the shear ring ($\sigma_{ys} = 68 \times 10^3 \times$ lb/in^2).

C. Summary

The following results summarize the analysis of head motion discussed above:

Peak displacement of head under slug impact $w_{max} = 0.102$ inch

Peak displacement at IRP-LRP joint, $w = 0.050$ inch

Time of peak displacement, $t_{max} = 0.680$ msec

Natural period of head, $T = 1.93$ msec

Peak shear ring stress/unit length, $\sigma_{smax} = 3.59 \times 10^4$ psi/inch